EPFL

Comprehensive Interactive Soft Interfaces for Wearable Tactile Feedback

Harshal Arun SONAR

■ École
polytechnique
fédérale
de Lausanne

2021

Acknowledgments

I would like to express my sincere gratitude to Prof. Jamie Paik for seeing potential in me and inviting me to RRL. Her trust in my abilities and always motivating me to push the boundaries helped me grow both in my personal and professional career. I also want to thank my thesis committee: Prof. Tamar Makin, Prof. Michaël Wiertlewski, Prof. Herb Shea, and Prof. Silvestro Micera, for reviewing my research work and their insightful comments.

The journey of Ph.D. has been filled with the ups and downs of research successes and challenges; I want to thank all my friends spread across the globe, my buddies Sujay, Nahit, Mukul, Mangesh, Sudeep, Nihar, Sachin, Neha, Varsha, Salil and all of you whom I couldn't mention. A special one to Sonal for not forgetting to call and let me forget that I always forget to call and is always a soul to resonate with. I want to extend my sincere gratitude to all the RRL members, both present and past, especially Z, JL, Sagar, Chris, Matt, Juan, Fred, and Mete, for your support and having such a strong lab culture beyond the friendships to more like a family. Thank you Ben and Michelle, our comet visitors from US, to further cheer and foster the ideas for next generation of soft robots. I want to sincerely thank our administrative support Anouk, Monica, Carole, Joanna, and Julia, for always being there and taking care of the administrative sides right from the first invitation letter until the organization of my thesis preprints.

I want to thank my funding source, the SNSF and NCCR robotics consortium for enabling a collaborative environment and bringing the sense of community filled with opportunities for interdisciplinary research further enriching various dimensions of robotics. It allowed me as a young scientist to be able to reach in person to many prominent researchers across the robotics fields, have the possibility to conduct research together, and help address much broader challenges. I would like to thank all my collaborators for all the efforts we put together and the insightful discussions to propel the science further, especially Sanne, Raffa, Aaron and Marie, thank you. I want to thank EPFL HR, TTO, Research Office and endless efforts different EPFL programs have been putting together in to help students, researchers and future entrepreneurs to eventually benefit society as a whole.

Last but not the least, I thank my moral backbone: my mom, dad and my little brother for being there as a virtual extension and taking great care of themselves in my absence. I promise all these times I have been devoting towards a better world for all of us. Thank you Emeline to make especially these last months of stressful time livelier and Les Lamatins, my flatmates, all five of them, a big thanks and lots of love.

Harshal Sonar,

Lausanne, 11 May 2021.

Abstract

As the field of robotics continues to grow outside the manufacturing environment into our daily lives, the interactions between humans and robots are increasingly becoming close and dynamic. This type of environment requires robots to be less rigid, multi-functional, safer, and compliant with human bodies. These interactions can involve multiple modalities of information transfer to achieve a fully immersive experience with virtual reality (VR), auditory, olfactory or haptic feedback. Such robotics interfaces are ideally suited for medical rehabilitation, elderly assistance, to at-home entertainment devices. However, the traditional rigid robotic devices fail to address some of the design criteria posed for safety, compliance, material functionality, physical limitations on the mechanical design. In some particular cases, the system design and complex control algorithms solve the problem of active compliance, but still, the solutions are generally non-adaptable, heavy, and costly.

In the case of wearable technologies, the robotic device requires high interactivity with humans demanding requirements in terms of- (1) material properties as lightweight, compliant, and safe interface and (2) interface to provide smooth communication and interaction strategies with human and robot. The traditional robotic systems are fast, accurate, and can handle large torques. However, they are also, application-specific and not suitable as it is for the wearable scenario due to the contradictory design requirements. In the past decade, soft robotics has emerged as a novel approach to solve the complex problems faced by rigid robots using inherent softness and compliant material properties. The design for the future interactive wearable interfaces thus may lie in the intersection of developments in the fields of wearable technology and soft robotics.

Although it is an attractive idea to use soft materials to solve the contradictory design needs faced by traditional wearable robots, there are challenges in finding the right materials, designing actuators, sensors, and their integration to fulfill the application requirements. In addition, soft robotics being a recently emergent field in robotics, the existing tools in terms of materials, mathematical modeling, and robot design limit the applicability domain of soft robots. These problems are tackled through rapidly emerging functional materials, finite element analysis (FEA) of soft materials, manufacturing techniques like 3D printing, smart composite manufacturing (SCM), and laser micro-machining. By relying on structural and compliance, the properties of soft robots greatly reduce the load on system design and control loop as far as safety in interaction is concerned.

Designing a wearable interactive interface with soft materials for wearability, portability, cost-effectiveness, easy customization, and modularity as per the task requirement in mind would be one of the ideal solutions to tackle the wearability challenge. It can be a cost-effective solution for at-home assistive rehabilitation or a wearable interface for entertainment with high customization. It also allows developing novel methods of soft sensing, soft actuation, development of control strategies, and human in loop protocols to maximize the utilization of inherent material properties and environment around the robotic device.

Hence, in my Ph.D. research, I develop and create hardware and software towards an immersive interactive soft virtual-tactile environment focusing on the wearability, portability, easy customization, and modularity aspects. I developed a low profile soft pneumatic actuator-skin (SPA-skin)

with distributed sensing and actuation capabilities for testing various levels of complex vibrotactile feedback: the multilayer composite of high-sensitivity PZT pressure sensors and vibratory SPA can produce up to 3 N output force at 0-100 Hz. This demonstrated that SPA-skin produces distinctive and dynamic haptic force feedback under modulated varying time, force, and spatial resolution.

Furthermore, a complete framework for designing a tactile feedback skin for specific wearable applications is developed, starting from the material selection and actuator design and concluding with the validation of the subject's perceived feedback. As soon as the SPA-skin is required to be worn by humans, the complexity of the problem multiplies due to lack of proper grounding to ensure the blocked forces. The platform is further optimized for application space in fMRI compliant environment and a user study protocol for somatosensory thresholds is designed. The modulable and controllable nature of SPA-skin's tactile feedback provides much-needed validation using BOLD signals from brain imaging.

SPA-skin, and the findings presented herein, provide a foundational platform to further investigate the sensitivity of human skin and decipher mechanoreceptor reactions for a diverse range of human-robot interactions and wearable technologies. This design framework is also extended for studying the bidirectional interaction with human-in-loop VR applications.

Keywords

Soft Sensors, Soft Robotics, Wearable Haptics, Tactile Feedback, Virtual Tactile Reality, Soft Pneumatic Actuator Skin

Résumé

Alors que le domaine de la robotique continue de s'étendre au-delà du domaine industriel dans notre vie quotidienne, les interactions entre l'homme et les robots deviennent de plus en plus étroites et dynamiques. Ce type d'environnement exige que les robots soient moins rigides, multifonctionnels, plus sûrs et compatibles avec le corps humain. Ces interactions peuvent impliquer de multiples modalités de transfert d'informations afin d'obtenir une expérience totalement immersive avec une réalité virtuelle (VR), un retour auditif, olfactif ou haptique. Ces interfaces robotiques conviennent parfaitement à la rééducation médicale, à l'assistance aux personnes âgées ou encore aux dispositifs de divertissement à domicile. Cependant, les dispositifs robotiques rigides traditionnels ne répondent pas à certains critères de conception tels que la sécurité, la conformité, la fonctionnalité des matériaux et les limitations physiques de la conception mécanique. Dans certains cas particuliers, la conception du système et les algorithmes de contrôle complexes résolvent le problème de la conformité active, mais les solutions restent généralement non adaptables, lourdes et coûteuses.

Dans le cas des technologies portables, le dispositif robotique nécessite une grande interactivité avec les humains, ce qui exige des exigences en termes de : (1) propriétés matérielles pour une interface légère, souple et sûre et (2) interface pour fournir une communication fluide et des stratégies d'interaction avec l'homme et le robot. Les systèmes robotiques traditionnels sont rapides, précis et peuvent gérer des couples importants. Cependant, ils sont également spécifiques à une application et ne sont pas adaptés dans un scénario portable par l'humain en raison d'exigences de conception contradictoires. Au cours de la dernière décennie, la robotique molle est apparue comme une nouvelle approche pour résoudre les problèmes complexes rencontrés par les robots rigides en utilisant la douceur inhérente et les propriétés des matériaux souples. La conception des futures interfaces portables interactives pourrait donc se situer à l'intersection des développements dans les domaines de la technologie portable et de la robotique molle.

Bien que l'idée d'utiliser des matériaux souples pour résoudre les besoins de conception contradictoires des robots portables traditionnels soit séduisante, il est difficile de trouver les bons matériaux, de concevoir les bons actionneurs et capteurs et de les intégrer au sein d'une même plateforme pour répondre aux exigences de leur application. En outre, la robotique molle étant un domaine récemment apparu en robotique, les outils existants en termes de matériaux, de modélisation mathématique et de conception de robots limitent le domaine d'application des robots mous. Ces problèmes sont résolus grâce à l'émergence rapide de matériaux fonctionnels, à l'analyse par éléments finis (FEA) des matériaux souples, aux techniques de fabrication telles que l'impression 3D, la fabrication de composites intelligents (SCM) et le micro-usinage au laser. En s'appuyant sur les propriétés structurelles et de conformité des robots mous, on réduit considérablement la charge sur la conception du système et la boucle de contrôle en ce qui concerne la sécurité de l'interaction.

La conception d'une interface interactive portable avec des matériaux souples pour la portabilité, la rentabilité, la facilité de personnalisation et la modularité en fonction de la tâche à accomplir serait l'une des solutions idéales pour relever le défi de la portabilité. Il peut s'agir d'une solution

rentable pour la rééducation assistée à domicile ou d'une interface portable pour le divertissement avec une personnalisation élevée. Elle permet également de développer de nouvelles méthodes de détection et d'actionnement souples, ainsi que des stratégies de contrôle et des protocoles humains en boucle, afin de maximiser l'utilisation des propriétés inhérentes des matériaux et de l'environnement du dispositif robotique.

Par conséquent, dans le cadre de ma recherche doctorale, je développe et crée du matériel et des logiciels destinés à un environnement virtuel-tactile immersif et interactif en mettant l'accent sur les aspects de portabilité, de facilité de personnalisation et de modularité. J'ai développé une peau-actionneur pneumatique souple à profil bas (SPA-skin) avec des capacités de détection et d'actionnement distribuées pour tester différents niveaux de retour vibrotactile complexe : le composite multicouche de capteurs de pression PZT à haute sensibilité et de SPA vibrant peut produire jusqu'à 3 N de force de sortie à 0-100 Hz. Cela démontre que la peau SPA produit un retour de force haptique distinctif et dynamique sous une résolution modulée variable en termes de temps, de force et d'espace.

En outre, j'ai développé un cadre complet pour la conception d'une peau de retour tactile pour des applications portables spécifiques, de la sélection des matériaux et la conception de l'actionneur, et à la validation des valeurs perçues par les sujets pour l'application. Dès que la peau SPA doit être portée par des humains, la complexité du problème se multiplie en raison de l'absence d'une mise à la terre appropriée pour assurer les forces bloquées. La plateforme est ensuite optimisée pour l'utilisation dans un environnement conforme à l'IRMf et un protocole d'étude des utilisateurs pour les seuils somato-sensoriels est conçu. La nature modulable et contrôlable du retour tactile de SPA-skin fournit la validation nécessaire en utilisant les signaux BOLD de l'imagerie cérébrale.

SPA-skin et les résultats présentés dans ce document constituent une plateforme fondamentale pour étudier plus avant la sensibilité de la peau humaine et déchiffrer les réactions des mécano-récepteurs pour une gamme variée d'interactions homme-robot et de technologies portables. Ce cadre de conception est également étendu à l'étude de l'interaction bidirectionnelle avec les applications de RV à boucle humaine.

Mots-clés

Capteurs souples, robotique molle, haptique portable, retour tactile, réalité tactile virtuelle, peau d'actionneur pneumatique souple.

Contents

List of Figures

List of Tables

List of Equations

Chapter 1　Introduction

1.1　Background

As the field of robotics continues to grow outside the manufacturing environment into our daily lives, the interactions between humans and robots are increasingly becoming dynamic and physical. These interactions require robots to be less rigid, multi-functional, safer, and compliant to interact with human bodies. These interactions can involve multiple modalities of information transfer to achieve an organic and fully immersive experience with virtual reality with visual, auditory, olfactory, or haptic feedback. Such robotics interfaces are ideally suited for applications like medical rehabilitation [1], medical technologies [2], entertainment, telepresence and, virtual or augmented reality [3], further blurring the borders between humans and robots while extending human capabilities. However, the traditional rigid robotic devices fail to address some of the design criteria posed for safety, compliance, material functionality, physical limitations on the mechanical design. In some particular cases, the system design and complex control algorithms solve the problem of active compliance but still, the solutions are generally non-adaptable, heavy and costly [4]–[7].

In the case of wearable technologies, where the frontiers of physical human-robot interaction (pHRI [4], [8]) lies, the robotic device not only requires a high level of interactivity with humans but also demands- (1) material properties such as light weight, compliant and safe interfacing, and (2) interface to provide a smooth communication and interaction strategies with human and robot. The traditional robotic systems are fast, accurate, and can handle large torques. However, they are also, application-specific and not suitable, as it is, for the wearable scenario due to the contradictory design requirements. In the past decade, soft robotics has emerged as a novel approach to solve the complex problems faced by rigid robots using inherent softness and compliant material properties. The wearability of soft technology can further be used to improve the traditional haptic communication devices that provide limited wearability due to their bulky and rigid-form factors [9]–[11]. The design for the future interactive wearable interfaces thus may lie in the intersection of developments in the fields of wearable technology and soft robotics.

Although it is an attractive idea to use soft materials to solve the contradictory design needs faced by traditional wearable robots, there are challenges in finding the right materials, designing actuators, sensors, and their integration to fulfill the application requirements. In addition, soft robotics being a recent field in robotics the existing tools in terms of materials, mathematical modeling and unconventional robot design approaches limit the applicability. Soft materials usually exhibit complex mechanical behavior due to the hyperelastic nature of the silicone materials. Such a behavior makes it complicated to accurately predict actuation amplitude or output blocked forces with analytical or linear material models. The use of finite element analysis and integration of sensing elements to acquire information about the actuation state is hence necessary for a controlled actuation [12]–[14]. It is difficult to control distributed motions in high speed. A completely active approach to control is not practical. Passive characteristics of device materials and mechanisms should be utilized [47].

Subsequently, human haptic perception, which in addition to visual and auditory feedback, plays a key role in understanding and exploring our local environment, needs to be well understood while developing such interactive interfaces. Sense of touch, haptics, has evolved as a medium of human-robot communication over the past few decades, where communication via haptic interfaces is used to deliver tactile cues for applications such as alert messages [15], [16] augmented feedback for sensory substitution in prosthetics [17], [18] or for the visually impaired [19]. Additionally, *a versatile user interface can optimally utilize the limitations of the human sensory system to simplify its design*. The knowhow from haptics research along with the unique challenges for wearable interfaces motivate to further investigate possible solutions that not only combine rich haptic feedback with a wearable interface but further expand their applicability and effectiveness.

1.2   Wearable interactive interfaces: requirements and challenges

Human haptic perception, in addition to visual and auditory feedback, plays a key role in understanding and exploring our local environment [1]. Desktop-scale haptic devices specifically dedicated to providing tactile stimulation have proven their efficacy in various applications [1]–[3]. More compact vibratory haptic actuators have been integrated into the system for human-machine interactions such as, car steering wheels, and joysticks [5],[6]; However, these implementations provide limited physical feedback such as in mobile phones and joysticks that can mainly modulate its frequency. Furthermore, this frequency and amplitude modulation are not feedback-controlled. The recent advances in linear resonant actuator (LRA) based and voice coil based actuation are able to generate the much-needed finer control over modulation for a range of frequencies. Even though in most of the cases open-loop operation of tactile actuators is sufficient to provide basic tactile feedback cues, for wearable technology to have accurate physical feedback to the wearer, it needs to be like any other robotic device, produce feedback-controlled actuation. As such, the requirements for wearable devices, which include adaptability and conformability to the body of a human wearer, extend to the haptic technology itself. Existing haptic technologies, however, do not meet the physical requirements necessary to achieve these demanding characteristics. These unique requirements and challenges posed for the wearable interactive interfaces can be summarized as below (Figure 1.1):

Physical interface
- Light-weight & compliant materials
- High bandwidth
- Safe interaction

Control environment
- Matching real-virtual models
- Sensor feedback control
- Zero latency

Human-in-loop
- Wearability
- Multi-modal information transfer limitations
- Sense of touch
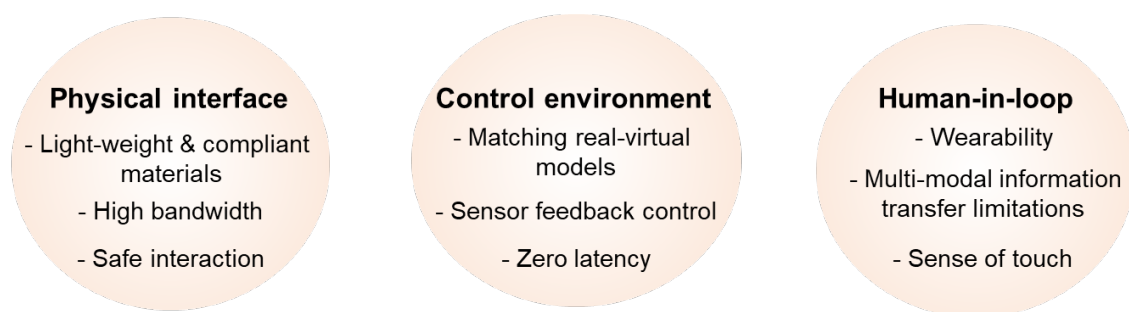
Figure 1:1 **General requirements and challenges towards designing wearable interactive interfaces.**

Physical interface: Interfaces that are conformably interacting with human skin should be made of thin elastic materials that have moduli similar to skin, 0.3 - 2 MPa [10],[21]–[24]. This way, the interface can conform to the body. They shall still be able to operate over a wide frequency range (10 - 400 Hz) and forces up to 1 N [27]. Currently available tactile feedback devices primarily rely on rigid piezoelectric elements or electromechanical eccentric mass motors.[4],[6] Compliant actuators can be developed with elastomeric materials such as soft silicones that have elastic moduli

similar to human skin [23], [24], [26]. The softness and compliance of the soft robotic systems have been useful in many wearable applications ranging from assistive technologies, medical rehabilitation to entertainment.[11], [28]–[32]. Vibrotactile displays using electro-active polymer (EAP) based soft actuators have tackled many of the challenges associated with conventional, rigid vibrotactile devices, but provide limited wearability as they require high-voltages [33]–[36]. Soft material-based pneumatic actuators, composed of elastically inflatable fluidic chambers, have demonstrated their benefits in robotic applications through large-scale deformation and high compliance, and have the potential to be adapted for wearable haptic applications [13], [37]–[43]. However, the pneumatically powered actuators though are suitable for wearable systems, have a limitation due to the requirement of external pump that limits the portability.

At the same time, as the most commonly used vibration motors function by exploiting the resonance of the vibration motor, so their output bandwidth is limited around the resonant actuation frequency of 10 Hz centered around 120 - 250 Hz. That had resulted in limited work has been done for interfaces at relatively low frequencies (in the range 10 to 100 Hz) [44]. One reason for this is while voice coil actuators can be used to meet this requirement, they suffer from their bulky size and hence limited wearability of the system [45]. Furthermore, there is no available tactile platform with integrated sensors to modulate actuation force, frequency, and stimulation pattern accurately, which limits the quantitative measurement of the stimulation parameters in this range. These all challenges and requirements get further stringent with electromagnetic interference or compliance (EMI/EMC) rules when the interfaces need to be functional in fMRI or BMI environment.

Control environment: Wearable haptic devices need to ensure that the force imparted on the wearer is consistent with respect to the perceived performance: this depends on how the interface fits and moves with the body. The effective tactile feedback also requires accurate and coherent force transfer from the actuator to the wearer regardless of the external loading or manufacturing variations. This requires embedded sensing of the actuator state and corresponding corrective measures through closed-loop control. There has been significant development in entirely soft and stretchable physical sensors to measure crucial parameters as strain and pressure are experienced.[28], [30], [46]–[49] Advanced manufacturing technologies like soft 3D printing have combined soft sensing within soft actuation.[50] Such integration of soft sensing with soft actuation creates the possibility of closed-loop control, which is essential to adapt to the external loading conditions suitable for wearable scenarios. The use of a distributed network of localized sensors cannot only correct for actuation but also helps to understand the surrounding environment for a better model of the world for the robot. However, no wearable haptic device has demonstrated closed-loop control capabilities with embedded sensing. It has been particularly difficult to design soft stretchable sensors, which can perform under high strains and high strain rates needed for state estimation of high-speed vibratory actuation.

Extending further toward applications in virtual reality, the control environment needs an understanding of the state of the human body in virtual for the robotic interface to generate respective audio, visual or tactile feedback. Special care needs to be taken in system design and integration to enable zero latency while providing corresponding tactile feedback through a lower-level control system for seamless human-robot interaction.

Human-in-loop considerations: To have effective communication via human skin, the limitations of human somatosensory perception beyond mechanical grounding, play a key role in determining how much information can be transferred. These have been studied by delivering bursts of vibration onto the forearm using an array of actuators [9], [10], [44]. Notably, the vibrotactile sensitivity and localization thresholds of the non-glabrous skin of the forearm have been measured along the entire forearm, from elbow to wrist, using seven equally-spaced piezo

ceramic tactors [10]. The haptic perception is responsive over a range of 20 to 400 Hz, with decreasing skin sensitivity at higher frequencies [51]. In this range, we have two major mechano-receptors, the rapidly accelerating type –I (RA-I), the Meissner corpuscles and rapidly accelerating type–II (RA-II), the Pacinian corpuscles that are responsible for the perception of tactile feedback. The RA-I type mechano-receptors offer high localization sensitivity as they are located just below the surface of the skin, whereas RA-II type mechano-receptors, targeted by most vibratory tactile interfaces, have low localization sensitivity and higher amplitude sensitivity [10], [52]. This difference in the mechanical properties of mechano receptors make their study interesting and important for the development of a stimulation-rich tactile feedback platform. Such displays shall also cater for the two-point threshold detection and distribution density of as high as possible for stimulation points, ranging from 2 mm for a fingertip to 18 mm at the forearm, respectively. To better adapt this for future tactile displays, we not only need a test platform but also human-in-loop testing protocols that can quantify the somatosensory thresholds of actuation amplitude, traveling wave delay, and the frequency difference perceived by real human skin, particularly in its most sensitive range, 10-100 Hz.

Finally, the way humans perceive a physical object is a mix of six different properties associated with the object namely: rough texture, fine texture, lateral friction, size, temperature, or weight [7–9]. To successfully recreate a realistic feeling of touch, a tactile feedback device should be able to integrate more than one of these multi-modal sensations [9]. Researchers have characterized, modeled and rendered tactile properties such as surface texture and hardness on tabletop interfaces [7,8,10]. It is particularly challenging to develop a wearable tactile-feedback device able to generate for example: texture feedback, as this requires delivering a wide range of actuation frequencies. Recent technological efforts in wearable prototypes relied heavily on the use of vibrotactile electromechanical actuators; however, their localization capability and the range of actuation frequencies remain restricted. The use of voice coil actuators at the fingertips [11–13] or the proximal phalanges [14] helped to improve the actuation range; however, this actuator solution is impractical in terms of size and weight needed to achieve a reasonable spatial resolution. Dielectric elastomer actuator (DEA) – based haptic devices combined with a wearable platform supply the much-needed mechanical compliance with human skin [15,16]. However, they have a high voltage requirement and provide limited actuation forces in the range of 0.3 - 0.6N.

In conclusion, existing solutions for haptic feedback are compelling for a defined range of frequencies and forces in the present format of a tabletop or for a few wearable platforms. However, currently, there is no comprehensive solution or design that allows rendering a rich set of tactile feedback and verify the effectiveness of this physical feedback, especially in a wearable format. In fact, *what is lacking is a low-profile platform, mechanically transparent, capable of providing high fidelity tactile feedback.*

1.3   Thesis statement

Today's robots need to be and are becoming increasingly aware of the environment including the presence of humans around them. Bringing robots into direct contact with humans requires them to be inherently safe and compliant during the interaction. Especially in wearable robotic devices, the interactivity between humans and robots is significantly higher. To create an interactive wearable robotic interface, two challenges need to be addressed: (1) wearable technology that is safe, lightweight, and compliant in actuation and (2) augmented interactivity through different modes of interaction with humans.

Recent research efforts on novel materials and soft actuation mechanisms show a promising future for using *soft robotics* in wearable devices. Soft robots have provided preliminary solutions in safety, customisability, and simple control desired by any wearable system. However, fully integrated solutions for such applications are yet to be realized. The second challenge is achieving augmented interactivity through different modes of interaction with humans. These interactions can be multi-modal for a fully immersive experience through visual, auditory, and haptic feedback. This requires further integration of tactile interfaces and virtual reality with the soft wearable interfaces to achieve an intuitive, immersive, and safe interface for the user. Therefore, understanding developments in tactile interfaces, virtual reality components, and their integration with soft wearable technology becomes crucial.

In this thesis, we focus on the goal of creating hardware and software technologies towards *an immersive interactive soft virtual-tactile environment* by considering wearability, portability, easy customization, and modularity properties. This would be a cost-effective solution for applications in home assistive rehabilitation, haptics research, and a plug-n-play wearable interface for entertainment with high customization. The development of novel soft sensors, soft actuators for such wearable interfaces will allow validation of capabilities of soft robotic interfaces and provide research opportunities for unconventional system design, prototyping techniques, and control method development approaches. Further, the platform will be a pivotal tool to develop and explore the human-in-loop feedback and somatosensory considerations for optimal haptics.

This dissertation attempts to tackle these challenges of wearable interfaces for human-robot interaction with the following key questions:

How can we match the mechanical compliance of a robotic device with human body for wearable and dynamic feedback?

A *wearable* interface facilitates humans and robots being physically coupled and moving together to achieve a final common goal. This by nature requires a lightweight, low-profile, mechanically transparent mechanism that can impart a wide range of actuation stimuli to convey tactile information. The robotic interface shall also have a proper mechanical grounding, ideally mechanical impedance similar to that of human skin with elasticity moduli 0.3 - 2 MPa[12], [23]–[26] for maximum compliance. We address this by investigating and developing novel soft material-based sensors and actuators, specifically soft pneumatic actuators (SPAs). SPAs, characterized by their inflatable, low-weight silicone rubber membranes, and their innate environmental compliance,[1–3] play a major role in the soft robotics field. Diverse applications of SPAs already exist, including biomimetic systems [7–12] showing versatile locomotion [7,9,11,13] and grasping capabilities,[1,11,12,14] surgical tools,[15] limb exoskeletons,[16] and devices for muscle rehabilitation in hands.[17] Although the scalability, customizability, and diversity of SPAs are widely recognized,[18–20] comprehensive techniques for designing, modeling, and fabricating soft actuators are not yet in place. Our goal here is to achieve a low-profile, customizable SPA design that is capable of providing *dynamic* tactile feedback in the range of 10-400 Hz and force range

of 0.1-1 N where human skin is most receptive [27]. We achieve this goal with a soft silicone-based skin-like SPA design with submillimetre thickness, fabricated with layer-by-layer manufacturing. Similarly, compliance matching for transparent wearability shall allow for a wearable interface to be coupled with human body without any hindrance in range of motion or accumulated stresses. A more systematic metric and measurement protocol shall be developed to quantify the wearable system's performance. We focused on achieving this using intrinsic compliance matching of the wearable interface with materials that behave similar to human skin (0.5-2 MPa) and are low profile (1-2 mm) in form factor.

The soft materials may be compliant but exhibit a complex mechanical behavior due to their hyperelastic nature. Accurately predicting the output blocked forces, as well as facilitating simulation-based iterative design, is challenging with the traditional analytical modeling approach. We develop a finite element analysis-based modeling tool to investigate the SPA design as well as investigate additional distributed sensing to enable controlled feedback and mitigate the non-linearity through intelligent control algorithms. The addition of an extra sensing layer will not only enable controlled feedback but also dampens manufacturing defects. This additional sensing layer requires the sensing elements to be ultra-thin, flexible, customizable, and to be distributed over the surface. We further investigate the trade-off between cost, design customization, stretchability, sensitivity, and non-linearity for sensor selection and integration with the SPA layer. We also investigate different shapes, materials, and configurations in terms of *nxn* array to achieve a high-density distributed bi-directional soft skin-like interface for vibrotactile feedback.

How do we 'model' for a multimodal system that has multiple physical parameters?

For an ideal human-robot interaction, the physical experience need not be limited to a single stimulation [1], [53]. This requires a dynamic interface that allows for intuitive information transfer between user environment and virtual environment using visual, aural, haptic, or even olfactory feedback to enable an immersive experience (Figure 1:2). The challenge here is to achieve augmented interactivity through these different modalities. This requires the integration of tactile interfaces and virtual reality components in the design framework of the soft wearable interface.

The user environment consisting of both the human body and the robotic platform has to have components that enable a bidirectional interaction translation between their respective virtual and physical representations (Figure 1:2). These components shall be coherent in translating the physical properties to an equivalent digital entity and vice-versa. We investigate design methodologies and process flow while keeping *modularity* and *adaptive* nature of physical hardware as well as the control environment to integrate with other virtual reality modes. This allows the control environment to be functional across different application requirements and to integrate various sensing, actuation, and control elements at the hardware and software level. A well-known consensus about multi-modal nature of interaction converge up to three modes of information simultaneously, more than that negatively hampers the user involvement, as studied but not limited for the field of robotic-rehabilitation [1]. Hence, it is also critical develop a structured framework considering an information theoretic approach to measure the effectiveness of performance with multimodal human-robot interface bandwidth.

We further developed system models and control algorithms to distinguish the environmental interactions, while keeping the low-level closed-loop control capabilities. Similarly, machine learning-based algorithms are explored to reduce the number of wires in distributed sensing with a reconfigurable localization. To help in improving the design preselection before fabrication as well as the forward kinematics for feedback control, material characterization and FEA-based SPA-design tools are developed.
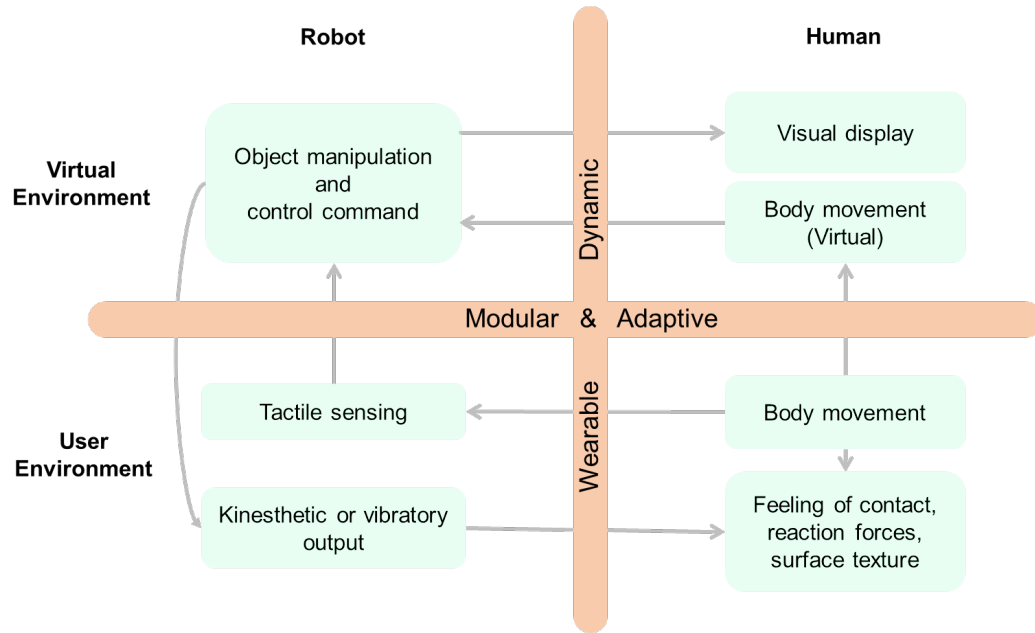
Figure 1:2 Human to robot interaction interface, and virtual physical user environment interaction interface

Finally, the multi-modal nature of the feeling of touch itself needs to be explored for the generation of a realistic and rich sensation through understanding the possible ways to recreate the haptic sensations like texture, size, and shape of an object. Specifically, for a wearable scenario where proper mechanical grounding and generation of a wide range of stimulation is a challenge. Most available wearable devices are limited to a single tactile mode, we attempt to integrate multiple tactile sensations to study the possibility of such a design and overall benefits.

How can we close the tactile virtual reality loop with human feedback?

It is essential to understand the human factors affecting the effectiveness of the feedback delivery, to help to optimize the tactile interfaces further and decide on the interface design paradigm. One way to close the loop with humans is through human-centric interface design that enables discovering the human cognitive and somatosensory thresholds that will be guidelines to device future interfaces. These thresholds will be a key data point to determine the mechanical performance requirement as well as to tune the tactile interface further to better match the expected feedback. The sensory thresholds like minimum amplitude (or force) detected over a range of actuation frequencies, the two-point threshold to determine the minimum distance between adjacent actuators and the maximum rate at which the information can be transferred to the device are a few of the important design parameters. Meanwhile, the available tactile feedback devices have mainly relied on electromagnetic components, even the ones used in understanding the nature of somatosensory feedbacks; this has been a limiting factor for actuation range in 100-350 Hz. While voice coil actuators can be used to meet this requirement, they suffer from their bulky size and hence limited wearability of the system [45]. However, there is no available tactile platform with integrated sensors to modulate actuation force, frequency, and stimulation pattern accurately, which limits the quantitative measurement of the stimulation parameters.

Similarly, we not only need to qualitatively measure the effectiveness of tactile feedback given to the body with user feedback, but the methods like fMRI imaging allow us to record a respective tactile stimulation in the sensory-motor cortex area of the brain and then use this information to tune the feedback modes. Specifically, we benefit from the use of soft silicone-based materials

and pneumatic actuation that can be used in fMRI or brain-machine interface (BMI) environments. This makes SPA-skin an ideal platform to expand the horizons of studying the human brain through novel high-fidelity tactile feedback cues derived based on stimulation duration, location, actuation level, and stimulation frequency. This also invites close collaboration between researchers in neuroimaging and roboticists to develop user studies and protocol designs *for qualitative and quantitative measurement of somatosensory thresholds using fMRI and soft interactive display*.

The modular, adaptive and highly configurable nature of the soft actuator skin interface helps in developing a plug-n-play platform to extend the capabilities of VR platforms, brain-machine interface, or fMRI imagining applications through a wearable interactive display array and a portable augmented feedback device.

The main contributions of this thesis hence can be summarized as:

1. **Design and development of a novel soft pneumatic actuator (SPA)-skin interface.** The SPA-skin acts as a single bi-directional input-output platform with distributed sensing and actuation capabilities, generating a wide range of tactile feedback at a variety of frequencies.

2. **Modeling, characterization and closed-loop control of SPAs with integrated sensing**. The dynamic performance characterization of SPA conducted to optimize the design geometry, material selection, and prediction of expected force/amplitude using Finite Element Analysis tool. Similarly, presenting an integrated low latency, high-speed control environment for virtual reality interactions to provide an immersive experience.

3. **Portable pneumatic control system and soft valve design**. The pneumatic flow control system and peripheral components, including tubing, valves, pressure regulator and controller inputs are optimized for the given application force and tubing length requirements to achieve maximum fidelity and portability.

4. **Validation of SPA-skin as a versatile wearable platform with human-in-loop system design.** Study of diverse vibrotactile feedback and protocol development to obtain various human somatosensory thresholds using brain-machine interface and fMRI in 10-100 Hz range.

1.4 Thesis Outline

In my PhD research, I develop and create hardware and software technologies towards *an immersive interactive soft virtual-tactile environment* focusing on the wearability, portability, easy customization and modularity aspects (Figure 1:3).
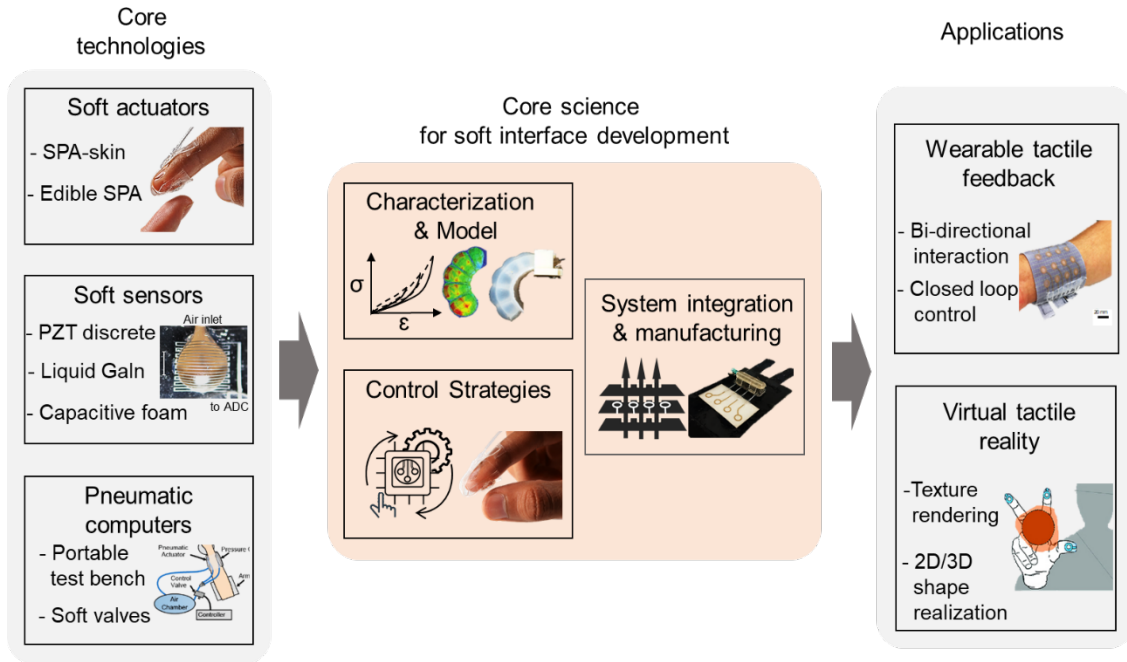
Figure 1:3 Development framework of soft robotic technologies and core science for immersive human-machine interactive environments.

In the following chapters, I discuss the design of soft wearable tactile transducers (Chapter 2), control strategies for soft interactive interfaces (Chapter 3), system-level integration (Chapter 4), work towards human-in-loop tactile feedback design (Chapter 5), and conclusions and outlook (Chapter 6).

In Chapter 2, I first describe my work in creating soft pneumatic actuators aimed towards an intimate human-robot interaction, and sensors for tactile interaction. The integration of these two types of transducers to create a novel low-profile soft pneumatic actuator-skin (SPA-skin) with distributed sensing and actuation is then presented, with details on design selection, material characterization, and dynamic performance characterization. Lastly, I discuss Modeling aspects of the SPA design using FEA tools aimed at improving the actuator performance and optimizing actuator design for different applications.

In Chapter 3, the control strategies for soft interactive interfaces are presented. I present first the potential to use piezoelectric transducers as an embedded sensing mechanism in the SPA-skin, given their desirable high-frequency responsiveness. Following this, I discuss the considerations for using soft sensors for an entirely soft SPA-skin. Finally, I present work on generating virtual environments for incorporating multimodal haptic feedback in a wearable system.

In Chapter 4, the system integration of the wearable tactile array is presented. I first discuss the SPA-skins tactile array design, material selection, characterization, and control. A mesoscale valve for pneumatic control and a discussion of the pneumatic flow path optimization is then discussed; Finally, I describe the peripheral interfaces for creating a fully port-able system compatible with fMRI environments for the future human-in-loop studies.

In Chapter 5, I discuss my work on using the SPA-skin as a platform for exploring human-in-loop tactile feedback design. I present work on using an SPA-skin to study the effect of stochastic resonance on proprioception. I then discuss work on using SPA-skins to characterize human somatosensory thresholds. This includes work on observing brain activity as a function of tactile feedback using functional magnetic resonance imaging (fMRI), a challenging environment due to its electromagnetic interference compliance greatly constraining the material selection.

In Chapter 6, I summarize the work presented in this thesis and discuss their impact on the field of wearable interactive interfaces and beyond. Lastly, I discuss potential avenues of future work in this field.

Chapter 2   Soft wearable interfaces: design, characterization, and Modeling

2.1   Introduction

The latest wearable technologies[1] demand more intuitive and sophisticated interfaces for communication, sensing, and feedback closer to the body. Such interfaces require flexibility and conformity without losing their functionality even on rigid surfaces. Although there have been various research efforts in creating tactile feedback to improve various haptic interfaces and master-slave manipulators, we are yet to see a comprehensive device that can both supply vibratory actuation and tactile sensing. Haptic feedback is generally divided into two classes – namely tactile and kinesthetic. The devices required for providing kinesthetic feedback are comparatively large and heavy [59]–[62] and thus less suitable for a wearable scenario. In wearable devices, vibrotactile feedback is considered as one of the safest and most popular ways to interact with the human body [27], [63].

The currently available wearable haptic interfaces mainly rely on producing feedback using electromechanical components, specifically using an eccentric mass motors that has resonance frequency centred around 120-250 Hz [4],[6]. They are compact in form factor but provide a limited wearability owing to their heavy and rigid structure (Table 2:1) . Furthermore, the tactile feedback

---

is limited in bandwidth due to mechanical resonance; the linear resonant actuators provide better control over actuation bandwidth but are still limited in wearability due to rigid form factor [64].

	C2	Haptuator	Tactaid	ERM pancake	ERM cylinder	SPA-skin
Min. Size	Φ: 30 mm h: 8mm	Φ : 14 mm h: 29 mm	w: 18.5 mm d: 25.4 mm h:10 mm	Φ : 10 mm h: 3.6 mm	Φ : 8.8 mm h: 25 mm	**Φ : 6 mm h: 1-2 mm**
Frequency	250 Hz	50 Hz	250 Hz	175 Hz	225 Hz	**0-100Hz**
Weight	17 g	15 g	6.5 g	2 g	4.6 g	**2g (with sensors)**
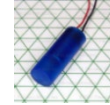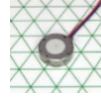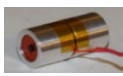
Table 2:1: Comparison of off-the-shelf electromechanical tactile feedback actuators with SPA-skin prototype

An ideal device for wearable tactile interfaces should be lightweight, compliant, safe, and incorporate multiple sensing and actuation points over a distributed surface. Such a conformable interface to interact with human skin with maximum compliance, should be made of thin elastic materials that have moduli similar to skin, 0.3 - 2 MPa [12], [23]–[26]. This way, the interface can conform to the body and deliver a wide frequency range (1 - 400 Hz) and forces up to 1 N, as required by human proprioception [27]. While, available tactile feedback devices primarily rely on rigid piezoelectric elements or electromechanical eccentric mass motors; compliant actuators can be developed with elastomeric materials such as soft silicones that have elastic moduli similar to human skin [23], [24], [26].

The softness and compliance of the soft robotic systems have been helpful in many wearable applications ranging from assistive technologies, medical rehabilitation to entertainment [11], [28]–[32]. Vibrotactile displays using electro-active polymer (EAP) or dielectric elastomeric actuators (DEA) based soft actuators have tackled many of the challenges associated with conventional, rigid vibrotactile devices but so far provide limited wearability as they require high-voltages [33], [34], [65], [65], [66] (Figure 2:1). The recent development in zipped hydraulic HAXEL have been able to encompass a multi-modal feedback with a high bandwidth actuation [65]. Soft material-based pneumatic actuators, composed of elastically inflatable fluidic chambers, have demonstrated their benefits in robotic applications through large-scale deformation and high compliance and have the potential to be adapted for wearable haptic applications [13], [37]–[43]. However, the significant shortcomings for the pneumatically powered actuators are the size of the power supply and tube length limiting the bandwidth for the high frequency of actuation, which we separately address in Chapter 4.

(A) SM polymer (B) SM Alloy (C) SPA

(D) DEA (E) DEA with pillar (F) HAXEL

Figure 2:2: **State of art technologies using novel soft material based novel actuation mechanisms** for wearable tactile feedback. (A) Shape memory polymer based high-density tactile display[67] (B) Shape memory alloy based wearable finger-tip haptic device[68]. (C) Soft pneumatic actuator based haptic glove for at home rehabilitation [69]. (D, E) DEA/EAP based wearable haptic feedback devices [66], [70]. The use of stiff pillar in the middle of DEA film allow for high force generation around resonant frequency in (E). (F)Haxel, uses hydraulically amplified zipping electrostatic actuation for EAP filled with a dielectric liquid for high-bandwidth, multimodal tactile feedback. [65]

In this chapter, we introduce the concept of a low-profile soft pneumatic actuator (SPA) based skin-like interface to tackle these challenges. The SPA-skin prototype allows for bidirectional tactile feedback for an intuitive and responsive wearable interface. We describe the design and fabrication of the first version of SPA-skin integrated with piezoelectric sensors. The integrated sensing facilitate for better understanding of external environment on the robot side for producing an adaptive and coherent tactile feedback. The sensor-actuator integrated SPA-skin is characterized for system identification and understanding the ability of this new interface for a covering range of human haptic sensations. The PZT based sensing layer is suitable for active distributed sensing but is not entirely soft and can only detect dynamic interactions. To tackle this, we develop another SPA-skin design with an entirely soft monolithic design using liquid metal meanders as sensing elements. We examine in detail the mechanical performance compared to the SPA model and the sensitivity of the sensors in both cases for the application in vibrotactile feedback.

The integration of sensing and actuation in SPA-skin paves the path for a more sophisticated tactile feedback actuation through closing the loop with the sensor layer. To enable this, we thoroughly characterize the sensor, SPA and integrated system performance for both static and dynamic behaviors. The system identification and robust performance metrics obtained in chapter 2 help in further development of more sophisticated control algorithms to provide a coherent tactile feedback over a broad range of actuation frequency and also, to integrate the SPA-skin with multimodal interactive control environment in chapter 3.

The SPA and soft sensing technologies are further extended to more environmentally friendly edible SPA development as well as developing pressure localizing soft sensor skin to cover interactive surfaces in section 2.4. Use of gelatin based SPA design allow to demonstrate the flexibility

and application of soft pneumatic actuator fabrication methods with a new material that is bio-degradable, repairable and provide comparable performance as that of silicone actuators. Followed this, the sensing abilities of wearable interfaces were explored with a novel distributed sensing scheme using capacitive soft foam as discussed in section 2.4. The latest advances in machine learning classification were used that demonstrated a novel way to use only 2 measurement points for n sensing locations leaving the need for individual physical address lines.

SPA-skin design while focused on compliance, wearability and integrated sensing, it critical also to optimize the actuator design for performance requirements. In section 2.5, we focused on developing a design optimization tool for soft material based actuators, which owing to their high-strain inflation and hyper-elastic nature of soft materials are complex to model. We developed a finite element analysis based Modeling tool kit to better predict the feasible designs for variation in material selection, required output blocked forces, and operational constraints. We further discuss how the FEA based Modeling is used and experimentally validated not only for traditional bending or linear chambered SPAs but also for the SPA skin, resulting in a ring shape actuator for optimal bandwidth and inflation profile in section 2.5.

2.2 A novel soft pneumatic actuator - skin with distributed sensing

The human tactile sensory response is scattered in frequency range, and both temporal and spatial resolution making the determination of the vibrotactile actuator's specifications difficult. In general, tactile sensation is perceived through four different types of mechanoreceptors inside human skin. The mechanoreceptors responsible for vibrotactile sensation are the rapidly adapting (RA) and pacinian corpuscle (PC) receptors with perceptible frequencies ranging from 3 to 100 Hz and 100 to 400 Hz, respectively [27]. Therefore for effective tactile sensing the operational frequency range is selected between one of the two along with a minimum spatial resolution of 1 - 2 mm for human fingers [71], [72].

We propose a soft pneumatic actuator (SPA) based skin-like interface to tackle the problem of compliant actuation requirements through its thin, lightweight, easily customizable and compliant design [73]. The design uses soft silicone-based 2D monolithic manufacturing to achieve pneumatic vibrotactile actuation with the desired properties. The addition of an extra sensing layer over the SPA-skin enables closed-loop control of the actuation amplitude and dampens manufacturing defects. This additional sensing layer requires the sensing elements to be ultra-thin, flexible, customizable, and to be distributed over the surface. Recent developments in wearable sensor technology have made it possible to embed piezoelectric element-based sensors [74], conductive fabrics, electro-active polymers [75], [76], and other families of stretchable and flexible sensors [77], [78] into soft silicone. The sensor selection has a trade-off between cost, design customization, stretchability, sensitivity, and nonlinearity. We selected piezo ceramic (PZT) sensors due to their high sensitivity, low cost, and customizability while losing on stretchability properties for integration into the SPA-skin. Multiple PZT sensors can be distributed over the actuation surface to provide multiple points for sensing. To demonstrate the benefit of the SPA-skin design we developed a circular shaped multi-actuator SPA-skin for application on human fingertips. A similar construction could be adopted for other vibrotactile feedback applications.

2.2.1 SPA-skin design

The SPA-skin is a thin wearable device that contains sensor-embedded pneumatic actuators with multiple actuation points for vibrotactile feedback, as shown in Figure 2:1. Since it is made of silicone, the SPA-skin's overall material property is dictated by the pliant silicone. It is lightweight, inherently compliant, and highly customizable, therefore, could cover wide and curvy surfaces (Figure 2:1(C)). These characteristics make the SPA-skin ideal as a wearable device covering various parts of the human body. Further, we used Dragon Skin 30 silicone to make SPA skin for a medically safe (Smooth On Inc. 2015) and compliant interface with human skin. In this Section, we explain the design and fabrication process of SPA-skin (actuation layer), PZT sensing layer and their integration.
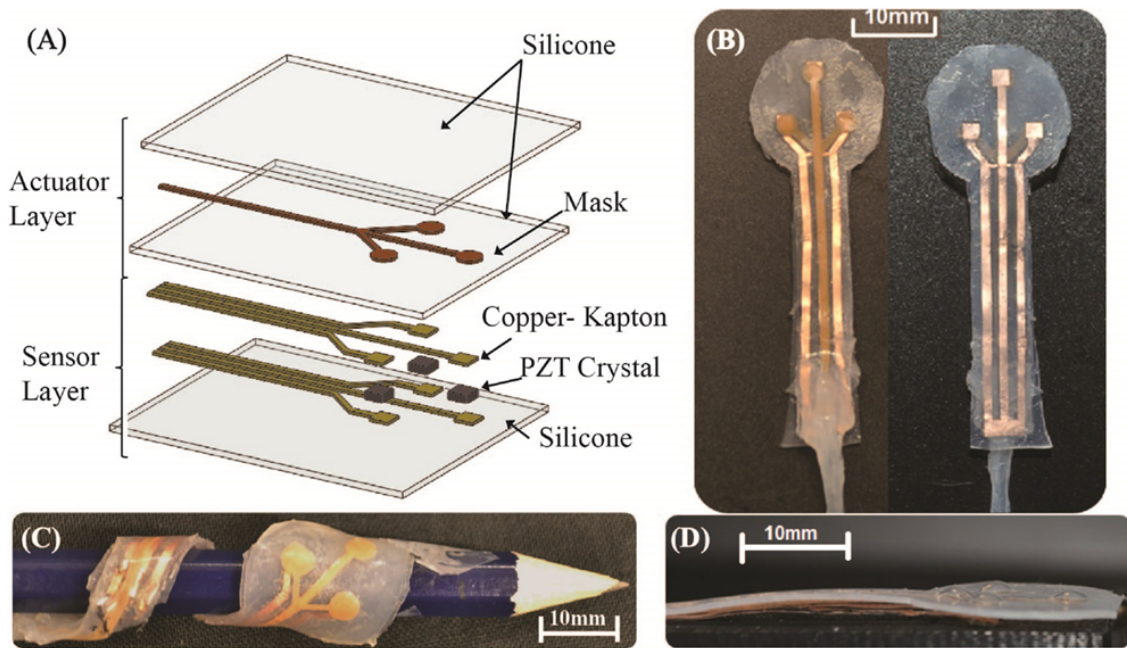
Figure 2:3**The construction of the SPA-skin with integrated PZT sensors**. The schematic of the multi-layer construction of SPA-skin (A). The prototype shows three sensor pixels for independent measurement (B). Functional SPA-skin prototype on a curvy surface (C). The three 4 mm diameter vibratory actuators generate 0.8 - 1 mm vertical amplitude range (D).

Actuator design: The actuation layer of SPA-skin consists of two silicone layers and a masking layer sandwiched in between. The first three layers in Figure 2:1(A) constitutes for the SPA layer. The masking layer fabricated using a polypropylene adhesive tape, avoids bonding between these two soft silicone layers, which after curing facilitates the passage of air through the masked layer creating desired shape inflation. The shape and design of actuator is determined by laser cutting of the masking tape according to the application. The requirements for the actuator diameter and distributed actuator density are based on the feedback application location on human body [72]. From these requirements, we can then decide the average input pressure and the desired output blocked force needed for manipulation from a single actuator. Our prototype demonstrates distributed sensing and vibrotactile feedback capabilities of SPA-skin designed for

human fingers. We obtained a sufficient blocked force of **0.3 N with a 3 - 4 mm diameter bubble** shaped actuator with 0.4 mm silicone thickness for this application. The distributed actuator single input channel SPA-skin is capable of generating tactile feedback for a variety of actuation frequencies ranging from **5 - 100 Hz**.

Sensor design: Sensors for the SPA-skin need to be distributable over an area, thin and flexible to be wearable. For our application, we focused on achieving a high-level of sensitivity as well. Soft material matrix - based sensors are often considered for wearable devices but display high drift and slow response that are not suitable for our goal. Piezoelectric ceramics (PZT) are known to be highly sensitive to normal forces applied, and can be embedded into silicone substrates[74]. A PZT element can measure dynamic forces by converting the applied mechanical stress into electrical voltage. Our sensors have multiple pixels of PZT elements discretely distributed over a surface area in the form of grid. The PZT elements are connected using flexible circuit tracks manufactured by laser cutting the copper plated kapton (polyamide) material. The construction is then embedded inside silicone material for additional support and electrical insulation as shown in Figure 2:1(A).
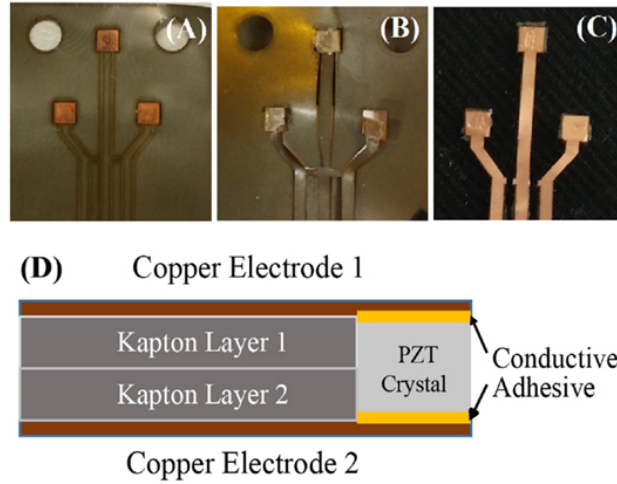
Figure 2:4 **Pixel PZT Sensor Layer Composition.** The copper-kapton sheet is engraved using a micro-UV laser to facilitate electrical contact with PZT material (A). Conductive adhesive tape is attached to bond the PZT crystal (B). The same process is repeated for another copper-kapton sheet and then both electrodes are placed on top of other with PZT crystal sandwiched in between (C). Schematic view of the sensor construction (D).

The sensors for SPA-skin use 2×2 mm^2 size PZT element sandwiched between flexible copper-kapton circuit track. Initially the copper-kapton sheet is finely engraved with a low power laser to remove the kapton layer and make the copper layer visible for connection with PZT element as shown in Figure 2:2 (A). After the engraving process the copper-kapton sheet is cut into the specific shape required to form electrodes. A two way Z-direction conductive adhesive tape (3M^{TM}-9705) is used to bond individual PZT element with the copper-kapton electrodes as shown in Figure 2:2 (B). This sensor manufacturing procedure enables both signal conducting electrodes to be placed on top of the other without causing a short circuit. The Kapton layer between the electrodes acts as an electrical insulator as depicted in Figure 2:2 (D). This helps reduce the area required for electronic tracks and also improves the sensor density for distributed sensing. For our prototype design we manufactured three sensors, evenly distributed on a 6 mm circular periphery to sense both the internal and external interactions with the SPA-skin, as shown in Figure 2:2 (C).

Sensor actuator integration The critical challenge for multi-layer based sensors is their integration in parallel. The integration process is simplified by independently manufacturing the sensors and SPA-skin. Additionally, this helps to reduce the failure modes as both sensing and actuation components can be tested before final integration. The layerwise construction of SPA-skin and the integrated PZT sensors is depicted in Figure 2:1 (A). The sensitivity of vibration feedback is maximized by placing the sensing elements exactly below the bubble shaped actuator. The flexible circuit tracks are then designed and laser cut, based on the distributed configuration of the sensor elements. The integration process of the PZT sensors into SPA-skin starts by spin coating a thin layer of uncured Dragon Skin 30 onto a cured 400 µm thick layer for bonding purpose. A properly connected working sensor is then placed on this uncured silicone. The SPA-skin prototype is then aligned with the sensors and placed on the uncured layer. A small weight is placed on this setup to avoid air bubbles forming inside the bonding layer and the assembly is cured at 60°C for 1 hour to ensure seamless bonding. Figure 2:1 (B) shows the final SPA-skin prototype with integrated sensors consisting three sensors and three actuators distributed over the soft surface. Using this design procedure, we obtained following parameters for sensor integrated SPA-skin as shown in Table 2:1:

SPA skin parameters	Value
Single actuator diameter (mm)	4
Single sensor size (mm)	2 × 2
Overall thickness (mm)	1.4–1.5
Modulation height (maximum) (mm)	1
PZT sensitivity (Acer et al., 2015)	0.25 V/N
Maximum input pressure (kPa)	90
Actuator bandwidth (Hz)	55

Table 2:2Geometric and functional specifications of the fist SPA-skin prototype

2.2.2 SPA-skin: embedded sensing mechanism and dynamic model

The sensorized, tactile SPA-skin prototype focuses on two main functionalities; it not only detects vibrotactile feedback amplitude but also measures external interactive forces. Even with high sensitivity PZT sensors it is challenging to accurately estimate the dynamical forces on the system as the real world interaction forces the human body experiences are small (in the order of 0.1 - 3 N) [72]. Also, the wearable application requires raw sensor signal to be carried along relatively long wires from application area to the electronics unit, which adds extra capacitance and external signal noise. These issues in combination lowers the signal to noise ratio, which requires external amplification and active filtering of noise to improve PZT signal quality. In this Section, we discuss the embedded sensing mechanism for SPA-skin to obtain the operational specifications for the embedded PZT elements both mathematically and experimentally. These specifications are then used to design the electronics for the distributed sensing system. This is followed by the design of the control system for augmenting the SPA actuation amplitude with sensor data.

Embedded sensing mechanism A PZT sensor does not provide a static signal as the piezoelectric effect only occurs when external forces cause a change in the PZT crystal's physical dimensions. Due to their high sensitivity PZT, sensors are suitable for measuring dynamically changing signals such as vibration or impact force. The sensors produce electrical field, E, proportional to the stress, σ, generated by an external force, F_{piezo}, specifically in the normal direction. The transfer function for the generated electrical voltage changed can be obtained using the direct piezo electric effect given as $E = g_{33} \times \sigma$ where, g_{33} is the piezoelectric voltage coefficient in the normal direction. The relationship in terms of generated open circuit voltage, V, becomes $V = (g_{33} \times t_A) \times F_{piezo} V = (g_{33} \times t_A) \times F_{piezo}$ where 't' is thickness of PZT and 'A' is the PZT area under stress. For the PZT material (PSI-5H4E) we obtained $V = 0.6 \times F_{piezo}$ with $g_{33} = 19.0 \times 10^{-3} - 319.0 \times 10^{-3}$ V_m/N, t= 0.127 mm and A= 2×2 mm^2. Using the Equations (124), (125) from ("IEEE Standard on Piezoelectricity" 1988) for quasi-static applications, the unloaded or free piezo sensitivity can be mapped to a clamped piezo sensitivity value through the electro-mechanical coupling factor, k_{33}, as shown in Equation 2:1 and 2:2 .

$$\epsilon_{r_{free}} = \left(1 - k_{33}^2\right)\epsilon_{r_{clamped}}$$

<div align="right">Equation 2:1</div>

This translates to,

$$V_{clamped} = \left(1 - k_{33}^2\right) \times V_{free} = \left(1 - 0.75^2\right) \times 0.6 \times F_{piezo} = 0.2625 \ V/N \times F_{piezo}$$

<div align="right">Equation 2:2</div>

Where, ϵ_r is the relative permittivity of PZT crystal in normal direction, Although significantly better than silicone-based sensors, PZTs too suffer from nonlinearities in the form of hysteresis and creep as piezo electric constant (d_{33}) and dielectric constant (ϵ_r) changes on the application of stress [79], [80]. In our sensor application, we obtain the maximum stress of 0.75 MPa for three N load, which generates the maximum electric field of 0.0145 KV/mm. These values are much lower than the nominal stress (5 MPa) or electric field (0.5 KV/mm) to observe significant hysteresis as presented in [79], [80] for PZT-5H (soft PZT). Also, the dielectric constant and piezo electric constants do not change for applied stress of <1 MPa [81]. Furthermore, the material dynamic equation for the silicone embedded PZT sensor is complex to model due to the hyperelastic properties of silicone, which are more dominant than PZT nonlinearities. The transfer function is also modulated by the thickness of the silicone layer [74]. We experimentally obtained a sensitivity value of 0.24 - 0.26 V/N for a silicone thickness of 0.4 mm from the graph shown in Figure 2:3(A). The sensor response is linearly dependent upon the impact force. These results are comparable with the results in Equation (2) and the result obtained in [74] for the characterization of silicone embedded PZT sensors.
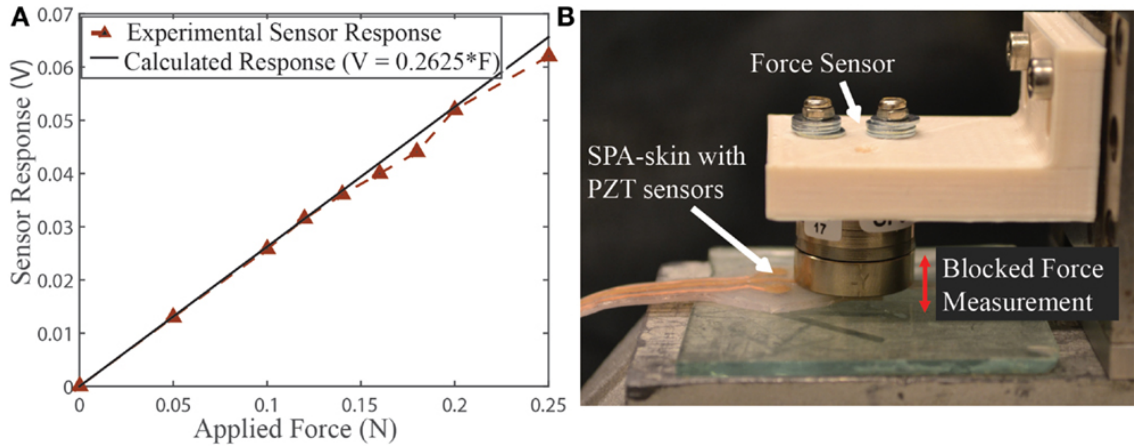
Figure 2:5 **Silicone embedded PZT sensor characteristics.** Silicone integrated PZT sensor response (A) obtained for a 10 Hz stepped force input of different amplitude. Test setup with *Nano*-17 force sensor used for the PZT sensor and soft actuator characterization (B). The *Nano*-17 sensor position can be adjusted precisely in the z-direction to accommodate the exact thickness of SPA-skin.

Integrated system dynamic model The system response of the 4 mm diameter actuation chamber is measured by applying a 10 Hz on-off input signal to the actuator placed under a *Nano*-17 force sensor and a flat plate. The distance between force sensor and the flat plate is same as the actuator thickness (1.4 mm). Figure 2:4 shows the actual blocked force recorded for actuator inflation and deflation. The rise time for the actuator's dynamic response is obtained by first order dynamic system model approximation fitted using the input output data (Figure 2:4 (A)). The presented model has the first-order transfer function $356/(j\omega+356)$, which subsequently yields a time constant of 28 ms and actuator bandwidth of $356/(2\pi)$ = 56 Hz as plotted in Figure 2:4 (B). When a similar system response is recorded using the PZT sensor placed just below the actuator, we obtain a bandwidth of 40 Hz (Figure 2:4 (B)) instead of the modeled bandwidth of 56 Hz. This discrepancy is due to the low pass filtering effect introduced by the charge amplification stage in the sensor readings. This amplifier has a cut-off frequency of 86 Hz, as discussed in the following section. This limits the overall cut-off frequency to 44 Hz, as shown by brown dotted line in Figure 2:4 (B), which is very close to the actual cut-off frequency observed using PZT sensors.
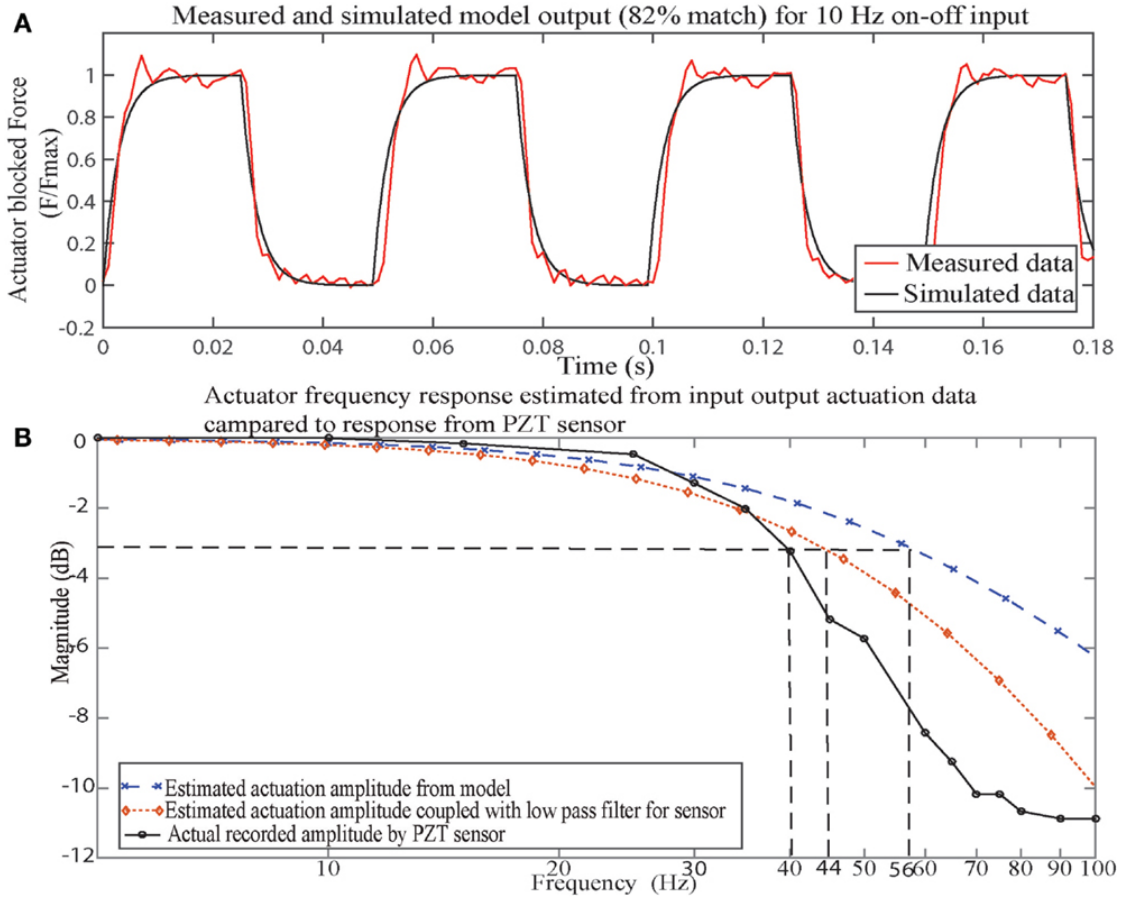
Figure 2:6 **SPA-skin system vibration control response**. SPA-skin actuated at 10 Hz to experimentally obtain the rise-time and bandwidth of the actuator. First-order dynamical system model's output compared to experimentally recorded blocked force output at 10 Hz (A). The rise time of 0.028 ms is obtained with 82 % model fit. The corresponding bandwidth of 56 Hz for first-order transfer function compared with the actual recorded bandwidth of 40 Hz using PZT sensors (B). Low pass filtering at 86 Hz in PZT signal amplification coupled with estimated actuator bandwidth lowers the measured bandwidth to 44 Hz from 56 Hz.

2.2.3 High density distributed sensing and active filtering for wearable environments

Distributed sensing is a critical aspect of the design of any wearable platform. A dense grid of distributed sensing elements makes wearable systems interactive and adaptive towards changes in the physical environment. Furthermore, the sensing layer faces critical challenges, including the signal quality in noisy interactions, sensor density over a specific area, bio-compatibility, flexibility and weight constraints. The PZT sensors are specifically developed for distributed sensing. The novelty in our design includes customizability, high density, parallel information gathering and the possibility of active feedback control. The system design is optimized for distributed sensing by moving most of the signal processing inside a compact digital platform. The block diagram in Figure 2:5 represents the system design for signal acquisition, processing, evaluation and finally active control of the desired vibrotactile feedback. The PZT signal is processed accordingly to obtain a reliable peak value for the periodic force exerted by the soft actuator. A peak detection algorithm and notch filter are developed for decoupling the line noise, external interaction signal and SPA generated interaction signal for improving the signal quality to facilitate feedback control as follows:
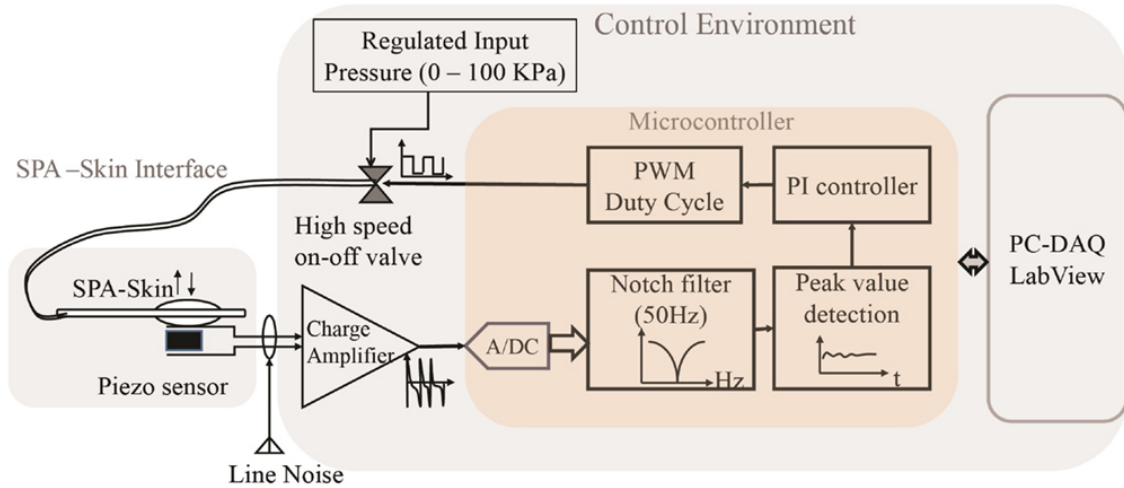
Figure 2:7 **Block diagram for SPA-skin interfaced with the control environment** for a single sensor and actuator. The SPA-skin interface receives pneumatic input and produces piezo electric output. The control environment performs signal acquisition, amplification, conditioning, control and output actuation tasks from the raw PZT signal. Microcontroller based signal processing reduces the circuit area required for multiple sensors, as only a new charge amplifier is added per sensor. The long connecting electrodes from PZT sensor capture external line noise, which gets amplified through charge amplifier block.

Dynamic force sensing and filtering: The SPA-skin is ultimately aimed at measuring and analyzing the various interaction forces with the human skin in everyday life. The distributed PZT sensors are sensitive to dynamic forces producing electric charge spikes proportional to the impact force. The actual interaction forces exerted on PZT crystals are proportional to the peak value of the electrical voltage generated. Therefore for the detection of the impact force, the microcontroller tracks the maximum value of the PZT signal over a complete on-period for the given PWM frequency, f. This peak value is then updated for the next timing cycle and thus, the system has a delay of 1/f . Also, the forces exerted in this case are expected to be less than 3 N/finger [82]. The maximum force exerted by the SPA-skin upon actuation is around 0.3 N at actuation pressure of 70 kPa. This produces a raw signal peak of 75 mV with the given sensitivity of 0.25 V/N. The signal has low amplitude and is susceptible to electrical loading if driven directly through a low impedance circuit. Therefore, a charge amplifier was designed to act both as a buffer circuit and an amplification stage. The PZT signal is amplified and low-pass filtered by the charge amplifier. The amplification factor of 3.9 allows a maximum external force detection up to 10 N with a 2.5 V amplifier output swing, and a cut off frequency of 86 Hz allows filtering of high-frequency noise harmonics. The conditioned signal is then converted into 10 bit digital signal sampled at 1000 Hz for further analysis and recording, as shown in Figure 2:5 . Every PZT sensor requires an analog signal amplification before it can be connected to a low impedance A/D converter pin.

Distributed Sensor Noise Cancellation: A high density of distributed sensing elements comes with an added cost of increased electrical track and wire lengths. These long wires act like an antenna and capture the noise from a variety of AC sources in their environment. Low amplitude PZT signal and noise signal are amplified to the same extent through charge amplifier; to mitigate this effect, we used a second-order digital notch filter Figure 2:6A and B show the components of 50 Hz noise compared to the PZT sensor generated values at 20 Hz and 70 Hz respectively. A separate second-order digital Butterworth filter is implemented for every sensor to remove the 50 Hz signal component. The dashed lines in Figure 2:6A and B show the signal spectrum after removal of the AC noise and display the clear acquisition of the repeated actuator signal. A digital

filter is preferred an analog filter as it reduces the size of the physical system considering one physical filter would be required for each sensor. Furthermore, the digital filter is equally reliable due to a relatively high sampling frequency of 1 kHz.
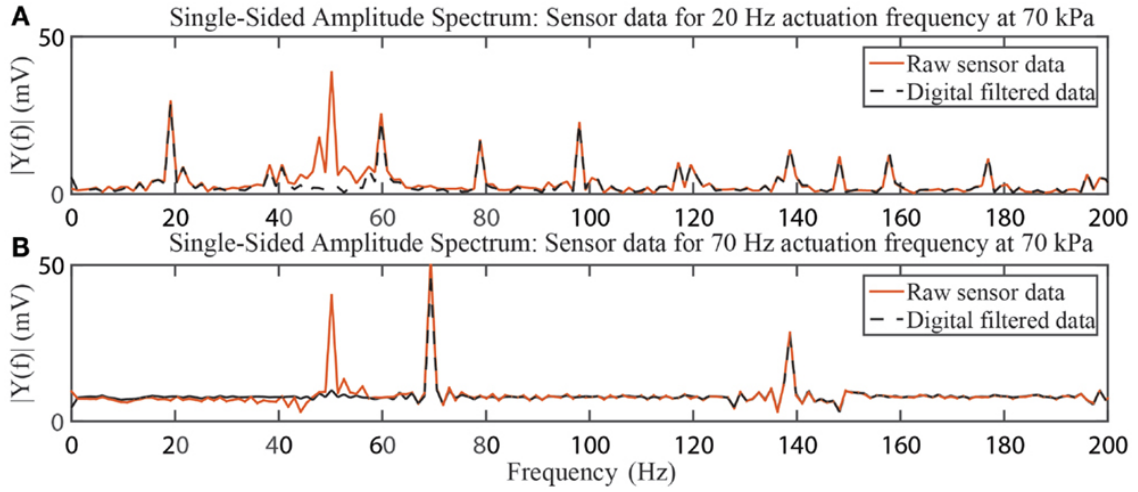
Figure 2:8 **Filtering effect of second order notch-filter on PZT signal quality.** The raw sensor data is acquired for vibrotactile actuation of 20 Hz (A) and 70 Hz (B). The raw sensor data contain large component of line noise which is suppressed using the second digital notch filter.

2.2.4 Conclusions

We introduced a unique, compliant, and distributable actuation system with an embedded grid of sensing capabilities. The distributed sensing with high customizability makes the SPA-skin more versatile to accommodate multiple configurations for wearable applications. Because of its softness and flexibility, it can cover wide and curvy surfaces for actuation and sensing. Furthermore, the presented SPA-skin is both an input and output device that produces modulating vibrotactile feedback over a range of frequencies. The embedded PZT sensors help SPA-skin to precisely sense vibration and to detect external forces and contacts. The novel method of sensor manufacturing allows placing a grid of sensor electrodes over a surface. However, these capabilities are limited by the tethered wires that create a noisy environment. Digital filtering becomes necessary as the sensed signal amplitude is comparable to the line noise captured by the long-running wires acting as an antenna.

Furthermore, the PZT sensor-based sensing layer provides active sensing with high-sensitivity and ultra-thin fabrication. However, it is limited to the flexibility of connecting electrodes and can only measure dynamic changes in interaction forces. The design of sensor electrodes allow for some degree of stretchability for a tight fit on user's body; however as the size of actuator will increase above 5 mm, the SPA inflation will cause shear stress accumulation at the rigid-sensor interface that would lead to delamination with current 2x2 mm^2 sensor pixel size. To tackle these challenges, we updated the SPA-skin design further to create not only a composite and conformant but also a stretchable and monolithic interface with integrated liquid metal sensors, as discussed in Section 2.3.

2.3 An entirely soft self-sensing pneumatic actuator skin for controlled wearable tactile feedback

Wearable haptic devices need to ensure that the force imparted on the wearer is consistent with respect to the perceived performance: this depends on how the interface fits and moves with the body. The effective tactile feedback also requires accurate and coherent force transfer from the actuator to the wearer regardless of the external loading or manufacturing variations. This requires embedded sensing of the actuator state and corresponding corrective measures through closed-loop control. There has been significant development in entirely soft and stretchable physical sensors to measure crucial parameters like strain and pressure experienced.[28], [30], [46]–[49] Advanced manufacturing technologies like soft 3D printing have combined soft sensing within soft actuation.[50] Such an integration of soft sensing with soft actuation creates possibility of closed-loop control, which is essential to adapt to the external loading conditions suitable for wearable scenarios. However, no wearable haptic device has demonstrated such capabilities with embedded sensing, as it has been particularly difficult to design soft stretchable sensors, which can perform under high strains and high strain rates needed for state estimation of high-speed vibratory actuation.

In this section, we propose an updated SPA platform with an entirely soft sensor integrated design enabling flexible, conformal, and distributable interfaces over a variety of surfaces. The integrated sensing with active closed-loop control provide accurate modulation of actuation amplitude and frequency for rich feedback, independent of external loading. The major contributions of this work include:

- Design of an entirely soft tactile interface based on a pneumatic actuation and integrated stretchable liquid metal sensors.

- Characterization of SPA-skin for high-fidelity (0-100 Hz) operation and analytical model to estimate the actuator inflation state using sensor resistance.

2.3.1 SPA-skin design for a monolithic interface

The SPA-skin – a sensor-actuator laminate- is composed of soft silicone elastomers and thin biphasic metal films, as depicted Figure 2:7a. The actuator layer, SPA, consists of an elastomeric membrane that can be pneumatically inflated with a positive pressure input as discussed in previous Section 2.2.1 [54]. This actuator is also fabricated with three thin layers: a middle flexible mask layer (50 μm) to define the actuator's shape, sandwiched between two silicone layers, with a total thickness of 500 μm [54]. However, the process defers in the selection of soft silicone material, which is plasma bondable to enable a monolithic integration with the sensing layer later. The polypropylene mask in the middle masking layer adheres to the bottom silicone and ensures that, upon inflation, deformation occurs in the top membrane. The actuator geometry is governed by the spatial resolution requirement of 20 mm and force requirement of up to 1 N for sensitivity on the application areas on the human back or wrist.[83], [84] The actuator has an area of 10 mm in diameter and has a 2 mm inlet tube (Figure 2a). The sensor layer, an eGaIn filled micro channel membrane, on the other side is prepared with a biphasic (liquid-solid) Gallium-based metallization patterned on a thin silicone membrane [47]. It is then laminated on top of the actuator to complete the soft actuator-sensor interface. The layout of the strain sensor covers the entire area of the SPA in order to record changes in strain upon inflation with positive input pressure. The soft sensor-skin hosts metallic meanders on a 40 μm thick (substrate and encapsulation) on Polydimethylsiloxane (PDMS) film patterned at the resolution limit of the biphasic metallization technique in order to maximize the sensor sensitivity.

The entire SPA-skin is fabricated using PDMS (Dow Corning Sylgard 184) because of its low viscoelasticity [85] and because multiple layers can be covalently bonded with oxygen plasma treatment. The intentional use of the same material for both the actuator and the sensor substrate yields a robust monolithic functional skin with embedded sensing and actuation capabilities. The softness of SPA-skin manufactured matches with that of the human skin to have a compliant and wearable prototype.

2.3.2 SPA-skin characterization

The frequency range of somatic perception for human skin varies from 0 - 100 Hz for rapidly adapting sensor receptors and 100 - 400 Hz Pacinian corpuscles.[27] In order to apply a controlled feedback of the integrated SPA-skin system over such a variety of modulable amplitude and frequency ranges, an accurate model of the steady state and transient behavior is first needed. We, therefore, perform static and dynamic characterization of the SPA-skin to obtain all relevant system parameters necessary for implementing closed-loop control.

Static characterization Despite the addition of extra sensor-layer, we observe a minimal mechanical loading on the SPA with less than 10 % change in the actuator inflation (Figure 2:7b). The covalent bonding between sensor and actuator layers ensures the conformity of the sensor layer around the SPA during inflation. This enables the accurate measure of the strain experienced by the SPA through the soft sensors, even at high strain rates. Upon inflation of the SPA, the resistance of the soft sensor increases due as the biaxial strain increases. The gauge factor (GF) observed for the stretchable metallization is approximately unity and independent of the strain rate[55]. The SPA-skin system exhibited a robust behavior, with less than 10 % deviation in the relative change in resistance ($\Delta R/R$) obtained during high strain rate operation at 20 Hz to a pressure of 25 kPa for a million cycles (Figure 2:7c). Such a robustness highlights the ability of the SPA-skin to be used in the wearable applications over long duration under dynamic operation. The sensors also demonstrate rapid response times under 1 ms, meeting the demands of the high frequency action for vibrotactile feedback. During the cyclic test of 1 million cycles at 20 Hz, a 10 % change of resistance per cycle was observed. This corresponds to an average strain rate of 400 %/s (10 % x 2 x 20 Hz) experienced by the SPA-skin for a million cycles, with continuous current consumption at 1.25 mA throughout the 14 h of testing period.

Dynamic characterization This SPA-skin prototype can modulate the actuation amplitude over 100 Hz of dynamic range of frequencies derived from human mechano-reception capabilities. The SPA-skin is actuated with an on-off pressure input that is regulated at set amplitudes between, 5 kPa and 30 kPa. The dynamic response shows an increase in the relative change in resistance, $\Delta R/R_0$, concomitant to the increase of the actuation pressure at 5 Hz (Figure 2:7d). The inflation and deflation behavior of the sensor-actuator system is repeatable over a range of actuation frequencies, as seen in the five consecutive cycles shown in Figure 2:7c. The system dynamics resulting from the material elastic properties and the actuator geometry with φ 2 mm and tube length of 300 mm, limit the maximum rate of change in inflation/deflation. This manifests as an increase in the baseline and decrease in the maximum output as the operational frequency increases (Figure 2:7e). The cutoff frequency of our SPA-skin design is measured to be 30 Hz, above which the actuation amplitude is less than 70 % of its maximum value. Although the vibration amplitude decreases above 30 Hz, it is still measurable and perceivable to the human skin for the frequencies up to 100 Hz (Figure 2:7f).[83] The measurement system can measure the resistance of sensor dynamically with an accuracy of 0.4 % at 1600 samples per second which enabled recording of 16 samples at 100 Hz. This level of accuracy allowed for measurement of 25 distinct levels for 10 % change in SPA strain.
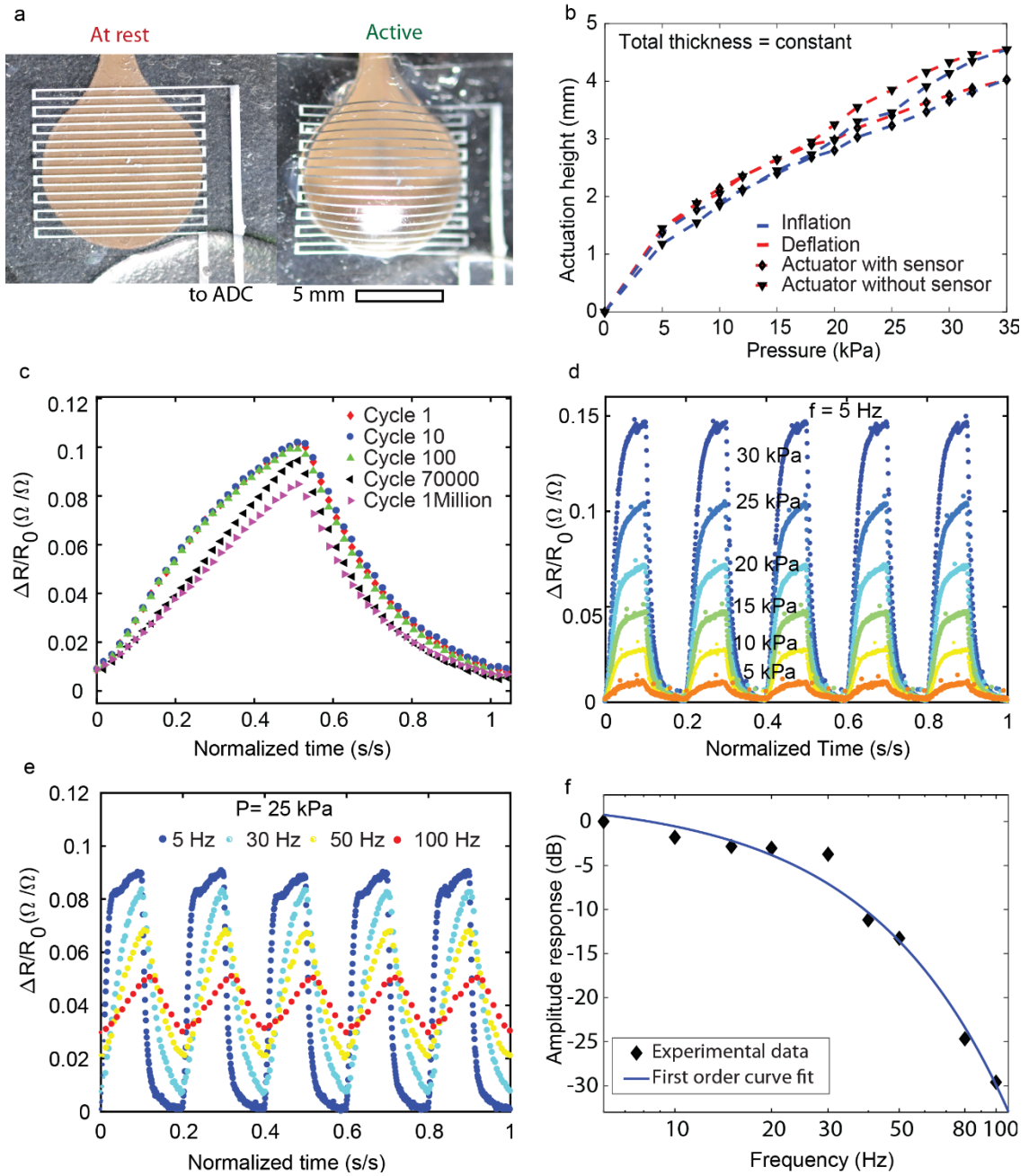
Figure 2:9 **Characterization of SPA-Skin**. (a) An SPA-skin prototype before and during inflation. (b) Actuators of the same thickness with and without laminated sensors show little change in performance. (c) Sensor performance over a million cycles. (d) SPA-skin response for variation input pressure set points from 5 kPa to 30 kPa at 5 Hz. (e) SPA-skin response for variation of actuation frequency from 5 Hz to 100 Hz at 25 kPa pressure set point. (f) SPA-skin amplitude response for variation in actuation frequency.

2.3.3   Analytical model

The static and dynamic characteristics of SPA-skin show the integrated system is repeatable and stable over a range of actuation frequencies and amplitude. The sensor feedback therefore can be used to actively control the SPA inflation height if the relationship between actuation amplitude and measured resistance can be developed. It is also important to note that the soft actuators exhibit complex mechanical behavior upon inflation due to the hyper-elastic nature of the

silicone materials. Such a behavior makes it complicated to accurately maintain the actuator inflation amplitude or output blocked force only with open-loop analytical model without a feedback sensing mechanism. We utilized the integrated resistive strain sensors to predict the average strain experienced by actuator and map it to the actuation height. We developed and experimentally verified an analytical model for the actuator behavior upon inflation, based on the results obtained from the integrated resistive sensor-skin, an external inflation height sensor, and an external pressure sensor (Figure 2:8a). Our model maps the measured resistance change ($\Delta R/R_0$) from sensor to inflation height (h) analytically, based on the actuator inflation geometry and biaxial deformation of material upon inflation. In the first stage, we developed geometrical mapping function for the measured strain for a given inflation height (Figure 2:8a). As the strain experienced by the sensor meanders is equibiaxial, we then map it to corresponding change in resistance value resulting from the actuator inflation.

Assuming a Poisson's ratio (v) of 0.5 for PDMS and an isotropic nature of the soft material, we can assume equibiaxial stress in the actuator membrane upon inflation. Also, the effect of reduction in the remaining dimensions ($-\varepsilon'$) for applied strain (ε) in one dimension for a given Poisson's ratio is:

$$(1 - \varepsilon') = (1 + \varepsilon)^{-v} \quad \text{(Equation 2:3)}$$

Therefore, the change in dimensions of a single meander channel with length (l_0), width (w_0), and thickness (t_0) from equibiaxial strain upon inflation ($\varepsilon = \varepsilon_l = \varepsilon_w$) can be given as:

$$l = l_0 + \Delta l_l - \Delta l_w = l_0 (1 + \varepsilon_l - \varepsilon'_w) = l_0[(1 + \varepsilon)^{-v} + \varepsilon];$$

$$w = w_0 - \Delta w_l + \Delta w_w = w_0(1 - \varepsilon'_l + \varepsilon_w) = w_0 [(1 + \varepsilon)^{-v} + \varepsilon];$$

$$t = t_0 - \Delta t_l - \Delta t_w = t_0 (1 - \varepsilon'_l + 1 - \varepsilon'_w - 1) = t_0[2(1 + \varepsilon)^{-v} - 1] \quad \text{(Equation 2:4)}$$

Where, $\Delta l_{l/w}, \Delta w_{l/w}$ and $\Delta t_{l/w}$ are changes in length, width and height of the soft material due to strain in the direction of length/width (l/w), respectively.

Hence, the change in resistance of the biphasic metal encapsulated within the silicone membranes can be given as:

$$\frac{R}{R_0} = \frac{l/l_0}{(w/w_0)(t/t_0)} = \frac{1}{2(1+\varepsilon)^{-v}-1} \quad \text{(Equation 2:5)}$$

Furthermore, the correlation between uniaxial strain and actuator inflation height can be formulated using the volumetric change in the actuator and spatial distribution of sensor meanders on the actuator. The actuator of diameter (d) inflated to height (h) takes the approximate shape of a scooped sphere with a variable radius (r) (Figure 2:8a, b). The radius decreases from infinity to 5 mm as actuator inflates from 0 mm to 5 mm height. The average uniaxial strain in a single meander during inflation to height can be described as:

$$\varepsilon = \frac{l - l_0}{l_0} = \frac{\sin^{-1}\frac{x}{r}}{\frac{x}{r}} - 1 \quad \text{(Equation 2:6)}$$

Where, x is the actuator radius, l is the final length, l_0 is initial length, and $r = \sqrt{x^2 + (r - h)^2}$. The sensor meander pattern consists of 18 parallel lines equally distribute along the surface of the actuator membrane. The ith stripe of the sensor channel is distance (d_i) from center of the actuator and during inflation reaches height (h_i):

$$h_i = h_{max} - r + \sqrt{r^2 - d_i^2} \quad \text{(Equation 2:7)}$$

From Equations 3 and 4, the average strain experienced by all the sensor meanders on the actuator surface is given as:

$$\varepsilon_{\text{avg}} = \sum_{i=1}^{n} \frac{\varepsilon_i}{n} = \frac{1}{n} \sum_{i=1}^{n} \left\{ \frac{\sin^{-1} \frac{x}{r_i}}{\frac{x}{r_i}} - 1 \right\} \approx \frac{\Delta R}{R} \quad \text{(Equation 2:8)}$$

Where, the GF is 1 [47]

Hence, to deduce the inflation height (h) by measuring change in resistance ($\Delta R/R_0$) an explicit mapping from $\Delta R/R_0 \rightarrow h$ is necessary. However, it is impossible to obtain, as Equation 2 is a coupled equation. Therefore, a piecewise polynomial curve fit is obtained for the inverse mapping of Equation 2:5 (Figure 2:8c):

$$h = 49800 \left(\frac{\Delta R}{R_0} \right)^3 - 2890 \left(\frac{\Delta R}{R_0} \right)^2 + 74.6 \left(\frac{\Delta R}{R_0} \right) + 0.109 \; for \; 0 < \left(\frac{\Delta R}{R_0} \right) < 0.025$$

$$h = 33 \left(\frac{\Delta R}{R_0} \right)^3 - 31 \left(\frac{\Delta R}{R_0} \right)^2 + 16 \left(\frac{\Delta R}{R_0} \right) + 0.63 \; for \; 0.025 < \left(\frac{\Delta R}{R_0} \right) < 0.4 \quad \text{(Equation 2:9)}$$

with, Error Norm= 0.0079.

2.3.4 Model validation

We developed a custom high-speed data acquisition test-setup that can record inflation height, input pressure and strain sensor resistance to process the data for validation of the analytical model developed in previous section. We measured the maximum height (h_{max}) during inflation at the given pressure with an external laser displacement sensor and recording the sensor response as depicted in Figure 2:8b. We inflated SPA-skin at various input pressure and took images for fitting a curve of radius 'r' and while simultaneously measuring the observed inflation height (h). The experimental values of curved fitted radii with the scooped sphere approximation for given inflation height matches closely with the expected geometrical model (Figure 2:8b). Afterwards, we derived the average strain values from the Equation 5 and the external height sensor reading. Assuming the GF of 1 we obtained the analytical model plot of expected resistance change ($\frac{\Delta R}{R}$) for given inflation height in Figure 2:8c**.** The subsequent experimental measurements shows the resistance change over inflation height of SPA-skin for three different samples are well in agreement with the analytical model (Figure 2:8c and Figure 2:9).
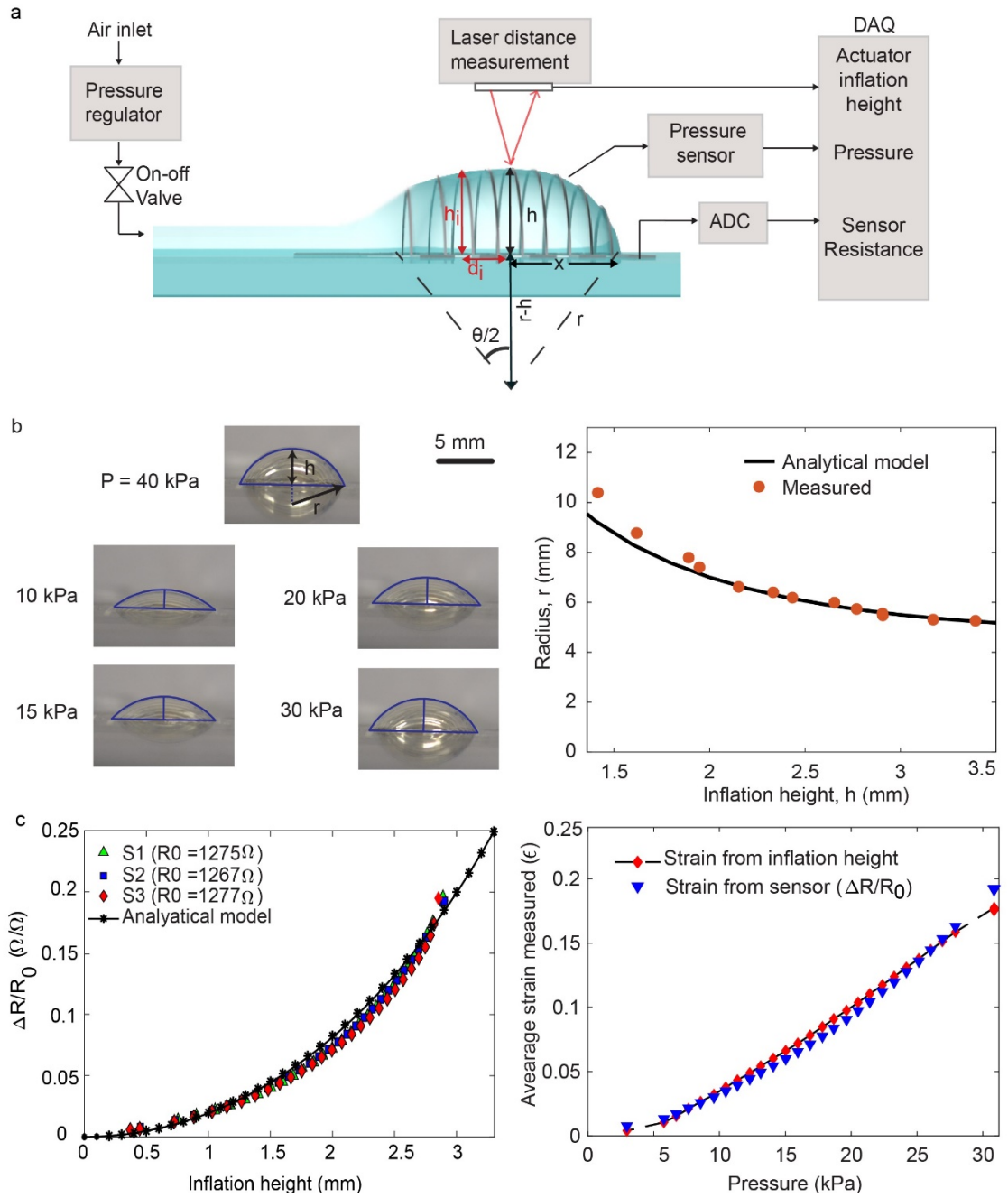
Figure 2:10 **Experimental setup and model.** (a) Experimental setup for validating the sensor embedded SPA model upon actuation, overlaying the geometric parameters used in the analytical model. (b) Images showing the SPA inflation over a range of actuation pressures are used to measure the inflation radius (r) and the inflation height (h) for geometrical model validation. The measured inflation radius is compared with the geometric model assuming the SPA inflation geometry as a part of a scooped sphere. (c) Average measured and computed strains for given inflation heights. (d) Average strain as a function of input pressure (red dots: model, blue dots:
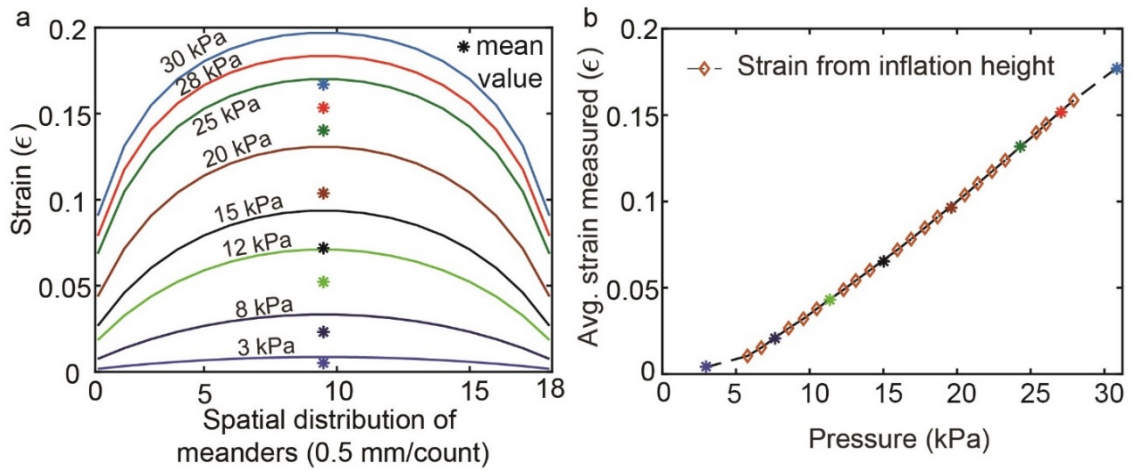
Figure 2:11 **Experimental validation of the analytical model.**(a) The analytical model predicting uniaxial strain over each sensor meander using the measured inflation height. The mean value of the sensor strain determines the measured change in the resistance of the sensor. (b) The measured average strain from the analytical model is plotted with respect to the actuator input pressure. Each colored (*) marker maps to the corresponding mean value of the strain in Figure b and is then used to validate the strain model with measurements from sensor resistance (Figure 2:8c).

This confirmed the integrated strain sensor could effectively be used to measure the actuator inflation height, eliminating the dependency of actuator performance on the manufacturing variations and input pressure. Next, we developed a strain controller to have the strain sensor for active closed-loop control, which is discussed in detail in the Chapter 3.

2.4   Developing edible soft actuator and pressure localizing soft sensor skin

The methods and tools developed for the SPA-skin can further be explored with different material composition and intelligent measurement techniques to help create next generation of soft robotic technologies and wearable interfaces. In this section, we will discuss two of such technologies I co-developed to provide extra core technologies that will be useful across a range of soft robotics applications. The first development is a Gelatin based soft pneumatic actuator developed keeping non-reusable and non-biodegradable nature of traditional silicone material based SPA (Figure 2:10A) and the second one is using exfoliated graphite infused soft sensor skin that uses similar quasi 2D manufacturing technique as SPA-skin (Figure 2:10B).
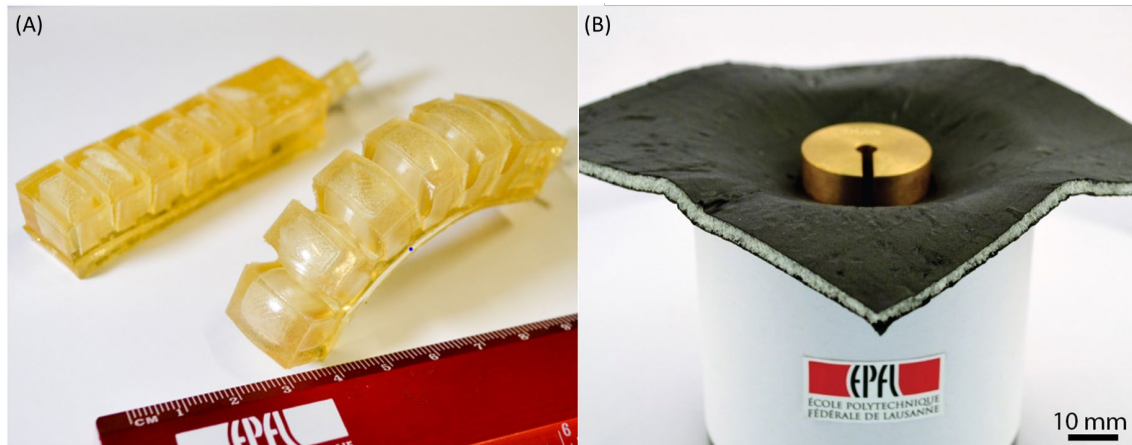
Figure 2:12(A) **Edible soft pneumatic gelatin actuator prototype.** (left) actuator in the non-pressurized state. (right) actuator in a pressurized state. (B) **The soft monolithic silicone-based capacitive sensor skin** deforming into a mug. The sensor skin measures 120x120x4 mm3 with 70 pF of overall capacitance.

The main novelties of these works can be summarized as below:

1. We present a fully edible pneumatic actuator based on gelatin-glycerol composite. The actuator is monolithic, fabricated via a molding process, and measures 90 mm in length, 20 mm in width, and 17 mm in thickness. Thanks to the composite mechanical characteristics similar to those of silicone elastomers, the actuator exhibits a bending angle of 170.3 ∘ and a blocked force of 0.34 N at the applied pressure of 25 kPa. These values are comparable to elastomer based pneumatic actuators. These edible actuators, combined with other recent edible materials and electronics, could lay the foundation for a new type of edible robots.

2. We present a large area, monolithic silicone foam based capacitive sensor and a sensing method to localise the pressure application point without extra wires. In contrast to pressure sensor arrays composed of n × n discrete sensors, we utilize a single sensor body with a single instrumentation interface to detect n pixels. We interrogate the capacitive sensor at different frequencies, thus modulating the effective length of the sensor. These interrogation frequencies are governed by the sensor's total capacitance, resistance, and desired spatial resolution of the sensor. The experimental tests on a 1 × n sensor strip and an n × n sensor sheet and showed that we could attain greater than 90% accuracy in predicting the location of the applied pressure using a model generated by a multiclass kernel support vector machine.

2.4.1   Soft pneumatic gelatin actuator (SPGA) for edible robotics [42]

Revisiting the material foundations of robotic components can lead to novel functionalities and application fields. For example, soft robotics, where robots are composed of compliant materials has led to superior features, such as improved mechanical robustness and simplified structure and control, and safer and more compliant functionalities [43], [86]. Here we propose the use of edible materials for a new type of robotic architecture, which we call "*Edible Robotics*". Edible robots can be biodegradable, biocompatible, and environmentally sustainable with none or lower level of toxicity. These functionalities can already be seen in organic electronics made of edible materials [87] to fabricate transistors [88], sensors [89], batteries [90], electrodes [91], and capacitors [92]. The (still missing) availability of edible actuators could pave the way to fully edible robots. The components of such edible robots could also me mixed with nutrient or pharmaceutical components for digestion and metabolization. Potential applications are disposable robots for exploration (as also mentioned in [93], [94]), digestible robots for medical purposes in humans and animals, and food transportation where the robot does not require additional payload because the robot is the food. So far, the use of edible materials in robotics remains very limited. Researchers have developed a gelatin hydrogel actuator immersed in NaOH solution [93], and an ingestible robot that uses the intestines of pigs as folding parts [95]. Both cases require external electric and magnetic fields, which can make them challenging to use outside of a specific environment. In this paper, we describe a soft gelatin pneumatic actuator for edible robotics. Soft actuators, especially the ones with pneumatic configuration, have been widely developed and applied in various robotic applications thanks to their simple structure that can be extended to form a robot itself [43], [86]. Therefore, developing edible soft pneumatic actuator is a promising approach that can immediately lead to the realization of edible robots. Gelatin is an edible material, and can be polymerized when an edible plasticizer, (glycerol in this work), is used to form a protein network [96]. eGlatinglycerol composite could replace silicone elastomers, a compliant material often used in soft robots. Once dissolved into aqueous solution, the composite can be used in molding fabrication of soft actuators in the same manner as more traditional elastomers.

Characterization of gelatin-glycerol membrane

Sample preparation Gelatin (48723) and glycerol (G5516) were purchased from Sigma Aldrich (Switzerland). These materials were used as received. Aqueous solutions containing gelatin (GEL), glycerol (GLY), and distilled water (WAT) were prepared by mixing the contents for 30 min at 80° C. Two different solutions were prepared: GEL/GLY/WAT = 1:1:8 and 1:2:8. The solutions were cast on an acrylic mold (20 g solution/mold) and dried at room temperature (25 ∘C) for 48 h inside a chemical hood. After drying, a membrane thickness of 0.5 mm was formed in the mold. The membrane was then cut by a laser machine (Speedy 300, Trotec Laser) to obtain the dogbone shaped samples for uniaxial tensile testing. This dogbone shape sample was fabricated according to ASTM guidelines [97]. The drying time of 48h was experimentally determined prior to the sample preparation, based on the changes observed for mass of the membrane, which became almost constant at 48 h (Figure 2:11(a)).
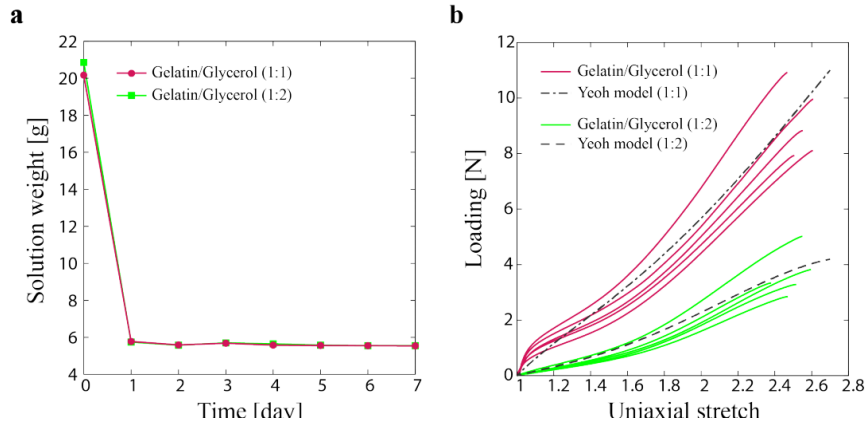
Figure 2:13 **Characterization results for the gelatin/glycerol composite samples.** (a) Variation in the mass of the compositions over time. The water content takes equilibrium after 48 h. (b) Loading as a function of uniaxial stretch for the two different compositions. Dashed lines represent calculated result using Eq. 8.

Results and discussion Figure 2:11(b) plots the result of the tensile testing for two different gelatin(GEL)/glycerol(GLY) composition of 1:1 and 1:2. The samples exhibit hyperelastic (nonlinear) behavior similar to silicone elastomers. The dashed lines shown in the figure are the calculated loading based on Yeoh model. The material constants and properties obtained are summarized in Table 2:2: (I) and Table 2:2:(II) , respectively. The measured Young's modulus is 2.7 ± 0.5 MPa for GEL/GLY = 1:1, and 0.7 ± 0.2 MPa for GEL/GLY = 1:2, respectively. These values of the modulus are in the same range of silicone elastomers used for soft robots (0.125 MPa for Smooth-On Ecoflex 00-30 [98] , and 1.3-3.0 MPa for Dow Corning Sylgard 184 [99]). Also, it can be seen that the composition ratio changes the modulus; larger the glycerol contents, softer the material is. Therefore, desired modulus may be achieved by adjusting the ratio of gelatin and glycerol. Similar to the Young's modulus, the tensile strength for the two compositions (9.3 ± 1.2 MPa for GEL/GLY = 1:1, and 3.7 ± 0.9 MPa for GEL/GLY = 1:2) are in the same range of silicone elastomers (3.5-7.7 MPa for Sylgard 184 [99] , and 1.4 MPa for Ecoflex 00-30 [100]). The elongation at break obtained for the two is almost the same value; 154.8 ± 6.2 % for GEL/GLY = 1:1, and 150.3 ± 8.2 % for GEL/GLY = 1:2, respectively. The value is reasonable for GEL/GLY = 1:1 because silicone elastomers with high modulus exhibit similar elongation at break (80- 170 % for Sylgard 184 [19]). On the other hand, the value of GEL/GLY = 1:2, 150.3 ± 8.2 % is significantly smaller than those of soft elastomers (900 % for Ecoflex 00-30 [100]).

Development and characterization of soft pneumatic gelatin actuator

Design and fabrication The actuator is shown in Figure 2:10 has multiple, half-separated chambers in the monolithic structure, similar to the configuration initially reported in [101]. As shown in Figure 2:10, when pressurized air is injected, the inflation of the chambers happens in the upper part (shifted position from the neutral plane), resulting in a bending of the structure. The dimensions of the device were 90 mm in length, 20 mm in width, and 17 mm in thickness. The actuator was fabricated based on a molding method commonly used for silicone elastomer-based pneumatic actuators.

TABLE I

MATERIAL CONSTANTS OF GELATIN(GEL)-GLYCEROL(GLY)
COMPOSITE OBTAINED FROM TENSILE TESTING

Constant [MPa]	GEL/GLY (1:1)	GEL/GLY (1:2)
C_1	0.45 ± 0.09	0.12 ± 0.03
C_2	$5.72 \pm 1.08 \times 10^{-2}$	$4.60 \pm 0.87 \times 10^{-2}$
C_3	$-0.21 \pm 0.11 \times 10^{-2}$	$-0.33 \pm 0.07 \times 10^{-2}$

TABLE II

MATERIAL PROPERTIES OF GELATIN(GEL)-GLYCEROL(GLY)
COMPOSITE OBTAINED FROM TENSILE TESTING

Property	GEL/GLY (1:1)	GEL/GLY (1:2)
Young's modulus [MPa]	2.7 ± 0.5	0.7 ± 0.2
Tensile strength [MPa]	9.3 ± 1.2	3.7 ± 0.9
Elongation at break [%]	154.8 ± 6.2	150.3 ± 8.2

Table 2:3: (I) Material constants of GELatine and GLYcerol composites from material testing and (II) corresponding material properties for 1:1 and 1:2 by weight constituent ratio samples
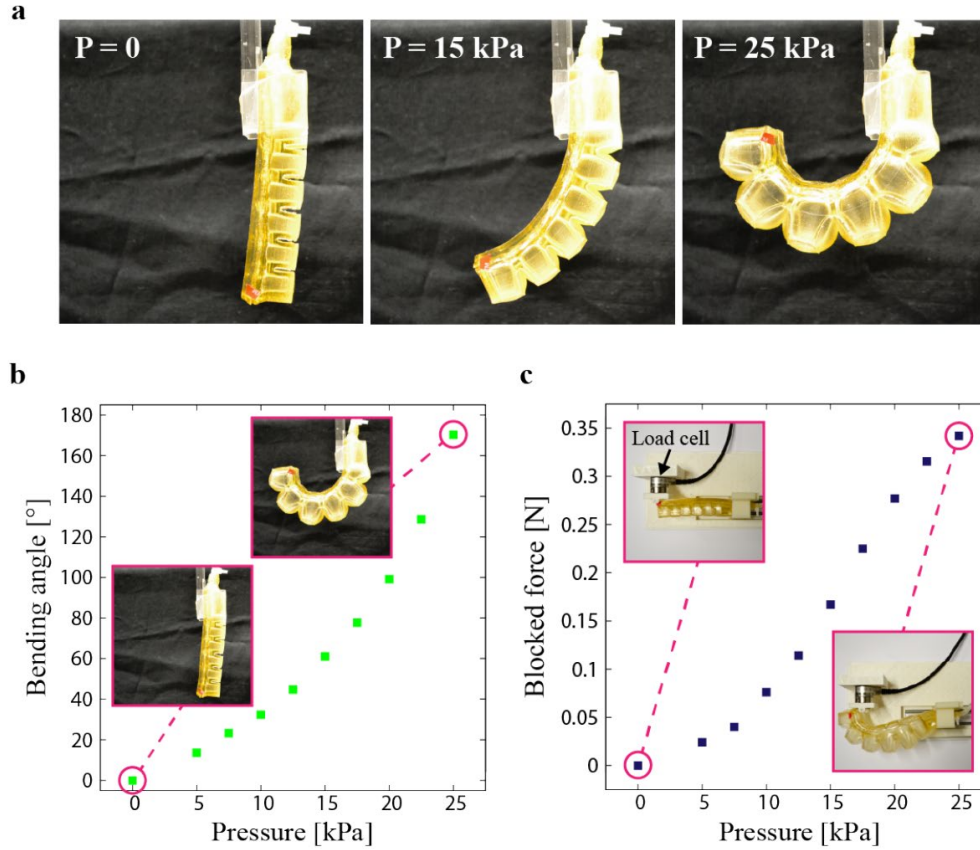
Figure 2:14 Characterization results of the soft pneumatic gelatin actuator. (a) Bending of the actuator in different pressured states. P stands for the gauge pressure. (b) Bending angle as a function of the applied pressure. A bending angle of 170.3 ∘ was observed at 25 kPa. (b) Blocked force as a function of the applied pressure. A force of 0.34 N was measured at 25 kPa.

Bending angle and blocked force The bending angle of the actuator was defined as the tip angle difference from the initial angle, which was recorded by a CMOS camera. The blocked force of the actuator was measured by putting a load cell (Nano 17, ATI Industrial Automation) on the tip in the way blocking the bending actuation (Figure 2:12 (C) inset) In these characterizations, pressurized air of up to 25 kPa was applied via a setup consisted of a valve, a compressor, and a computer running LabView.

Results Figure 2:12 plots the bending angle as a function of the applied pressure. The angle increased with the pressure, and took a value 170.3° at 25 kPa. Similar trend was observed in the blocked force, and a force value of 0.34 N was recorded at 25 kPa. These results represent the fact that the performance of the actuator, the actuation angle and the force, are pressure-controllable. We found our edible soft actuator exhibited comparable performance to existing silicone elastomer based actuators, as summarized in Table III. During the test, we observed the actuator showed fast motion (~0.5 s), and was capable of withstand numerous cycles of actuation (see supplemental video).

Demonstration of robotic application In order to demonstrate the applicability of the edible soft pneumatic actuator to robotic application, we integrated the two actuators into a form of two-finger gripper and performed grasping test for various objects. The gripper, shown in Figure 2:13(a-i), has the open-finger at the initial state. The fingers can further be opened by sucking air from the chambers (Figure 2:13 (a-ii)).
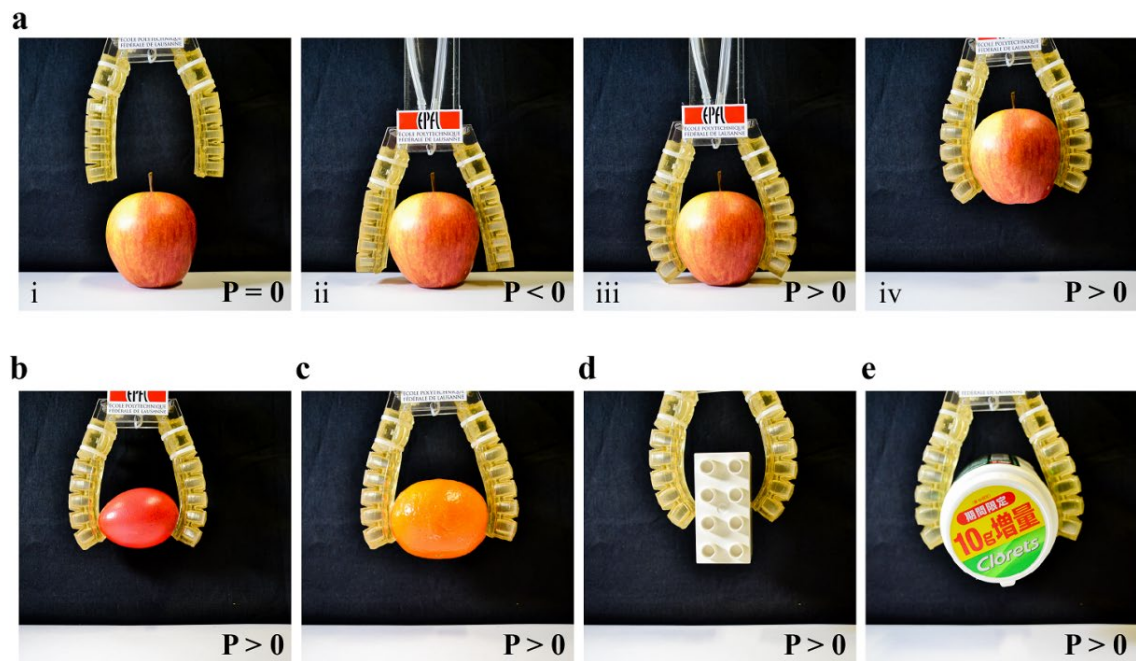
Figure 2:15 **Soft gripper grasping test.** P stands for the gauge pressure. (a-i) The gripper is placed above the object, here an apple mass of 95.6 g. (a-ii) The device approaches the object. (a-iii) Applying pressure conforms the adaptation of the fingers. (a-iv) The actuated force of the gripper makes it possible to picked up the object. The gripper demonstrated handling of other objects: (b) a boiled egg (47.7 g), (c) an orange (104.8 g), (e) A LEGO brick (25.7 g), and (f) A bottle of chewing gums (153.1 g).

Discussion

The edible material used for the actuator, the gelatinglycerol composite, shows similar mechanical properties to those of silicone elastomers. Assessment of other characteristics such as durability and viscoelasticity with varied composition ratios will provide more insight about applicability of the composite material for robotic applications. Environmental conditions such as humidity and temperature, are also important aspects of robots that operate in uncontrolled environments. The gelatin-glycerol composite appears to reach an equilibrium water content, suggesting that the mechanical properties may (Figure 2:11), suggesting that the mechanical properties may change corresponding to humidity of the surrounding air. However, this is not a major problem because edible coatings to preserve the water content are already available [102]. Temperature may also effect to the mechanical properties because the melting temperature of gelatin is around 35°C. The melting point can be higher once plasticizers and other proteins are added. For example, a composite of gelatin, chitosan (a polysaccharide), and glycerol has a melting point of 67°C [103]. Investigation of above mentioned characteristics will contribute towards the improved design of the actuators and robots, and their applicable tasks

To demonstrate the possibility soft pneumatic actuator towards robotic application, we integrated the two actuators into a form of two-finger gripper and performed grasping test for various objects. The versatile nature of the gripper illustrates high performance of our edible actuator. Higher performance may be expected if the actuator is designed with aid of analytical Modeling [104] or FEM [13] where the material properties obtained from the characterization are incorporated. This will also enable the design of actuators of different geometries and sizes. For the future generation of the edible actuators, further characterization of cycles and repeatability should be performed. Given the melting feature of gelatin, our actuator could be capable of self-healing and become re-usable, which are added capabilities that existing soft pneumatic actuators usually do not exhibit. The edible robotic gripper described here shows possibility of creating edible robots based on these materials. Given the simplicity of the actuator design, it could be implemented to many different types of robots. Along with all the functionalities—biodegradability, biocompatibility, environmental sustainability, digestibility, metabolizability, selfheal ability, and re-usability—those edible robots could bring novel applications. For example, as discussed in the literature [105] about the animal navigation in the wild, fully edible robots would help to study how wild animals collectively behave. The robots could also take a role of animals prey to observe their hunting behaviors or to train protected animals to do predation. Once medical components are mixed into the edible composition, the robots could help the preservation of wild animals or heal inside of the human body. When edible robots can be metabolized, they also function as energy storage providing an advantage in terms of increased payload with respect to non-edible robots that must be loaded with a food payload. This would be effective in rescue scenarios where the metabolizable robots can reach survivors in isolated places like inside a crevice or up on mountain. Last, but not least, since edible materials can generate electric energy [90], [106]–[108], one could envisage autophagy (self-eating) function, like that of octopus [109], to extend their lifetime.

2.4.2 Capacitive soft sensor skin for distributed pressure localization [56]

Robotic systems that interact with their surroundings need to detect and localize the contact with an object. Pressure sensor arrays are a well-developed technology with multiple commercially available devices (TakkTiles, Sensitronics, Tekscan, Sensing Tex, BodiTrak, SureTouch). However, the majority of these commercial devices incorporate materials that are stiffer or more strain-limited than those commonly demanded by softer interfaces, hindering their integration. Researchers have developed various approaches to "soften" pressure sensing for soft

robotics, human-computer interactive system, and wearable applications. Two common approaches for measuring pressure are by measuring the resistance of a deformable, soft, or fluid conductor or by measuring the capacitance of a deformable capacitor. Some resistive sensing approaches include the use of conductive polymer composites [110]–[112] or embedding liquid-metal microchannels in silicone elastomer [98], [113]–[115]. Capacitive sensing approaches use a variety of materials for both the conductive electrodes and the dielectric layer. Electrode materials can be broadly classified into metal thin film [77], [116]–[118], liquid metal [119], [120], , conductive silicone composite [121]–[124], conductive fabrics [125]–[127], hydrogels [128], carbon nanotubes [129], and carbon grease [130], [131]. The dielectric layers have been composed of silicone foam [77], [116], [125], native silicone [41], [118]–[120], [122], [124], [128], [129], polyurethane [117], and acrylic foam tape [130], [131]. Though the transduction means to convert pressure to a signal may differ, the majority of these devices utilize a single sensor to make a single measurement of pressure. In order to distribute sensing capability over larger areas, researchers have patterned multiple pixels individually [74], [77], [113], [126]] over the sensing region at the desired spatial resolution. However, as the number of sensors increases, so does the number of interfaces to the electronics. For the practice, the sheer number of wires can become unwieldy, prone to breakage, increasing the stiffness of the system, and therefore, higher resolution uniform surface systems are difficult to design and implement. One way to mitigate this issue in scalability is to use the electrodes on the top and bottom of the substrate in orthogonal rows and columns to create pixels at the intersections [110], [116]–[119], [124], [127]–[129]. This approach reduces the number of interfaces for an n-by-n grid from $O(n^2)$ to $O(n)$, a further improvement is to leverage the frequency-dependent characteristics of large-area capacitors to **reduce the number of interfaces to two for an $n \times n$ pixel array**. Interrogating a capacitor at multiple frequencies effectively creates multiple sensing regions within the area of a single capacitive sensor body [130]–[132]. Another interesting way to reduce the number of electrodes for touch-sensing applications is to use electric field tomography on a large conductive film [132].

In this work, we present a pressure sensing methodology for localization of point pressures on a monolithic, soft capacitive sensor (Figure 2:10(A).) by interrogating the sensor at multiple frequencies to modulate the effective length of the capacitive sensor "seen" by the measurement system. Using the resistance and capacitance values of a physical sensor prototype, we developed an analytical model for the 1D representation of the capacitive sensor. Using this model, we calculated the frequency response of the sensor at different effective sensor lengths to find their corresponding cutoff frequencies. We then used the calculated cutoff frequencies as the interrogation frequencies in experimental tests. Experiments were performed by pressing at various locations on a 1D sensor strip and a 2D sensor sheet wherein the series resistance (Rs) and parallel capacitance (Cp) of the sensor were measured using an LCR meter at the interrogation frequencies. Because the sensors are monolithic, with no pre-determined measurement locations, we discretized the sensors into different sized pixels to attain different levels of spatial resolution. We then input the Rs and Cp values into a multi-class kernel support vector machine (KSVM) to create a classification model for localizing the point pressures. Through evaluation of the SVM using a confusion matrix, we found that we achieved between 90-100% accuracy in predicting the location of the applied pressure which is discussed in detailed in Chapter 3.
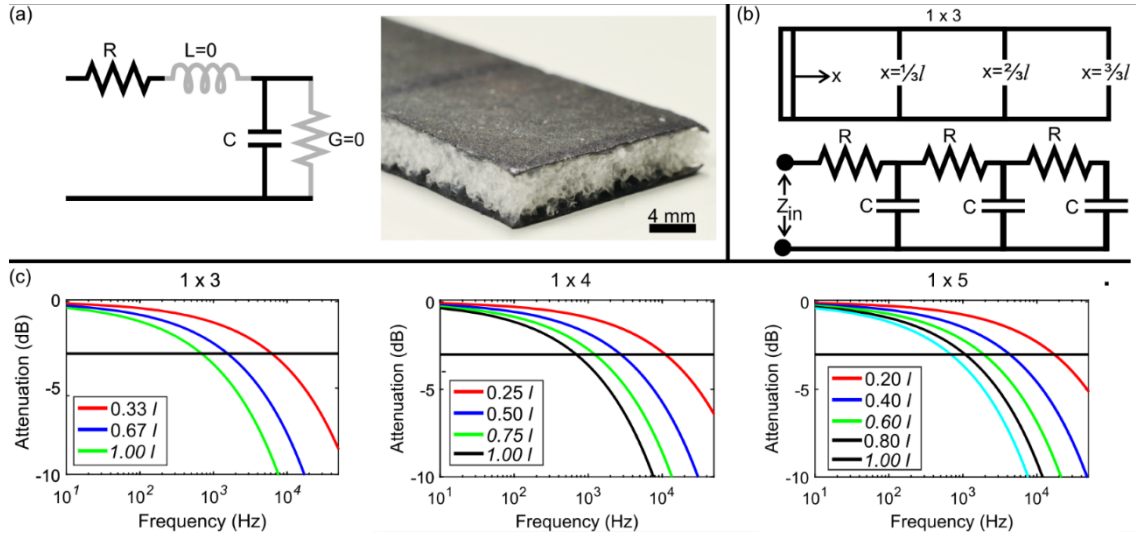
Figure 2:16 **Electrical equivalent circuit diagram and results of the analytical model of the 1D sensor strip.** (a) Schematic of a single element in the 1D sensor strip. A photo of the sensor cross-section of the sensor strip. (b) Model of a 1 x 3 pixel array. The interface is located on the left end; the distance or pixel index increases from this point along the sensor. The top schematic shows a top view of the physical device; the bottom schematic shows the corresponding electrical equivalent circuit. (c) Plots of the signal amplitude calculated at each node over a frequency sweep. The black horizontal line marks the -3dB threshold. The interrogation frequencies are the frequencies at which the signal amplitude curves intersect the -3dB lin

Physical Embodiment

The sensors were fabricated as a large, parallel plate capacitor using silicone and expanded graphite composite for the conductive electrodes and silicone foam for the dielectric layer. The two components were made separately and then glued together using a thin layer of silicone. As pressure is applied to this deformable capacitor, the thickness of the dielectric layer decreases, increasing capacitance. The conductive composite material was fabricated in a thin film using a rod-coating method as described in [133]. In this work, we modified the graphite loading to in-crease the sheet resistance from 1 kΩ to 50 kΩ, reducing the sensitivity of the sensor to electro-magnetic noise and decreasing the cutoff frequency. By using a conductive composite material, it is possible to modify the sheet resistance of the capacitor's electrodes to better accommodate the interrogation frequency capabilities of the LCR measurement system or vice versa. The sili-cone foam was fabricated by mixing silicone elastomer (DragonSkin 10 Slow, Smooth-On) with various sizes of sugar spheres (Suglets, Colorcon) to create a very soft, open-cell foam. We mixed 40 g silicone with 120 g of sugar spheres with diameters between 500-1700 µm and then pressed the mixture into a 4 mm deep frame to form a large, thick sheet. After the silicone cured, the sheet was submerged in 80° C water for 6 hours to cause the sugar to dissolve out of the foam, changing the water every hour. After allowing the water to evaporate from the pores, the foam sheet was adhered on both sides to the conductive composite film using a thin silicone glue layer. The final area of the capacitive sensor was cut manually using a precision knife. In addition to the customizability of the electrode sheet resistance, the unit capacitance of the sensor sheet can be modified by changing the thickness of the silicone dielectric foam. Furthermore, the stiffness of the foam can be tuned by changing the ratio of sugar spheres to silicone or by choosing silicones of different stiffnesses.

Analytical model

The sensor is modeled as a network of coupled resistances and capacitances spread across the sensor plane [134]. For our application, our goal was to locate the pressure point that is effectively changing the overall sensor capacitance. The model was developed by dividing the sensor into infinitesimally small 1-dimensional resistive and capacitive components (Figure 2:14 (a)) spread over the length of the sensor (Figure 2:14 (b)). The voltage and the current equations for modeling the sensor can then be derived from the Telegrapher's equations on an electrical transmission line [134] as follows:

$$\frac{\partial V(x,t)}{\partial x} = -(R + j\omega L)I(x,t) = -RI(x,t)$$

$$\frac{\partial I(x,t)}{\partial x} = -(G + j\omega C)V(x,t) = -j\omega CV(x,t) \qquad \text{Equation 2:10}$$

where, x is the distance from the voltage application point and R, L, C, and G are the characteristic values for line components per unit length. In the case of our sensor, we have a negligible inductance(L ≈ 0) and trans-conductance (G ≈ 0) (Figure 2(a)). Combining Eq. 2:10, we obtain the full form of the equations as:

$$\frac{\partial^2 V(x,t)}{\partial x^2} = \gamma^2 V(x,t); \quad \frac{\partial^2 I(x,t)}{\partial x^2} = \gamma^2 I(x,t) \qquad \text{Equation 2:11}$$

where, the propagation constant, γ = α + jβ = √ jωRC. The sensor with length l can be divided into n virtual sensor pixels, each represented as an RC couple (Figure 2:14 (b)). In order to distinguish the pressing of each individual pixel, we need at least n−1 interrogation frequencies. We chose the interrogation frequencies ({f_1, .f_i , .f_n}) to be the frequencies at which the diffusing voltage wave at distances x_i = il/n for i ∈ 1 : n (i.e., the distance between the interface and the "end" of each pixel) is attenuated to half power. The attenuation factor, α, for the diffusing voltage wave is:

$$\alpha(f) = e(-Re(\gamma)x) = e(-\pi RCfx) \qquad \text{Equation 2:12}$$

Hence, the attenuation functions for each pixel end point l in an 1 × n pixel sensor are:

$$\alpha_i(f) = e(-Re(\gamma)xi) = e(-\pi RCfxi) \ \forall i \in 1: n \quad \text{Equation 2:13}$$

At half power attenuation, α_i = 1/2, and thus the interrogation frequencies can be calculated as:

$$f_i = \frac{(ln \ \alpha_i(f))^2}{\pi RCx_i^2} = \frac{0.0382}{RCx_i^2} \ for \ i \in 1:n \qquad \text{Equation 2:14}$$

The interrogation frequencies f_i were obtained for our 1D sensor prototype (Figure 2:14(a)), with dimensions 100mm × 20mm, the series resistance of 50kΩ/mm, and capacitance of 108 fF/mm. The plots of αi(f) for the 1x3, 1x4, and 1x5 pixel sensor networks are shown in Figure 2:14 (c). The interrogation frequencies corresponding to where α_i = 1/ √ 2 were used in the following experi-

mental section to obtain the features like Resistance and/capacitance at these interrogation frequencies. These recorded features will be then used to train a machine learning model for classification of intercepted pressure location based on collected dataset.

Experimental Results

We performed a series of experiments to evaluate the proposed method for localizing point pressures. Six total configurations were tested: $1 \times n$ sensor strip and $n \times n$ sensor skin, and by discretization, the full-length l into 3, 4, and 5 (virtual) pixels. In each test, we applied a 2 mm displacement to each pixel to double the capacitance of each pressed region. We then performed frequency measurements at all fi for $1 \times n$ ($\forall n \in 3 : 5$) pixel sensor array while recording the R_s and C_p values using an LCR meter (Hioki IM3253). Six repetitions of the frequency sweep for each pixel were obtained to form a feature-rich dataset. We then input these datasets (f_i, $R_s(f_i)$, $C_p(f_i) \forall f_i$) into a multi-class kernel support vector machine (KSVM) to generate a model to classify which pixel ($1 \times n$ sensor strip) or pixel column ($n \times n$ sensor skin reduced to $1 \times n$ sensor strip) was pressed.

Machine learning (K-SVM classification). Support vectors machines are widely used in learning based classification to divide the dataset into separate classes. While standard SVMs are designed for linear classification between binary classes using a hyper-plane passing through maximal margin of separation between the two classes [135]**.** We require n-class classification for a 1xn pixelated matrix. Furthermore, the non-linearity of R_s and C_p as a function of frequency (Figure 2:14 (c)) demands a non-linear classifier model. Thus, we employed a multi-class K-SVM classification method for the pixel **localization** [136] using the error correcting output codes *(ecoc)* model in the Matlab Statistics and Machine Learning Toolbox (Mathworks). For each class (pressed pixel, i), the training data consisted of the R_s and C_p values measured in the interrogation frequency sweep. The SVM's classification performance was assessed using a k-fold cross-validation model applied on the training data that randomly partitions the data into k sets where $k - 1$ sets was used to train the model and the remaining set was used for cross-validation of the model. The accuracy of the model was reported as a confusion matrix, where the model's predicted pixel (Output Class) was compared against the true pixel (Target Class).

$1 \times n$ sensor stripe We first performed the experiments on a sensor strip that was discretized to form 1x3, 1x4, and 1x5 pixel arrays (Figure 2:15, top row). The data collected during these experiments are shown in Figure 2:15, middle row. As reported in the analytical model, at lower frequencies, the measured capacitance was found to be the same, regardless of which pixel is pressed. As the frequency increases, however, we begin to see differentiation in the capacitance depending on which pixel was pressed. When the first pixel is pressed, a larger capacitance (relative to an un-pressed sensor) is "seen" across all interrogation frequencies. However, when a more distant pixel i is pressed, at frequencies above the cutoff frequency f_i, the effective length of the capacitor has shortened behind the pixel such that the pressed pixel is not "seen." The multi-class KSVM showed nearly perfect performance in classifying which pixels were pressed. The confusion matrices (Figure 2:15 (bottom row)) show an overall classification percentage of 100 % for the 1x3 and 1x4 tests and 96.7 % for the 1x5 test. In the 1x5 test, the error was in misclassifying the 4th and 5th pixels. This result can be directly observed in the capacitance vs. frequency plot for the 1x5 case which shows prominent overlapping between the curves of the two most distal pixels.

 n × n sensor skin We expanded upon the 1 × n experiments to n × n sensor sheets discretized into 3x3, 4x4, and 5x5 pixel arrays (Figure 2:16). Our goal in this study was to correctly identify the column j in which a pixel (i, j) was pressed when probing from the y-axis. From the extension of the 1D analytical model to 2D, the cutoff frequencies were calculated to be identical to the 1D case. However, we found experimentally that the cutoff frequencies (i.e., where there were maximal differences in measured Cp and Rs depending on which column's pixel was pressed) were in fact five times higher, ranging from 1kHz to 200kHz. We, therefore, interrogated the sensor at 20 frequencies logarithmically spaced between 1kHz and 200kHz to create an even more feature-
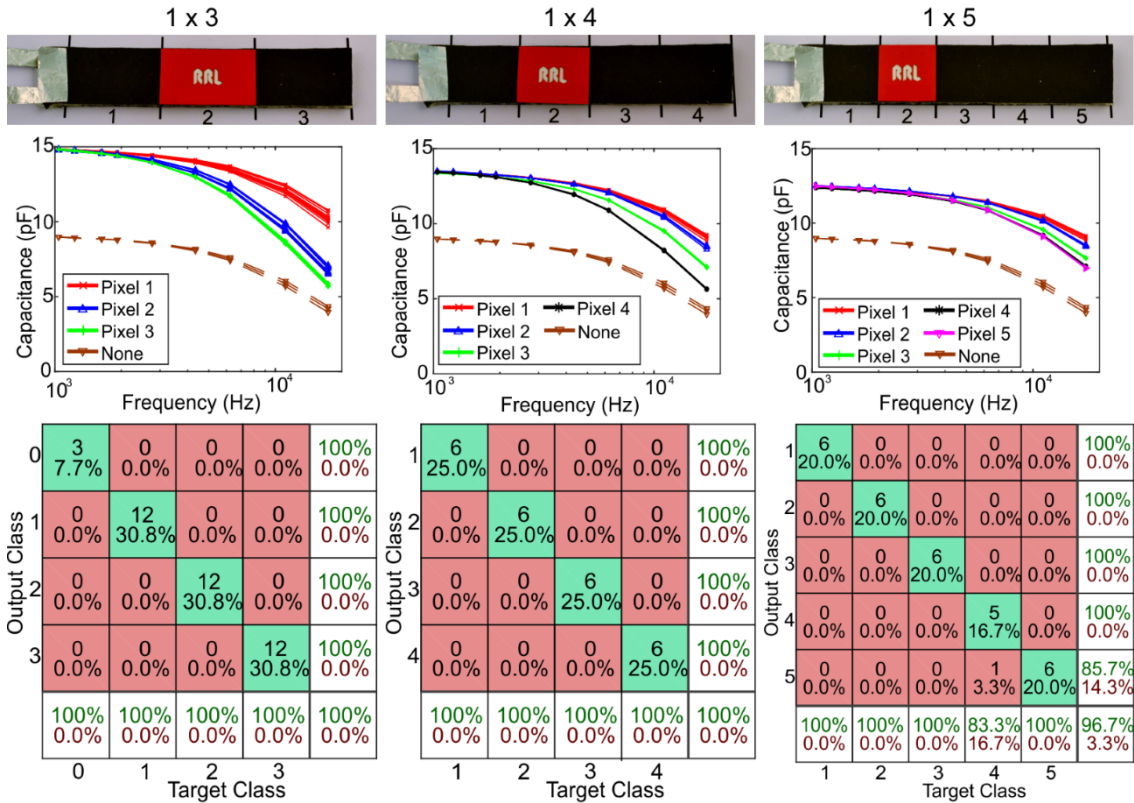
Figure 2:17 **Single dimensional 1×n sensor strip experiments**. (Top row) Photos of the same 1×n sensor with differently sized pressure applicators to create 1x3, 1x4, and 1x5 pixel arrays, from left to right. (Middle row) Plots of capacitance over a frequency sweep while different pixels are pressed. (Bottom row) Confusion matrices are used to evaluate the efficacy of the support vector machine in classifying each pixel press. An extra class (0) representing "No pixel pressed" in 1x3 confusion matrix shows that the model can detect when a pixel is pressed.

rich dataset with which to build the classification model. The results for training and prediction for 1xn th column classification are presented in Figure 4(c). It is important to note that the 2D classification results have n times lower sensitivity as 1D example. Use of 20 interrogation frequencies and feature extraction from both resistance and capacitance change of the sensor sheet improved the classification from ≈ 60% using 10 frequencies to >90% for the 3x3 and 4x4 matrices. As the pixel size reduces, the change in capacitance from pressing a pixel relative to the overall sensor capacitance decreases. The reduction in sensitivity results in a lower classification accuracy wherein the misclassified pixels are predicted to be in one of the adjacent columns (Figure 4(c) 5x5). We observe that the classification accuracy decreases at pixels furthest away from the interface, where the sensitivity of the measurement method is lowest. The performance degradation becomes even more evident as we increase the resolution beyond the 5x5 matrix, at

which point the limits of the current measurement system are reached. By superimposing measurements and classifications from interrogating at both the x- and y-axes, improved classification of pixel location can be obtained.
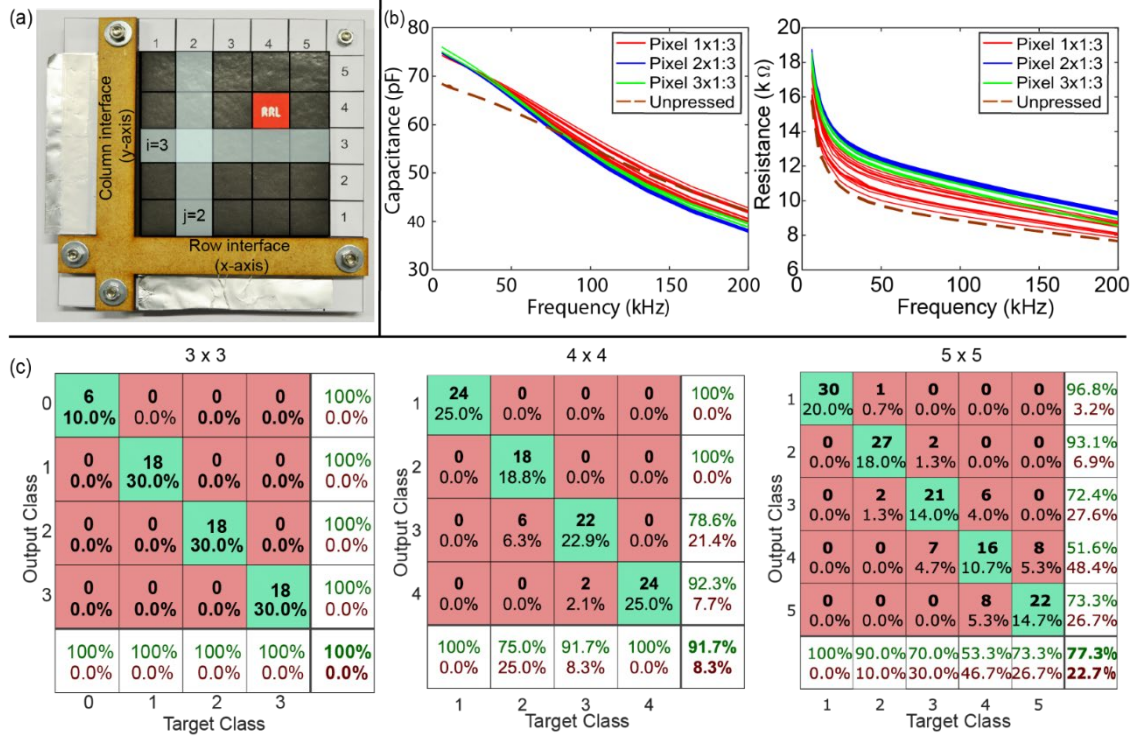
Figure 2:18 (a) Photo of the 2D sensor sheet with a pressure applicator for the 5x5 pixel discretization. The foil protruding under the wood frame along the left and bottom edges was used to interface the LCR meter to the sensor electrodes. The index nomenclature is overlaid on top. (b) Frequency responses of Rs and Cp measured in the 3x3 matrix experiments. (c) Confusion matrices for the 3x3, 4x4, and 5x5 sensor configurations, respectively, after training using a multi-class support vector machine. An extra class (0) representing "No pixel pressed" was added solely to the 3x3 classification

Discussion

In comparison to a sensing region composed of n × n discrete sensors, the proposed approach greatly simplifies fabrication and drastically reduces the number of interfaces from n^2 to just two, facilitating integration of surface pressure measurement in soft robots. We demonstrated that pressures could be localized by interrogating the sensor at multiple frequencies to record the C_p and R_s values, and inputting those measurements into a trained kernel support vector machine to report the location of pressure in both 1×n and n×n pixel arrays. We used a KSVM to perform non-linear, multi-class classification that yielded excellent results in both the 1 × n and n × n pixel arrays.

From this preliminary study, there are many directions in which to take this work: improving localization accuracy in the 2D case, investigating the spatial resolution and load sensitivity of the system, further testing using differently shaped objects and non-flat surfaces, and measurement of multiple contact points by interrogating from more than two interface locations. To improve the localization accuracy within a 2D array, we found preliminary results that showed that the KSVM could also be used to predict the pressure location in rows (i) orthogonal to the interface (y-axis), in addition to columns (j). While the accuracy of this model expectedly is lower, the results

nonetheless demonstrated that there is further information encoded in the Rs and Cp values gathered from a single interface beyond just the localization within columns parallel to the interface. Thus, we hypothesize that we can utilize the two sets of Rs and Cp values gathered by interrogating from the two axes to train four KSVMs and then convolve the KSVM models to improve localization accuracy. Furthermore, we would like to investigate the sensitivity of the system in terms of the spatial resolution. As we found in our 2D experiments, the sensitivity of the pressure sensor reduces as we travel away from the interface. A sensitivity and information theoretic analysis [121] would provide information on the pixel size limits, based upon the magnitude of the smallest measurable capacitance change, as a function of distance from the interface.

In terms of implementation on a soft robotic system, there remain several open questions in using this system. These opportunities include measurement of continuous values of pressure, localization of multiple contact points, identification of pressure application with non-square shapes, implementation of the sensor on curved surfaces, and investigating the effect of stretch on the system. The methods that we have presented in utilizing a soft, capacitive sensor skin to localize pressure application leverages the unique properties of a large-area, deformable capacitor while providing the benefits of monolithic fabrication, more efficient interfacing, and a more physically robust device. This approach enables applications beyond soft roboticists to more easily determine interactions between soft robot systems and their surroundings, by distributing contact pressure sensing across any surface.

2.5 FEA methods to model SPAs and SPA-skin

Increasing focus in human-cantered technology has been fueling research in soft technologies. Softness of material results in several inherent advantages such as light-weight, compliance, safe physical human-robot interaction. It is not enough to only rely on the intuition and rapid proto-typing techniques for SPA fabrication especially when the requirements demand specific output forces or displacement. Modeling hyper-elastic materials is a complex process that hinders the analytical analysis of SPA behavior in simulation. However, the advent of modern computational analysis methods can simulate non-linear material behaviors using Finite Element Analysis. In this section, we present a comprehensive open-source simulation and design tool for Soft pneumatic actuators (SPAs) using finite element method, compatible and extensible to a diverse range of soft materials and design parameters.

In this section a thorough characterization of the hyperelastic and viscoelastic behavior is illustrated using a sample soft material (Ecoflex 00_30), and an appropriate material constitutive law. SPA performance (displacement and blocked-force) are simulated for two types of SPA and validated with experimental testing. Real-world case studies are presented in which SPA designs are iteratively optimized through simulation to meet specified performance criteria and geometric constraints. Followed by these, we present adaptation of this open-source scripts of *spa-design-tool* [13] to develop and extend the SPA Modeling to Elastosil and Dragon-skin 30. We then obtain the sub-sequent hyper elastic material model parameters and simulate the geometries for a Vacuum-SPA [58] and SPA-skin (ring shape).

2.5.1 FEA based Modeling for SPA design

The design tools which exist for PAMs [137], [138] are inapplicable to the new functionalities enabled by SPAs, and the existing literature on mathematical models for SPAs [139]–[142]] lacks the necessary level of detail and accuracy. In this work we attempt to provide the engineering community with a cohesive simulation and design tool for SPAs, compatible and extensible to a diverse range of materials and design parameters.

Numerical Modeling Finite element analysis of SPAs has often been limited to very specific materials, geometries, and applications [143].] The finite element method (FEM) has been applied to a Manta-like swimming robot,[144]] a bending SPA for hand rehabilitation, [142], a miniature soft gripper, [145] and an SPA prototype mimicking the form and function of a human heart. [146]. Due to the complexity involved in modeling the extremely high strains, some of these models are based on inflated rubber matrix materials, [142], [144], [145], [147]], while other studies have focused solely on fiber-reinforced elastic materials. [142], [148]. Currently, there is no modeling framework that is applicable to the commonly-used SPA configurations (bending and linear) and to multiple materials.[149]. Additionally, although the general hyperelastic behavior of soft materials is well understood, several researchers focus on the linear material response at small strains when capturing the mechanical behavior of SPAs. [141], [146]. Material laws such as the Mooney–Rivlin [145], [147], and Neo-Hookean [148] models are based on linear approximations of the strain invariants, and although they may be accurate in these low-strain regimes, the accuracy of these simplified models is highly limited at higher strains. [150]. Instead, a general hyperelastic model should be calibrated across a large range of realistic strains appropriate for the application. General hyperelastic models typically fall into two broad categories: phenomenological models based on descriptions of observed material behavior, and mechanistic models

derived from information about the underlying material structures. The Ogden [151] and Yeoh [150] models, as well as other polynomial-type models, [152] are widely used phenomenological models which can be expected to yield good results for soft materials. [153] Mechanistic models based on statistical mechanics, such as the Arruda–Boyce [154] and the Van-derWaals [155] models, may provide accurate solutions at smaller strains, but are not readily applicable to SPA modeling, where more complex models are desired in order to capture the material behavior determined through multiple modes of experimental testing. Given these complexities, there are only a few examples of existing FEM SPA modeling research which have appropriately captured the non-linear, hyperelastic soft material behaviors, [142], [156] none of which have additionally considered the viscoelastic effects. While useful for the specific applications, those studies are limited to their selected geometry and material.

Characterization of soft materials for Modeling

The definition and application of suitable hyperelastic and viscoelastic models that fully capture the soft material behavior is critical for reliable, accurate simulations. In this section, both hyperelastic and viscoelastic properties of soft material are studied, and their effects on the final SPA modeling is discussed. Ecoflex 00–30 is used as the sample material, but the same procedure can be followed for other materials using the *spa_hyperelastic_modeling* and *spa_viscoelastic_modeling* tools available as part of the *spa_guided_design_tool*.

Determination of Hyperelastic Properties Hyperelastic material properties are typically determined through simple tests on small material samples, performed across a large range of relevant strains. The primary tests are tension and compression tests in the uniaxial, biaxial, and planar (plane stress) directions. As SPAs are not loaded in compression, those tests are not considered here. Additionally, while uniaxial and planar tests can be performed with standard test equipment, biaxial testing requires specialized equipment in order to achieve properly-equilibrated two directional strains. Therefore, only uniaxial and planar tests in tension are performed here. The *spa_hyperelastic_modeling* tools allow the user to choose from and evaluate multiple general hyperelastic constitutive laws which may be expected to produce reasonable results for a broad range of materials. After testing compatibility with the material data, the model ultimately selected for this material is the Ogden model, defined by a strain energy potential function in the form:

$$U(\lambda_1, \lambda_2, \lambda_3, J) \sum_{i1}^{N} \frac{2\mu_i}{\alpha_i^2} \left(\lambda_1^{\alpha_i} + \lambda_2^{\alpha_i} + \lambda_3^{\alpha_i} - 3 \right) + \sum_{i1}^{N} \frac{1}{D_i} (J - 1)^{2i}$$

Equation 2:15

The model can be used with any number of terms N, where m_i and a_i are the primary fitting parameters, multiplied by the three principal stretches l. The second summation term contains the D_i fitting parameters to the volumetric deformation and the material Jacobian J. Without volumetric test data, the D_i parameters may be estimated directly from a given Poisson ratio. The formulas for stress given strain can be determined for the different tests through differentiations of Equation 1 with the appropriate strain conditions. Once the experimental data are acquired, a least-squares fit of the stress–strain equations can be computed to determine the parameters of the hyperelastic model [157]. The uniaxial and planar data are plotted with this initial fit in Figure 2:17a. After this fit has been calculated, an additional fitting step is taken in order to find the otherwise difficult to measure biaxial stress, resulting in the curves shown in Figure 2:17b. The additional fitting step is performed using an optimization loop which runs simulations of linear

actuators for free-displacement and blocked force and compares the results against experimental data.

Ogden3 model coefficients after optimization are: m_1 =0.024361, m_2 = 6.6703105 , m_3 = 4.5381104 , a_1 =1.7138, a_2 =7.0679, a_3 =3.3659, D_1 =3.2587, D_2 =D_3= 0.0. All m terms are in units of N mm^2, all a terms are dimensionless, and all D terms are in units of (N mm^2). The predictions of the model for uniaxial, biaxial, and planar loading are plotted with the experimental data in Figure 2:17.

.

(a)   (b)
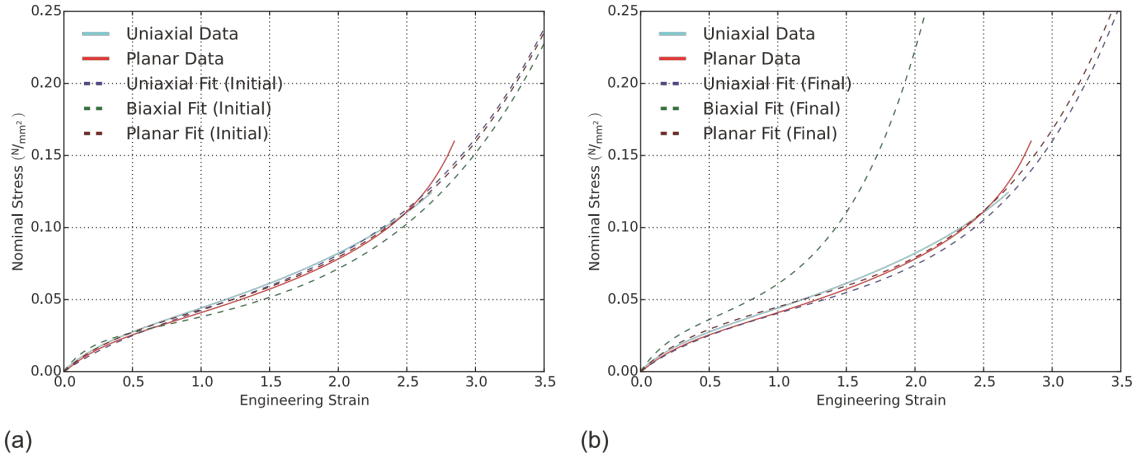
Figure 2:19 **Stress–strain curves from hyperelastic material testing showing the Ogden fit** with only the data gathered from a material testing (a), and an additional optimization process using the material testing data plus data from linear SPA displacements and forces (b). The optimization process uses the initial fit (a) as a starting point to iterate toward the desired actuator behavior. Experimental plots show representative data from the testing of multiple same-sized samples.

Modeling of SPAs using the FEM and experimental validation

We use the commercial FEM software Abaqus to calculate quasi-static solutions to model the response of SPAs under various pressure loadings. The quasi-static solution would improve the convergence of the model at high pressures (i.e., high strains) compared to a fully static solution, but requires some care to ensure that kinematic effects do not play a significant role. Here, a small amount of Rayleigh damping is applied to the model to keep kinetic effects to a minimum.

The dynamics of the air and airflow into the chambers are disregarded, and the air pressure is modeled simply as an applied pressure boundary condition on the face of each internal surface, which ramps up linearly in pseudo-time from zero to the desired value. The actuator itself is modeled using quarter-symmetry (linear actuators) or half-symmetry (bending actuators) to re-duce the computational cost. In this article, gravity is not considered in the model due to the very low masses of the actuators (<50 g). SPA properties are defined by the hyperelastic constitutive law determined in the previous section, along with the Ecoflex 00–30 Poisson's ratio of 0.48 and density of 0.00107 g mm^{-3}. We developed a tool, *spa_create_geometry*, which interfaces with Abaqus in order to automate the process of creating, meshing, and applying boundary conditions to a user-defined geometry.

As the functionality and performance of the actuators are directly dictated by the material, geometry, and boundary conditions, virtually infinite parameter combinations and design variations can be tested without having to produce individual prototypes. This design iteration process can be performed automatically using the *spa_optimize_geometric_parameters* tool. We prototyped actuators with the found parameters from the *Modeling tool* and compared their performance to the simulation results. The FEM model is validated against experimental data from two types of SPAs, for both displacement and blocked-force testing. The possible sources of error, in the actuators, in the experiments, and in the computational model, are investigated.

Validation of Simulations for Linear Actuators Experimental data is collected for linear actuators undergoing displacement and blocked-force testing. Computationally, these tests are modeled using quarter-symmetry, with the initial inlet tube and the external face containing the inlet fixed in all directions.
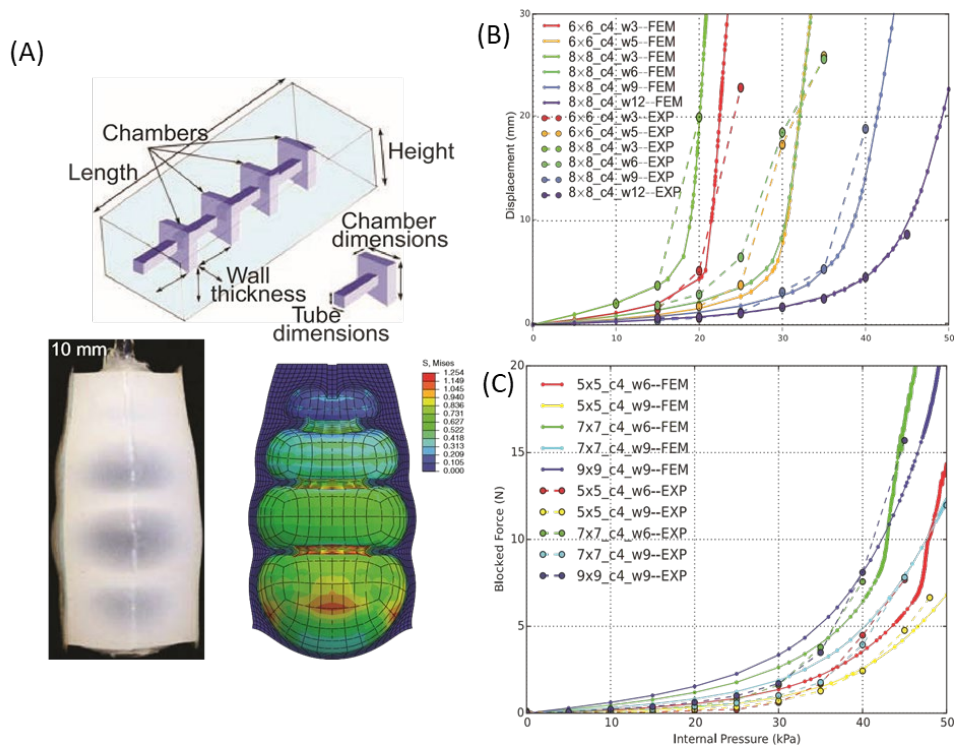
Figure 2:20 **Linear SPAs**. (A)Top: schematic of linear actuators and the geometric parameters relevant to the design of SPAs. Bottom-left: an 8 8_c4_w7 linear SPA under load at 35 kPa (after 2 s). Bottom right: a simulation of an identical linear actuator. Note that linear actuators are modeled in quarter-symmetry, but are shown here in half-symmetry for easier viewing. (B) Comparison of simulation and experimental results for linear SPAs of various dimensions in displacement testing. Predictions are consistent with experimental values at low and medium pressures across the range of geometries tested. (C) Comparison of simulation and experimental results for linear actuators of various dimensions in blocked-force.

Figure 2:18 shows a schematic of the linear SPA, along with a photo and simulation results of a four-chamber linear SPA under load. This particular sample is denoted with the short-hand notation 8 8_c4_w7, referring to an actuator with 4 chambers of 8x8 mm^2 cross-section, and a wall thickness of 7 mm. A desired pressure is applied as a constant load for 2 s and then released to ensure the non-bursting condition is captured. Figure 2:18b shows experimental results for six actuator samples of varying sizes fabricated using the same procedure in different batches. During linear actuator blocked-force testing, the displacements stabilizes during the first second of loading (unlike during displacement testing) and the pressure is maintained for 3 s before unloading. The results of the experiments and simulations are shown in Figure 2:18c. It can be seen

that the FEM results well-approximate the experimental results across a range of chamber sizes and wall thicknesses.

Validation of Simulations for Bending Actuators Bending actuators are tested for bending-angle, defined as shown in Figure 2:19, and blocked-force. This test is modeled using half-symmetry, and the SPA-infused silk membrane uses silk material properties on 0.5 mm-thick membrane elements, which have no bending resistance. Results for the bending actuator bending-angle tests are shown in Figure 2:19b. The simulations capture the behavior at low pressure as well as the trends at high pressure where the significant rotation occurs. Note that under the loading conditions here, the bending actuators do not experience the bursting seen in the linear actuators; the bending actuators are stable at each pressure presented here, despite the high displacements.

The blocked-force testing for the bending actuators requires a specific setup in order to measure the desired force without unnecessarily constricting the bending motion which occurs during loading. The simulations functionally mirror this setup, with the proximal end fixed and the distal end of the bending actuator allowed to slide friction-free across the load-cell. The bending actuator blocked-force results in Figure 2:19c predict the trends from the experiments, although the simulations predict the rapid increase in force approximately 5 kPa earlier than seen in experiments: small bending resistance in the inextensible layer and friction in the experimental setup defects could be the main factors.
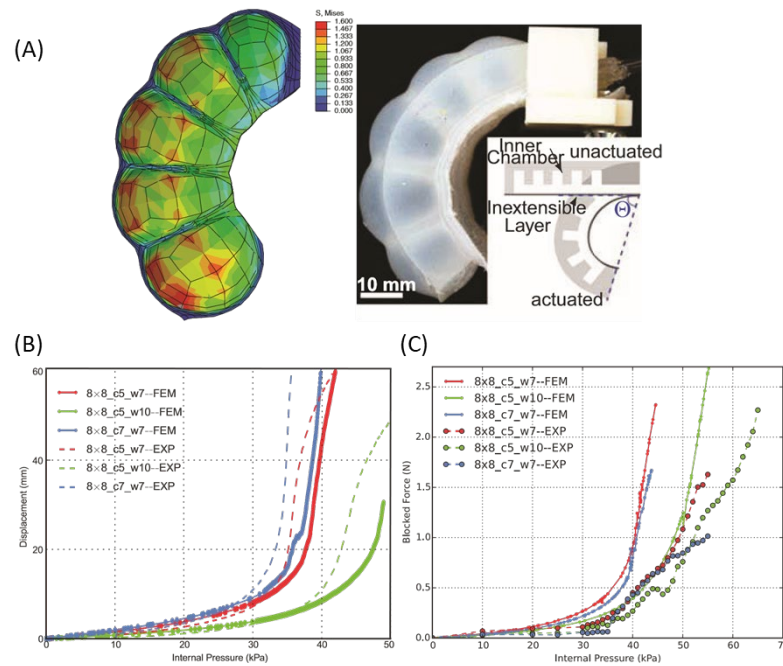
Figure 2:21 **Bending actuators.** (A) Left: maximum principal Von Mises stresses for a bending actuator in displacement testing at 45 kPa (8x8_c5_w7). Top right: a 8x8_c5_w7 bending SPA while loaded at 45 kPa. Bottom right corner: cross-sectional diagram of a bending SPA in the initial and bent configurations. u is the bending angle. (B) Comparison of simulation and experimental results for bending actuators of various dimensions in bending-angle (B) and blocked-force (C) testings. The simulations match the experimental results at low pressures and capture the experimental trends at high pressures where significant rotation occurs.

Conclusions

We have presented a computational tool and its experimentally validated results for the design and characterization of complex hyper-viscoelastic SPAs. This tool can aid researchers in solving challenging and time-consuming questions related to material choice and/or actuator design without requiring expertise in mechanical engineering, materials science, or robotics. The *spa_guided_design_tool* enables the engineering community to model and optimize the mechanistic properties of a wide range of SPA designs and to explore the universe of solutions created by the combination of geometric features and material choice. The validity and utility of the proposed approach are shown through experimental comparisons of two distinct types of SPAs and two corresponding case studies with proven real-life applicability. Additionally, the *spa_optimize_geometric_parameters* tool allows for automatic computational evaluation and optimization of a design, enabling rapid discovery of non-evident high-performing SPA configurations.

2.5.2 FEA modeling of V-SPAs: mechanical testing and constitutive material model fit

Foam-based negative pressure-driven Vacuum SPAs or V-SPAs, are developed towards applications in modular and compliant soft robotics [40]. These are novel actuators that are supported by foam structures inside a thin layer of silicone material that collapses upon actuation of vacuum, creating a linear or bending motion based on the structure. Foam material, similar to soft silicones exhibits non-linear behavior making V-SPAs difficult to model using traditional analytical approaches. However, by combining the hyper-elastic modeling techniques of *spa-design-tool* scripts with the material data from foam, it is possible to simulate the V-SPA behavior and further optimize it for specific applications.

Hence, computational modeling was done by using Finite Element Analysis (FEA) in ABAQUS/Standard (Simulia, Dassault Systems) to simulate the performance of the V-SPAs. 3-D models were created for the individual modules as well as for the entire assistive device. Models were developed to simulate both the linear and the bending modes of motion obtainable with each module. The details of the models are described in [58]. To model the highly non-linear mechanical behavior of the foam actuator body, an appropriate constitutive model needs to be used. Hyperfoam materials are typically highly compressible. After testing compatibility with the material data, the model ultimately selected for the foam used to build the modules was the Hyperfoam model. The Abaqus Hyperfoam model is a nonlinear, isotropic material model that is valid for cellular solids with porosity that permits large volumetric changes, and is suitable for hyperelastic foams. Material properties were determined through multiple tests on small material samples, performed across a large range of relevant strains. The types of experimental data that are used for modeling foam materials include uniaxial, biaxial, planar, simple shear and volumetric. Since the actuator module under current study is primarily designed for loading in compression and bending, multiple cycles of uniaxial compression tests and simple shear tests were performed (shown in Figure 2:20). The Hyperfoam model is defined by a strain energy potential function (*U*) in the form:

$$U(\hat{\lambda}_1, \hat{\lambda}_2, \hat{\lambda}_3) = \sum_{i=1}^{N} \frac{2\mu_i}{\alpha_i^2} [\hat{\lambda}_1^{\alpha_i} + \hat{\lambda}_2^{\alpha_i} + \hat{\lambda}_3^{\alpha_i} - 3$$
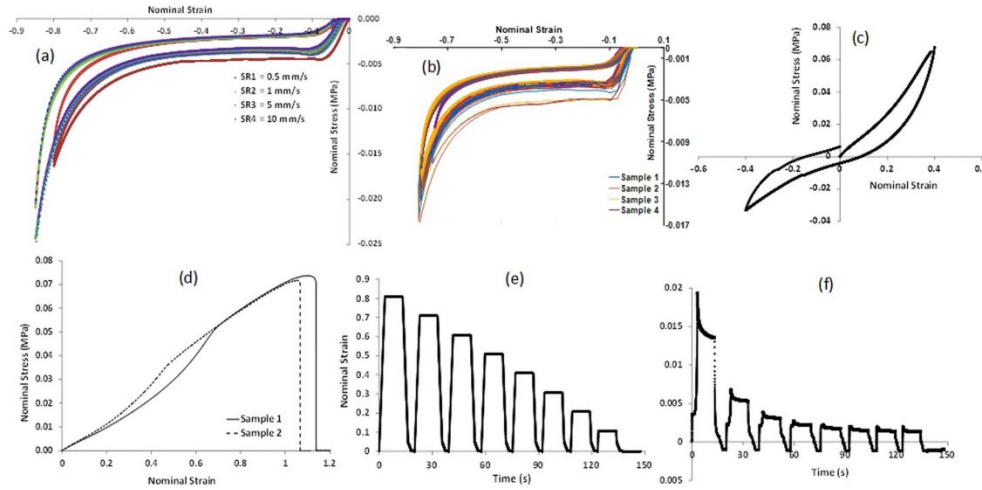
Figure 2:22 **Stress-strain data for polyurethane foam samples undergoing mechanical testing under diferent modes of deformation.** (a) Stress-strain data from uniaxial compression tests at different strain rates. The sample undergoes compression up to 80% of its original volume. (b) Cyclic test results in uniaxial compression. (c) Test results from simple shear testing. (d) Uniaxial tension test results. (e, f) Stress relaxation test results showing the decay of strain and stress vs. time, respectively

The model can be used with any number of terms N, where μ, α and β are the primary fitting parameters. The independent variables λ_1, λ_2 and λ_3 are the three principal stretches and are related to the strain in a continuum. The term J^{el} is the elastic volume ratio, and is a function of the principal stretches. The β_i parameters may be estimated directly from a given Poisson ratio, v. The formulas for stress given strain can be determined for the different tests through differentiations of 1 with the appropriate strain conditions. A material density of 0.0378 g/cm^3, calculated experimentally using mass and volume measurements is assumed for the foam in the model.

In addition, time-dependent behavior of the foam within the duration of the loading is taken into account by incorporating viscoelastic effects into the model. To accomplish this, stress relaxation data is gathered to study the decay of the shear modulus as a function of time. To perform stress relaxation testing, a high tensile compressive strain is rapidly applied to a test specimen and held constant for a period of time, during which the stress is measured. The testing is carried out on a 20 mm cube sample of the foam. Cross-sectional area of sample is 400 mm^2. Testing is carried out by compressing the sample upto 80% of its original volume, waiting for 10 seconds and observing the decay of stress at constant strain input (shown in Figure 2:20 e,f). Then the sample is taken back to its original position. This procedure is repeated multiple times. The decay of the stress is recorded as the material relaxes internally and then fit to the Prony series mathematical model in Abaqus.

Since the foam-based actuator chambers are designed to undergo rapid deformations over multiple loading sequences, the foam material samples were also subjected to cyclic loading tests to understand and incorporate the stress-strain behavior of the samples over repetitive loading conditions. Permanent deformations were observed in the foam after loading for a few cycles. Thus, the samples were conditioned for 20 cycles before the stress-strain curve saturated to a repeatable level. The saturated stress-strain curves were then used as an input to the FE model to capture the module behavior post multiple cycles of loading and predict the long-term operation performance obtainable. Using the above described sets of experimental data as an input, the coefficients of the material model were calculated using the in-built functionality in Abaqus^{TM}. These fitted coefficients for the material model were then directly used in the simulations without

any further changes. The coefficients thus obtained are reported in Table 2:3 for the Hyperfoam model fit.

I	MU_I	ALPHA_I	NU_I
1	0.284002	13.2805	0.00000
2	−0.283367	13.9800	0.00000
3	4.680466E-07	−4.77281	0.00000

Table 2:4 Hyperfoam Model Coefficients

To model the non-linear behavior of the reinforcement skin material (Elastosil), an incompressible, hyperelastic model was used. The Yeoh material model [150] was used to describe the mechanical behavior of the skin. The material coefficients used for this model were $C_1 = 0.11$ MPa, $C_2 = 0.02$ MPa [142]. A material density of 1.07 g/cm^3 is assumed for Elastosil in the model. In the simulations, a tie constraint is imposed between the inner surface of the skin and the outer surface of the foam body along the entire circumference of the module to replicate this adhesive contact between the two interacting surfaces.
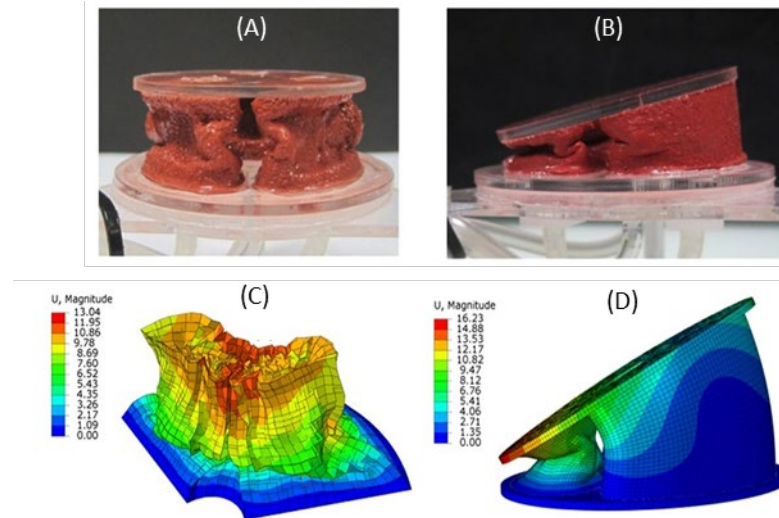
Figure 2:23 **V-SPA module with hyper-foam model simulation and experimental prototype** (A) Image of the module exhibiting linear displacement profile with all chambers subjected to vacuum pressure. (B) Image of module exhibiting bending motion profile with two chambers subjected to vacuum pressure. (C,D) Simulation results for linear and bending tests for V-SPA module.

Conclusions

The results obtained for actuator modules which deliver bending and linear displacement profiles using the same platform, depending on the actuator loading conditions. The motion profiles achieved with the modules are shown to qualitatively verify the buckling of the V-SPA. Accurate and experimentally validated computational models have been developed using FEM for the actuator modules as well as for the assembled device. Such a FEM model enable the simulation of the actuator and device performance under a variety of different loading scenarios and provides predictions on their capabilities prior to fabrication. Also, The stress concentration regions indicated in the simulations provide useful information regarding the design of the system and its failure regime.

2.5.3 Optimization for SPA-skin geometry for uniform force with high bandwidth

In section 2.5.1 we demonstrated iterative design process for two different linear and bending type of SPAs using FEA based tool. These actuators were designed extensively using Ecoflex 30®[100] material and the modeling script for material optimization are limited to traditional SPA-geometry. In this section, however we use a new material Dragon-skin 30®[158] with higher shore hardness which, is yet to characterized using Ogden-3 or Ogden-6 model in spa-design-tool and simulate different actuator designs for SPA-skin and experimentally validate them.

The objective here is to obtain a uniform inflation across the actuation area with minimum volume, so that the actuation bandwidth can be maximized without letting go on the output force. This design is ideally suited for generation of high-fidelity tactile stimulation including sub-threshold stochastic tactile stimulation, which requires a random pink noise input to be given to these actuators in the range of 20- 120 Hz for a specific study we intend to use the SPA-skin for [159], [160].

For the SPA simulation, we first characterized the Dragon skin 30 material with 3 planer and 5 dog bone samples according to ISTM standards to obtain the Ogden3 and polynomial data fit with 0.98 and 0.99 accuracy, which was not possible with the other models like Yeoh [150]. The material characterization data and the output of model fit is shown in Figure 2:22 and Figure 4:5.

The 3D model in Abaqus design tool consists of 0.4 mm thickness SPA-layers, then inflated thorugh a 50 um thick air channel inside to a static pressure input until The SPAs consist of two stretchable silicone layers (thickness 0.4 mm, Dragon Skin 30, Smooth On Inc., Macungie, PA, USA) interleaved with a customizable matrix that creates an inflatable cavity. Mesh refinements of different sizes were conducted to ensure stability of the results
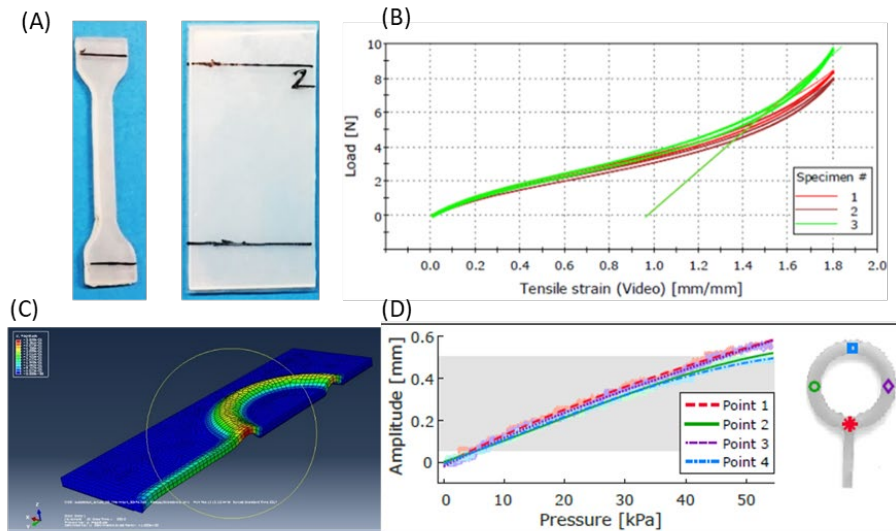
Figure 2:24 **SPA-skin FEA Modeling and experimental validation.** (A) Dogbone and planer samples for DS 30 characterization. Multi specimen characterization stress-strain curve for Dragon Skin 30® (B). Quarter geometry simulation results for SPA-skin ring-shaped design (C) and the inflation measurements at four different points displaying uniform levels of inflation that matched with experimental values (D).

We created various SPA-skin with different geometries to cover the maximum area with high bandwidth of actuation. This also allowed us to validate the rapid validation nature of the simulation environment for future applications where we do not necessarily have to validate each design choice through fabrication and testing. Figure 2:23 shows the physical designs and simulated versions of the prototype samples. At the end, we selected a bubble-shaped and a ring shape actuator for application where high force is needed and where wide bandwidth is needed, respectively.
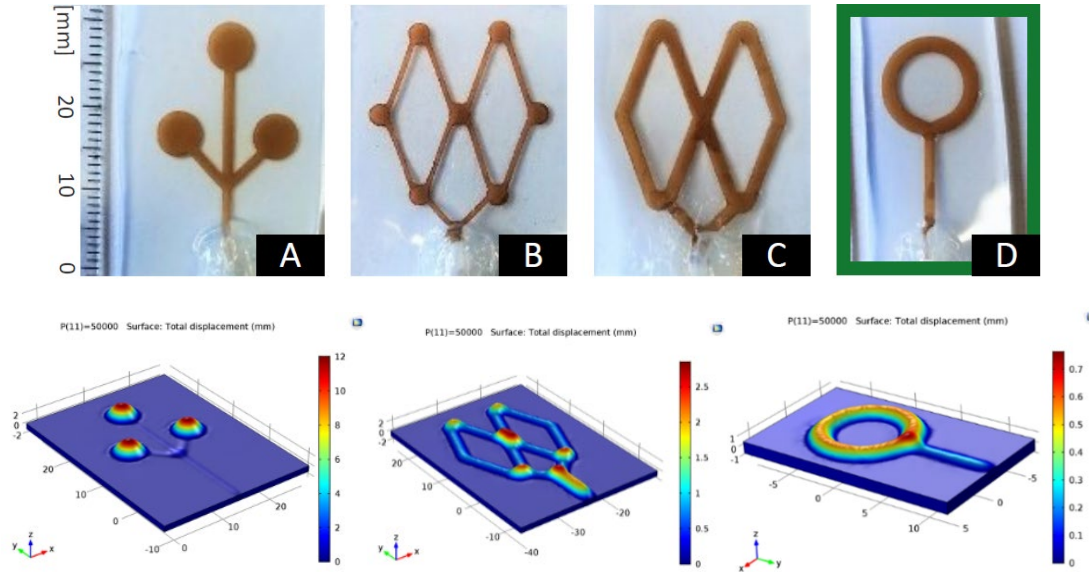
Figure 2:25 **SPA-skin FEA based design for uniform inflation based on material datal for Dragon-skin 30 ®.** Top: bubble-tree (A), bubble-duct (B), channel (C) and ring (D) shaped SPA structures. In the final application, we implemented the latter design. Bottom-row: static inflation simulation of the ring structure for a pressure of P = 50 kPa above ambient. Material properties were approximated as linear elastic with Young's modulus E = 500 kPa, Poison's ratio = 0:49 and density=1080 Kgm^3 . Bottom-right: Non-inflated (left) and inflated (right) state of the ring actuator shape. Our design supports very uniform and small inflation amplitudes covering a large area.

2.5.4   Actuator fabrication and dynamic characterization:

Effect of shape and thickness: These selected ring and bubble shapes of actuators were further developed, while keeping the actuation area constant with different thickness and extensively tested for variation in frequency and amplitude to measure the actuation in terms of output blocked force and inflation-height. Actuators were placed below the force sensor and inflated with different pressures and frequencies. The bubble actuator achieved 2.8 N of output force, whereas the ring actuator could achieve a little lower than 2.5 N of output force for 800 um thickness. Whereas in these cases the bandwidth shifts from ~40 Hz to ~60 Hz i.e. by 50% for 12% reduction in output blocked force. The numbers follow similar trend for 1200 um thickness with 25-30% lower output force as seen from
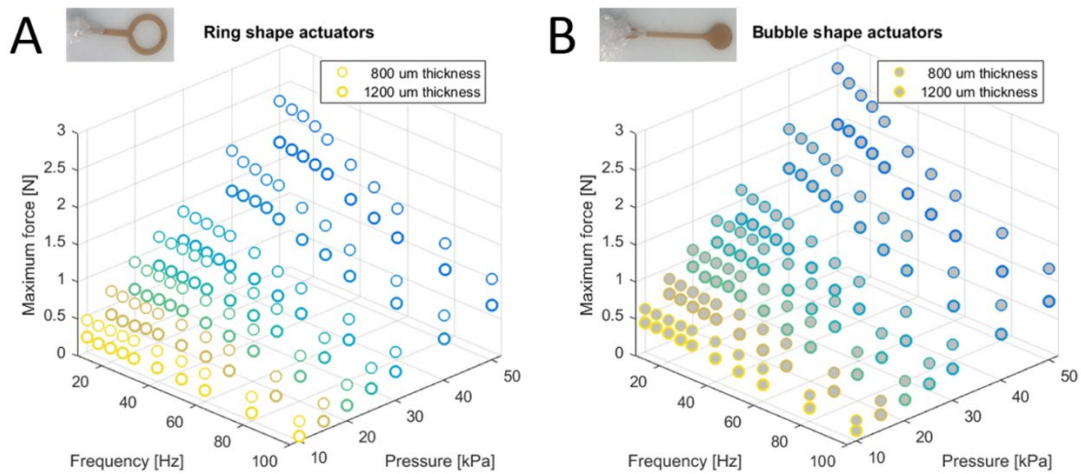
Figure 2:26 **Blocked force behavior over the different pressure and frequency combinations** for (A) ring shape, and (B) bubble shape SPA-skin. Higher pressures lead to higher inflation forces, whereas higher frequencies decrease the time available to inflate the actuator cavity completely thus reducing the maximum force. Both actuators show an approximately linear relationship between the thickness and the maximum force.

2.6 Discussion: soft wearable interfaces using SPA-skin

In this chapter, we introduced a unique, compliant, and distributable actuation system with an embedded grid of sensing capabilities. Additionally, the distributed sensing and actuation locations with high customizability makes the SPA-skin more versatile to accommodate multiple configurations for wearable applications.

Wearable interface design: Owing to the softness and flexibility of soft materials, SPA-skin can cover wide and curvy surfaces for actuation and sensing. Furthermore, it can acts as both an input and output device that produces modulating vibrotactile feedback over a range of frequencies. The ability of producing moderate to high output forces above 0.1 N at 100 Hz, make SPA-skin uniquely suitable for generation of complex tactile feedback that is necessary to emulate realistically features of object in nature.

	A) HC-DEA based	B) SPA-skin	C) Fabric SPA-skin	D) Haxel	E) DEA with stiff pillar
Year	2014	2016	2016	2020	2021
Frequency range	<10 Hz	0 - 100 Hz	N.A.	0 - 200 Hz	100 - 400 Hz
Output force	0.5 N @ 4.5kV	1 N @ 40 kPa	2.2 N	0.3 N @ 80Hz 1.4kV	7 N @ 300 Hz 4.5kV
Compactness	ø10 x 7 mm^2	ø6 x 1-2 mm^2	ø6 x 5 mm^2	ø6 x 0.8 mm^2	ø15 x 8 mm^2

Figure 2:27 Development of state of art fingertip wearable soft tactile displays for high-bandwidth, low-profile design. The soft wearable displays are mainly driven using SPA (B,C) or high-

voltage DEA based actuation (A,D,E) [66], [70], [65]. The years reflect first fingertip wearable version followed by the bandwidth, output force and compactness.

Figure 2:27 shows, how the SPA skin performance compares with existing wearable soft tactile interfaces. Over past few years, the state of art in compliant tactile displays evolved to provide wider range of complex tactile feedback while maintaining the low profile, soft wearable design. SPA-skin maintained a low profile design with wide bandwidth of actuation with cut-off frequency in excess of 100 Hz with the recent ring shaped designed 1N of output force for 6 mm actuator diameter. The recent development in HAXEL actuator can reach up to 300 mN of output force at 80 Hz while introducing a multimodal feedback using EAP technology.

Embedded sensing: The traditionally available tactile feedback devices are mainly open-loop in control, which allows them to be cost effective as well as a simple to implement. This also works well for generation of simple tactile feedback, especially considering human skin itself not being very accurate for sensory perception. However, in order to have a coherent feedback, specifically with a soft compliant actuator, which would not be able to produce intended feedback, under loading, a closed loop control is needed. Addition of sensing layer also helps to better understand the surrounding environment for robotic interface to augment the extended input-interface capabilities.

We implemented embedded sensing using two technologies while maintaining the low profile and wearability aspect. The localized sensing help SPA-skin to precisely sense vibration and to detect external forces and contacts. The novel methods of sensor manufacturing allows placing a grid of sensor electrodes over a surface. However, these capabilities are limited by the tethered wires that create a noisy environment. Digital filtering becomes necessary, as the sensed signal amplitude is comparable to the line noise captured by the long-running wires acting as an antenna. Furthermore, in case of the PZT sensor-based sensing layer provides active sensing with high-sensitivity and ultra-thin fabrication. However, it is limited to the flexibility of connecting electrodes and can only measure dynamic changes in interaction forces. The design of sensor electrodes allow for some degree of stretachbility for tight fit on user's body, however as the size of actuator increases above 5 mm, the SPA inflation will cause shear stress accumulation at the rigid-sensor interface that would lead for delamination with current 2x2 mm^2 sensor pixel size. To tackle these challenges we updated the SPA-skin design further to create not only a composite and conformant but also a stretchable and monolithic interface with integrated liquid metal sensors as discussed in Section 2.3. The high-speed data acquisition circuit, plasma bonded monolithic fabrication combined with geometrical bi-axial strain modelling yields an accurate measurement of inflation height. These sensors are designed to be worn for applications like a virtual or augmented reality gloves that raises practical concerns like lack of touch sensitivity due to SPA-skin interface coming in between user and physical environment. The change of temperature of the objects being touched by the wearer also would affect adversely as the thermal conductivity of GaIn metal is very high. We need to address these challenges possibly through simulating the interaction by amplifying the recorded forces by PZT/GaIn sensors through SPA actuation for a virtually transparent augmented interaction of user with surrounding environment, and using a sacrificial strain gauge with the pressure sensing liquid metal sensor for differentiating the temperature variation from pressure application.

Portability and pneumatic actuation: The choice of pneumatic actuation in the range of mesoscale wearable applications is motivated with high-force actuation and physical decoupling of actuator from actuation source. The available soft pneumatically actuated systems still suffer from bulky compressors powering these SPAs. One solution to achieve portability is use of high-pressure rechargeable cartridge for powering SPAs, which is controlled through miniature regulators and control valves. Currently, we focused on creating a portable solution to take SPA-skin from lab to the real world application by optimizing each possible component through material characterization (Section 2.4), SPA-shape optimization (Section 2.5.3) towards system level integration with tubing and pneumatic flow optimization as discussed later in Chapter 4.

Furthermore, currently an individual SPA requires an individual pneumatic supply line, making it difficult to scale or miniaturise the system beyond a certain point. We envision integration of novel valve technology would help reducing the number of wires, which I develop later in Section 4.2. Particularly, if it is needed to produce a portable and wearable solution with very high-resolution there are trade-offs to be made between output force, bandwidth of actuation, and external power requirements like high-voltage or bulky power-supply. Finally, we use SPA-skin technology coupled with plug-n-play pneumatic controller as a wearable tactile feedback platform to better understand human sense of touch and cues for improved tactile feedback in Chapter 5.

Chapter 3 Control strategies for wearable soft interfaces

3.1 Introduction

Tactile feedback plays an important role in human-robot interaction. The human sense of touch, or tactile perception, consists of multiple experiences, which can be categorized as rough texture, fine-texture, lateral friction, size, temperature or weight [161]–[163]. In order to successfully recreate a realistic feeling of touch in a virtual environment, a tactile feedback device should be able to integrate more than one of these multi-modal sensations[163].

Researchers have characterized, modeled and rendered tactile properties such as surface texture and hardness on tabletop interfaces [62], [161], [162]. It is particularly challenging to develop a wearable tactile-feedback device able to generate texture feedback, as this requires delivering a wide range of actuation frequencies. Recent technological effort in wearable prototypes relied heavily on the use of vibrotactile electromechanical actuators; however, their localization capability and the range of actuation frequencies remain restricted. Use of voice coil actuators at the finger tips[164]–[166] or the proximal phalanges[167] helped to improve the actuation range; however, this actuator solution is impractical in terms of size and weight needed to achieve a reasonable spatial resolution. Dielectric elastomer actuator (DEA) – based haptic devices combined with a wearable platform supply the much-needed mechanical compliance with human skin [70], [168]. However, they have a high voltage requirement and provide limited actuation forces in the range of 0.3 - 0.6N. In conclusion, existing solutions for haptic feedback are compelling for a defined range of frequencies and forces in the preset format of a tabletop or for a few wearable platforms. However, currently, there is no comprehensive solution or design that allows rendering a rich set of tactile feedback and actually verify the effectiveness of this physical feedback, especially in a wearable format. In fact, what is lacking is a low-profile platform, thin enough to be mechanically transparent, which not only provides high-fidelity tactile feedback but also allows fingers to be free for simultaneous and instantaneous environmental exploration.

Similarly, translating a virtual object's shape has been another principal focus of the haptics field. One way of recreating a shape is by actuating a 2.5D shape display, which consists of actuated pin arrays that can alter the heights of multiple pins in a grid [169]–[171]. Some of these devices not only render the shape but further expand possibilities by integrating force control for dynamic interpretation of force and stiffness of materials [172], [173]. Although these pin-based shape displays allow multi-point and multimodal cutaneous feedback for exploring virtual environments, the interactions are limited to a plane and a modulated height - 2.5D experience. In addition, this type of shape display needs a large number of actuators (from 50 to several hundred), which with a high aspect ratio (usually higher than 30) to map the shape of objects; this solution cannot be applied to a fully-3D environment. To generate shapes entirely in 3D, there are several interactive interfaces based on unconventional materials and actuators, such as soft pneumatic actuators[174]–[176], jamming materials[177], or shape memory materials[178], [179]. Shape generation, however, is still restricted by the number of actuators, despite a few model-based designs achieving target shape with relatively small numbers of actuators[180], [181]. Some wearable/handheld devices[165], [166], [182], [183] provide an alternative solution for tangibly perceiving shapes and spatial information. They enable a more natural interaction and larger workspaces for shape exploration in contrast to tabletop devices, which have limited workspace.

In this chapter we discuss in detail intelligent control algorithms for controlled feedback from SPA skin [2] as well as integration of the interface with a comprehensive control environment for a multi-modal VR interactivity.

We divide the control strategies for the soft interfaces in two groups:

> *High level control environment:* It involves the control environment as whole with virtual physics engine for interaction, human pose estimation, and commands being sent to various actuators. In this section, we present for the first time, the design of a comprehensive and coherent tactile information transfer system and an experimental protocol for validating the tactile feedback. Our approach utilizes a novel soft interactive interface linked to a soft malleable object. The soft interactive interface consists of a soft pneumatic actuator (SPA) layer integrated with PZT sensors or liquid metal GaIn sensor to form an SPA-skin, providing a wide range of controlled vibratory feedback to the fingertips. The control environment enable for a human-in-loop evaluation is critical for validating the tactile feedback at the interface and how well the human is integrated or immersed in the process. Here, the haptic-feedback loop is closed through the user's actions (Figure 3:1 b,c), and comparison between the moldable object's final shape and the intended virtual shape is a measure of the effectiveness of the SPA-skin platform.

> *Low level closed-loop control:* Here we develop closed loop controllers and filtering algorithms based on the system models as developed in Chapter 2 to provide a controlled feedback to the wearer. The FEA based analysis helps in predicting the feedforward model, where as, filtered and signal conditioned sensor data is used for controlled error tracking for constant dynamic force or strain tracking. The controlled feedback then able to generate texture and auxiliary tactile response, bought about by actuation frequencies being proportional to the distance from the target shape, therefore guiding users towards the intended shape.

Overall, we explore the applicability of the SPA-skin as a tactile-feedback device in a set of experiments that investigate a variety of haptic experiences, possible through the sensation of touch and tactile perception. We first begin with the low-level controllability and achieving a modular control for dynamic feedback for each sensor-actuator pair.

The major contributions of the presented work are:

1. A novel testbed and protocol design for validating the experience of rich haptic sensation (texture, size, and shape).

The material presented in this chapter is adopted from following self-authored publications:

[54] **H. A. Sonar** and J. Paik, "Soft Pneumatic Actuator Skin with Piezoelectric Sensors for Vibrotactile Feedback," *Front. Robot. AI*, vol. 2, 2016, doi: 10.3389/frobt.2015.00038

[55] **H. A. Sonar**, A. P. Gerratt, S. P. Lacour, and J. Paik, "Closed-loop haptic feedback control using a self-sensing soft pneumatic actuator skin," *Soft Robotics*, vol. 7, no. 1, pp. 22–29, 2020.

[184] **H. A. Sonar**, J.-L. Huang, and J. Paik, "Soft Touch using Soft Pneumatic Actuator–Skin as a Wearable Haptic Feedback Device," *Adv. Intell. Syst.*, vol. 3, no. 3, p. 2000168, 2021,

[†] *Physicalization:* in this context, is defined as the process of transferring the digital data to a physical/tangible form that people can explore and communicate with[185]

2. A unique PZT sensor-embedded SPA-skin and system design for high bandwidth tactile feedback, noise isolation from skin contact, controlled feedback, and software decoupling to observe user interactions while closed-loop controlling the actuator.

3. Using tactile cues to organically guide users to reconstruct simple planer shapes as a measure of the interaction response with the SPA-skin
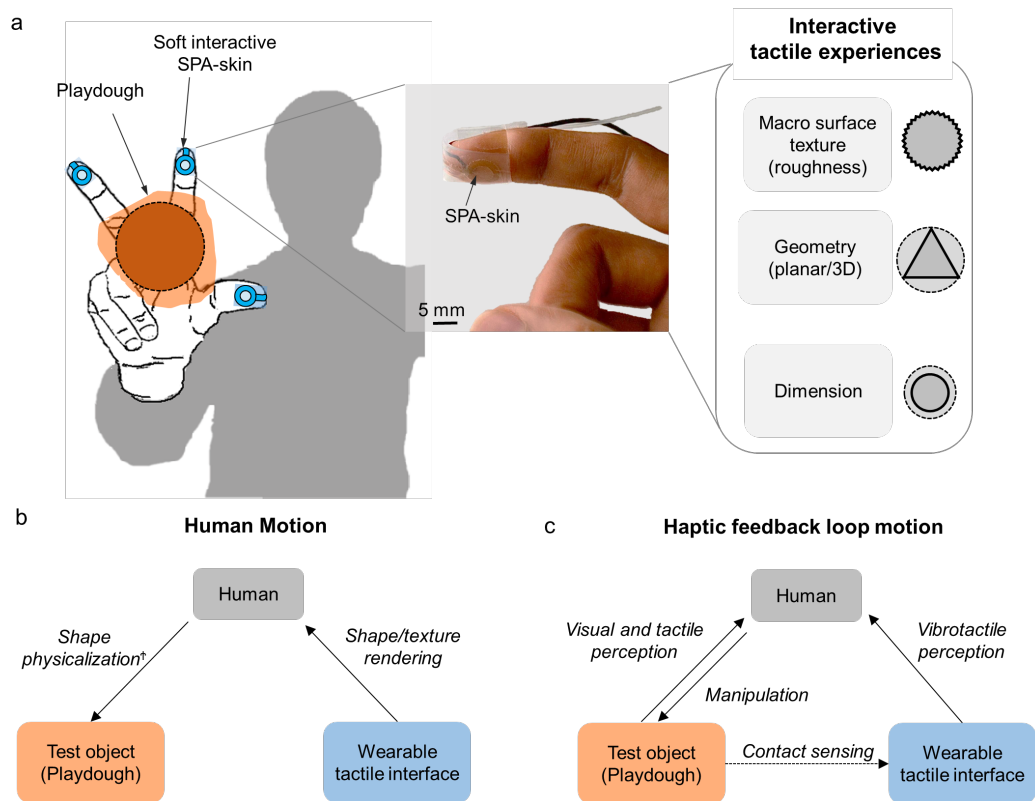
Figure 3:1**Wearable soft interactive interface** (a) A two-component system combining a wearable interactive SPA-skin with a passive soft playdough object to generate multi-experience tactile feedback of macro-surface textures, planar shapes, and size tracing. Multi-level tactile feedback is used for directed spatial localization of planar virtual shapes via a: (b) Human motion side and (c) Haptic feedback-loop motion side. Human motion and haptic feedback-loop motion block diagrams illustrate the separate actions of the human and computer units. The wearable tactile interface triggers the human motion to help in physical shape rendering, *physicalization*[†], of the moldable test object (b). The haptic feedback motion loop senses the location of the human fingers and the contact with the test object boundaries to generate multi-level tactile feedback (c).

3.2 Distributed discrete PZT sensor integration, Modeling and control with SPA-skin

3.2.1 SPA-skin control

The SPA-skin consists of an array of actuators that produce the desired inflation for a specific pneumatic input pressure. Any hardware actuator, including DC motors, pneumatic regulators, and pressure valves, requires a feedback mechanism to accurately control the actuation. However, we rarely observe this in vibratory actuators (Precision Microdrives Ltd. 2015). When we require closed-loop control, it is not feasible to rely on human sensory perception for actuator tuning or comparison as sensory perception varies drastically from one person to another. The integration of sensing elements in SPA-skin provides the necessary feedback to allow for closed-loop control of the vibration amplitude. In this section we evaluate the soft actuator's dynamics and the response of the integrated PZT sensor to determine the operational bandwidth of SPA-skin. This is followed by the design of a feedback controller to accurately control the vibrotactile stimulation with small disturbances.

3.2.2 Operational bandwidth of SPA-skin

Feedback through the physical interface is dictated by the level of the input frequency. Therefore the system response of the SPA-skin was investigated for a variety of actuation frequencies to determine the actual operational bandwidth and effectiveness of the vibrotactile feedback. The signal conditioning circuit has a cut-off frequency of 86 Hz, so we recorded data for the actuator's response between 10 - 90 Hz. The Figure [fig:bandwidth] shows the raw data recordings for a variety of frequencies at a constant input pressure. The actuator bandwidth obtained for the current setup with a tube length of 50 cm, an inlet diameter of 1 mm and an actuation chamber of 4 mm diameter is approximately 35 Hz. Ideally, this should limit the practical maximum control bandwidth for the vibrotactile feedback to 40 Hz. Human finger skin has sensitivity to vibrotactile stimuli of even lower amplitudes and forces [64] We experimentally obtained perceivable stimulation and measurable variation in the sensor reading from an input pressure of 19 kPa onwards for the SPA-skin setup. The response of this minimum perceivable signal is shown in Figure 3:1 together with the frequency response at nominal input pressure (70 kPa). We observe that even near the cutoff frequency, the amplitude of the nominal input signal is higher than the minimum perceivable amplitude for tactile sensation. This extends the operational bandwidth of the SPA actuator from 40 Hz to 90 Hz.

Actuator frequency response recorded through PZT signal with and without notch filter
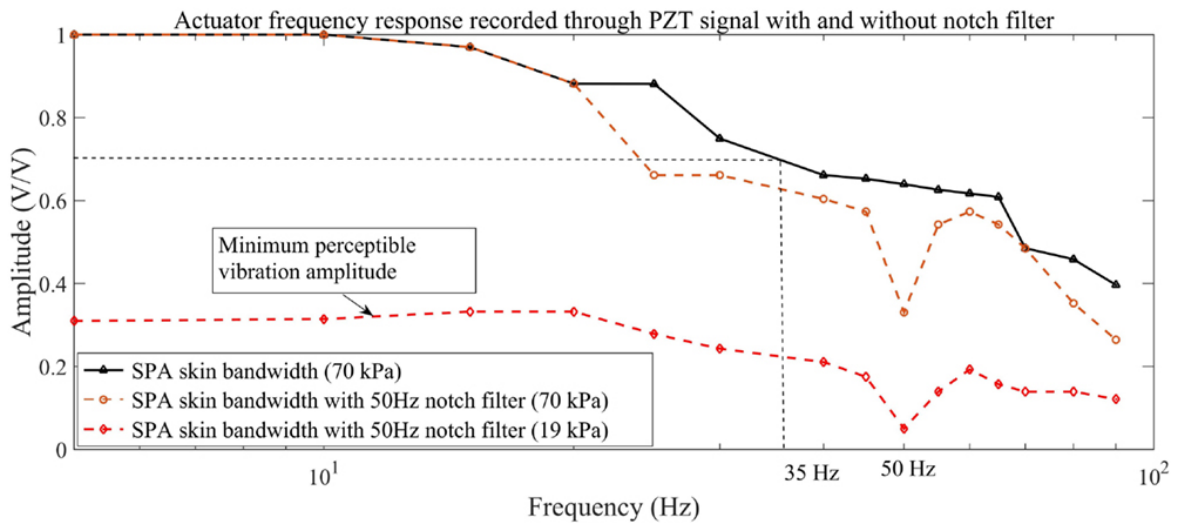
Figure 3:2 **Frequency response of sensor integrated SPA-skin as measured by the control environment.** The SPA-skin produces measurable vibrations from 19 kPa onwards of the regulator pressure. The SPA-skin amplitude response at 70 kPa is always above the minimum perceptible amplitude for the frequency range of 10 - 90 Hz.

3.2.3   Controller for augmented vibratory actuation

As the SPA-skin is composed of hyper-elastic material, the relationship between the input pressure and the output amplitude of the actuator is non-linear by nature. Furthermore, minute fabrication defects can cause variations in the properties of the SPA-skin. This makes open loop control of the actuation amplitude impractical. We, therefore, present a closed-loop feedback system for accurate vibrotactile stimulation.

We have an approximate model fit for the sensor-actuator system with first-order dynamics as discussed in Section 2.2.2. Assuming this linear range of operation PI(D) controller is implemented to demonstrate the active closed-loop feedback capability. The derivative term is zero to avoid noise amplification on discrete update of input signal (detected peak-value signal). The actuation amplitude is a function of the average pressure inside the inflated chamber. As the pressure regulator used in the setup has a time constant of 1.5 s, it can not be used for high-speed control of the input pressure. Instead, a high-speed on-off valve is added and its duty cycle is used as the control parameter for a desired average input pressure. The relationship between the percentage duty cycle and the maximum average pressure inside the actuation chamber is linear, independent of the frequency of actuation. The slope of this relationship is determined by the input pressure from the regulator. As previously shown in Figure 2:3 the sensor response is linearly proportional to the change is the normal applied force. Therefore, the sensor signal can be used to actively compensate for the deviation from the set point (SP) value. The PI control law for this system is as follows:

$$e(t) = SP - y(t)$$

$$u\left(t\right) = K_P e\left(t\right) + K_I \int_0^\tau e\left(t\right) d\tau$$

Equation 3:1

In the digital domain for sampling time, Ts, Equation (4) becomes,

$$U\left(z\right) = \left[K_P + \frac{K_I T_s}{1 - z^{-1}}\right] E\left(z\right)$$

Equation 3:2

and the corresponding difference equation for the controller is:

$$u\left[k\right] = u\left[k-1\right] + K_1 e\left[k\right] + K_2 e\left[k-1\right]$$

Equation 3:3

where, $K_1 = K_P + K_I T_1$ and $K_2 = -K_P$

The PI gains are tuned to obtain a stable controller response over a range of operating frequencies between 10 Hz and 90 Hz. For the current SPA-skin design, the set point value for a required blocked force ranges from 0 - 0.3 N, which translates to sensor readings of 0 - 300 mV. The experimental results for this closed-loop system are presented in Section 4 and demonstrate steady response for a given set point.

3.2.4 Closed-loop control of the SPA-skin prototype with internal and external inputs

In the first subsection, we evaluate the controller performance for desired step input for the input signal from SPA-skin's actuation at two different frequencies. The second subsection demonstrates the capability of the PZT sensors to detect external interaction forces and differentiate them from the internal vibrotactile actuation.

Closed-loop control of the vibratory motors of SPA-Skin at 15 Hz and 70 Hz
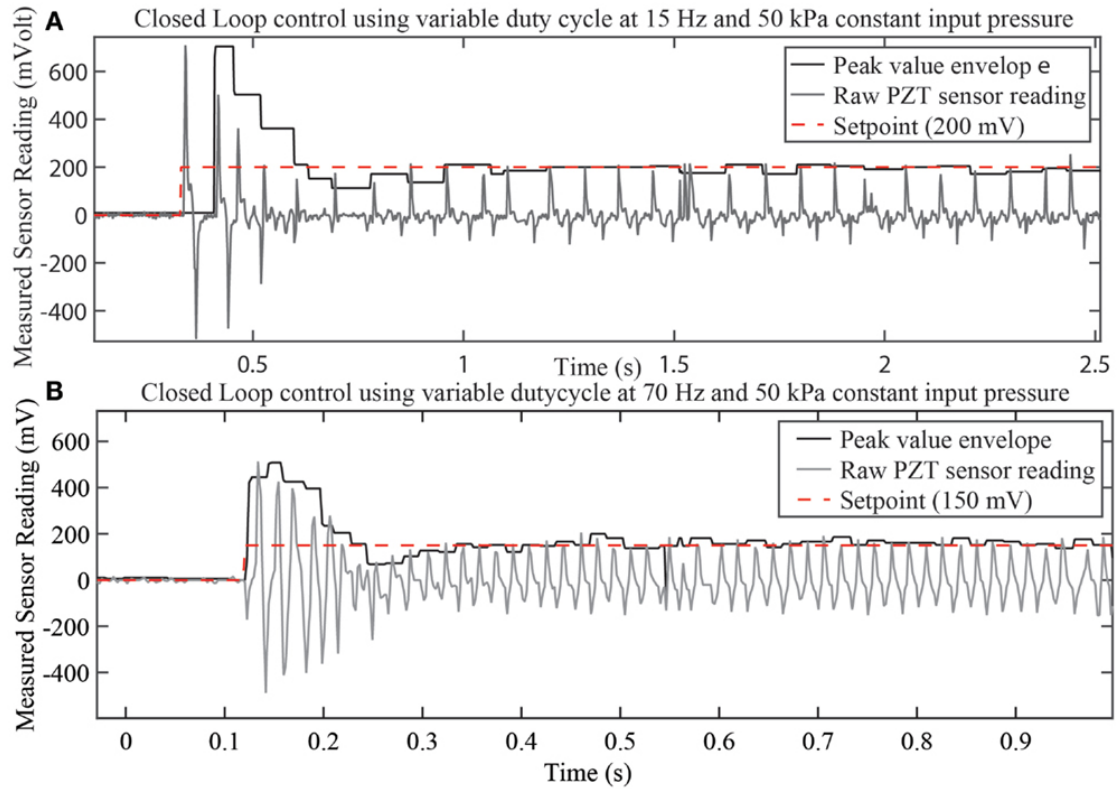
Figure 3:3 **Closed-loop control results for the PI-controller**. The SPA-skin is actuated at 15 Hz (A) and 70 Hz (B) at a constant regulator pressure of 50 kPa to validate the controller performance over range of actuation frequencies. The peak value envelope signal derived from the raw PZT sensor reading acts as a control signal to generate the desired duty cycle for the pneumatic valve.

The haptic feedback research has yet to focus on controlling the vibratory actuation. Not only is there a lack of measurable setup in both actuator and sensor, but also it has been more interesting to investigate on the vibrational effect upon the contact. In fact, it has been the human skin that served as the feedback mechanism in the loop. However, to understand and perceive the quantifiable effects of vibrations, we need to close-loop control the actuator. Because we already have the PZT sensors embedded within the actuator layer, we can use these PZT sensors to serve the double duty to control the actuation as well. To do this, we developed a PI based closed-loop

control to achieve active control over the vibration amplitude and consequently control the level of the vibrotactile feedback that will be perceived by the user. The peak value detected from PZT sensor signal during each on-off cycle of the output actuation is used as the input control signal. The digital controller takes control action as soon as a new peak value is available. The controller gains K_1 and K_2 (in Equation 3:3) are tuned in order to obtain a stable performance over a range of actuation frequencies without gain re-scheduling. The test results in Figure 3:3 show controller response for a set point step at a relatively lower vibration frequency of 15 Hz and at a relatively higher vibration frequency of 70 Hz. The controller output is used to drive the PWM duty cycle value of the on-off control valve which in turn change the average pressure inside actuation chamber. It can also be observed from Figure 3:3 that in both tests the controller settles in less than 0.5 s. During our experiment, the controller minimized the disturbances originated from minor manufacturing defects, variation in inlet tube length, and external loading during actuator placement on human body.

3.2.5   Detection of external interaction forces

The sensing capability of SPA-skin is not only limited to vibrotactile actuation amplitude but also can further be used to detect external interaction forces. Currently there are very few haptic devices that can embed contact force sensors, which allows monitoring and controlling of the vibration motors in a closed-loop. Therefore, the closed-loop controllable SPA-skin is even more suitable for the wearable application environments where it not only provides vibrotactile feedback but also measures the external forces the wearable body faces. As we only have a single sensor array for the contact input, we developed a decoupling algorithm to process the acquired PZT signal. We categorize the signal into two components, A) SPA-skin actuation and B) external interaction forces. External interactions are typically of low frequencies (<20 Hz) as observed from Figure 3:4(A). Therefore, we excited SPA-skin at a higher frequency (65 Hz) than frequency range of the external disturbance signal. The peak value detection algorithm uses the knowledge of actuation frequency to detect the PZT signal envelope. This detected envelope selectively suppresses the high frequency component due SPA-skin actuation and upon low pass filtering at 25 Hz the component of the SPA skin actuation frequency is completely decoupled. The frequency spectrum of the peak value envelop signal (Figure 3:4 (A)) shows complete suppression of vibration frequency at 65 Hz and preservation of disturbance signal. This technique is similar to the diode detector or the square law detection algorithm used in recovering the amplitude modulated (AM) signal [186].
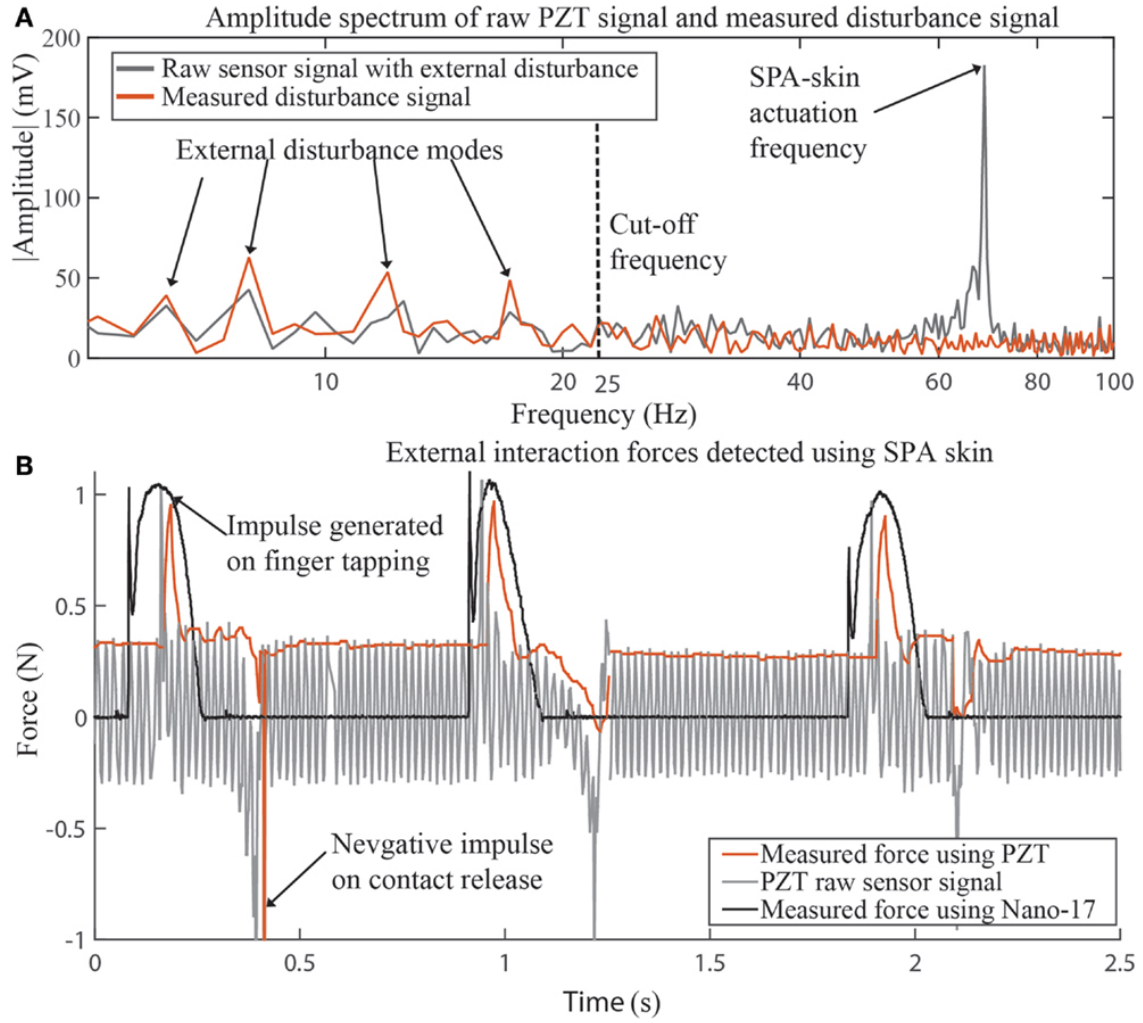
Figure 3:4 **SPA-skin external signal detection**. Frequency domain representation (A) of raw sensor signal and filtered peak value signal clearly demonstrates the capability to filter actuator vibrations and preserve disturbance signal. The external physical disturbances have interaction frequencies less than 20 Hz. Detection of external interaction due to finger tapping on previously actuated SPA-skin at 65 Hz (B). The force sensor data and filtered PZT data in (B) read comparable interaction force on positive impact-.

The SPA-skin vibrating at 65 Hz is placed on top of a *Nano*-17 force sensor to record the external impact force. We tapped on the actuation area multiple times to provide the disturbance input. When finger is tapped on the vibrating SPA-skin an impulse is generated as shown in Figure 3:4 (B) recorded by both the *Nano*-17 force sensor and the PZT sensors. As PZT sensors are embedded inside the soft silicone structure, they can also sense an impulse in negative direction (Figure 3:4 B)) on contact release. The rigid force sensor cannot not measure this interaction in the opposite direction. The force sensor measured 1 N impact force which is the coupled force of vibrotactile actuation and impact. The results obtained using force sensor are comparable with the dynamic interaction forces detected by PZT sensor though this requires initial calibration of the PZT sensor.

3.2.6   Conclusion

We developed an algorithm to decouple the internal and external interaction signals to maximize the detectable range of forces including feedback control of the vibratory actuators. The peak value generated on sensor by step actuation of the SPA contains the information about the blocked force exerted by the single actuation cell on the sensor. The filtered sensor data is therefore recorded over a complete PWM on-time to measure the peak value. This value is used by the closed-loop controller to take the necessary control action. The detected peak value is updated every period of the actuation frequency, limiting the control bandwidth to the frequency of SPA actuation. For the presented prototype, we concentrated on implementation of the controller and external signal detection for a single sensor and actuator. The present hardware and micro-controller platform can simultaneously detect peak values up to 16 sensors and control 16 actuators using independent feedback controllers at 1 kHz. The capabilities can be further extended based on the distributed sensing requirements. In near future more experiments will be carried out with variety of sensor and actuator sizes to evaluate the dynamic model and over all transfer function of the sensor integrated SPA-skin. Better techniques to minimize the noise through optimal shielding and robust filtering will be investigated. Efforts are being made to integrate the sensor embedded SPA-skin as a *plug-and-play* wearable vibrotactile component for a virtual reality system and a feedback mechanism for a rehabilitation device.

3.3   Modeling and design of entirely soft actuation system

3.3.1   Introduction

The SPA-skin interface, a sensor and actuator laminate, is specifically designed to provide a consistent vibrotactile feedback under variation of the input parameters: amplitude, vibratory frequency, and external loading force (Figure 3:5). Amplitude and frequency are the inputs set by the user-need, while external loading is dictated by the environmental interactions and disturbance. The sensor-integrated SPA compensates for these three inputs through an active closed-loop feedback control. Here, a seamlessly integrated stretchable strain sensor measures the strain experienced upon the actuator inflation by the resistance change. This measurement provides an estimate of the actuator amplitude, which is then used to maintain the SPA inflation to the set point by actively controlling the input pressure. We also developed a custom data acquisition platform to enable strain sensing and actuation control at high-speed (1 kHz) to reliably cover the SPA actuation frequency from 0 to 100 Hz.

We feedback controlled for the first time, an entirely soft haptic platform. We experimented this on an entirely soft design of SPA-skin, enabling flexible, conformal, and distributable interface over a variety of surfaces. In addition, the integrated sensing and active closed-loop control provide accurate modulation of actuation amplitude and frequency for rich feedback. In addition, as the closed-loop control also provided an accurate reading, the physical feedback is independent of any external loading.
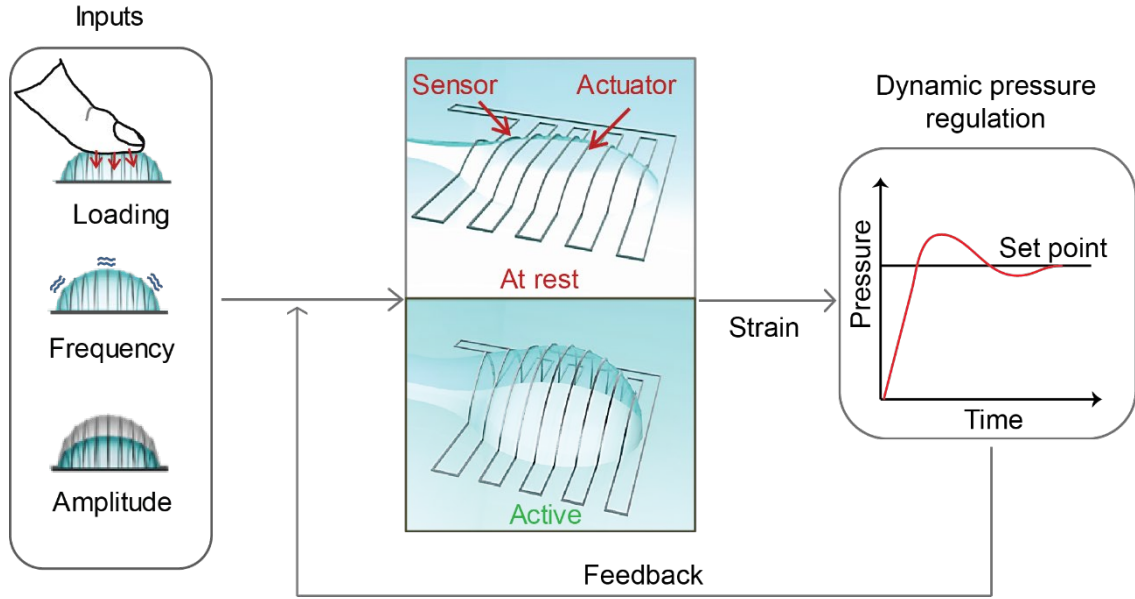
Figure 3:5 **Feedback control loop of entirely soft haptic system.** The SPA-skin provides a highly conformal interface. A strain sensor of stretchable metallization can be used as the input to a feedback loop used to control the actuator inflation and exerted force. High-speed data acquisition allows strain sensing and actuation over a range of actuation frequencies from 0 to 100 Hz.

3.3.2   Experimental setup

High-speed actuation of SPA-skin demands a test setup that provides a high data rate resistance measurement and a low settling time pressure regulation. We required at least 1000 samples/second of sensor resistance values in order to ensure reliable and accurate estimation of actuator state, as a digital control system needs at least 8-10 times more samples than the actual operational frequency of the system (100 Hz for SPA-skin). We developed a custom 16-bit high-speed data acquisition system with a low resistance multiplexer, A/DC (ADS8517, TI, USA) and an Arduino microcontroller board that measured the sensor resistance at 1600 Hz per channel with 0.4% accuracy (Figure 2:8b). The low resistance multiplexer reduced the effect of extra resistance added in the sensor resistance measurement. It was also necessary to have a pressure regulator that can react within 10 ms to be able to control the SPA-skin at 100 Hz of vibratory output. In practice, we obtained settling time of 20 ms with a piezo-actuator drive pressure for maximum pressure change from 0 to 100 kPa that allowed us to control SPA-skin up to 50 Hz. The Arduino microcontroller also directed the control commands to this piezo-pressure regulator to achieve the desired set point. The test setup is also equipped with an integrated pressure sensor (001BGAA5, Honeywell) and a laser interferometer (HG-C1030, Panasonic) to measure the SPA pressure and the inflation height, respectively. There is a micro-meter placed vertically and connected to a high precision 3D force sensor (Nano 17, ATI industrial automation, USA) for applying controlled blocked force externally to simulate disturbances.

3.3.3   Active control of the force exerted by the SPA-skin

A coherent and responsive haptic feedback from deformable soft interfaces relies on explicit control of the actuation force and frequency, regardless of the loading conditions. If not, the wearer will feel unstable feedback depending on how the device is positioned. Hence, we demonstrated the closed-loop capabilities to actively adapt for the changes in the loading and provide a coherent tactile feedback. We designed a setup which uses a 1 cm^3 cube of Ecoflex 30 silicone [24] to simulate contact with the human skin, placed over the SPA-skin (a). Ecoflex 30 is selected as its compressive behavior is comparable with that of human skin [187].

We have the relationship between the measured resistance and the biaxial strain on the system from the analytical model. Using the feedforward approach and assuming linear range of the operation, PID controller is developed to demonstrate the closed-loop control capabilities of the SPA-skin. During free, unloaded operation, the control loop easily achieved the arbitrary strain set points (Figure 3:6b). Additionally when external forces were introduced, the system continues to converge to the set point inflation, regardless of the pre-load (Figure 3:6c). The feedback from the embedded strain sensors guarantees the desired actuation, even when the external loading is an order of magnitude higher than the desired blocked-force produced by the SPA-skin (Figure 3:6d). Eventually, as the loading increases, the system's mechanical inertia increases, which leads to an increase in the overshoot in the control (Figure 3:6c). We tuned the PID gains conservatively to cover this fact and compensate for the overshoot, while degrading a little on the system settling time.
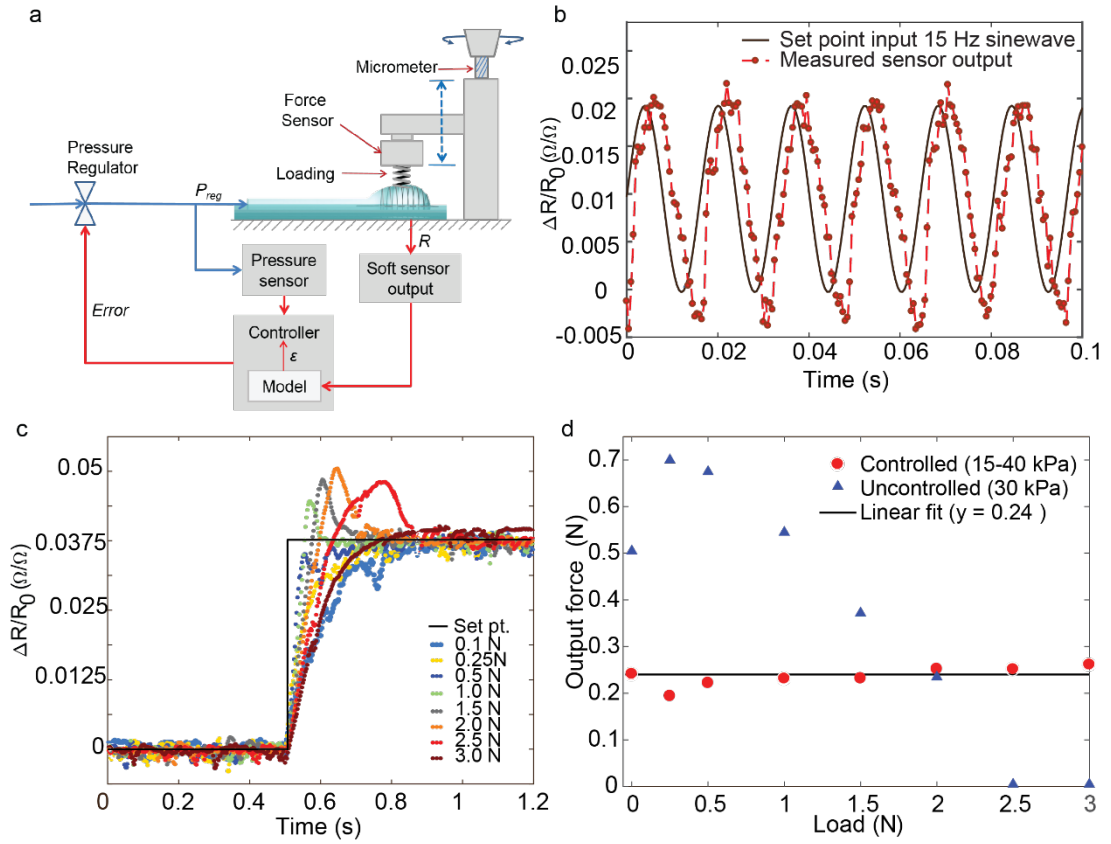
Figure 3:6: **Testbed for active closed-loop control**. (a) Control flow diagram of the SPA-skin with a soft, skin-like material placed between the actuator and an external force sensor, simulating external loading of the sensor against skin. A Vernier scale controls the displacement, and therefore blocked force. (b) Controller tracking a sinusoidal perturbation of set point input at 15 Hz. (c) Controller performance under eight different loading conditions. The controller has a damped response at 3 N as the pressure required to achieve the set point exceeds the 40 kPa pressure controller safety limit. (d) Effect of loading on the SPA-skin performance when controlled using a pressure sensor and when using an integrated strain sensor to achieve a 0.25 N blocked force set point.

3.3.4 Conclusion

For an effective wearable technology, we require an accurate understanding of the physical interactions between the device and the wearer's perception. We engineered a closed-loop control of an entirely soft wearable haptic platform over a wide range of vibrotactile feedback. We pro-

totyped a soft monolithic sensor integrated SPA with embedded sensing and actuation capabilities, and with soft sensors that have no mechanical loading impact on the actuator. In addition, the SPA-skin produced forces up to 1 N with controllability of 0.05 N, and actuation dynamics of up to 100 Hz with controllability of 0.1 Hz; these are essential for providing a wide range of proprioceptive feedback to the wearer. The system characterization of SPA-skin under continuous actuation and sensing showed robust and repeatable behavior over 1 million cycles thereby promising compatibility with "real life" wearable applications. We further demonstrated closed-loop control capabilities of this SPA-skin system at 15 Hz sinusoidal vibration at 1 kHz control speed. The closed-loop controller, based on an analytical model of the system, uses the sensor resistance to control the average strain of the actuator and allow for generating uniform output force under different loading conditions. This allowed the wearer to feel a consistent feedback independent of the wearing conditions. Furthermore, the bidirectional operations of the SPA-skin platform offer a wearable system that can, not only be used for haptic feedback but also quantification of human proprioceptive capabilities for a range of frequencies.

3.4 Virtual environments for multimodal wearable haptic feedback using SPA-skin

3.4.1 System overview

Many of today's virtual reality (VR) interfaces rely only on visual and auditory modes for the user interaction, limiting the user's level of immersion due to lack of haptic feedback. Developing a human-in-loop interactive system requires realistic tactile feedback producing an range of tactile experiences, such as perception of shape, size, surface-texture, and stiffness[162], [188]. Especially in the case of tactile exploration, texture and shape perception play inherent roles in gaining more information about the object being touched. Texture is perceived through the Meissner and Pacinian corpuscles (PC), which can detect variations in roughness and texture while contacting the surface[27], [162]. The range of detection frequencies of Meissner and Pacinian corpuscles is from 10-40 Hz to 60-400 Hz, respectively with maximum sensitivities around 30 and 250 Hz, respectively. As these frequencies demand a high-fidelity response from a device with appropriate actuation at the fingertips, only a few wearable platforms can currently render texture [ref]. Shape is the second fundamental property of an object necessary for human-computer interaction both for input and output devices. The ability to interact bidirectionally with shapes is essential for applications such as computer-aided design (CAD) and interactive digital fabrication[189], [190]. Tabletop shape displays provide possibilities for bidirectional interaction[191], [192] that make both perception and creation of shapes accessible, while most of the wearable/handheld haptic research has mainly focused on just perceiving the direction of shapes.

Indeed, shape perception is especially challenging for wearable devices due to the multi-modality of cutaneous sensation in bidirectional interaction, involving active exploration of the object's surface linked to intended motion coupling (sensory-motor coupling). Sense of shape relies on both *slowly adapting type 1 (SA1)* and *rapidly adapting (RA) afferents* [193]. *SA1* and *RA* afferents are two different types of mechano-receptive afferent fibers found in human skin, which convey tactile information. In addition, perceptions at these fibers have varied peak sensitivity frequencies, not easy to integrate into a single wearable haptic system.

Another uninvestigated problem is the way to quantify spatial or textural accuracy of haptic stimuli in wearable devices, despite the well-studied on precision of motion-tracking systems. There

is some research examining the potential of digital shape recreation using wearable haptic devices in VR environments [194]. However, the possibility of both perceiving and recreating shapes in a single human-in-the-loop integrated haptic system has rarely been considered or quantitatively evaluated.

Closing the haptic feedback loop with human action triggered by the tactile feedback would bring essential measures of applicability of the haptic feedback system and level of immersion. A platform, aware of human action and having active feedback control could be coupled to quantitative analysis of the integrated system.

To achieve the broad range of tactile perception frequencies and active feedback control, we propose a two-component system (Figure 3:1) consisting of an active wearable component and a passive soft and pliable test object to tackle the challenges of multi-modal tactile exploration:

Sensor-actuator bidirectional interface component: We used an *interactive soft pneumatic actuator (SPA)-skin* with integrated hi-fidelity actuation and sensing capabilities as the active component [195]. The SPA-skin is a low-profile soft interface containing a PZT sensor layer, an SPA layer and a controller controlling the SPA layer with a pneumatic regulator and high-speed on-off solenoid valves. The integrated sensing layer makes it possible to gather information about the local environmental loading conditions in order to modify the output required for a coherent feedback. Together, the integrated sensing layer and an external finger tracking system provides a bidirectional interaction between the SPA-skin and the user.

Test object component: A second challenge for system design lies in producing a static force-feedback allowing a sense of touch. A virtual shape may be perceived using a heavy and bulky electro-mechanical glove-like design but this has limited wearability. Here, we propose a test object made using playdough, which may be molded plastically into the desired shape according to the applied forces. Uniting the active interface and the test object provides a coherent tactile feedback for an immersive experience.

While shape recognition could be augmented by a kinesthetic haptic device with passive haptic assistance as discussed in[196], the integration of cutaneous sensation using playdough might be effective, as the spatial precision for macro-features of objects mainly relies on SA1 afferents, which have a lower frequency of peak sensitivities. The playdough not only grants a response to the perception of the shape but also serves as an output device for quantitatively evaluating the spatial resolution via the human as an intermedium, as depicted in Figure 3:1b. Playdough in fact serves as a means of *data physicalization*[185] a process transferring digital data to a physical/tangible form that people can explore and communicate with.

3.4.2   Experimental evaluation and protocol design:

Humans combine touching and physical exploration of an object to gain detailed information about the properties of the object being inspected. The surface exploration generates varying contour, hardness, and roughness profiles by dynamic shape exploration in space stimulating the particular mechano-receptors. In this section, we developed a protocol to produce realistic tactile feeling and to close the haptic loop with human interaction. For the first time we can validate tactile feedback in a physical manner. We used an SPA-skin interface granting actuation at required frequencies without losing on output amplitude combined with a human-in-loop exploration to generate a realistic feeling of two of the most important modes of dynamic exploration: texture and shape of a physical object recreated virtually.

SPA-skin in dynamic conditions and performance characterization

The SPA-skin interface was designed to generate a wide range of vibrotactile stimulation, targeting the RAI and PC mechano-receptors in the 10-100 Hz range [27]. Many traditional devices employ electromagnetic motors or voice coil actuators in the form of tabletop display or handheld displays to have a large actuation frequency range. However, they are limited to localized actuation and do not allow fingers to move freely in space to explore the environment as we naturally do. On the other hand, with SPA-skin we can customize the actuator size, ranging from 2 mm diameter for acute location on areas like the finger-tips, to 20 mm diameters for low-sensitivity areas like the back of the neck [195]. We selected 8 mm-diameter ring-shaped SPAs for their high bandwidth, equal actuation area, and uniform inflation across the surface, as shown in Figure 3:7b.

Dynamic characterization of the SPA-layer and PZT sensor layer: The SPAs were actuated over a wide spectrum of actuation frequencies, ranging from 0-120 Hz, producing 0.3 N static output blocked force under 0.1 N of initial static preload, to measure dynamic behavior (Figure 3:7a, c). The recorded frequency response is plotted for the SPA-layer using a Nano-17 external 3D force sensor (ATI Industrial Automation, USA) and the SPA with a PZT-sensor, measuring from the PZT-sensor (Figure 3:7c). A first order transfer function (*TF*) fits well for the SPA-skin and the integrated PZT-sensor dynamics, with R^2 values of 0.99 and 0.96, respectively, as given by Equations Equation 3:4 and Equation 3:5:

$$T.F._{SPA} = \frac{0.332}{(0.00775*S+1)} \ N \qquad \text{Equation 3:4}$$

$$T.F._{SPA+PZT} = \frac{0.111}{(0.0116*S+1)} \ V \qquad \text{Equation 3:5}$$

These *TFs* provide a combined sensor-actuator bandwidth of 86 Hz, measured through the PZT sensors, and 129 Hz for the SPA platform measured through the Nano-17 sensor. Even though the discrete PZT sensor with flexible electrodes has a relatively higher mechanical bandwidth due to a much higher stiffness (in GPa) than the SPA layer (1-2 MPa); the electrical properties of PZT sensors set the limit for the lower cut-off frequency of SPA-skin to 1.6-2.2 Hz (supplementary).

Controller for human-in-loop dynamic interactions: Humans explore with their fingers in lateral directions to understand the shape, size, hardness and surface roughness usually at 10-80 mm s^{-1} velocity [62], [161], [197]. We tested the dynamic behavior of the human finger to measure the lateral frictional forces produced with exploration velocities of 10 mm s^{-1} and 30 mm s^{-1}. The human finger produced lateral friction of 0.25 N for a 1 N applied normal force when used with an artificial sinusoidal surface fabricated with standard SLA material (Figure 2d). We then used a textured frictional cloth tape made of glass fiber (GL-96, Saint-Gobain performance plastics hold S.p.A., Italy) to replace the human finger and to replicate similar behavior in dynamic texture recording experimentally. This produced 0.3 N of lateral friction and a signature similar to that of the human finger in the tested frequency domain (Figure 3:7d).
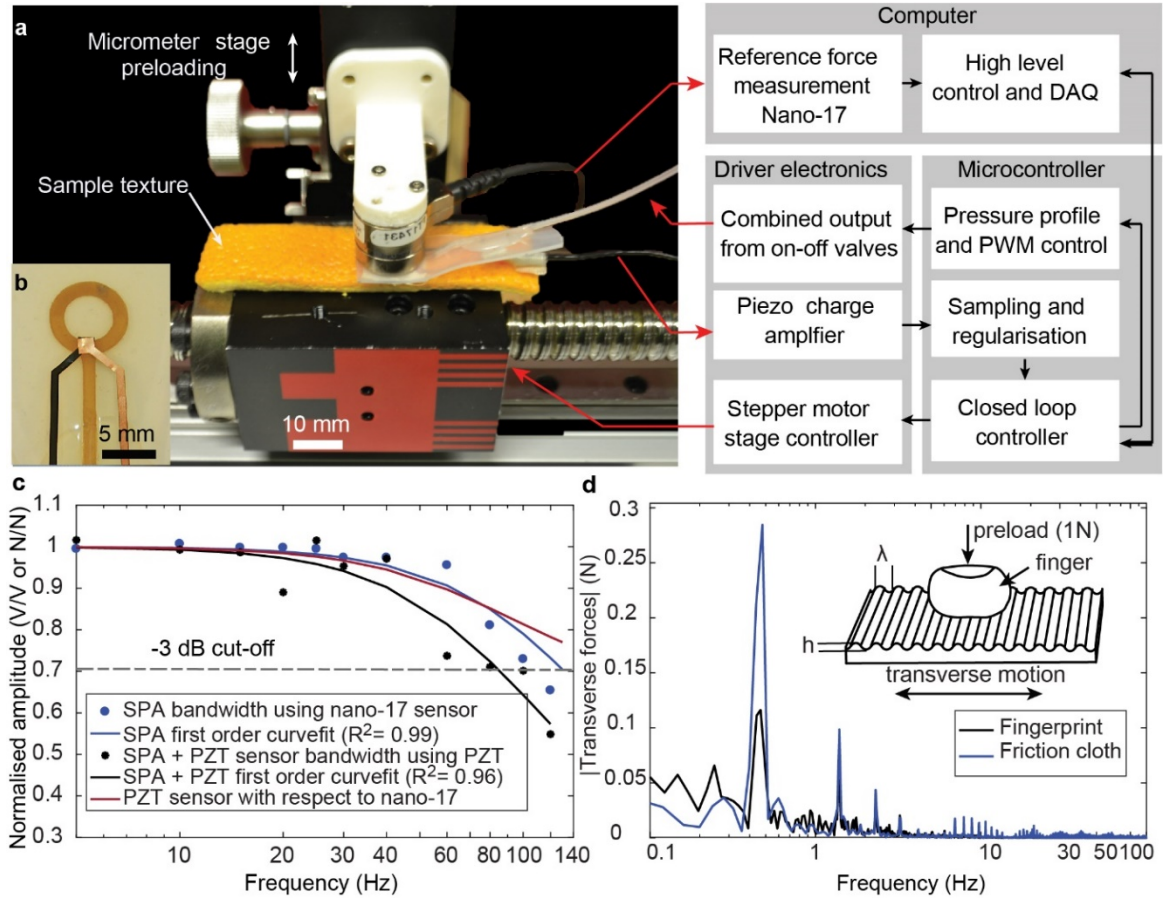
Figure 3:7 **Dynamic characteristics of SPA-skin.** (a) Block diagram of the system characterization setup to record and render texture and dynamic characterization of the SPA-skin. The micrometer stage allows constant preloading. An orange peel of 10x50 mm^2 was used as test texture (b) SPA-skin prototype with 8 mm-diameter SPA and 2 mm channel width and a 2x2 mm^2 PZT sensor placed at the intersection of the ring with inlet channel, where maximum inflation occurs. (c) SPA, PZT sensor and combined integrated sensor-actuator bandwidth was measured using an external Nano-17 sensor and PZT sensor. The first order transfer function fit provides 86 Hz and 129 Hz with sensor combined and an independent bandwidth of the SPA respectively.(d) Comparison of frequency components observed with the human finger and friction cloth tape of 10 x 10 mm^2, while recording the transverse forces generated with 1 N preload against a plain 3D-printed PLA material (*h*= 0 mm). The human finger produced average of 0.25 N lateral force, whereas the friction cloth tape produced 0.3 N for similar loading conditions.

Texture recording and reconstruction experiment

Experimental setups for reconstructing texture exist. However, as tabletop or handheld devices they have limited range of motion and often only provide texture feedback without shape exploration, due to the different interaction modes[198]. SPA-skin offers a compliant, low profile wearable platform, leaving hands and fingers free for doing their usual activity. We decided to use the wide bandwidth of SPA-skin to generate a realistic tactile feedback. For the experimental design, we chose three simple sinusoidal shapes with no gap, a single-gap or a double-gap between two consecutive sine waves. The surface-roughness height (*h*) was selected as 300 μm[199] (Figure 3:7d), as it lies in the range of rough texture that can be felt on static pressing, but still requires human fingers to explore it laterally[161], [197], [200]. Also, when subjected to 10-50 mm s-1 exploration tests, it will naturally generate the fundamental frequencies of 2-50 Hz, well within the range of the SPA-skin's performance, at a spatial wavelength (λ) of 1.5mm (Figure 3:7d).

A control algorithm using a fast Fourier analysis and detection of peaks from the spectral graph allowed a discrete generation of the required waveform at an approximate level. The currently available pressure regulators have a very limited bandwidth of less than 3 Hz due to integrated PID controllers and higher-solenoid inertia (ITV1011, SMC Corporation, USA). To recreate the recorded spectrum, we, therefore, combined output from 2 on-off solenoid valves, tuned to the required spectral frequencies (Figure S1b in [184]]). The difference in actuation amplitude was controlled using the duty cycle of the valve actuation, and the overall average output force by controlling the pressure globally through the low-bandwidth regulator. Added capabilities of faster regulatory options (like a piezo pressure regulator) allow covering much wider spectral signals. The signals lying at higher frequency than the bandwidth of the regulator may be controlled using on-off valves actuated at the principle frequency components.

Shape reconstruction experiment:

As mentioned above, most of the current haptic research is focused on creating perceptions and qualitatively evaluating the feeling by haptic devices. In fact, quantitative studies of the perception received and how humans respond are rare; it is especially challenging to quantify performance with human-in-the-loop, human behavior is not usually reproducible and is difficult to measure. Here we propose a test protocol and quantify shape sensation at the fingers.

The objective of the experiment is to evaluate the capacity of the active interactive interface to deliver spatial information sensations of virtual objects in terms of shape and size to the user who simultaneously physicalizes the sensations via the test object. We used vibrotactile feedback through SPA-skin as the active interactive interface and playdough as the test object, as shown in Figure 3:1b and c.

The assumption for the experiment is that active exploration of shapes and concurrent hand motion control shaping the playdough can be achieved using the SPA-skin due to its soft material properties and broad vibration frequency bandwidth; the rigidity of other wearable devices might be an obstacle for exploring and creating virtual shapes. We also presume that playdough can be a base for shape sensation in active exploring, and the effectiveness is comparable to other wearable devices having kinesthetic feedback assistance [165].

The experimental setup is shown in Figure 3:8**.** The proposed task was to shape the playdough to match pre-defined geometries, guided only by the vibrotactile feedback through the SPA-skin and feel of the playdough. There was no visual feedback or shape contour information. The target shapes were limited to 2D contours instead of 3D geometries to simplify the task, cancel undesired noise, and relieve workload. The playdough was placed on a smooth transparent glass platform. A camera was installed underneath the glass platform to track colored markers attached to the fingers. The sampling rate of finger position was 10 Hz. The captured images provided the spatial information, allowing tactile sensation of the virtual objects by the SPA-skin in real space. The SPA-skin vibrated when the fingers approached or reached the 2D contour of the virtual object. Then, the 2D contour of the virtual object was recreated physically, manipulating the playdough. Finally, the trajectories of fingers and the final contours of the playdough were recorded to examine the effectiveness of spatial information delivery.

We defined three different target contours: rectangle, trapezoid and circle, to provide flat lines, inclined lines and curves with respect to the grasping motion of the fingers. We gave one target contour per test. The target contours were relatively simple without detailed features or concave lines, designed mainly to promote simple grasping gestures, avoiding complex manipulation and thereby, interference from other factors. Furthermore, there were two horizontal cuts on the glass

as boundaries to the shape generation motion, as shown in Figure 3:8. With the boundary constraint, shaping progress was focused on grasping motion control and tactile perception of the fingers, without larger movements of entire hands or arms. The shaping process lasted 2 minutes per test. 9 tests for each target contour were carried out on three subjects whose age ranged from 28 to 34 years.
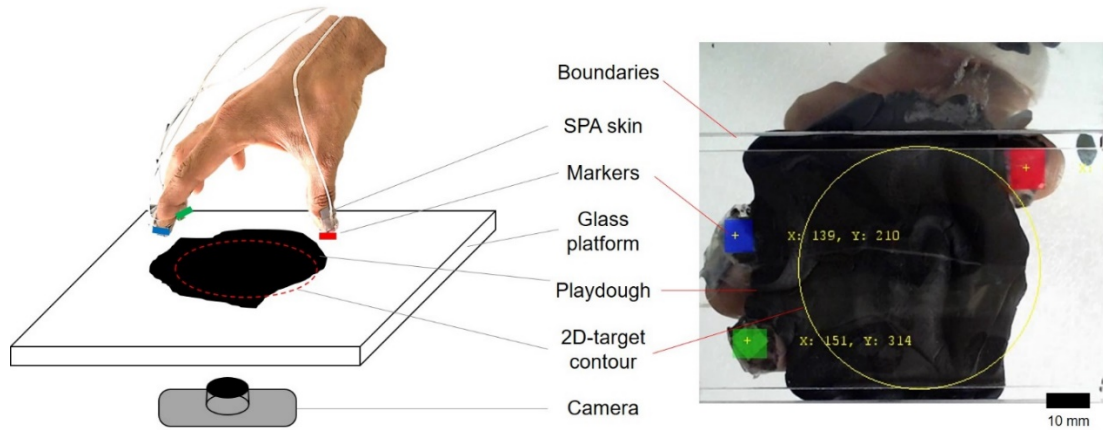
Figure 3:8 **Experimental setup for interactive shape generation using SPA-skin and playdough as a test object.** The image on the right is the computer vision of the control system.

3.4.3   Results and Discussion

SPA-skin delivered a wide range of modulation experiences proven by the dynamic characterization. Coupling the SPA-skin to a texture-reconstruction testbed or a camera-monitored test object produced experimental results that validated, for the first time, how artificially-created tactile feedback could indeed simulate physical interaction. Furthermore, the two devised experiments showed that the SPA-skin platform facilitated the transfer of rich tactile information from virtual objects, such as surface roughness, dimension, and shape. Shape information could be reconstructed by transferring a virtual experience effectively to a physical one.

4.1 *Texture reconstruction experiment:*

To have a realistic measure of texture feedback we devised a frequency-based approach, where principle components of frequencies were selected and generated using on-off solenoid valves, which have bandwidth in excess of 100 Hz (Figure 3:7c). This approach allowed control of the principle frequency components: as the spatial exploration velocity (v) changes, the actuation frequency changes linearly ($f = v/\lambda$). With the current experimental setup we could integrate discrete output from 2 principle frequency components and their natural harmonics.

We preloaded the friction fabric-coated SPA-skin at 0.1 N and recorded the blocked force using PZT sensors and a Nano-17 sensor at 10 kS s^{-1} for three sets of waveforms (Figure 3:9a). With a 1.5 mm spatial wavelength, we observed a principle frequency component at 2.3 Hz for 10 mm s^{-1} exploration speed and 6.9 Hz for 30 mm s^{-1} exploration speed. We set the SPA-actuation frequency to 2.3 Hz and regulator pressure to have a similar 0.3 N average output, which showed a successful reconstruction of the recorded amplitude spectrum of the actual texture (Figure 3:9a).
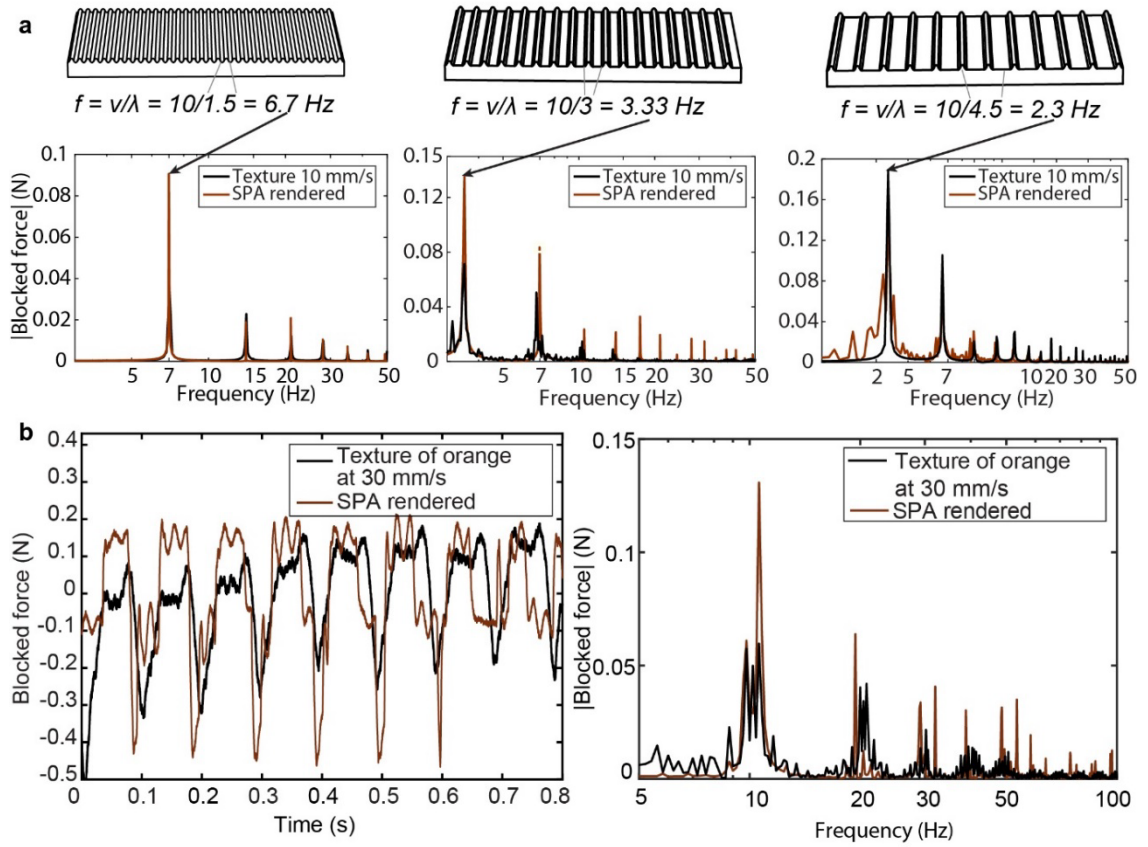
Figure 3:9 **Texture reconstruction experimental results** (a) Frequency response of three different sinusoidal textures recorded at 10 mm s^{-1} exploration velocity and texture rendering using the SPA-skin. (b) A phase-matched time domain response and frequency components of fresh orange-peel texture recorded at 30 mm s^{-1} compared to the rendered texture using the SPA skin at 0.3 N peak-to-peak blocked force.

In the last set of experiments, we used a 10x50 mm^2 piece of orange peel with approximately 2 mm spatial indentations as the textured surface, and recorded the forces using the PZT and Nano-17 force sensors. The frequency domain measurements showed two peak frequencies at 9.7 Hz and 10.6 Hz. On reconstruction, we observed a very similar frequency spectrum to the SPA-skin (Figure 3:9b). These frequencies also held for generation of a slow moving tone of 0.9 Hz, which had an organic feeling, similar to soft-surface exploration.

4.2 Shape reconstruction experiment:

To evaluate the spatial accuracy and effectiveness of the tactile exploration, the final contour of the playdough after the shaping process was compared to the target contour, as shown in Figure 1b. The accuracy of the shaping process was defined as the correlation coefficient of the area. The finger trajectory shaping-process was recorded and the sets of experimental results are shown overlapping in Figure 3:10a, for multiple test subjects and for three shapes and sizes. The temporal exploration by the human fingers during the reconstruction process is shown in Figure 3:10b. The two red dashed-lines are boundaries limiting the workspace of the shaping process. The playdough contour outside of the workspace, is removed in the figure for the accuracy calculation. The colored dots from light to dark represent the finger center locations from the start to the end of one set of experiments. There are three concentric circles, representing the boundaries of the 1st feedback edge, 2nd feedback edge and the target contour, respectively. The 1st and 2nd feedback edges were defined as 20 pixels and 10 pixels from the target, respectively as shown in Figure 3:10b. The control system gave a 15 Hz vibrotactile signal signifying the approach of

the target contour when the fingers reached the 1st feedback edge. A higher 35 Hz frequency signal was generated on the SPA-skin to give the sensation that fingers were really touching the boundary of the target shape when the finger center reached the 2nd feedback edge. As mentioned previously, both SA1 and RA afferents are relevant in grasping control. The vibration frequency of the 2nd feedback edge was close to the frequency of peak sensitivity for RA afferents and could be an effective stimulus for grasping control. The 10-pixel distance from the target contour was the definition as we roughly defined a 6 mm thickness for fingertips, and one pixel equaled 0.29 mm in the region of interest. In Figure 3:10b, most finger-tracking points are located between the 1st and 2nd feedback edges and only a few of them between the target and 2nd feedback edge. It shows that the system gave an effective vibrotactile signal for acknowledging the appearance of virtual boundaries. The contact forces from grasping the playdough were also present at the same time in this case.

Horizontal grasping motions were frequently used to shape the playdough, observed by the trajectories of fingers in Figure 3:10b. Thus, the spatial accuracy of the grasping motion could also be evaluated by calculating the area difference as the area is the horizontal difference integral along the y-axis. The calculated accuracy of all data sets is shown in Figure 3:10c and the image processing for accuracy comparison please refer supplementary section [150]. We achieved almost 90% accuracy for the rectangle contour and almost 80% accuracy for the circle contour using vibrotactile feedback. The circle contour had a lower average accuracy, and we also saw a possible outlier for the circle case. A suggested reason for the lower accuracy could be the stop of airflow in the SPA-skin due to the large bending on the rubber tube, which led to a lower amplitude vibrotactile feedback.

In order to investigate the effectiveness of the proposed SPA-skin feedback system in grasping control, we studied the distribution of the error area to find the ratio of the error area inside the target boundary to that outside the boundary and the image processing as shown in Figure 3:10a and Supplementary Figure S2d in [150]. The error distribution showed that there was no significant difference between error inside the target boundary (8.5%) or outside the boundary (7.8%), which suggested that the vibrotactile feedback from the SPA-skin is effective for grasping control.

To further examine if outside factors had a significant effect on the accuracy, we performed one-way ANOVA tests on the target shapes, participants, and test order (divided into three groups: tests 1 to 3, tests 4 to 6, and tests 7 to 9). In these cases, F critical value, F_{crit} = 3.4 at α = 0.05. The F-ratios were 3.2, 2.3, and 0.4, respectively, namely $F_{crit} > F$-ratio; hence, the results showed that none of the factors had a significant effect on the accuracy with a 95% confidence interval. The influence of the tested shapes on accuracy was minor; however, the contours tested were designed for rough geometries without detailed features, mostly composed of straight lines and uniform curvature lines. The accuracy of reconstructed shapes with detailed features with respect to dimension and geometry of the fingertips could be further studied. In addition, we observed that the learning factor was not significant in ANOVA tests of test order. Further studies could be done with more sets of experiments and changing the design of the test-shape order to examine learning factor influence on the same shape, as the current test shapes were hidden, picked at random before each test.
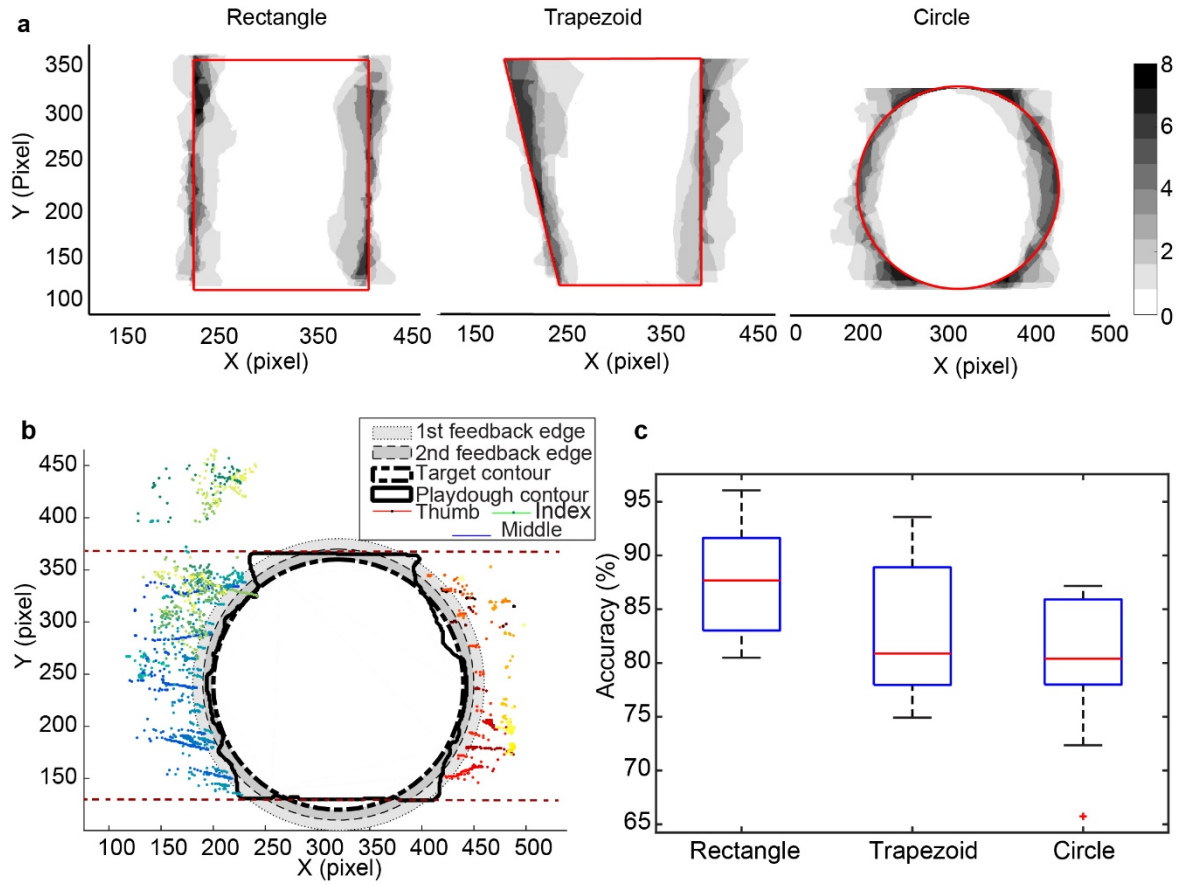
Figure 3:10 **Results of the shape reconstruction experiments**. **(a)** Intensity map of the shape difference between the playdough shape and target shape. The error intensity mapping for the shape reconstruction experiments for three target shapes: rectangle, trapezoid, and circle. The darkest color represents the higher trends of error distributed in the 2D-plane. The red line is the target contour. **(b)** The finger trajectory shaping process and the comparison between target and playdough contours. The different feedback frequencies acknowledging approaching the target contour or reaching the target contour are shown as different shaded areas. The two horizontal red dashed-lines are the boundaries limiting the workspace of the grasping motion. **(c)** Calculated average area accuracy of shape reconstruction.

3.4.4   Conclusion

For an effective wearable haptic feedback device, we require an accurate understanding of the physical interactions between the device and the wearer's perception. We propose a two-component system to achieve a multi-experience tactile feedback and for the first time, human-in-loop 'physical' validation of user actions, closing the haptic feedback loop. We use SPA-skin for its low profile form factor, high-bandwidth capabilities and integrated sensing as an active bidirectional interface. Special design measures in PZT sensor signal conditioning like high sensitivity instrumentation amplifiers with noise filtering using coaxial cables and line noise notch-filters allow for on body placement and accurate measurements.

In the first stage, we designed and validated abilities of the SPA-skin interface to record a set of sinusoidal textures with similar indentation but different spatial resolution, which then were analyzed for the principle frequencies in the Fourier domain. The SPAs were then used to recreate the texture feedback approximately. It was seen that the natural textures also had a range of harmonics similar to what we obtained with the on-off nature of the SPA's actuations. We recreated the natural texture of orange peel with two principle frequency components with cross-correlation of 59% explored at 30 mm s^{-1}. These texture patterns once recorded could be shifted linearly in actuation frequencies, based on the real-time exploration velocity, making it an immersive experience for the human.

We then designed and validated a haptic system in which the delivery of tactile feedback and spatial accuracy was quantitatively studied for bi-directional human-in-the-loop system. A 2D planer platform was used to *physicalize* a given virtual shape using a soft test object based on two-level tactile cues guiding the human actions. The test object play dough, on being molded, provided the sense of shape and size, whereas active tactile feedback from SPA-skin overlayed the texture cues. The results showed almost 90% accuracy for the rectangular shape and greater than 80% for the trapezoidal and circular shape physicalization using SPA-skin for tactile guidance. We employed a two-stage actuation with a low frequency stimulation when approaching the contour shape, followed by a high-frequency vibration when reaching the actual contour for ease of exploration.

The two experiments showed that SPA-skin is an effective haptic platform and provided a rich tactile feedback in a wearable scenario. The tactile feedback loop was closed with human actions and was quantitatively validated for the level of immersion and quality of tactile feedback. There is plenty of room for further studies of multimodal perception with wearable soft haptic devices due to the customizability of both material properties and control frequencies.

3.5   Discussion: Control strategies for wearable soft interfaces

In this chapter we developed two level control strategy namely, high-level and low-level control to achieve an intuitive interaction between human and wearable interface. The high-level strategy enables an adaptive and modular framework to integrate SPA-skin platform in other multi-modal interactive interfaces seamlessly. Development of such hierarchical control facilitated the continuous improvement of each individual component to be carried out independently and allowed to customize the setup for multiple application requirements. However, the phase lag due to pneumatic actuation can cause a perception delay and hence, the tube length has a limitation up to 20 ms traveling delay. The multimodal interaction is also limited by the maximum bandwidth of human perception, limiting the maximum number of simultaneous modes of interaction to usually 3. This invites a more systematic human-in-loop study to engage the user for optimum information transfer for the given application.

The low-level control strategy focuses on closed-loop control capabilities of this SPA-skin system for a wide range of controller inputs in amplitude and frequency. Even though human perceptive system is not very accurate and it is possible to provide good enough tactile feedback with traditional open-loop controlled actuators, closed loop control of SPA becomes necessary to ensure the soft actuators are still performing reliably, as being soft they can be squeezed under external loading, as opposed to the rigid body tactile actuators. The use of localized sensing has added benefit that minimizes the manufacturing in consistencies or non-linearity due to soft silicone material behaviors. The uniform output feedback hence allows the wearer to feel a consistent feedback independent of the wearing or dynamic loading conditions. Furthermore, the bidirectional operations of the SPA-skin platform offer a wearable system that can, not only be used for haptic feedback but also quantification of human proprioceptive capabilities for a range of frequencies. We implement the sensing layer for low-level control using PZT and liquid metal GaIn sensors for their high sensitivity and low profile nature as discussed in Chapter 2. Each of these sensors have their limitations with PZT sensors only dynamic forces can be measured which are desirable for vibratory feedback but not useful in environments requiring to measure static external loading.

Yet another challenge the mechanically transparent and compliant wearable interfaces face is to preserve the perception ability of human skin while the user is exploring the external environment while being actively provided with tactile feedback. With soft silicone material of SPA-skin, we are known to have a first-order damping of external interaction forces, which limits our dexterity while manipulating. Currently, the control environment lacks the ability to correct for such a filtering; however with integrated PZT sensing, we envision a degree of additional dynamic actuation added to SPA to restore this lack of touch. The preliminary results we obtained with the texture and shape generation, open up discussion for the next generation of haptic feedback devices, which are mechanically transparent for human wearability and provide ranges of tactile sensations inherent to the object and perceived by the human sense of touch.

Chapter 4   System integration and manufacturing of soft pneumatic interfaces

In this chapter[3], we discuss the system integration and manufacturing design aspects of soft pneumatic interfaces considering the wearability, portability and multi-point actuation-sensing of overall system. The peripheral system components powering any robot usually not get the attention towards their integration and component level optimization beyond the packaging, power or heating requirements. However, the wearable and mobile applications demand for the whole system beyond input-output interface to be portable while providing as much wearability and comfort as possible.

As we discussed in previously in chapter 2 and 3 about the high-fidelity feedback with compliant nature of SPA-skin interface make it an ideal candidate for wearable applications, but, like any pneumatically powered system, the SPA-skin also needs a peripheral system that needs to be integrated in making pneumatically powered wearables, a truly portable solution.

Figure 4:1 **Wearable SPA-skin array prototype for the forearm.** The SPA-skin platform in the form of 4x4 tactile cells (taxels) with independent modulation of force and frequency of each individual taxel. This prototype has 10 mm diameter ring shaped SPAs spaced 20 mm apart to be worn on a forearm. Multi-layer view of the SPA-skin fabrication, showing the fabric layer that supports the SPA array as well as miti-gate the effect of channel vibrations and cross-talk during the operation (B). The top and middle layer of silicone form the pneumatic seal for the ring-shaped mask. Inclusion of a wearable on-off mesoscale valve design concept to reduce the pneumatic input lines (C). The valve is developed using advanced manufac-turing methods to have a monolithic structure facilitating a miniaturized leak-proof design.

In order to extend the abilities of SPA-skin from a high-fidelity and bi-directional feedback device to a real-world *plug-n-play* interface that can augment the capabilities of existing robotic inter-face or perform as a standalone wearable robotic platform; a careful consideration of individual components and their interdependence is needed. As a first step towards this evaluation, we started with designing an application-specific wearble tactile interface using SPA-skin as a 4x4 bidirectional display for a human forearm. This allowed to detail the step-by-step process involved from material selection, actuator shape and size optimization, sensor signal conditioning, system integration with control environment aspects. This also showcases the scalability, wearability, and modularity of the integrated system.
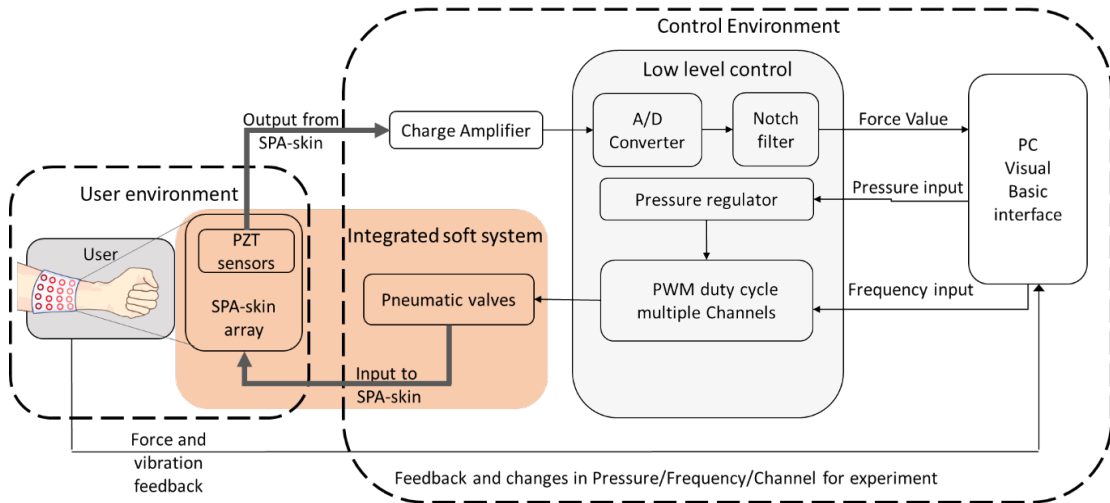
Figure 4:2 **Functional block diagram of interactive SPA-skin system architecture and control flow be-tween peripherals.** The user environment consists of the user and SPA-skin setup with pneumatic inputs to SPA and PZT output and user response to the control environment. The control environment is further divided into two levels namely, higher-level control through a visual basic interface and lower-level control with Arduino. The low-level controller can control up to 16 solenoid valves independently, using the pressure regulated airflow. A pressure cuff bracelet is used to cover the SPA-skin after wearing by the user to ensure a uniform pre-load of 5kPa during user studies. The PZT sensor placed on top of the actuator generates a charge output signal from the actuator's vibration, which is amplified using a piezo charge amplifier and then passed through a 50 Hz twin-T notch filter to remover external line-noise. The amplified and filtered signal is then recorded through the ADC as force value (in visual basic).

The second step is to optimize the selection of individual peripheral components or design for a wearable interface. We develop novel soft valves that can then be directly integrated with the SPA-skin reducing the number of pneumatic input lines and improving the fidelity.

The flow diagram of soft actuation and sensing control shows individual peripheral components through which the integrated soft system is connected to the user environment and the control environment. Our contribution in creating a more wearable, portable and versatile pneumatic system is three-fold:

- Our first focus is to design a bidirectional wearable 4x4 tactile display for wide range of interactivity and then use this display to study and develop various user interaction protocols. We outline the design flow from material selection, selecting the actuator shape, dynamic characterization, sensor signal conditioning and control environment design while keeping application requirement for wearability on the forearm as the criteria.

- The second, important challenge we attempted to tackle was to bring the pneumatic valves from the rigid traditionally non-wearable form-factor design to an integrated component level design, that can potentially be integrated directly on the tactile display array, drastically reducing the number of pneumatic lines and improving the actuation fidelity.

- We also present an optimization framework for pneumatic power supply (PSS) side. The framework allow optimizing the overall (SPA+PSS) system performance using the metrics of maximum actuation frequency, air and energy consumption per actuation cycle. Here, we systematically investigate the effect of five parameters: SPA size, tubing diameter and length, source pressure and valve flow capacity, on the performance and portability of SPAs and experimentally validate them.

4.1 Developing an integrated SPA-array platform

The actuation of the SPA-skin is targeted to stimulate the 10-100 Hz range specifically, to explore and quantify the effects of vibration stimulus on the human skin in this range. The distributed network of discrete PZT sensors have a sensitivity higher than those of SA-I, RA-I and RA-II type mechano-receptors in human skin to ensure a quantitative measure of the stimulation thresholds. These measures help performance optimization of the SPA-skin for required application location and also to decipher the specific mechano-receptor reaction based on the dynamic applied forces, as we will discuss later. The SPA-skin also provides independent control of actuation amplitude and frequency with a wide actuation bandwidth. The SPA-skin design is highly modifiable, allowing customized actuation solutions for specific wearable applications. However, the challenge is to design appropriately a soft material-based actuator for the desired actuation force and amplitude, due to the non-linearity in soft material properties. We adopted a material based FEM design that uses SPA design toolkit for tailoring SPA-skin to the required inflation amplitude or force for human forearm [57]. This toolkit allows quasi-static simulation of the SPA behavior for a given geometry and hyper-elastic model through input parameters.

Type of mechano receptor	Frequency range [Hz]	Spatial resolution sensitivity [mm]	Sensitivity to input threshold	Location
RA-I and SA-I (Meissner corpuscles and merkel cells)	10-40	High (~3-5)	Relatively low	Epidermal layer
RA-II (Pacinian corpuscles)	60-400	Poor (~20)	High (maximum at 250 Hz)	Deep tissue

Table 4:1 Mechano reception sensitivities and activation ranges for RA-I and RA-II type of mechano receptors in human fingers, forearm and foot [10], [52].

We customized and fabricated an SPA-skin array with 4 x 4 tactile cells (taxels) for application on the human forearm (Figure 4:1). The size of the array and minimum distance between two taxels was determined by the two-point threshold (approximately 20 mm) of the forearm area distance [52]. This organization in the form of an array provides a wearable platform to design and conduct studies to help understand human tactile perception thresholds of SPA-skin. We then used this array to measure the minimum amplitude necessary to feel a burst of vibration at a given frequency, the ability to localize a stimulus over a given area and the ability to detect and characterize a simple-shaped apparent movement.

Major contributions of this work are:

- Designing and prototyping a novel wearable platform of soft pneumatic actuator-skin (SPA- skin) with a controller that gives a bi-directional wearable tactile force-feedback display with 4x4 tactile cells (taxels).

- Modeling and characterizing the dynamic performance of the SPA-skin for a desired actuation amplitude and force using FEA-based model and dynamic tactile feedback.

- Devising a protocol and studying diverse vibrotactile feedback and its impact on human perception at lower actuation frequencies (10 - 100 Hz) using the SPA-skin array.

4.1.1 SPA-skin 4x4 array design framework

Based on the sensitivity values from Table 4:1, we need a platform suitable for a forearm, which required stimulation amplitude of up to 1 N over an actuation range of 0-100 Hz with a 20 mm grid (Figure 4:1) [52]. In order to achieve this performance, we constructed and modeled a preliminary design of the soft pneumatic actuators. However, due to their hyper-elastic nature, soft materials exhibit non-linear mechanical behavior with loading [12], [57]. In order to achieve faster iteration times, the material model-based FEA tools were used to calculate the required output force and/or displacement.

We employed the phenomenological model, Ogden [157], for modeling, as this was more likely to fit our large strain load case, an input pressure of 0-25kPa. After the first set of simulations, using different boundary conditions and materials, the second round of simulations was made, and these results were compared with the experimental data of the inflation of the actuator. The problem was set as a quasi-static dynamic using an implicit integration scheme. The preliminary design used a simple hemispherical shape for simulation, and our model was validated experimentally (Figure 4:3).
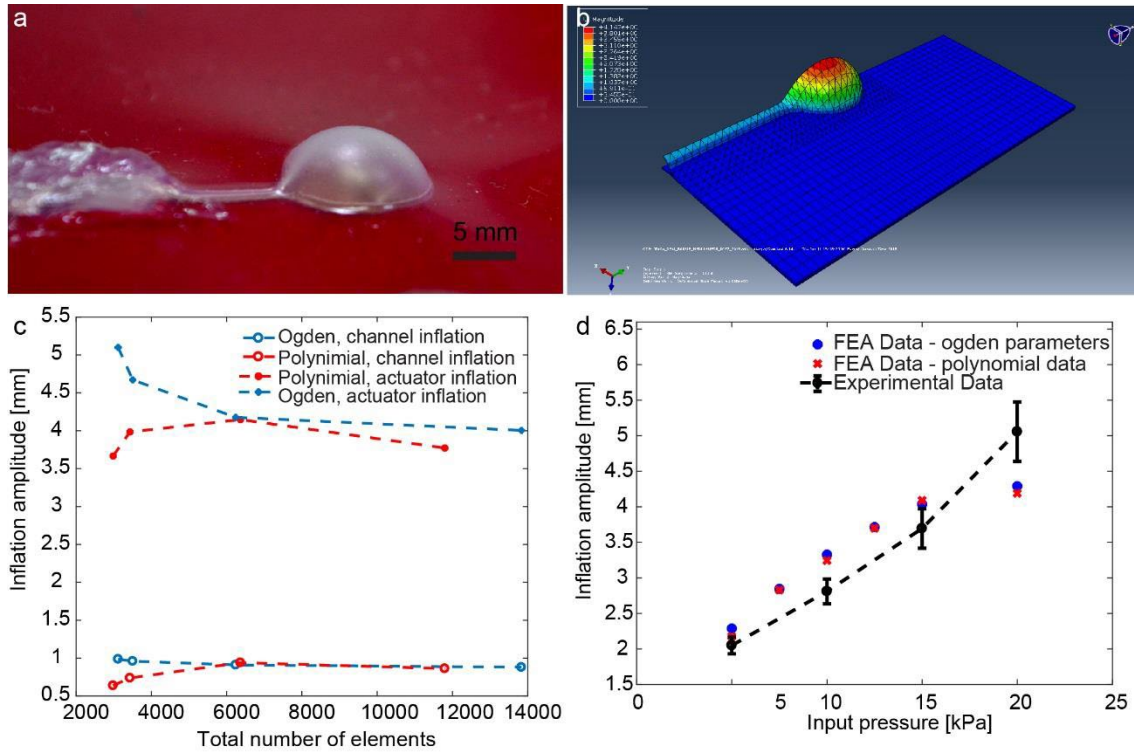
Figure 4:3: **Experimental validation of FEA based hyperelastic model.** (A) SPA-skin prototype inflated at 20 kPa. The fabricated prototype has 10 mm actuation diameter, 2 mm diameter inlet channel and 200 um thickness of upper actuation layer.(B) FE simulation of the same SPA-skin. (C) Convergence results for Polynomial (red) and Ogden-6 (blue) models for variation in meshing elements. We observed stable results above 7000 elements. (d) Comparison of experimental data from the multiple actuators with the FEA models.

For optimal dynamic performance, the surface area of the actuator should be maximized, while the volume of fluid required for inflation and deflation should be minimized. This was achieved using a toroidal shape actuator that yielded a 2.5 mm channel width for a 10 mm diameter actuator, enabling optimal bandwidth and output force. However, due to practical limitations, we selected a channel width of approximately 2.0 mm channel width to prevent delamination at the inner side of the actuator. We then used ring-shaped actuators (Figure 4:3 A, B), which displayed a uniform inflation surface while significantly improving the bandwidth (Figure 4:3 D).
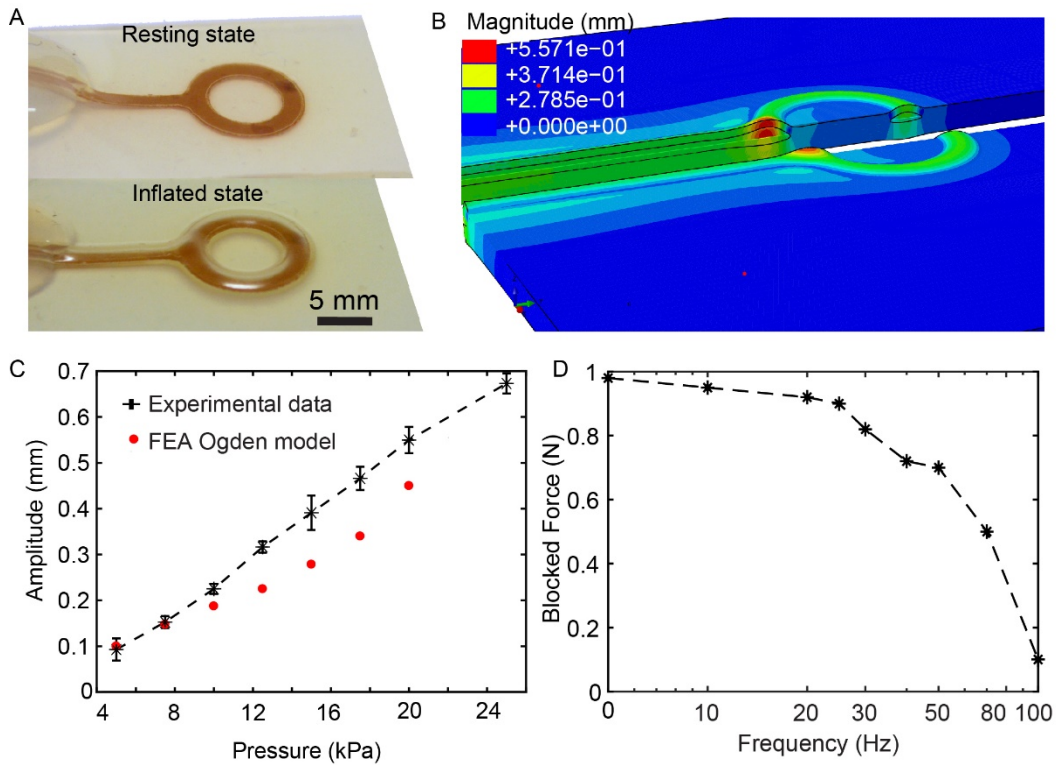
Figure 4:4**: Experimental validation of the hyper-elastic model and dynamic characterization of SPA.** (A) SPA-skin prototype inflated at 15 kPa. This fabricated prototype has a 10 mm actuation diameter, 2 mm diameter inlet channel and 450 µm thick upper actuation layer. (B) FE simulation of the same SPA-skin geometry at 15 kPa input pressure. The simulation confirms uniform inflation across the actuation area with 0.278 mm inflation height. (C) Dynamic blocked-force characterization of SPA prototype having a 35 Hz bandwidth and 0.1 N output force at 100 Hz, large enough to be perceived by a human finger and forearm.[4]

The selected SPA design of these ring shape actuators was then characterized for the dynamic force feedback, where we obtained a bandwidth of 35 Hz. Although the output peak-to-peak force drops from 1 N to 0.1 N at 100 Hz (Figure 4:4), this force is still distinguishable by a human finger or forearm.

4.1.2 Materials and methods: SPA-skin array fabrication

The layer-by-layer fabrication of SPA-skin is adapted from the fabrication technique discussed in [195] for SPA-skin array design using the film applicator (Zehntner ZAA 2300; Zehntner GmbH Testing Instruments). An additional fabric layer with carefully laser-cut places for the actuator is cured with a silicone layer of about 150 µm in thickness (Figure 4:1). This intermediate fabric layer prevents cross-talk from the channel vibration felt by the wearer. The fabric layer is also stretchable in the direction of the silicone channels, which allows for an elastic-wrapping on the human arm for improved grounding and support. As the minimum threshold lies around 0.07-0.08 N, measurement of channel inflation force below the fabric layer will help to tune the performance of the SPA-skin further.

---

[4] The aforementioned bandwidth is also limited by the on-off control valve's characteristics which is now improved well above 100 Hz

The available material charactersiation data from the spa-design-toolkit is limited to Ecoflex-30®[24], [57]. We conducted experimental uniaxial and planar tests to obtain the stress-strain characteristics of the Dragon Skin® 30 with dog-bone and rectangular samples, prepared according to the ISTM standards as shown in Figure 4:5 [57], [202]. Afterwards, using the SPA design tool [57] and Abaqus IDE we set up a simulation environment for SPA-skin design with a simple hemispheric shape to validate the material model and at different pressure set points. All simulations used the Ogden-6 parameters computed with the SPA design tool. The symmetry of the problem is also exploited for time efficient simulation (Figure 4:4B).
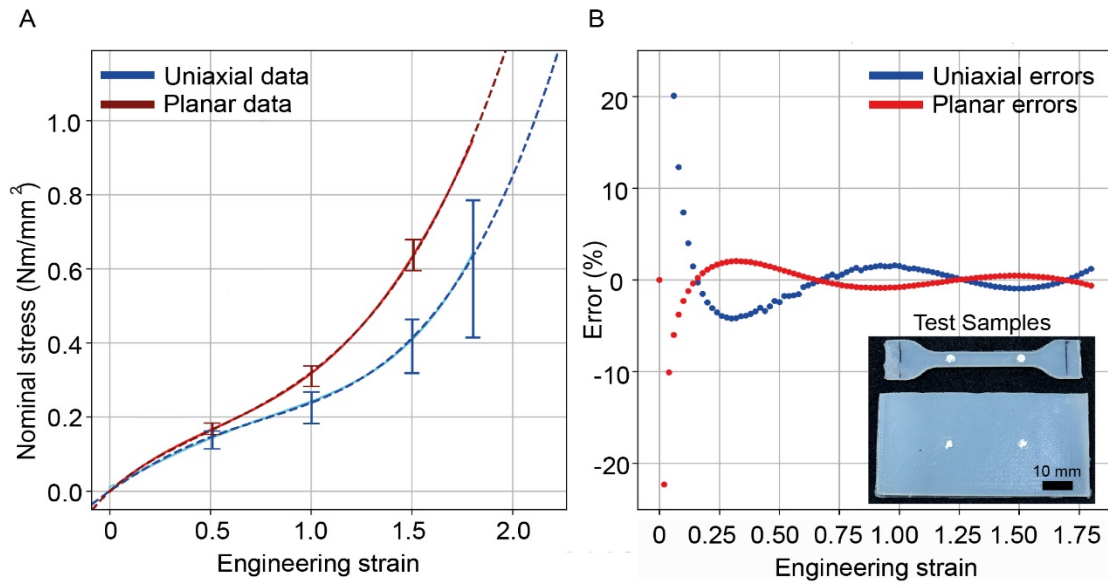
Figure 4:5 **Material characterization of Dragon skin 30** (A) Ogden-6 model-fit (dashed) for the average stress-strain curve obtained from 6 experimental samples over 5 cycles each of uni-axial and planar data. (B) Relative errors for changes in strain between the experimental data and Ogden model are less than 5% for both the uniaxial and planar tests

4.1.3   SPA-skin dynamic characterization with integrated sensor

Practical e-sensors for wearables need to be thin, pliant and distributed in order to optimize compatibility with human skin. Considering these prerequisites, we selected piezoelectric ceramic based (PZT-5H) sensors due to their high sensitivity for the applied dynamic forces normal to the surface [74]. The ring-shaped actuators selected following the FEA and experimental validation, which provided a high-fidelity dynamic feedback, were then characterized with the PZT sensor to obtain the transfer function of sensor output for the SPA output blocked force.

The integration of PZT sensors with the SPAs enable localized force measurement when the wearer feels the tactile stimulation as shown in Figure 4:6 A,B. Averaging the response for three different sensor-actuator pairs, we obtained a quadratic relationship for the dynamic force measured using a nano-17 sensor (ATI industrial automation) and the peak-to-peak output from the PZT sensing circuit (Figure 4:6). The sensitivity of the PZT was measured over the full range of SPA-skin actuation for two different set-points, 100 mV and 200 mV, peak-to-peak for the equivalent measured blocked force using the nano-17 sensor (Figure 4:6D). As seen in Figure 4:5D, due to bandwidth limitations of the SPA, the SPA amplitude cannot reach the 200 mV set point above 80 Hz.
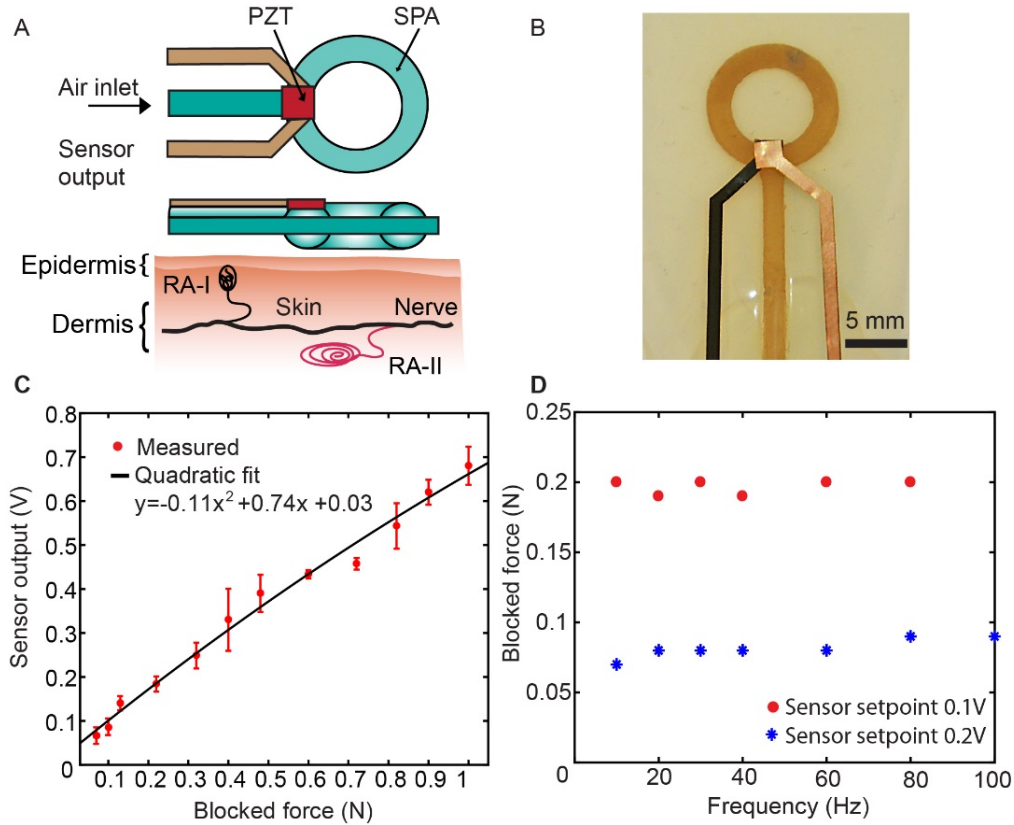
Figure 4:6 **SPA-skin characterization with an integrated PZT sensor.** (A) schematic and (B) photograph of the 2x2 mm integrated PZT sensor in the 10 mm-diameter SPA of 2mm channel-width. Relative positioning of RA-I and RA-II type mechano-receptors with respect to the epidermis and dermis layers of human skin. (C) Blocked force-measurement with a Nano-17 sensor covering the whole area of the actuator shows second-order behavior for the dynamic peak-to-peak force exerted by the SPA with respect to peak-to-peak voltage recorded by the charge amplifier after removing line noise. (D) PZT sensor and signal-conditioning circuit sensitivity over a range of actuation frequency for two different set-points. At 100 mV, the sensor set-point blocked force mean is 81mN (S.D. 7mN) and at the 200 mV set-point, the blocked force mean is 197 mN (S.D. 5mN) over the required full range of operation for SPA-skin.

4.1.4 SPA-skin control environment and experimental setup

The experimental setup for the SPA-skin platform can be divided into a user environment and a control environment as shown in the functional block diagram in Figure 4:2. The selected SPA-skin design based on the application also determines the required parameters for the control environment. For this experimental setup to measure effectively the performance of the SPA-skin and human perception, it should have a high degree of accuracy for sensor measurement and a wide range of operation for pneumatic control valves (0-200 Hz). We developed a high-sensitivity charge amplifier with a second order notch filter to limit the line noise for PZT measurement. The user environment has a coupled electro-mechanical feedback between the wearer and the SPA-skin platform where, the SPA-skin receives vibration input based on the user response and PZT sensor output received by the controller. The control environment for the SPA-skin setup is divided into two control loops. The higher-level control loop receives force values and user feedback to provide the desired pressure, frequency and actuation pattern. The lower-level control environment regulates the desired pressure and decodes the actuation frequency and patterns into individual PWM signals for high speed on-off valves.

4.1.5   Closed-loop interactions towards human-in-loop user environment setup

User is an integral part of the SPA-skin design framework as well as the control environment. The presented experimental setup is versatile for changes in application for end users. The control environment adapts to the user environment dynamically based on the feedback received by the user specifically to change the stimulation force, frequency, or the actuation pattern. We continuously monitored PZT output for changes in loading conditions by comparing it with the expected set point to ensure uniform performance during the subject studies.

We followed *a setup protocol* before beginning the experiment with subjects. The user environment was well lit and setup for the subject's comfort at room temperature. They were requested to put on headphones cancelling passively the external noise, in order to prevent influence from exterior sounds. The SPA-skin was then mounted and approximately tightened around their forearm, close to the wrist (Figure 4:1). The elbow and the hand of the subjects were laid on sandbags, in order to avoid external vibrations. The subjects were provided with a known stimulus of 30 kPa and 20 Hz for location 1 actuator to adjust the mechanical grounding to obtain 0.3 N dynamic force. A constant pressure of 5 kPa is externally applied using a pressure cuff during this time to ensure uniform preloading. All the 16 actuators can be activated one after another at 20 Hz for 500 ms delay to familiarize the users with the expected vibration feedback. The actuation frequency of 20 Hz was chosen as it lies in the middle of both SPA-skin's bandwidth and RA-I and SA-I type mechanoreceptor's range. Following this, we then introduced human-in-loop design experiments discussed in the next chapter to validate and improve the wearable interactivity of SPA-skin and understand better the mechano receptive thresholds for a human forearm.

4.2 MEsoscale Valve by Additive Manufacturing (MEVAM) for applications in haptic systems

4.2.1 Introduction

The use of SPAs allow for decoupling of actuation location from the compressed air source for a high-density, low profile, high-force applications. Furthermore, integration with soft pressure sensors allow for the generation of very precise closed-loop control to produce the desired actuation effect. Currently, classical on/off valves are being used to deliver the desired air volumes at different frequencies, but haptic systems consist of arrays of actuators, each element with independent actuation, which results in complex assemblies of tube and valve networks that can hinder movement and which are prone to failure. There is currently no alternative to standard commercial solenoid valves, which are soft, flexible or thin-enough to be integrated with the SPA-skin. This is a major limiting factor in having a single pneumatic tube carrying pressurized air to the SPA array and integrated valves actuating the individual tactile cells (taxel).

The advent of additive manufacturing has created a disruption in the manufacturing industry thanks to the many benefits it can bring to the production of parts and products, and all industries are embracing the technology in some way or another. AM is traditionally associated with cost savings by reducing complexity and assembly steps, however there are 3 main limitations restraining competition with traditional subtractive manufacturing : low mechanical properties, a relatively slow production rate, and a limited printing resolution. Whether for metal or polymer printing, this latter constraint explains that use cases generally target medium to large parts with low dimensional or surface finish tolerance. However, an increasing understanding of the printing parameters as well as recent advances in material characterization and robotic control have enabled us to refine the printed resolution thus opening way to printing smaller elements.

Valves have successfully been manufactured using AM, but the potential of micro-Additive Manufacturing has not yet been leveraged for valves at this mesoscale ($\sim$10x10 mm^2). Printable micro-valves would allow a tighter integration of haptic systems by combining the manufacturing of the pneumatic tubes, valves, and supporting structure in a monolithic fashion[5]. There is also a large potential for production cost reduction, although yet to be demonstrated, by saving on assembly steps. This new valve paradigm would benefit applications of haptic feedback based on pneumatic actuation, such as a multi-cell tactile display from braille on fingers, wearable armband to VR-based rehabilitation. The rigidity and large size (Φ7.6 x 31 mm^2) limit the wearability and localized deployment of currently available solenoid valves. Having low-profile, soft pneumatic valves would be an enabler for new applications in wearable devices, thanks to a reduction in system complexity, improved wearability, and high-bandwidth due to reduction in tube length.

My contributions from RRL: I was the sole person involve in development of this project from RRL with our lab PI: Prof. Jamie Paik. I was responsible for valve specification detail, prototype concept evaluation, suggested development roadmap, risk analysis and project planning. In second phase: Integration of valve prototype with SPA-skin, Control loop design report: System identification and modelling of integrated system , Open-loop control and model validation, Closed-loop control design with integrated sensors and. Testing and validation of controller in bench-top and wearable scenario

CSEM contributions: selection of materials for stereo lithography based resolution, mechanical properties and maximum aspect ratio. Different valve designs will be conceptualised specifically for Additive manufacturing. Simulation using multi-physics and design optimization based on testing and SPA-integration results
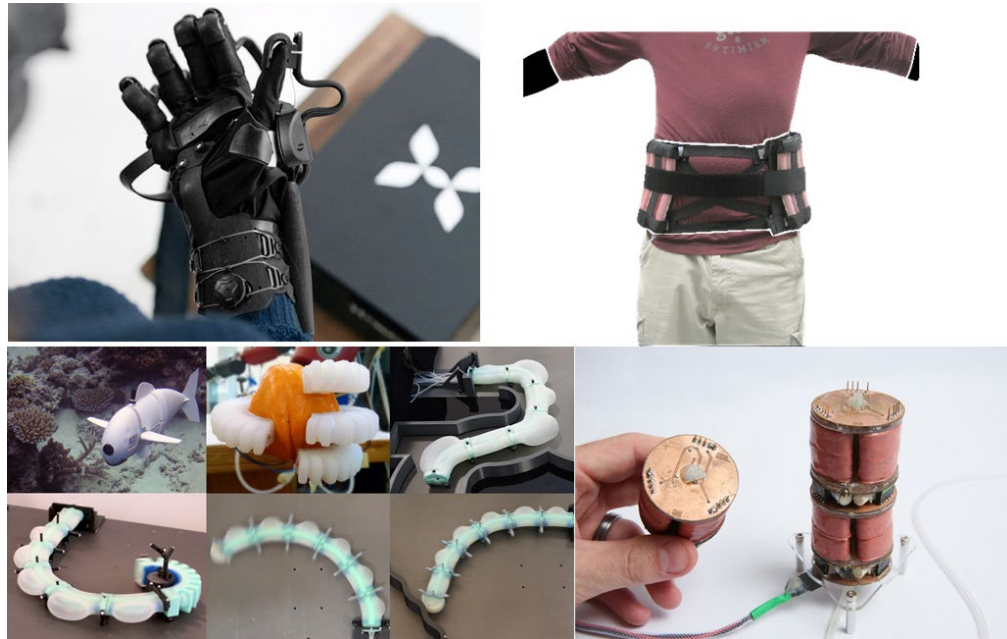
Figure 4:7 Wearable and modular soft robots that would benefit from integrated soft valves, removing need for the rigid parts or long tubes limiting the dynamic response time.(A) Haptx technologies, haptic glove with 130 actuation points. (B) Wearable posture assistance using SPA-packs.[203] (C) Modular multi-DoF soft robots with individual valves per actuator.[40]

Entertainment	Rehabilitation/assistive tech	Medical/clinical research	Industry
• Enhanced VR/AR interaction (haptic feedback) • Gaming suit for haptic feedback (RRL patent)	• Feedback augmentation for prosthetic devices/limbs (e.g. direct vibration feedback from grasp/touch…) • Prosthetic limbs: dynamic stiffness change for better comfort and adaptation, stump/socket interface • Assistive: at home rehabilitation for neuro-motor skill impairments using VR+SPA Skin (e.g. gauntlet)	• Tele-operation (surgery, augmented feedback) • EMI compatible Brain-machine I/F • Dynamic tactile stimulation in FMRI environment	• Car steering wheel feedback • Content-derived physical buttons • Alerts in risky/noisy environment (mining, scuba divers…)

Table 4:2 Selection of haptic feedback applications enabled by a printed micro-valve

As outlined in Table 4:2 Selection of haptic feedback applications enabled by a printed micro-valve, some of the envisaged applications are targeting the healthcare and medical sectors. Soft haptic devices, made possible by valves printed in soft material and tightly embedded in the system, can lead to new prosthetic limbs with vibration feedback on the stump instead of complex neuro-muscular interfaces, or even enable the use of non-metallic wearable devices during MRI scans for controlled stimulation of body areas. Another application field is soft robotics, to which the valve would provide a great improvement (compact designs, cheaper production) which, added to the inherently safe aspect of the soft actuators, would facilitate access to young students to learn robotics.

4.2.2 Pneumatic control valves for soft robots

The soft material based robots powered with pneumatics mainly rely on a pneumatic control source for their actuation. The robot computer determines required output pressure for actuation. Based on this, a pneumatic control source (regulator or valve gate) is controlled. In general, the position of the pneumatic channel opening is controlled through the activation of an active element like a solenoid coil or a piezo-stack. Most of the currently available valve solutions use a rigid encasing for pneumatic channels and an active component to control the on-off/variable gate. As the portability of desired applications became important these valves became smaller. However they are still rigid and bulky where it is desirable to have a simple on-off soft valve that can be integrated with the SPA to make it a plug-n-play solution for wearable or modular robotic applications. Initial efforts have been taken in developing a soft on-off valve which is triggered pneumatically; however, a low profile, a high-fidelity solution is yet to be realized (Figure 4:8 C).
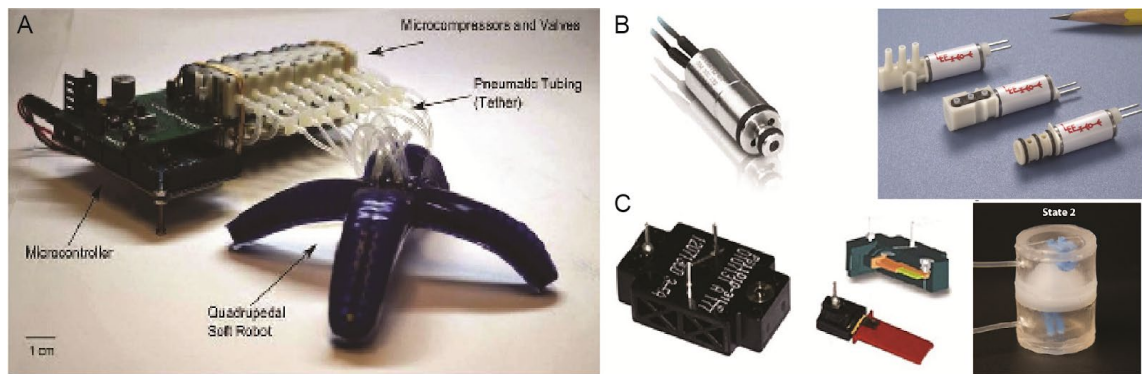
Figure 4:8 **Pneumatic valves for powering soft robots.** (A) A general scenario showing application of SPA based robots with solenoid valves (outside the soft-robot) [204] (B) Some of the smallest solenoid valve available commercially with dimensions Φ7 x 20 mm^2 (C7 miniature cartridge solenoid valve, Parker) and Φ7.6 x 39 mm^2 (LHDA0521111H, Lee valves). (C) Non-solenoid based valves using piezo material based actuation and a pneumatically actuated bistable soft-structure.[205]

4.2.3 MEVAM valve specifications and proof of concept design

With the rise of soft pneumatic actuation and wearable haptics, there is a demand for relatively low pressure (<150 kPa), but a high-flow rate (>2 standard L/min) and high-bandwidth of valves. These valves need not be as robust as industrial valves, which often are designed for 400-800 kPa operations and hence are limited in bulkiness and/or slower due to high inertia. Using advanced manufacturing techniques like AM and we envision a soft on-off pneumatic valve that uses electromagnetic actuation similar to the ones used in standard solenoid valves but replaces the other mechanical components like spring and rigid air-tight encasing with a soft-material based structure.

Human skin is sensitive to the application forces in the range of 1 N and vibratory frequency 10 Hz- 400 Hz. The current design of SPA-skin [2] has an actuation volume of 5 ml which will require a flow rate of 3 L/min at 10 Hz actuation and 15 L/min at 100 Hz actuation at 40kPa operating pressure. Based on these considerations, a set of detailed specifications as presented in Table 4:3.

Specification	Targeted value	Current value
Frequency	>10 Hz	Closing time <10ms, more precise measurements to be carreid at RRL
Size constraints	13x13x5mm^3	9x9x9.5mm^3
Valve type	3 ports 2 positions	3 ports 2 positions
Flow rate	>3 L/min	>3 L/min
Operation pressure	40kPa	>40kPa
Leak rate when closed	~0	~0

Table 4:3 **Initial specifications for valve design based on human factors** as targeted values and the obtained values from the latest final prototype design of MEVAM valve.

Elementary design: In order to validate the concept of a monolithic soft-valve, we used a simple SPA-skin channel sandwiched between a permanent magnet and an electromagnet (Figure 4:9.). Upon excitation of the copper coil, the PM gets attracted towards the coil closing the pneumatic channel. This type of valve closing, being two-way in nature, does not provide a metric only by measuring the pressure at the output of the valve. Hence, we evaluated the functional working by applying an on-off PWM pressure signal at 10 Hz at two different input pressures (25kPa and 35kPa). As the excitation voltage of the coil increases, the peak-to-peak changes recorded by the pressure sensor on the other side of tubing reduces effectively, capturing the closing the valve. The tubing length and diameter limit the dynamic changes observed during the operation even when the electromagnet is not excited, which shows 10 kPa variation for 25 kPa static pressure and 16 kPa variation peak-to-peak for 35 kPa input pressure.
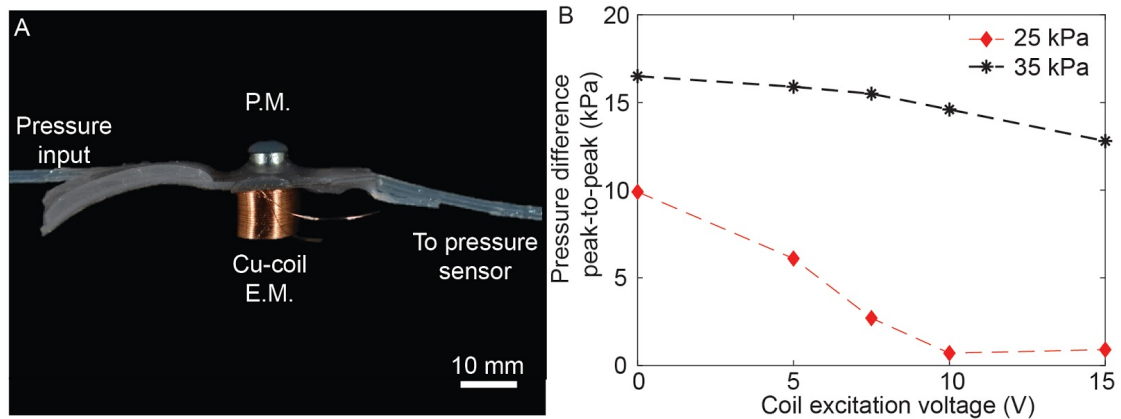
Figure 4:9 (A) **Elementary proof of concept prototype of a soft pneumatic on-off valve**. The SPA-skin has 2 mm channel with 1 mm thickness, sandwiched in between a P.M. and a cu-coil acting as E.M. (B) Effect of excitation voltage on the peak-to-peak output pressure for two different set-point pressure inputs at 10 Hz.

Advanced functional prototype: We started with a multi-component valve design, where a permanent magnet is integrated inside a diaphragm that would be moved upon-excitation to open or close the valve position. This major limitation of this design comes from the material properties of 3D printed material. After 2 more iterations, our latest design has achieved most of the specifications, particularly the pressure (>50 kPa) inside the flow due to the high flow rate and the actuation speed >10 Hz. The valve has been produced, as planned, from a single material and without assembly, except the actuation coil. Picture of the concept and the realization are presented below in Figure 4:10 **MEVAM functional prototype.** (a) Schematic of prototype valve design using monolithic 3D printing with integrated permanent magnet. (b) Functional valve prototype and (c) actuation characteristic for on-off operation for pressures ranging from 5-50 kPa.
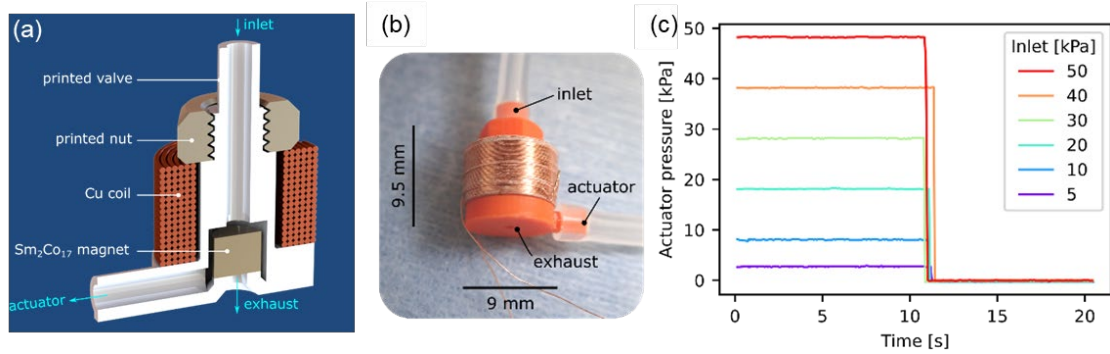
Figure 4:10 **MEVAM functional prototype.** (a) Schematic of prototype valve design using monolithic 3D printing with integrated permanent magnet. (b) Functional valve prototype and (c) actuation characteristic for on-off operation for pressures ranging from 5-50 kPa.

4.2.4   Final design and integration of MEVAM valve with SPA-skin

Keeping the goal control of soft pneumatic actuators (SPA-skin) to build a wearable soft interactive haptic platform. A solenoid 3/2 way valve design is considered. The final design is composed of a copper solenoid electromagnet controlling the position of a permanent magnet plunger, to achieve high-frequency actuation. Additive manufacturing grants design flexibility and fewer parts for improved integration with the actuators. Our first concept was based on the use of resins yielding flexible parts upon printing. A permanent magnet is attached to a flexible membrane, acting both as a guide and spring for the magnet. We successfully printed this prototype design (Figure 4:11A) which yielded a maximum operating pressure of 12 kPa. This pressure is much lower than the required 30 kPa. To further improve the design, we fabricated a membrane-less valve that would not hinder the permanent magnet motion while allowing the fabrication of a monolithic design (Figure 4:11B), by inserting the magnet during the printing process. These valve prototypes met the requirements of a 10 Hz actuation at a pressure able to actuate the SPA-skin (30 kPa, Figure 4:11C). This actuation was performed at 1.5 W with an operating temperature of around 120°C (Figure 4:11D). Higher operating pressures, up to 50 kPa, could be reached using a higher operating power (3W), but the heat generated would damage the valves and even the solenoid themselves. Despite the mitigated operating temperature, the plastic printed valves would still crack and fail after several minutes of operation. We implemented a two fold strategy to tackle this issue. First, we designed a 3D printed metal heat sink for passive cooling of the solenoid coil down to 80°C (Figure 4:11D). Second, we purchased a commercial resin rated for high temperatures whose mechanical properties are not impacted at 80°C. According to an aging test performed on four different valves using a custom setup built for the occasion, these strategies resulted in valves operating for 5 million cycles before failure (6 days continuous operation at 10Hz). These valves were then integrated into a demonstrator with four SPA-skin actuators using flexible 3D printed manifolds (Figure 4:11E) to generate a variety of tactile feedback from 0-50 Hz at different duty cycles for modulable amplitude and traveling wave for multimodal haptic information transfer using a single pneumatic inlet tube.

The next step is developing a fully integrated haptic system including these electromagnetic valves. The sensors integrated inside SPA-skin will be used to close the loop between the valve actuation and SPA-skin feedback for wide range of controlled force feedback. In parallel, an optimization of the coil design will determine its geometry and for an improved dynamics.

	Composite soft valve featuring a membrane	Monolithic hard valve without heat sink	Monolithic hard valve with heat sink
Operating pressure / power / temperature	12kPa / 3W / >250°C	50kPa / 3W / >250°C 30kPa / 1.5W / 123°C	30kPa / 1.5W / 80°C
Dimensions	20×20×20 mm³	9×9×12 mm³	15×15×12 mm³
Lifetime	Untested ~20 cycles	Untested ~50 cycles	> 5 million cycles

Table 4:4 **Operational specifications and dimensional evolution of three MEVAM designs** over 12 months. The reduction of operational temperature improves the valve's lifetime up to 5 million cycles.
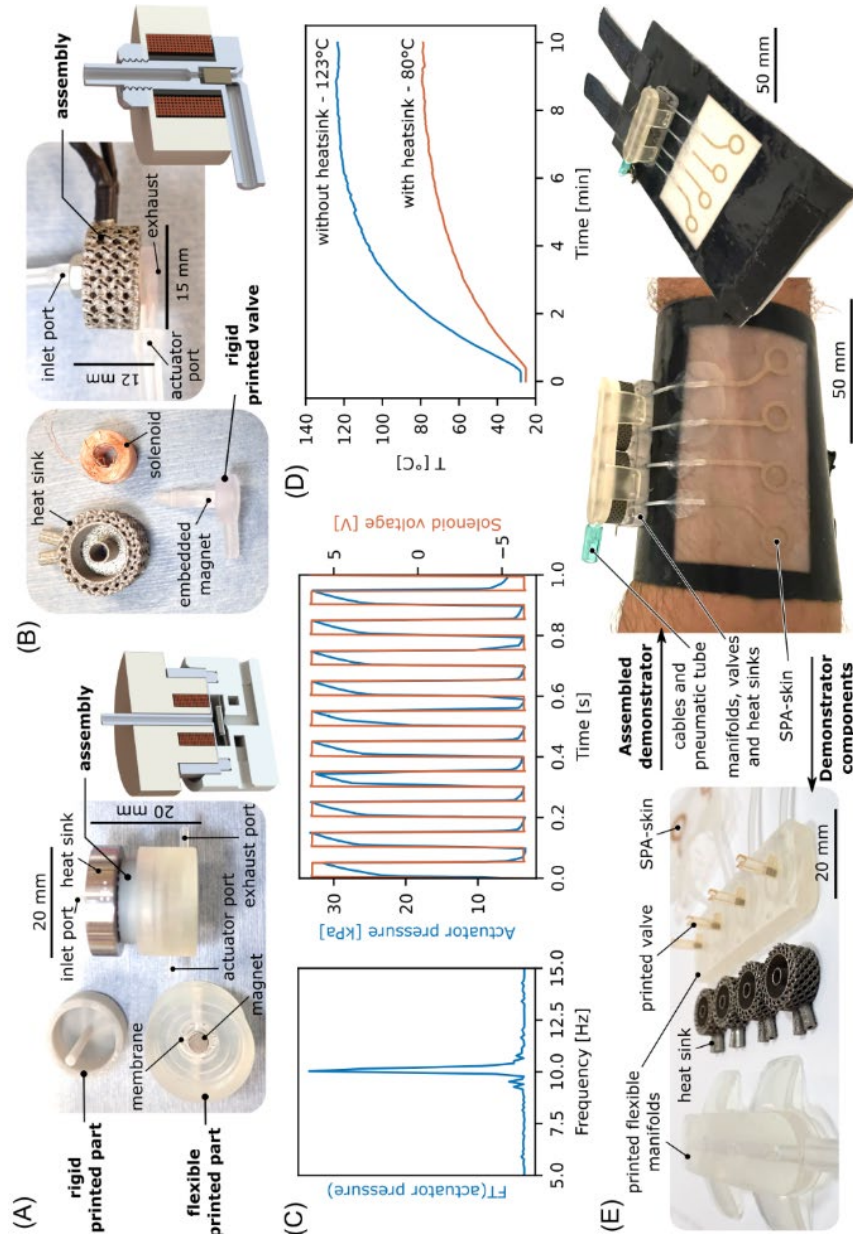
Figure 4:11 **Exploded view and characteristics of MEVAM prototype integrated in SPA-skin.** Composite soft valve design with a flexible membrane (A). PM embedded monolithic prototype of valve with printed heat-sink and off the shelf solenoid coil (B). Dynamic characterization of final prototype design (c) and temperature effects of heat sink (d). Wearable prototype with 4x1 haptic display for up to 50 Hz actuation at 30 kPa input pressure.

4.3 Flow path optimization for soft pneumatic actuators: Towards optimal performance and portability

4.3.1 Introduction

Soft pneumatic actuators (SPAs),[6] are highly desirable for interactive robotics applications owing to their unconventional properties like high compliance, safe human-machine interaction, and adaptable design space. Especially for applications such as wearable devices [37], [69], [195], [206]–[208] , mobile robots [209]–[213] and material handling [139], [214], [215], soft actuators have shown promising potential [216]. In addition to its design, the SPA dynamics are governed by pneumatic supply systems (PSSs) consisting of source, valve, and tubing. Although their functionality is well-known, the inter-dependence of PSS components and their impact on the SPA behavior has not been quantified, especially in the context of performance and portability. Using the metrics of maximum actuation frequency, air, and energy consumption per actuation cycle, here we systematically investigate the effect of five parameters: SPA size, tubing diameter and length, source pressure and valve flow capacity, on the performance and portability of SPAs.

In the case of SPA actuation, the pressurized air is provided by pneumatic supply systems (PSSs), most commonly consisting of three main components: source, to generate the pressurized air, valve, to control the direction of flow, and tubing, to connect the different components to each other [217]. While the actuation mode, force, and displacement are governed by the SPA design and loading conditions [218], the actuation speed is determined by the pressure and flow dynamics of the SPA, which are governed by the PSS [217]. The force and displacement requirements for a given application can be fulfilled by selecting or designing the appropriate SPA. Once these requirements are met, an important metric that defines the SPA performance is the maximum achievable speed of actuation, involving sequential inflation and deflation.

Figure 4:12 **Flow-path optimization of SPAs.** (A) Schematic of the experimental setup for powering the SPAs. We use an external regulated source, and standard commercial valve and tubing. We measure pressure at the source and SPA using pressure sensors, and the in-flow and out-flow using flow sensors. (B) Three generic SPAs: SPA-pack [147], [219], fast pneumatic actuator [147], [220], and SPA-skin [55], [195], [221]with different volume ranges and application requirements to evaluate the optimization model. (C) Examples of SPAs in literature, comparable to those tested in this study, ranging from wearable haptic devices [55], [195], [221] to grippers [220] or manipulators [222], [223]

For instance, it impacts the locomotion speed of a mobile robot [209]–[211], [211]–[213], the frequency of vibrotactile stimulation in a haptic device [55], [195], or the number of objects that could be manipulated by a gripper in a given time. For applications requiring untethered operation, another important factor to be considered is portability. This can be defined in terms of the amount of air and energy consumed by the SPA in one actuation cycle. The total duration of untethered operation can then be defined using the maximum number of actuation cycles attainable in a single charge. Even for tethered robots, air and energy consumed per actuation cycle are important as they directly affect the economic costs, for instance an SPA used for gripping and manipulating objects in an industrial workspace. As the generated air is provided by the PSS, it is evident that the appropriate sizing, selection, and control of its components is critical for achieving the desired SPA output. Despite its importance, studies on the effect of the PSS on the SPA with respect to its performance and portability have been limited. Wehner et al. [69] studied different options for providing the pressurized air, and compared them with respect to their flow, air capacity and weights. However, this study focused only on the source, not accounting for the valve and tubing, and was independent of the SPA used. In our previous work [217], we modeled the pressure and flow dynamics of SPAs, studied the effect of its model parameters, and optimized them for meeting application-specific metrics for performance and user-defined constraints such as size and weight. However, this study did not explicitly investigate the practical decisions for selection and control of components towards performance and portability. For example, a SPA with long tubing requires an additional amount of air and energy for pressurizing the extra dead volume of the tubing. To compensate this, the diameter can be reduced, but this increases flow resistance which reduces actuation speed. In such a case, the source pressure can be increased for faster inflation response, but at an increased pressurization energy cost. Such inter-dependencies and trade-offs among different components and their properties affect performance and portability of SPAs. While a well-tuned set of these parameters could be achieved heuristically, it would be time-consuming, without guarantee of optimality, and would require re-tuning if a PSS component or SPA is replaced. It is yet to be studied in detail how the selection and control of PSS components can be optimized to maximize the actuation speed, while minimizing the air and energy consumption.

In this section, as a follow-up study to [217], we investigate and model the effect of five parameters: SPA size, tubing length, tubing diameter, source pressure, and valve conductance; and how they can be optimized towards improved performance and portability. Specifically, we study how they impact the maximum actuation frequency, energy consumption, and air consumption. We first model the pressure and flow dynamics of the PSS while considering the effect of source, valve, tubing, and SPA. We numerically solve this model to simulate the SPA pressure response for a range of parameter combinations to study their effect on maximum actuation frequency. To validate our results experimentally, we define an experimental protocol and test in a total of 162 parameter combinations which included: three each of SPA, tubing diameter, tubing length and source pressure, and two valves. In addition to defining and studying these parameter combinations, we also address practical necessities such as characterizing the flow through a PSS component, and delays due to response times of the valves. The experimental results are consistent and

coherent with the model predictions, and help to understand better the trends of how various parameters affect SPA performance. Our comprehensive approach considers the dynamics of the complete system, SPA and PSS, thus going beyond the state of art, which have considered material selection [12] or quasi-static mechanical behavior [40], [57]. Furthermore, the analysis of air and energy consumption helps to evaluate the portability and operational costs for a given SPA and PSS. The universal applicability of our model along with comprehensive test protocols consider the complete system, PSS and SPA, and enable to optimize the selection and control of PSS components for performance and portability. The main contributions of this work are:

• Soft actuator performance Modeling and development of a systematic understanding of the complete system, PSS, and SPA, based on the effect and inter-dependencies of five parameters: SPA size, tubing length and diameter, source pressure, and valve flow capacity.

 • Design of experiment, parametric definition and development of protocols to optimize PSS towards performance and portability for a given robotic application.

• Experimental validation of SPA performance model with consistency and conformity of predictions for 162 unique parameter combinations, using three commonly used SPA designs (Figure 4:12B).

4.3.2   Modeling SPA dynamics

The actuation speed of a SPA is determined by its pressure and flow dynamics, governed by the PSS. Similarly, the total air and energy consumed by the PSS is governed by the properties of the SPA and PSS. To better understand their effect, and to enable PSS optimization, we model the pressure and flow dynamics and the air and energy consumed.

A. SPA pressure dynamics PSSs consist of three main components, the source, valve and pneumatic line. To model the pressure and flow dynamics of the PSS, we first make some assumptions [224]–[229]: : (i) air behaves like an ideal gas; (ii) there is no leakage; (iii) the ambient is at standard temperature, $T_0 = 293.15$ K, and pressure, $P_0 = 0$ kPa; iv) all processes occur at standard temperature T_0; (v) pressure in the actuated volume is uniform. We define the source using its pressure, P_{src}, the valve by its flow capacity, as explained later, and the tubing by its diameter, D, and length, L. We model the SPA as a chamber with variable internal volume ranging from V_i at P_0, to V_f at the operating pressure P_{op}. As the tubing between the valve and SPA is also pressurized during actuation, it cannot be ignored, especially when its volume is comparable to that of the SPA. Therefore, we consider the tubing in the overall SPA volume V_{spa}, and model its pressure dynamics as:

$$\dot{P}_{spa}V_{spa} + P_{spa}\dot{V}_{spa} = \frac{RT_0}{M_{air}}\rho_{air}Q_{spa} \qquad \text{Equation}$$

Where R is the ideal gas constant, M_{air} is the molar mass of air, ρ_{air} is air density at P_0, T_0, Q_{spa} is the mass flow to the SPA expressed as flow rate (L/s), under standard conditions. For one mole of air at standard conditions, $V_0 \times 10^{-3} = M_{air}/\rho_{air}$, where V_0 is the volume of one mole of air at P_0, T_0. The 10^{-3} term is seen because V_0 is expressed in L instead of m^3 . Similarly, the ideal gas law for one mole is: $P_0V_0 \times 10{-3} = RT_0$. Using these relations in Eq. 1 we get,

$$\dot{P}_{spa}V_{spa} + P_{spa}\dot{V}_{spa} = P_0Q_{spa}$$

Equation 4:2

B. Modeling pneumatic flow through PSS From Eq. 2, we see that the SPA pressure dynamics are directly affected by the flow through the PSS. We model it using the ISO 6358 [228] standards, because it is readily useable with most commercial components, as well as networks of components connected in series or parallel. It models the flow as follows:

$$Q = C\Psi P_{High}$$

$$\Psi = \begin{cases} \sqrt{1 - \left(\dfrac{\frac{P_{Low}}{P_{High}} - b}{1 - b}\right)^2}, & \dfrac{P_{Low}}{P_{High}} \geq b \\[4mm] 1, & \dfrac{P_{Low}}{P_{High}} < b \end{cases}$$

Equation 4:3

Where P_{High} and P_{Low} are the absolute upstream and downstream pressures, respectively; C and b are the sonic conductance and critical ratio respectively of the component, and Ψ is the flow function defined in Eq. 3. When the pressure ratio is below the critical value, b, the flow is choked and only depends on source pressure. When the pressure ratio is above the critical value, it follows an elliptical relationship with the pressure ratio and becomes zero at a pressure ratio of 1. For the tubing, the above parameters can be calculated as [227], [230]:

$$C_{tubing} = \frac{0.029 D^2}{\sqrt{\frac{L}{D^{1.25}} + 510}}; \qquad b = \frac{474C}{D^2}$$

Equation 4:4

where L and D are the tubing length and inner diameter respectively in m. For the valve and other components such as pneumatic connectors, C and b can be found in the technical manual, or if unavailable, experimentally characterized as described in previous sections and Fig. 2. The effect of multiple interconnected components can be modeled by calculating the equivalent conductance, C_{eq}, and critical ratio b_{eq}, using the appropriate expressions for series and parallel connections as described in the Supplementary information. We see that the equivalent conductance, C_{eq}, is always lesser than that of smallest value in the set of components connected in series. Each and every component in the flow path must, therefore, be selected carefully as a single poorly selected component could cause the PSS as a whole to underperform.

C. Modeling air and energy consumption. Here, we consider the amount of air and energy consumed in one actuation cycle of inflation-deflation. For an untethered PSS, the overall portability then can be defined in terms of the total number of actuations that can be powered in one single charge. Let V_i and V_f be the initial and final internal volumes respectively of the SPA. After adding the tubing volume $V_{tube} = \pi D^2 L/4$, the internal volume increases from $V_i + V_{tube}$ to $V_f + V_{tube}$ at the SPA operating pressure, Pop. Taking the difference, the total air required to inflate the SPA from P_0 to P_{op} is given by:

$$A = \frac{P_{op}(V_f + V_{tube}) - P_0(V_i + V_{tube})}{P_0}$$

Equation 4:5

The energy required by the source to pressurize and store this amount of air at P_{src} is given by:

$$E = Air\ Consumed \times P_0 log_e \frac{P_{src}}{P_0}$$

<div align="right">Equation 4:6</div>

Thus, even though the SPA is powered to Pop, the energy consumed is dependent on the pressure at which the air is generated and stored in the PSS. A higher P_{src} will lead to higher flow, leading to a faster inflation response of the SPA, but at the price of higher energy consumption.

D. Defining the optimization problem Eq. 2 - 7 model the dynamics and air and energy consumption of an SPA. For a given application, if the SPA is selected, the designer has the liberty to choose the PSS components and their parameters: (i) the source characterized by its pressure P_{src}, (ii) the valve, characterized by its conductance C_{valve}, and (iii) the tubing, characterized by its diameter D and length L. The careful selection, sizing and control of these components is crucial to achieve the desired performance and portability. As described earlier, the maximum achievable frequency of sequential actuation, fmax, is an important factor for many applications. Similarly, the amount of air consumed, A, and energy consumed, E, per actuation cycle are indicators of how long the PSS can power the SPA in a single charge. Therefore, selecting these three as our metrics, we define a multiple-objective optimization problem for optimal performance and portability as follows:

$$min f(x) = w_1 \frac{1}{f_{max}(x)} + w_2 A(x) + w_3 E(x)$$

<div align="right">Equation 4:7</div>

where x is the PSS design variable holding values of P_{src}, C_{valve}, D and L, and w_1, w_2 and w_3 are weights denoting the relative importance of each objective. Table I summarizes the effect of the design variables on the three metrics. Additionally, it also signifies how the SPA size affects them.

<div align="center">TABLE I</div>
<div align="center">DIFFERENT PARAMETERS STUDIED IN THIS PAPER</div>

Parameter	f_{max}	A	E
Source pressure, P_{src}	↑	-	↑
Valve conductance, C_{valve}	↑	-	-
Tubing diameter, D	↕	↑	↑
Tubing length, L	↓	↑	↑
SPA volumes, V_i, V_f	↓	↑	↑

The above relations are straightforward for most parameters: increase in source pressure would increase fmax, but at a cost of higher E. Or that increasing valve conductance would lead to higher flow, and ultimately higher fmax, and so on. The relation for tubing diameter, however, is not so simple. As D increases, the flow resistance decreases, meaning that there would be more flow through the PSS, indicating a faster response. However, the amount of air required also increases, slowing down the overall response, which is why we denote its effect on fmax using A and E.

4.3.3   Simulations and experimental protocol

In this section, we study the effect of five parameters, source pressure, valve conductance, tubing diameter, tubing length, and SPA size on the actuation frequency, air consumption and energy consumption. Using Eq. 2 to 7, we first numerically simulate the inflation and deflation cycles. We

then validate the model predictions experimentally using 162 combination of parameters consisting of different SPAs, valves, source pressures and tubing sizes.

A. Simulation study We modeled Eq. 2 to 7 in MATLAB, and solved the differential equation 2 to simulate SPA pressure response from P_0 to P_{op} = 50 kPa. While we chose an operating pressure of 50 kPa, the presented methods can be repeated for any other value. In order to study the effect of the different parameters, we carried out the simulations while varying the values of the parameters defined in Table I. The different parameter values during simulations were selected based on commonly used components in soft robotics. Similarly, the three SPAs modeled were of three sizes, large, medium and small, so as to represent and encompass currently existing designs. SPA size, We considered three SPAs of different sizes as shown in Fig. 1B and as described below: 1) SPA-pack, consists of four fibre-reinforced cylindrical SPAs, held together in a soft silicone matrix. Its internal volume is V_i = 57 mL at P_0, and V_f = 60 mL at P_{op} = 50 kPa. 2) Pneunet, is one of the widely used bending SPAs. Its internal volumes are V_i = 3.2 mL at P_0, and V_f = 10.7 mL at P_{op} = 50 kPa. 3) SPA-skin, is a low-profile SPA providing vibrotactile feedback. It is constructed by introducing an air gap between two layers of silicone. Its internal volumes are V_i = 0.1 mL, and V_f = 0.5 mL at P_{op} = 50 kPa. Tubing, We considered three values of tubing length L = 1, 2 and 5m; and 25 linearly increasing values of tubing diameter from D=2 mm to 5 mm (resolution 0.125 mm). Source pressure, We considered three values of P_{src} = 60, 80 and 100 kPa. Valve conductance, We considered the following two valves: SMC VZ100 series (Valve 1) and Festo MH3 series (Valve 2). The ISO6358 model parameter values for these valves were calculated by experimental characterization, as explained in section 3.3.2 Figure 4:13 and Table II. We used a standard numerical solver, *ode45*, in MATLAB to simulate the inflation and deflation response for the above conditions. For simulating the SPA expansion during pressurization, we assumed that the SPA volume, V_{spa} varies linearly with the SPA pressure P_{spa}, from $V_i + V_{tube}$ at P_0 to $V_f + V_{tube}$ at P_{op} [217] Using the simulated pressure response in inflation and deflation, we calculated the maximum actuation frequency as: f_{max} = $(T_{rise} + T_{fall})$ −1 , where T_{rise} and T_{fall} are rise time and fall time of the SPA pressure from 2% to 98% and 98% to 2% respectively, of P_{op}. Similarly, we calculated the air consumption, A, and energy consumption, E, using Eq. 6 and 7 respectively.
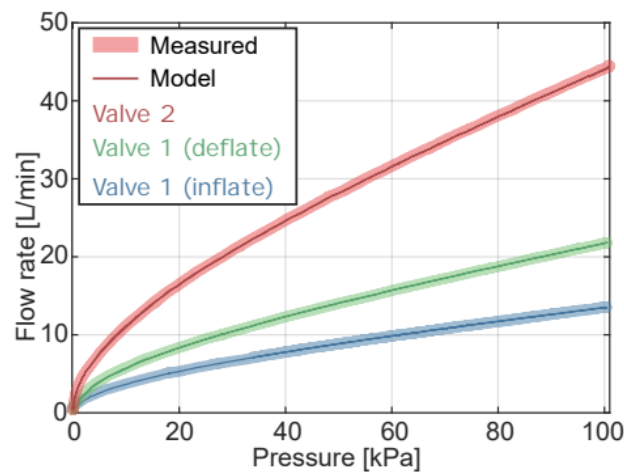
Figure 4:13 **Experimental characterization of the valves used.** We connected the valves to a source, varied the pressure, and measured the flow through their inflation and deflation paths. Using a non-linear solver, we fitted the measured flow to the ISO 6358 model [228], [231]shown in Eq.4.

B. Experimental testing. We test three SPAs described earlier to validate our simulation results from the model. For all parameters except tubing diameter, we chose the same values as that for the simulations. For the diameter, we chose three sizes: 2.5, 3 and 4 mm, based on commonly used commercially available options. This led to a total of 162 testing conditions with 3 SPA types, 3 source pressures, 3 tubing lengths and 3 tubing diameters, and 2 valves. The experimental setup (Figure 4:12A) consisted of an external regulated pressure source, a solenoid valve (Valve 1 or 2), the SPA (SPA-pack, pneunet or SPA-skin) and tubing (L = 1, 2 or 5 m; D = 2.5, 3 or 4 mm). We use two flow sensors (Honeywell Zephyr series) to measure the inflow and outflow, and pressure sensors (Honeywell HSC series) for measuring source pressure, and SPA pressure. We used a microcontroller (Teensy 4.1) to read all sensor values at 1 kHz and control the valves to inflate or deflate the SPA. Prior to testing, we characterized the two valves used. This was necessary, as the C and b values for Valve 1 were different for inflation or deflation, and those for Valve 2 were not available in the technical datasheet. We connected the valve to the source and measured the valve flow through the inflation (source to SPA) and deflation (SPA to ambient) paths, while varying the source pressure. Using a non-linear least squares solver, 'lsqcurvefit' in MATLAB, we fit the measured pressure and flow data to ISO 6358 parameters C and b for the two valves in inflation and deflation. Figure 4:13 shows the fitted model vs. measured flow through the valve and Table II shows the root mean squared errors (RMSE) between the two. This method can be readily applied to any other PSS component to characterize the flow vs. pressure relationship.

TABLE II

ISO 6358 PARAMETERS AND RMSE FOR VALVES 1 AND 2

Valve path	C [lpm/kPa]	b	$RMSE$ [lpm]
Valve 1 - Inflation	7.8×10^{-2}	0.197	0.1
Valve 1 - Deflation	12.4×10^{-2}	0.04	0.17
Valve 2 -Inflation/deflation	25.3×10^{-2}	0	0.30

We connected the various options of the SPA and PSS, and tested them in the 162 parameter combinations as described earlier. For every testing condition, lasting 10 s each, the microcontroller controlled the valve state to cyclically inflate and deflate the SPA between 1 and 49 kPa. Initially, we used a simple control algorithm, that changes the valve state when the SPA pressure reaches one of its two limits, as follows:

$$if(P_{spa} > 49\,kPa\,\&\,input == 1)$$
$$input = 0;$$
$$else\,if(P_{spa} < 1\,kPa\,\&\,input == 0)$$
$$input = 1;$$
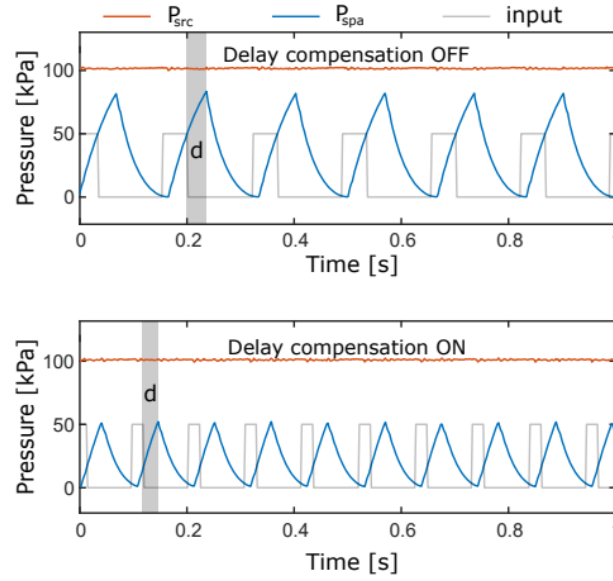
Figure 4:14 **Comparison of SPA-skin pressure response with and without delay compensation.** Without delay compensation, the SPA-skin is over-pressurized up to 80 kPa which is not only slower, but also harmful for the SPA. With delay compensation, the valve is switched preemptively, predicting when the SPA will reach its target. This increased the SPA-skin fmax from 6 Hz to 9.6 Hz and reduced A from 6.2 mL to 3.8 mL.
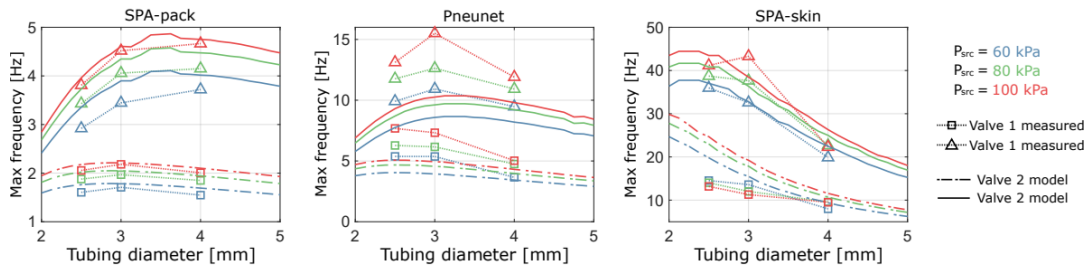
Figure 4:15 **Comparison of predicted vs. measured values of the maximum actuation frequencies**, fmax, for the SPA-pack, pneunet and SPA-skin, for a tubing length of 1 m. We observe that fmax increases with valve conductance and source pressure, and reduces with SPA size. For the tubing diameter, interestingly, we find the existence of a value with the largest fmax, such that fmax reduces above or below this value of D. Furthermore, this diameter changes with the SPA size and valve conductance. For instance, it is 3 and 4mm for the SPA-pack, whereas it is 2.5 and 3 mm for the pneunet for valve 1 and 2 respectively.

However, this led to over-pressure, especially for the SPA-skin reaching upto 80 kPa when powered at P_{src} = 100 kPa. This occurred because the response time of the valve introduced a delay in the system. In addition to reducing fmax and increasing A and E, over-pressure could cause failure via bursting of the SPA. To address this, we modified the control algorithm to compensated for the valve delay as follows:

$$if(P_{spa} + \dot{P}_{spa}.d > 49\,kPa\ \&\ input == 1)$$
$$input = 0;$$
$$else\ if(P_{spa} + \dot{P}_{spa}.d < 1\,kPa\ \&\ input == 0)$$
$$input = 1;$$

where, d is the delay due to valve response time. This modified algorithm uses the known value of valve delay, predicts when the SPA will reach its target, and pre-emptively switches the valve ON or OFF to prevent over-pressure. We calculated this value using the time-lag in the measured pressure response and applied signal, equal to 25 ms and 8 ms for Valve 1 in deflation and inflation respectively and 3 ms for Valve 2. Figure 4:15 shows the effect of this delay compensation algorithm for the SPA-skin. As seen from the Figure 4:15., this led to a 60% increase in fmax from 6 Hz to 9.6 Hz, and reduction in A by 35%, from 6.2 mL to 3.8 mL.
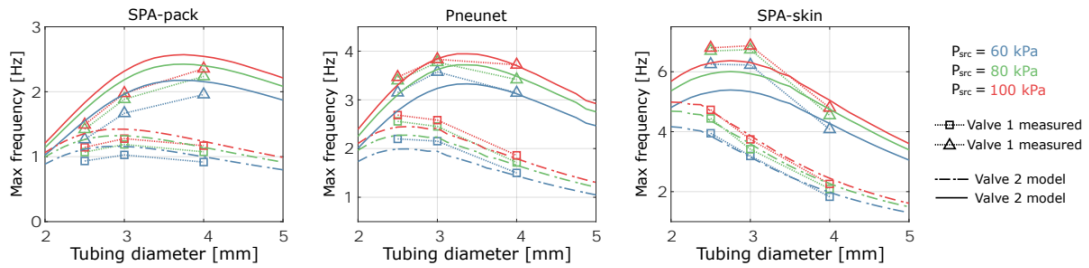
Figure 4:16 **Comparison of predicted vs. measured values of the maximum actuation frequencies for the SPA-pack**, pneunet and SPA-skin, for a tubing length of 5m. As for the tubing length 1 m, we observe similar trends here with f_{max} increasing with P_{src} and C_{valve}, reducing with SPA size, and the existence of the optimal tubing diameter, with largest f_{max}. Another observation is that while f_{max} is expected to reduce with L, the reduction is significantly higher for the SPA-skin, followed by the pneunet and least for the SPA-pack. This occurs because of the relative size differences between the three SPAs.

4.3.4   Results and conclusion

Here, we analyze the results from our simulations and experiments and compare them to evaluate the accuracy of the model. Figure 4:15 and Figure 4:16 compare the measured f_{max} to that from simulations. Our model accurately captures the behavior of f_{max} for the different SPAs at varying tubing lengths, diameters, $P_{src,}$ and valves, with the exception of pneunet at 1m tubing length. The differences are large for the pneunet with 1 m tubing because at frequencies above 5 Hz, it could not completely bend as expected, and started oscillating at a partially expanded/bent state between fully expanded and deflated positions. This led to a mismatch between the modeled values of V_i and V_f , and eventually, the deviation from the predicted response. These two oscillation modes can be seen in supplementary video S1, where, for a tubing length of 2m, we see the transition between normal and abnormal oscillations. For larger tube lengths and therefore lower f_{max} values, however, the measured values do match the model predictions. We can also see that the data matches the trends as predicted in Table I. As expected, f_{max} increases with P_{src} and valve conductance, and decreases with SPA size and tubing length. The fastest response, with 44 Hz for the following parameter combination: Valve 2, tubing length and diameter of 1 m and 2.5 mm respectively and P_{src} of 100 kPa. This is logical as a lesser amount of air is required for powering a smaller SPA. Conversely, we see a reduction in f_{max} with increase in tubing length due

to increased V_{spa}. The relative difference in f_{max} between 1 m and 5 m tubing is more for the smaller SPA-skin, as a much more significant proportion of V_{spa} is due to the tubing. As opposed to other parameters, the tubing diameter shows a very interesting trend as seen from the figures. We see that there is a unique diameter for a given set of SPA, source pressure, valve, and tubing length that gives the fastest response. This diameter, with the largest f_{max}, is larger for large SPA and system with higher valve conductance. For example, for the SPA-pack, this diameter is 3 mm for valve 1 and 4 mm for valve 2. Similarly, for the pneunet, it is 2.5 mm for valve 1 and 3 mm for valve 2. For SPA-skin, the tubing with 2.5 mm diameter has highest f_{max} for all conditions. Thus, the tubing diameter has to be selected appropriately according to the valve used, as well as SPA size. In addition to f_{max}, we calculated the air and energy consumed for the different parameter combinations. For calculating energy consumption, we take values from this figure and use Eq. 7. From Figure 4:15 and Figure 4:16, we observe for a given PSS (P_{src}, C_{valve}, D and L) that A has an inverse relation with f_{max}. For example, for tubing of size 2 mm diameter and 1 m length, the SPA-pack and SPA-skin frequencies are 2.9 Hz and 43.5 Hz, and corresponding A values are 38.5 and 2.2 mL. This is because, the product of f_{max} and A is the average flow output per sec for the PSS, which would be roughly the same even while powering different SPAs. Furthermore, this product is proportional to the product of P_{src} and C_{valve}, which is an indication of the flow capacity of the system, as seen from Eq. 3. Using these results, we can compare different options and select the optimal components for the given objective function. We explore two examples, as shown below in Table III.

TABLE III
MULTI-OBJECTIVE OPTIMIZATION FOR PERFORMANCE AND PORTABILITY

SPA-pack $L = 1$ m $f_{max} = 4$ Hz

D [mm]	P_{src} [kPa]	A [mL]	E [J]
3.25	60	35	**1.66**
2.75	80	33.8	1.99
2.5	100	**33.3**	2.33

SPA-skin $L = 5$ m $f_{max} = 6$ Hz

D [mm]	P_{src} [kPa]	A [mL]	E [J]
2.75	60	14.9	0.88
2.25	100	**10.2**	**0.71**

To achieve f_{max} of 4 Hz with the SPA-pack with 1 m tubings, we note from Figure 4:15 that we need valve 2. We can achieve 4 Hz by choosing one of the three options as shown in Table III. If E has to be minimized, then the first option is preferable. But if P_{src} = 100 kPa is accessible without extra costs, then the third option has to be chosen as it will minimize A. Taking another example with the SPA-skin, to achieve 6Hz with 5m tubing, we will again need valve 2, and we can choose one of the two options shown in Table III. In this case, the second option with smaller diameter and higher pressure is the optimal solution as it minimizes both A and E.

In conclusion, we developed a pressure dynamics model for the entire PSS and SPA system using first principles. We designed an experimental protocol including flow characterization of PSS components, valve control strategy for maximizing actuation frequency and definition and selection of PSS and SPA parameter combinations. Using this protocol, we simulated and experimentally measured the maximum actuation frequency for 162 parameter combinations, based on commonly used components and 3 SPA designs: SPA-pack, Pneunet, and SPA-skin. Results from

experiments and simulations show a good agreement, depicting the trends of how different parameters affect SPA performance. We also observe that there exists an optimal tubing diameter that maximizes the actuation frequency for the remaining set of four parameters. By further analyzing air and energy consumption, this work allows us to define and solve a multi-objective optimization problem to select and control PSS components in order to simultaneously optimize the SPA performance and portability

4.4 Peripheral interfaces for SPA control: Portable pneumatic controllers

4.4.1 Problem formulation and design optimization for fMRI

We had an opportunity to develop and optimize the SPA-skin system for developing a plug-n-play interface compatible for an fMRI. SPA-skin being made up of soft-silicone which is bio-compatible and is driven by pneumatic air, made it as a safe way to provide tactile feedback inside an fMRI scanner. However, here the most important challenge is tube length of 5-6 m to stimulate SPA as the electromagnetic control valves will be outside the faraday's cage of fMRI device, which will severely limit the operational bandwidth.

To optimize for this scenario, we described this system as a pneumatic circuit (Fig. 1), with four major components: Pressure source, pneumatic valve, tubing, and the SPA-skin inspired by the flow path optimization model [201]. As the length of the tubing is large (over 2 metres), the tube diameter becomes a critical factor that affects the performance of the actuator. A smaller tube diameter causes increased flow resistance, which delays the response. Conversely, a large tube diameter increases the total amount of air required to pressurize the actuator, which can also slow the response due to the higher flow rates required. To better understand the system performance, we modeled the SPA-skin's pneumatic circuit using a flow-based analysis.
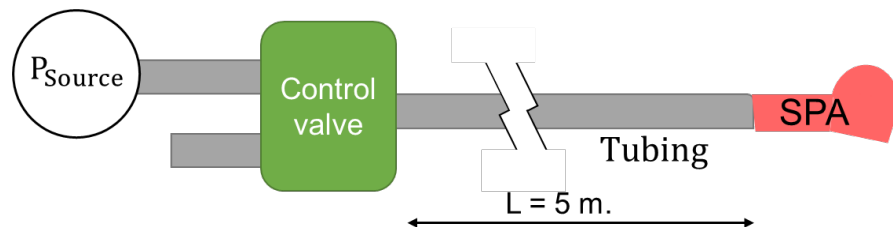
Figure 4:17 **Schematic of SPA-skin pneumatic power supply system**

The current setup used in NCM Lab at ETHZ has 5 m long tube with 2.6 mm inner diameter and a valve with 40 l/min flow rate (at input pressure 2 bar). Our model predicts that this system has a maximum bandwidth of '5 Hz' for an actuation pressure of 50kPa at the SPA (Figure 4:5). At an actuating frequency above 5 Hz, the peak-to-peak actuation amplitude will reduce.

We conducted an optimization study of the pneumatic circuit in order to improve the performance of the current system. Based on our results, we recommend using a bigger valve (200l/min flowrate), 4 mm inner diameter tubing, and a head pressure of 5 bar to increase the actuation frequency to 11 Hz.
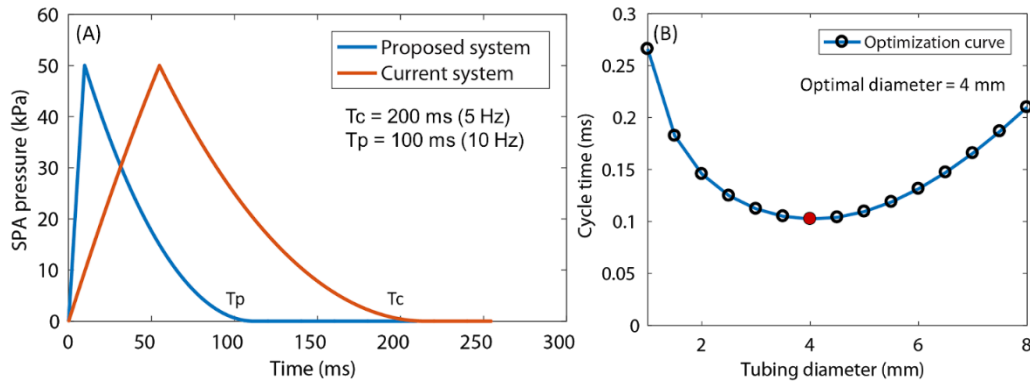
Table 4:5 **Parametric optimization results for 5 m tube-length**. The bandwidth improves from 5 Hz to 11 Hz with 25/75 on/off duty cycle (A) and selection of 4 mm I.D. for tubing

The current system at NCM Lab in ETHZ uses the ON and OFF timings of the valves (duty cycle) as 50%-50%. As seen from Figure 4:5, we need the ON-OFF timing of the valve PWM signal to be 25%-75%, respectively. The actuators will still work at higher frequencies up to 50 Hz with reduced amplitude, which can be perceived on the skin.

4.4.2   Portable pneumatic control system prototypes:
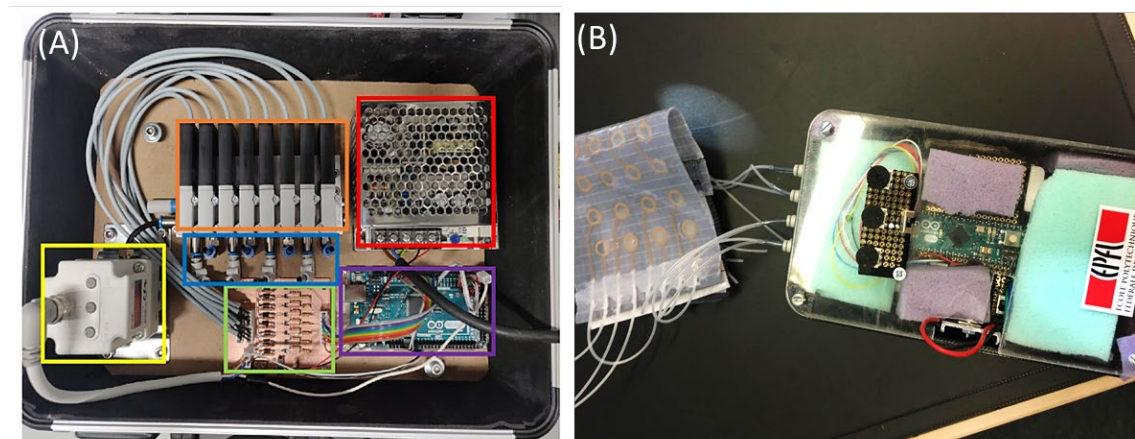
Figure 4:18 Portable pneumatic controller prototypes for driving multichannel SPA-skin. (A) a high-bandwidth custom setup gives upto 200 Hz of actuation with 200l/min flow at 24V actuation. (B) The portable setup hosts a 4 independent pneumatic control valves to drive a 2x4 patch of SPA-skin. The system is powered through a 12V DC pump, which can produce pressures up to 100kPa. The integrated microcontroller allows for generation of multi modal vibratory actuation or travelling wave patterns controlled through three potentiometer knobs.

Device specifications:

	Portable A/C powered	Handheld DC Battery powered
Dimensions	450x350x150 mm3	150 x 90x 80 mm3 With pump
Controller	Arduino	Arduino Micro board
Frequency range	0-200 Hz	0 – 200 Hz
Pressure range	0-200 kPa	0 – 100 kPa
Independent actuation	8 valves	4 valves
Number of actuators supported	8/16	8 actuators
Battery (2 Nos.)	N.A.	11.1V - 750mAh per each
Power consumption	120 W (Max.) 10-15 W (Avg.)	600mA (Avg.) -> 2.5 Hours backup 900mA (Max.) -> 1.3 Hours backup

Table 4:6 Device specifications for the two SPA-skin portable pneumatic supply devices designed for a portable heavy duty application like fMRI (A) and a handheld battery operated tactile feedback device (B)

Chapter 5 Towards human-in-loop tactile feedback design with SPA-skin

Humans are an intricate part of human-robot interactive systems. Motivated by the compliance and mechanically impedance matched feedback, we developed SPA-skin platform that is wearable, low profile and capable of providing wide range of controlled feedback actuation at given location as discussed in Chapter 2. In this chapter, we attempt to close the loop with human side to validate the effectiveness of our technology. In particular, the limitations of human somatosensory perception plays a key role in determining how much information, can be transferred between the user and the haptic interface.

For any haptic interface to effectively deliver physical signals to humans, the information encoding needs to be derived from the tactile cues above certain thresholds and within the bandwidth of human perception. A numerous studies have been done in deriving the tactile perception thresholds for different locations on the body [9], [10], [44], [232]. Even though human haptic perception is responsive over a range of 20 to 400 Hz [51]; these studies have been mainly restricted to high frequencies (100-350 Hz) [9]. Only a limited work has been done on studying skin sensitivity at relatively low frequencies (in the range 10 to 100 Hz) [44]. The most commonly used vibration motors function by exploiting the resonance of the vibration motor, so their output bandwidth is limited around the resonant actuation frequency from 100 - 350 Hz. There is hardly any available tactile platform with integrated sensors to modulate actuation force, frequency and stimulation pattern accurately, which limits the quantitative measurement of the stimulation parameters in this range.

Beyond being in the range of human perception of touch, an interactive interface also needs to quantify the forces to be applied for realistic communication. Most tactile feedback interfaces employed a qualitative analysis for the detection of tactile stimuli for the validation. Further experimental protocols need to be developed to quantify the measurements of the performance of wearable haptic platforms. One way, to qualitatively and quantitatively validate the tactile feedback through somatosensory thresholds protocols for tactile perception thresholds at different part of the body.

The SPA-skin presented herein, with its embedded sensing capacity and specific actuation range (0-100 Hz), provides a suitable platform for validating the human-in-loop protocols and the SPA-technology itself as wearable tactile feedback interface. We conducted three different experiments where SPA-skin design is specifically adapted for each application case, as developed in Chapter 4. We designed the first experiment to identify the perceptual threshold amplitude, traveling wave delay and difference in perceived frequency using up-down-transfer rule method (UDTR) [233]. The aim of this experiment is to develop generic protocol for human-in-loop characterization of tactile feedback devices and to quantify the required threshold values using SPA-skin. For this, we used 4x4 SPA-skin array with high-sensitivity piezo sensors specifically developed in Section 4.1 for wearability near forearm area.

The piezo sensing layer not only help control the feedback stimulation but also, to quantify these amplitude stimulation for a range of frequencies often not covered in other research, as the electro-mechanical stimulation devices lack the actuation bandwidth below 100 Hz. The results obtained in pilot study show insights about minimum threshold values and the link with sensory neurons. Followed by this, we used SPA-skin as a plug-n-play device to integrate with a rehabili-

tation robotic device (Reflex)[234], to study effect of stochastic stimulations on human proprioception capabilities. A limitation of the UDTR type approach is that it depends on the participant's detection, which is known to be biased. A more robust approach requires comparison of the stimuli features. Keeping this in mind, we developed a novel solution using SPA-skin which is fMRI compliant and can record directly the impact of various stimuli with imaging of human brain for the next experiments.

Besides the wearability and high fidelity aspect, the soft silicone based construction and pneumatic actuation make it uniquely suitable for requirements of fMRI safe haptic displays. There hardly exists any device that can produce a localized and high amplitude feedback without introducing artefacts in the scanning. fMRI imaging enables to record, in real time the dynamic activities in brain upon an external stimulation at a specific location. We use SPA-skin with adapted control system (discussed in Section 4.4) to stimulate various locations on human body at specific frequencies between 5-30 Hz (based on the experiment). We discuss the protocol design, various experimental considerations and results for all the three experiments in the following Sections.

The main topics of this chapter that discuss multiple human-in-loop subject studies employing the SPA-skin are:

1. Quantification of the somatosensory thresholds for actuation amplitude, traveling wave delay, and the frequency difference perceived by the user, particularly in 10-100 Hz range.
2. Design of protocol and studying diverse vibrotactile feedback and its impact on human proprioception used for wrist proprioception (in collaboration with SMS Lab, ETHZ)
3. Somato-sensory stimuli differentiations using fMRI brain imaging with a novel soft tactile stimulator platform. (in collaboration with Plasticity Lab, UCL and NCM Lab,ETHZ)

5.1 Somato-sensory thresholds for human forearm using SPA-skin array

5.1.1 Introduction

We customized and fabricated a SPA-skin array with 4 x 4 tactile cells (taxels) for application on the human forearm (Figure 4:1). The size of the array and minimum distance between two taxels was determined by the two-point threshold (approximately 20 mm) of the forearm area distance [52]. This organization in the form of an array provides a wearable platform to design and conduct studies to help understand human tactile perception thresholds of SPA-skin. We then used this array to measure the minimum amplitude necessary to feel a burst of vibration at a given frequency, the ability to localize a stimulus over a given area, and the ability to detect and characterize a simple-shaped apparent movement.

We designed a protocol to obtain the threshold parameters in two user experiments. The first experiment aimed to measure the changes in amplitude thresholds of vibrotactile bursts of fixed duration and pause intervals for a given set of frequencies using the same procedures as previous studies [10]. Findings of this experiment are essential to ensure consistent vibratory feedback force delivered to the wearer for the range of actuation frequencies, specifically for the 10-40 Hz range, which has not been extensively studied. Furthermore, the limited taxel resolution on areas like the forearm requires us to create interesting patterns with different modalities for a higher degree of information transfer. Therefore, it is essential to know how rapidly such information-rich cues can be delivered. We designed the second experiment to determine the maximum speed of apparent movement that can be detected using a set of parameters as defined in previous studies [51], [235] and varying the burst duration and interval between bursts.

5.1.2   User study protocol with up down transfer rule (UDTR)

A versatile user interface optimally utilizes the limitations of the human sensory system to simplify its design: the information that can be transferred is determined and limited by the human sensory thresholds. To enable the SPA-skin system for effectively delivering physical signals to humans, the information encoding needs to be derived from the tactile cues above certain thresholds and within the bandwidth of human perception. The SPA-skin presented herein, with its embedded sensing capacity and specific actuation range (0-100 Hz), is capable of stimulating and measuring somatosensory thresholds for two main mechanoreceptors, RA-I and RA-II type [52]. To determine the actuation threshold and traveling wave delay threshold for the forearm area, we designed two experimental protocols using the SPA-skin array (7 healthy subjects, age 18 – 30).

Experimental Setup: Figure 5:1shows the experimental setup and the functional block diagram used for the characterization of SPA-skin array to study its effectiveness as a wearable tactile device. The conditions of pressure, frequency and channel are selected within the experiment through the Visual Basic interface (1), which communicates with the serial port of a couple of Arduino AT Mega 2560 (in master-slave configuration), and an Arduino Micro (2). The Arduino Micro sends a PWM Signal to the regulator to change the input air pressure of the actuators (3). The AT Mega (4) sends the PWM signal to 16 solenoid valves which generate a frequency modulation (5), using the pressure regulated air flow. This air enters the channels of the actuators and have the selected actuator to vibrate at a chosen frequency and pressure (6). The Bracelet's input pressure was set before experimentation to 5 kPa(7). The PZT sensor \cite{sonar_wearable_2016} is placed on top of the actuator and generates an output signal from the actuator's vibration (8). The signal is amplified and filtered (9), and converted into numerical values by the Arduino Micro. It is then acquired and recorded on the Visual Basic interface (1). The LEDs (10) are used in the experiments.
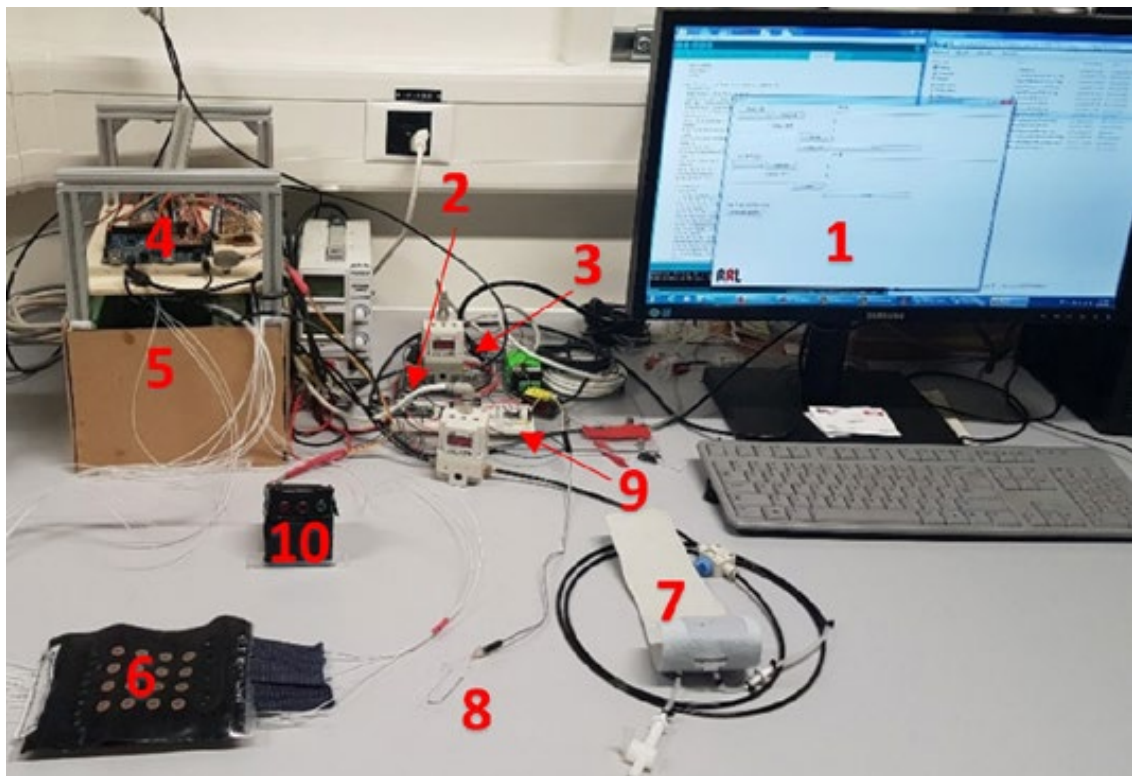
Figure 5:1 **Experimental setup for human-in-loop characterization of the SPA-skin.** Various components of the setup are depicted from 1 to 10 used for conducting the experiments.

Experiment 1, threshold force detection: This experiment is designed *to determine the min-imum vibrotactile threshold force* required for stimulation at different vibration frequencies**.** As with any soft interface, the SPA-skin does not yield repeatable output data for the actuation amplitude under variations in loading conditions. However, using dynamic system characteriza-tion, it is possible to measure the vibratory average threshold force exerted by the SPA on the human skin. This user study was conducted for frequencies of 10 Hz-100 Hz (results in Figure 5:2). During the study, a burst of the desired amplitude and frequency actuation was delivered for 500 ms, with a pause of 2 s, during either of the two green or red LED blinks (Figure 5:2B). If the user was able to feel the correct stimulation three consecutive times, the actuation threshold dropped by a 3 kPa. Where the user fails to notice the stimulation, the actuation threshold is increased by the same step of 3 kPa. This approach is known as transformed-rule up and down (UDTR) method, which is used to obtain the stimulus level required for at least 75 % correct responses [233]. In order to tune the PWM around the threshold, sufficiently high input air pressure is set before starting each experiment. The mean value of the input pressures required for reaching the thresh-old was recorded, as shown in Figure 5:2B. We obtained slightly higher average threshold values, 0.08 N, for lower frequency ranges (10-40 Hz),as compared to the, 0.07 N, for higher frequency ranges (60-100 Hz). This result suggests different mechano-receptors may have been responsible for the thresholds across the two regions.

Experiment 2, traveling wave delay: The SPA-skin array allows independent actuation of each individual taxel to create a variety of possible patterns. This enables the generation of distinct and traveling waves with specific directions and durations for various directional tactile cues. In this experiment, we focused on gathering widely usable threshold data. More specifically, the experiment was designed *to determine the speed limit at which the "Phi effect"* (see [232]) *(target stimulus) occurs* to be recognizable (in comparison with a non-target stimulus). We used a forced-choice tracking to determine the threshold ability to differentiate two stimuli, i.e. the target and non-target so-called "Phi effect" movements. The target stimulus was the actuation sequence, which went from the forearm to the wrist, before going back down to its initial point of departure (Figure 5:2A). The non-target stimulus was the inverse direction. The subject was required to identify the interval of occurrence for the target stimulus. When the subject consec-utively answered correctly three times, the speed of the wave was increased, with a constant step, using the formula relating inter stimulus onset interval (ISOI) and bursts duration (Eq. 5:1 & 5:2) for maximum the apparent traveling speed felt by the wearer [51]. We approximated the ISOI linearly, continuously in two parts as:

ISOI = -1.428 x (stimulus duration) + 71.42, If stimulus duration < 15 ms (Equation 5:1)

ISOI = 0.432 x (stimulus duration) + 43.51, If stimulus duration > 15 ms (Equation 5:2)

If the subject's answer was incorrect, the speed of the wave was decreased at the same rate. The amplitude of the wave was 15 dB above the threshold determined during Experiment 1, and was varied around this 15 dB. The results showed that the traveling delay did not vary significantly over the range of frequency tested. The observed mean value for minimum delay was 105 ms, 100 ms, and 100 ms for 10 Hz, 30 Hz, and 70 Hz, respectively, with a standard deviation of 20 ms for three tests across all the subjects.
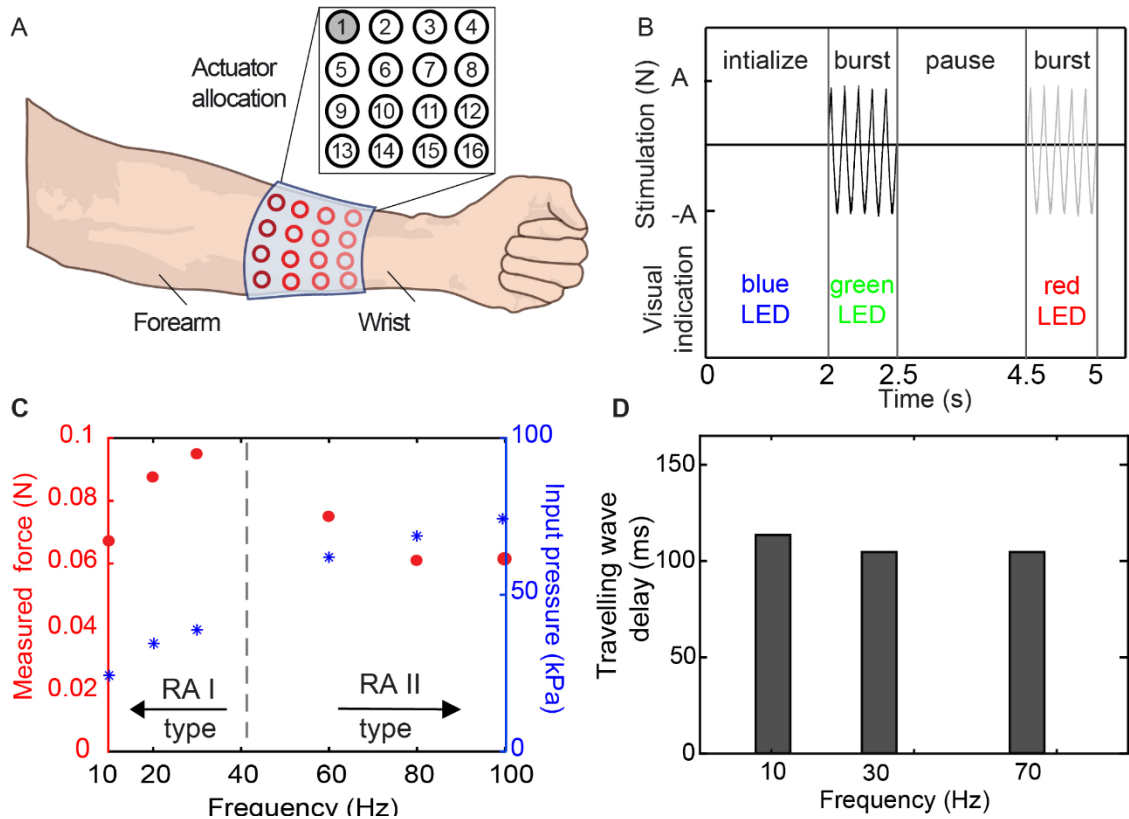
Figure 5:2 **Experimental user study with the placement of SPA-skin on forearm.** (A) Adjustment of SPA-skin on the forearm. Location 1 is used for the actuation for the amplitude threshold experiment. The direction of wave propagation from the forearm towards wrist and back. (B) Bursts of stimulation are given to the user during one of the two durations randomly. The variation in stimulation magnitude is according to UDTR method and the response from users. (C) Results for mean amplitude threshold for seven subjects over the actuation frequency range of 10 Hz to 100 Hz, with actuation at location 1 and with the PZT sensor. The average threshold force, 0.08N for 10-40 Hz is higher than the average stimulation threshold, 0.07N at 60-100 Hz range, suggesting two different mechano-receptor types (RA-I and RA-II) being stimulated. Input pressure increases with the increase in frequency due to limited bandwidth (D) Results for mean travel delay threshold for seven subjects over 10 Hz, 30 Hz and 70 Hz with 110ms, 100 ms and 100 ms average time-delay, respectively.

5.1.3   Discussion

In the first user experiment, as expected, we obtained lower thresholds at low frequencies as the non-Pacinian corpuscles are more sensitive [44], [236]. As the Pacinian corpuscles are located deep in the skin (Figure 4:6A), at higher frequencies it is easier for the waves to penetrate the skin and thresholds are lower. In addition, these corpuscles located deeper in the skin make detection of vibrations easier; however, perception of location is lowered. On the contrary the Meissner corpuscles are located just below the skin epidermis area; these corpuscles are responsible for detecting vibration in the lower range (10-40 Hz) and have a higher threshold for detection of vibration as suggested in the preliminary user studies (Table 5:1). At the same time, these corpuscles have better localization capacity as they are closer to the skin. This indicates using SPA-skin array in the 10-40 Hz range for information rich directional cues and the 60-100 Hz range for low information alerting messages where high sensitivity is desired. In the second experiment, the travelling delay threshold had minimum dependence on the actuation frequency and was observed to be constant around 100 ms throughout the user study. Changes in the frequency do

not have a prominent effect on the travelling wave delay, mainly due to the inter-taxel distance being already around the two-point threshold. However, as we rely on higher actuation pressure for the same output force at higher frequency, it would be beneficial to use the 10-40 Hz actuation range for the travelling waves.

Mechanore-ceptor type	Frequency range [Hz]	Experiment 1, Force threshold [N]	Experiment 2, travelling wave delay [ms]	Spatial resolution sensitivity	Suggested tactile application
RA-I & SA-I (Meissner corpuscles & Merkel cells)	10-40	0.065-0.09	~100	High	Directional, information rich cues
RA-II (Pacinian corpuscles)	60 – 100	0.06-0.07	100	Low	Alert messages, quick notifications

Table 5:1 Average stimulation threshold values and suggested tactile applications based on the mechano-receptors being stimulated at the specific frequency.

As the number of subjects are limited in the above studies, it lacks statistical significance. However, the user studies give promising insights that help formulate reliable tactile cues that will enable improved information transfer between the wearer and device, warranting a more rigorous study involving multiple subjects to derive statistically significant and robust conclusions. In the future, we expect to use the parameter values collected from these experiments to design an optimal communication protocol between a human and a wearable robotic platform through tactile perception. We envisage the SPA-skin array as a 'plug-and-play device for various multimodal information devices to increase immersion and information transfer between subject and media device (Figure 4:17A). Information-theoretic analysis about tactile cues per second that can be transferred through the human skin would yield insights into maximum or optimal bandwidth of human tactile perception from the perspective of digital information transfer. Yet another limitation of this approach is that it depends on the participant's detection, which is known to be biased. A more robust approach requires comparison of the stimuli features, for which, we developed next generation of tactile feedback device using SPA-skin that is fMRI compliant as discussed in section 5.3.

5.2   Effect of stochastic resonance on wrist proprioception generated using SPA-skin

The research findings support[7] that stochastic stimulation has a positive effect on balance, movement, and the sensation of touch. However, it remains unclear to what extent sub-threshold stochastic tactile stimulation can influence the position sense of the upper extremities.

In this study, we investigated the effect of sub-threshold stochastic tactile stimulation on wrist position sense. While previous studies on stochastic stimulation mostly focused on a motor response of the sensory-motor system, we aimed to examine how proprioception itself is affected when stochastic stimulation is applied. As proprioception deteriorates with age (Adamo et al., 2007; Wright et al., 2011; Rinderknecht et al., 2017), it was hypothesized that elderly adults estimate their wrist's position less accurately than young adults. Furthermore, it was hypothesized that sub-threshold stochastic tactile stimulation applied at the wrist joint reduces the errors made when estimating the wrist's position in elderly adults. The same effect was expected to be minuscule in young adults.

5.2.1   Stimulation characteristics:

To influence position sense, the stochastic stimulation employed in this study ought to replicate noise in the frequency band of muscle spindle activity. In the muscle spindle, type Ia (primary or dynamic) afferent fibers convey the rate of change of muscle length and, therefore movement. Type Ia fibers respond well to stimulation in the frequency band from 80 to 100Hz (maximum 150Hz)[237]. Additionally, type II (secondary or static) afferent fibers encode muscle length and, therefore joint position. Type II fibers respond well to stimulation in the frequency band from 10 to 30Hz)[237] maximum 60Hz. In this study, the frequency band for the stochastic stimulation was set to range from 20 to 120Hz. Currently, the available feedback solutions are rigid and have limited control operational frequencies for the requirement of the experiments on stochastic resonance as well as lack a localized controlled feedback. The SPA-skin technology proves to be the well suited device variable frequency vibration and distribution of vibration locations over human body.

In the healthy human body, most physiological patterns such as breathing or heart rates show colored noise characteristics [238] i.e., in those signals, the amplitudes of lower frequency components are typically greater than those of higher frequency components. Colored noise is considered to be superior to white noise for enhancing signal detectability[239]. In this study, a colored noise spectrum was selected for the stochastic stimulation to predominantly influence type II fibers and therefore joint position sense.

To evoke stochastic resonance effects, the stimulation amplitude should be between 60 and 90% of the participants' stimulus detection threshold. In this study, the stimulus detection thresholds were assessed experimentally using the method of ascending and descending limits [240]. Before each experimental session, thresholds were assessed for the ventral and dorsal sides of the forearm separately. The stimulation was then set to 80% of each threshold. To avoid an imbalance of

agonist-antagonistic spindle signals, which may bias movement or position sense, agonistic and antagonistic joint sides were always stimulated simultaneously [241]. The presence of PZT sensing layer along with pressure regulation ensured for measuring of the sub-threshold stochastic tactile stimulations. The design of SPA-skin was driven by these pink noise sub-threshold vibration requirements and then by the wrist anatomy. We tested different shapes and sizes of SPAs as discussed in Chapter 2 using both FEA simulation and experimental measurements to select the ring shaped actuator as seen in Figure 5:3. That has improved bandwidth and uniform inflation profile important to cater the sub threshold actuation over the flexion and extension muscle spindles of wrist without activating the sensory neurons [159].
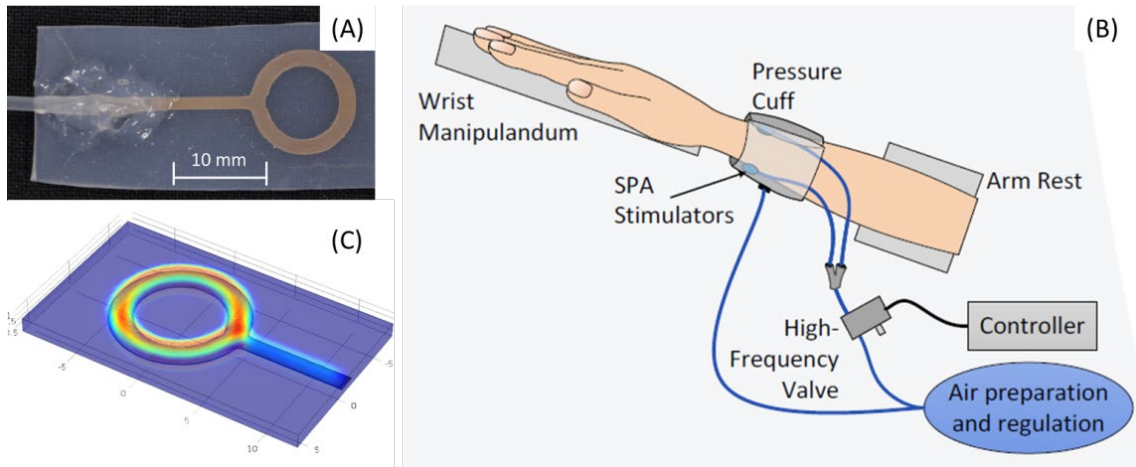
Figure 5:3 **SPA design for stochastic resonance feedback.** SPA prototype design with 10 mm actuator diameter and 2 mm inlet (A). Schematic of SPA interface as a plug-n-play device to an existing robotic platform developed to experimentally verify effect of stochastic resonance on proprioception (B). Actuator design simulation modeled using experimental soft material properties design (C). The improvised actuator has uniform inflation all over the actuation surface as required by the design (shown by red color) with up to 100 Hz of actuation fidelity.

5.2.2   Study setup and Results:

Fifteen young (24.5±1.5y) and 23 elderly (71.7±7.3y) unimpaired, right-handed adults completed a wrist position gauge-matching experiment. In each trial, the participant's concealed wrist was moved to a target position between 10 and 30° of wrist flexion or extension by a robotic manipulandum. The participant then estimated the wrist's position on a virtual gauge. During half of the trials, sub-threshold stochastic tactile stimulation was applied to the wrist muscle tendon areas. Stochastic stimulation did not significantly influence wrist position sense. In the elderly group, estimation errors decreased non-significantly when stimulation was applied compared to the trials without stimulation [mean constant error reduction $\Delta\mu(\theta^{of}_{con})$=0.8° in flexion and $\Delta\mu(\theta^{oe}_{con})$=0.7° in extension direction, p = 0.95]. This effect was less pronounced in the young group [$\Delta\mu(\theta^{y}_{con})$=0.2° in flexion and in extension direction, p = 0.99]. These improvements did not yield a relevant effect size (Cohen's d < 0.1). Estimation errors increased with target angle magnitude in both movement directions.

In young participants, estimation errors were non-symmetric, with estimations in flexion [$\mu(\theta^{yf}_{con})$=1.8°, $\sigma(\theta^{yf}_{con})$=7.0°] being significantly more accurate than in extension [$\mu(\theta^{ye}_{con})$=8.3°, $\sigma(\theta^{ye}_{con})$=9.3°, p < 0.01]. This asymmetry was not present in the elderly group, where estimations in flexion [$\mu(\theta^{of}_{con})$=7.5°, $\sigma(\theta^{of}_{con})$=9.8°] were similar to extension [$\mu(\theta^{oe}_{con})$=7.7°, $\sigma(\theta^{oe}_{con})$=9.3°]. Hence, young and elderly participants performed equally in extension direction, whereas wrist position sense in flexion direction deteriorated with age (p < 0.01). Though *unimpaired elderly*

adults did not benefit from stochastic stimulation, it cannot be deduced that individuals with more severe impairments of their sensory system do not profit from this treatment. While the errors in estimating wrist position are symmetric in flexion and extension in elderly adults, young adults are more accurate when estimating wrist flexion, an effect that has not been described before.

5.3   fMRI analysis of vibrotactile stimulation using SPA-skin

5.3.1   Introduction

The primary somatosensory cortex[8] contains a detailed map of our whole body, such that there is a point-to-point correspondence between a specific body part and a patch of S1 cortex. Using fMRI during tactile stimulation to or movement of different body parts, it has already been possible to detail the Somatotopic layout of S1 in detail. However, the exact somatotopy of the human S1 facial representation remains debated. Progress has mainly be hampered by the methodological challenge of how to apply automated vibrotactile stimuli to face areas in a manner that is (i) reliable despite different curvature depending on the face location; and (ii) MRI-safe and artefact-free when applied in the head-coil.

Here we overcame this challenge by using soft pneumatic actuator (SPA) technology [243] that, unlike common vibrotactile elements, does not contain metals or electrical circuits and also provides excellent control over actuation frequencies. This set-up allowed us to administer suprathreshold vibratory stimulation with a chosen amplitude and frequency independently to different skin sites. SPAs are made of a soft silicon material (Dragon Skin 30®, Smooth On Inc., USA) and be in- or deflated by means of airflow. SPAs have a small (1.4cm) diameter and are flexible in structure, enabling a good skin contact even on curved body surfaces (as on the face). They are safe to place in the head-coil of the MRI and do not induce artefacts.

In the current study, we aimed to provide a methodological advance by providing automated tactile vibration stimulation inside the head coil of the MRI scanner. As a sanity check, we first mapped the well-characterized finger layout in S1 using this novel device. Using this novel technology, we ultimately aimed to characterize the topographic face layout in S1. Based on these advances, we in parallel also use the fMRI imaging to validate effectiveness of different stimulations generated by SPA-skin interface. We device a set of experiments to check if different stimulation modes such as location specificity, amplitude change and frequency has a measurable impact on human brain activity. This will not only qualitatively but quantitatively be able to validate the interaction capacities of tactile feedback interfaces.

I have designed, developed and deployed the soft tactile platform with portable soft pneumatic controller to interface with fMRI systems. I co-developed the design of experiments for human in loop validation of SPA-skin device, specific firmware to integrate fMRI scripts in Matlab. Dr. Sanne Kikkert conducted the corresponding fMRI tests with subjects, design for fMRI side of study protocol, preconditioning and post processing of the imaging data, generation of the figures and graphs.

5.3.2 Pilot Study 1: Somatotopic layout for Hand and Face

Materials and Methods

Supra-threshold tactile stimulation was applied to the hand or face of healthy participants using an in-house build MRI-compatible pneumatic device that was able to independently vibrate SPAs. Intensive pilot experiment revealed that stimulating for 8 seconds at a time, alternating between 8 and 10Hz stimulation frequencies every 2 seconds minimizes peripheral adaptation. To ensure stable attention, we included 'silent periods' in a small subset of the stimulation trials and asked the participant to count the number of silent periods within each run.

Figure 5:4: Experimental placement map for SPAs (stimulators) on face, a dummy SPA for noise control on the thumb. fMRI mock-unit to validate SPA-skin setup function before actual testing and face mask used for improved mechanical grounding on the face. (Credits: Sanne Kikkert, ETHZ)

As a first application and validation of this novel device, we used 3T functional MRI (2.5mm^3 resolution) to assess brain activity while automated tactile stimulation was applied to participants' individual fingers of the left hand in a blocked design fashion. Secondly, we aimed to assess the S1 face representation in detail by applying tactile stimulation to the forehead, upper lip, chin, or thumb in a blocked design fashion. We quantified somatotopic representational patterns using representation similarity analysis. To uncover face area representational selectivity, we further employed a traveling wave paradigm.

Results

We found a typical somatotopic pattern of participants' fingers, similar to what has been reported previously. Our preliminary data further show that the thumb representation neighbors the forehead representation in S1. Within the face representation, we found that the lip representation is most distant from the forehead representation, with the chin represented in between. Together with our results show that, by providing vibrotactile stimulation using the SPA technology, we are able to reveal clear somatotopic representational patterns

(A) Contralateral hemisphere   **Ipsilateral hemisphere**

(B)

Distances controls $rh_s1_Handarea_noSII$

Distances controls $lh_s1_Handarea_noSII$

(C) Contralateral hemisphere   **Ipsilateral hemisphere**

Distances controls $rh_s1_Facearea_noSII$

Distances controls $lh_s1_Facearea_noSII$
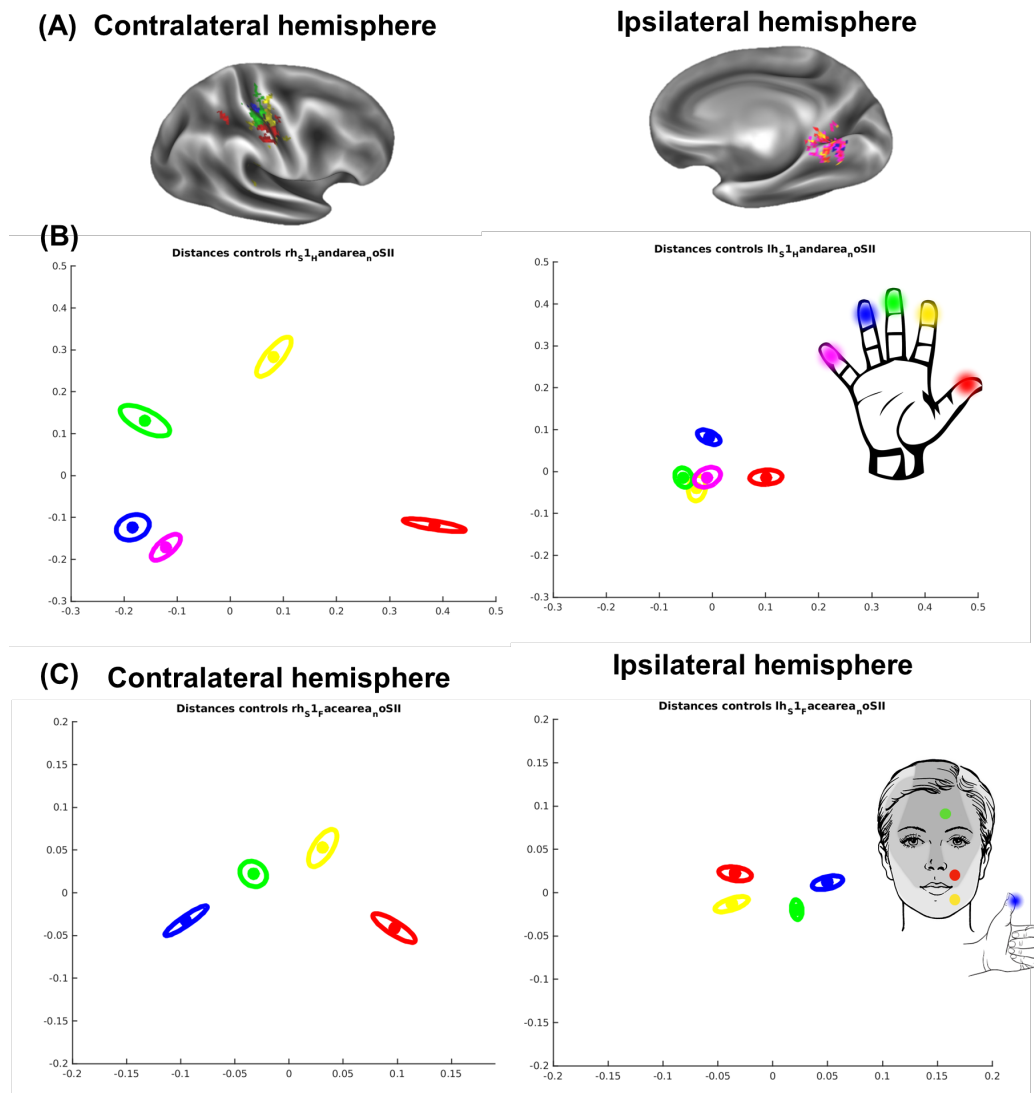
Figure 5:5 **Finger and face RSA representations combined for 8 subjects** (A, B) This is well known in the literature, and we can therefore use this result as qualitative + quantitative methods validation. The thumb is represented lowest in the brain, going up in the brain (in order) you should see the index, middle, ring, and little finger. Ipsilateral hemisphere is used as a control against the constrlateral hemisphere's representation. (C) Face representational map for three different locations on face. The thumb is known and reliable in location and can be used as a reference point. RSA is to investigate the face representations. *(As far as we are aware, we are the first to look at the face representation in this way)*

5.3.3 Pilot Study 2: Somatotopic layout for variation in Location, Amplitude and Frequency

Background

In this experiment[9], we want to test and validate the performance of SPA-skin using the brain activity generated inside the brain. This will allow replacing the standard subjective questionnaire about the performance of SPA-skin with measured brain activity.

In usual application scenarios, we use SPA-skin for vibratory feedback on the face, back of the neck, on the forearm (front and back), and fingers (thumb, middle) application. This experiment with successful information would enable us to decode the reparability of brain stimulation for variation in locations, frequency and strength of actuation. The main objective of the experiment is to observe respected brain activity corresponding to the stimulation pattern and user selected output. It is possible that the subject feels the change in frequency, which he/she will record on the device; however, we may not be able to see the subtle changes in brain activity. In addition, when give subthreshold stimulation the subject may not be able to feel these stimulation but there may be brain activity recorded corresponding to the stimulations.

Expected test values for the control parameters:

Control Parameters	Test values (tentative)	Range	Remarks
Locations	Face, neck, forearm, fingers	8 channels	2sec. stimulation/location
Frequency	5 Hz, 15 Hz, 30 Hz	35 Hz	
Amplitude	Low and High	20-120 kPa	Supra threshold
Muscle stimulation	With and without squeezing a soft-object	Passive and Active	

Materials and methods

fMRI experimental setup: We placed in-house printed 3D plates on top of the SPAs and attached the SPAs to the skin of different body parts using adhesive tape. Participants viewed a visual display through a mirror mounted on the head coil. Instructions and stimulations were delivered using Psychtoolbox (v3) implemented in Matlab (v2014). Matlab communicated with the Arduino implemented in the SPA set-up via a parallel port. Head motion was minimized using over-ear MRI-safe headphones or padded cushions.

Participants viewed a fixation cross on the screen. A change in fixation cross colour indicated a change in conditions: a white fixation cross indicated a rest condition, a red fixation cross indicated that stimulation would start in 0.8s, and a green fixation cross indicated an 8s stimulation trial. Stimulation was provided for 8s in 800ms bursts of stimulation on periods followed by a 400ms stimulation off periods to minimize peripheral adaptation. To ensure stable attention during the fMRI runs, 1s silent gaps were introduced into the middle of a small percentage of stimulation trials. Immediately following each run, the experimenter asked the participant to verbally report how many silent trials had appeared and provided feedback on the reported number.

Since a stronger sensation is expected to lead to a stronger BOLD response, we matched the sensation intensity across stimulation locations based on participant's self-report. A stimulation intensity matching task was carried out prior to the fMRI runs separately for the low stimulation intensity and the high stimulation intensity. First, participants were asked to set the optimal stimulation intensity for a reference location by means of button press responses. Participants were instructed that an optimal high amplitude stimulation would be as strong as possible while remaining focal (i.e. no spread to skin locations not directly underneath the stimulator) over the full 8s stimulation period. Participants were instructed that an optimal low amplitude stimulation would be as low as possible but should still be felt reliably for the full 8s stimulation period. The stimulation intensity was limited to not be below 20% duty cycle. Once the optimal stimulation intensity was chosen for the reference location, participants were asked to match the stimulation intensity for the other stimulation locations to this reference location. To enable this matching, participants were given an 8s stimulation trial for the reference location, immediately followed by a stimulation trial of one of the other stimulation locations.

Experiment 1, spatial layout: This experiment is aimed at exploring the spatial layout of body part representations using SPA technology. It was further aimed at exploring activity levels of low versus high amplitude stimulation. Participants' written informed consent was obtained prior to study onset. Ethical approval was granted by the Kantonale Ethikkommission Zürich (EK-2018-00937). We tested 4 healthy right-handed participants (2 females). SPAs were attached to the left back side of the neck, glabrous side of the left lower arm, hairy side of the left lower arm, the tip of the left thumb, and the tip of the left ring finger. Sensation intensity matching was done at 15Hz stimulation separately for low sensitive body sites (reference = neck, to be matched body part = glabrous lower arm) and high sensitive body sites (reference = hairy lower arm, to be matched body parts = thumb and ring finger.

During the main experiment, participants underwent 5Hz, 15Hz, and 30Hz high amplitude stimulation trials for each body site, as well as 15Hz low amplitude stimulation trials. These 20 conditions were repeated twice per run along with 8 rest conditions and presented in a randomized order. The order of conditions was different for each of the 8 runs.

Experiment 2, amplitude and frequency Layout: A similar experiment is setup for the validation of low vs high amplitude stimulation effect on S1 brain activity as well as to explore possible representational differences of changes in frequency. This experiment has been conducted in UCL.

We tested 4 healthy subjects (2 left-handed), here SPAs were attached in similar fashion as experiment 1 and the participants underwent with 15 Hz high amplitude and low amplitude stimulation trials as well as 5 Hz, 15 Hz and 30 Hz stimulation trials for finger locations. Here we reduced the frequency parameters to be able to increase total number of reputations at given amplitude. Similary, we reduce the locations to ensure we get good number of samples from finger location for variation in frequencies. As this has not been done before, finger is selected for know expected layout as well as higher stimulation due to large number of sensory neurons in this region.

Results:

Experiment 1: Figure 5:6 shows a clear distinction of different actuation locations, as not all the locations are as sensitive as human fingers or face, we observe relatively low and scattered activity across the S1 region. However, we validate the stimulation being felt by users over different frequencies at different locations as shown by Figure 5:6.
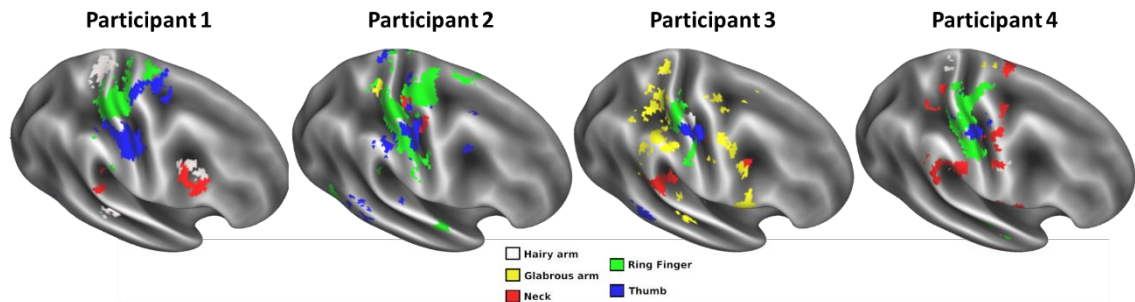
Figure 5:6 **Spatial layout of somatosensory body map representations obtained using the stimulations given by SPA-technology** Brain image map depicts active regions for Z-score > 2.3
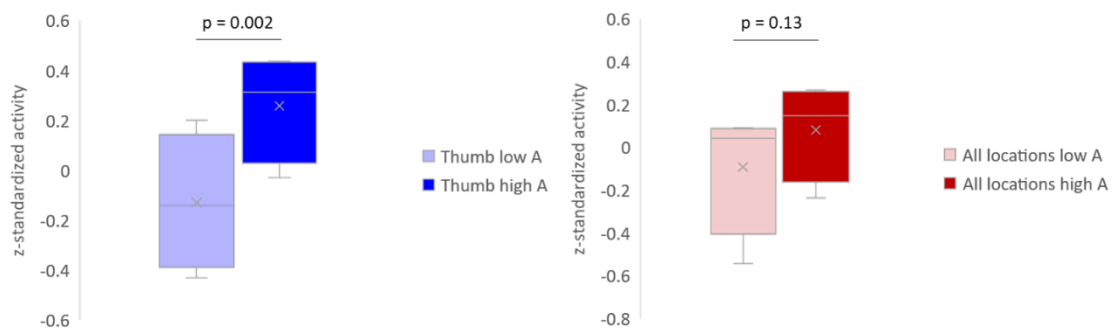
Figure 5:7 **Low amplitude vs High amplitude correlation** for thumb region (blue) and all 6 locations (red). A strong correlation is obtained for brain , suggesting the brain has distinctively different activities for low and high amplitude stimulation.

Experiment 2: Similar, to observations in Figure 5:7, Experiment 1, Figure 5:8 confirms different brain regions being activated for changes in SPA actuation frequency.
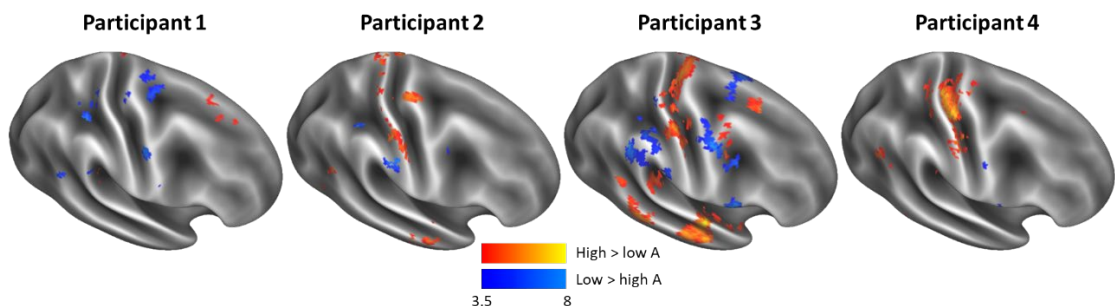
Figure 5:8 **Low amplitude actuation vs high amplitude actuation activity in the brain** with 4 subjects for thumb region (Z-score >3.5). High amplitude is contrasted with orange color for low amplitude in the background and Low amplitude is contrasted with blue color for high amplitude in background.

Differentiation of Frequency. In this experiment, we selected the finger as it is one of the most sensative region in somato-sensory maps and also there is a known possible region to obtain the stimulation location in S1 map. A classification model is trained for discriminating between the three frequencies 5 Hz, 15 Hz and 30 Hz seperately for expected region of interest (ROI) to have stimulation from actuation at finger (SI region) and then for control ROI (EVC region). Ideally, if there lies a differentiation features embedded in these brain stimuli, we shall be able to receive > 1/3 accuracy with our training dataset for SI region and <1/3 or ~1/3 accuracy of prediction due to lack of stimulation or randomness chance of prediction out of 3 choices in EVC or control ROI. Figure 5:9A shows the pleasant potential of embedded information in the SI region of brain for changes in frequency. Nevertheless, we are also confirmed to have brain activity for all the three stimulation for stimulated finger in all the subjects (Figure 5:9B)
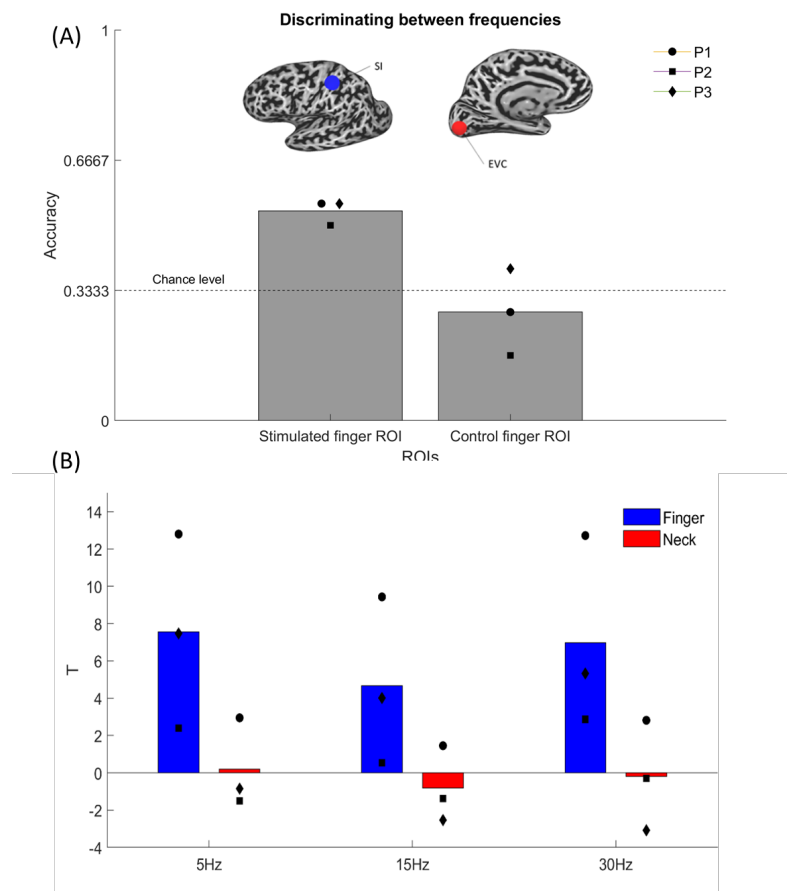
Figure 5:9 **Frequency differentiation layout** (A) Classification figure for information encoded in frequencies, (B) T-scores for S1 hand area for different stimulation frequencies for actuation at Ringfinger/Thumb compared with the neck as control measurement

fMRI data analysis

Preprocessing and coregistration: Common preprocessing steps were applied to each individual fMRI run using FSL's Expert Analysis Tool FEAT (version 6.0; https://fsl.fmrib.ox.ac.uk/fsl/fsl-wiki/FEAT). The following preprocessing steps were included: motion correction using MCFLIRT [244], brain extraction using automated brain extraction tool BET [245], spatial smoothing using a 3mm full-width-at-half-maximum (FWHM) Gaussian kernel, and high-pass temporal filtering

using a cut-off of 90s. Functional data were aligned to each participant's T1-weighted image initially using FLIRT [246] and optimized using boundary based registration [247].

Univariate analysis: First-level parameter estimates were computed using a voxel-based general linear model (GLM) based on the gamma hemodynamic response function and its temporal derivatives. Time-series statistical analysis was carried out using FILM (FMRIB's Improved Linear Model) with local autocorrelation correction. Contrasts were defined for each body part's low or high amplitude stimulation (i.e. regardless of stimulation frequency) versus rest. We then used a fixed effects higher-level analysis to average across runs for each individual participant. Z-statistic images were thresholded using clusters determined by Z > 3.1 and p < .05 family-wise-error-corrected cluster significance thresholding was applied. To visualise the activity maps of high amplitude stimulation, statistical parametric activity maps were projected onto cortical surface projections from each participant's T1-weighted image. To compare the level of activity for low versus high amplitude stimulation, he percent signal change was extracted for each contrast for all voxels underlying an anatomically defined S1 hand ROI (as in [248]).

Conclusions

Providing somatosensory stimulation in an MRI environment is challenging. Our setup is flexible, easy-to-implement, precise, portable, fast, and offers a cost-effective solution in comparison to commercially available devices that mostly induce artefacts and often require active shielding or hardware modifications. We could *confirm* an overall classical somatotopic layout of the body in S1 region using SPA technology: The body regions where SPAs are placed and stimulated match the expected somatotopic layout.

Our exploratory analysis suggested that for 3 out of 4 subjects were able to distinguish between the high and low amplitude stimulation applied via SPA technology, which effectively showed high activation level in the S1 region. To further zoom in on this effect we explored activity in the S1 hand area during thumb stimulation. We found significantly stronger activity during high amplitude thumb stimulation compared to low amplitude thumb stimulation. Our exploratory classification analysis further suggests differential patterns of activity during 5, 15, and 30 Hz stimulation applied using our SPA technology.

Chapter 6   Conclusion

6.1   Achieved results

In this thesis, my goal was to ***an immersive interactive soft virtual-tactile environment*** through hardware and software development considering wearability, portability, easy customization, and modularity properties. The main challenges for such an immersive tactile environment development lie in solving the safety and compliance requirements for pHRI, achieving seamless interactivity through a control environment across the modes for immersion, and closing the tactile feedback loop with humans.

Towards achieving this goal, our first research objective was to develop novel soft technologies, including soft sensors, soft actuators that utilize the capabilities of safety, compliance and simpler control through unconventional system design, prototyping techniques, and control method development approaches. Our second research objective was to develop a comprehensive control environment to have a seamless and coherent tactile information transfer and developing an experimental protocol for validating the tactile feedback through human interaction. We propose a two-component system to achieve multi-experience tactile feedback and for the first time, human-in-loop 'physical' validation of user actions. Followed by this the final aim was to develop a versatile plug-n-play interface that can be tuned for application specific requirements and use it to study human proprioceptive and somatosensory thresholds for an improved immersive interaction.

During my PhD studies, I developed and studied the following key core contributions:

1. Design of a novel soft pneumatic actuator skin with integrated sensing for dynamic and wearable feedback

2. A material characterization based FEA design tool for SPA Modeling and feedback controlled tactile actuation

3. A comprehensive design method for wearable tactile feedback using SPA-skin: from selection of material, actuator geometry, to pneumatic power supply components for an optimized system

4. Human-in-loop study of diverse vibrotactile feedback and protocol development to obtain key parameters for somatosensory thresholds

In this section, we attempt to tie back the contributions from my thesis to the research vision and questions for developing the wearable interfaces for human-robot interaction:

How can we match the mechanical compliance of a robotic device with human body for wearable and dynamic feedback?

For an effective wearable technology, we require an accurate understanding of the physical interactions between the device and the wearer's perception. We engineered a closed-loop control of an entirely soft wearable haptic platform over a wide range of vibrotactile feedback. We prototyped a soft monolithic sensor integrated SPA with embedded sensing and actuation capabilities, and with soft sensors that have no mechanical loading impact on the actuator. In addition, the SPA-skin produced forces up to 1 N with controllability of 0.05 N, and actuation dynamics of

up to 100 Hz with controllability of 0.1 Hz; these are essential for providing a wide range of proprioceptive feedback to the wearer. The system characterization of SPA-skin under continuous actuation and sensing showed robust and repeatable behavior over 1 million cycles thereby promising compatibility with "real life" wearable applications. We further demonstrated closed-loop control capabilities of this SPA-skin system at 15 Hz sinusoidal vibration at 1 kHz control speed. The closed-loop controller, based on an analytical model of the system, uses the sensor resistance to control the average strain of the actuator and allows for generating uniform output force under different loading conditions. This allowed the wearer to feel consistent feedback independent of the wearing conditions. Furthermore, the bidirectional operations of the SPA-skin platform offer a wearable system that can not only be used for haptic feedback but also quantification of human proprioceptive capabilities for a range of frequencies.

The comprehensive techniques for designing, modeling, and fabricating soft actuators were not yet in place. Accurately predicting the output blocked forces, as well as facilitating simulation-based iterative design, is challenging with the traditional analytical modeling approach. We developed a finite element analysis-based modeling tool to investigate the SPA design as well as investigate additional distributed sensing to enable controlled feedback and mitigated the non-linearity through intelligent control algorithms.

The key findings during the development of soft technology and Modeling tools led to several research publications and contributed to the field by integrating SPA with soft sensors, the closed-loop control for high-fidelity tactile feedback generation using a soft wearable platform:

[1] **Sonar, H. A.**, & Paik, J., "SPA-skin with piezoelectric sensors for vibrotactile feedback". *Frontiers in Robotics and AI* , 2(38), 2016.

[2] **Sonar, H. A.**, Gerratt, A. P., Lacour, S. P., & Paik, J., "Closed-loop haptic feedback control using a self-sensing soft pneumatic actuator skin". *Soft robotics* , 7(1), 22-29, 2020.

[3] **Sonar, H. A.**, Yuen, M. C. S., Kramer-Bottiglio, R., & Paik, J, "An any-resolution distributed pressure localization scheme using a capacitive soft sensor skin", *IEEE Int. Conference on Soft Robotics (RoboSoft)* ,pp. 170-175, 2018.

[4] **Sonar, H.A.**, Robertson, M., Joshi, S., Bhatnagar, T., & Jamie, P., "A Soft Portable Wearable Pneumatic Interactive Suit", *U.S. Appl. No. 62/514,234* . (filed Jun. 2, 2017)

[5] Moseley, P., Florez, J. M., **Sonar, H. A.**, Agarwal, G., Curtin, W., & Paik, J., "Modeling, design, and development of soft pneumatic actuators with finite element method". Advanced engineering materials, 18(6), 978-988, 2016.

[6] Agarwal, G., Robertson, M. A., **Sonar, H. A.**, & Paik, J., "Design and computational modeling of a modular, compliant robotic assembly for human lumbar unit and spinal cord assistance". *Nature Scientific reports* , 7(1), 1-11, 2017.

How do we 'model' for a multimodal system that has multiple physical parameters?

For an ideal human-robot interaction, the physical experience need not be limited to a single stimulation. This in addition to a wearability requires a dynamic interface that allows for intuitive information transfer between user environment and virtual environment using visual, aural, haptic, or even olfactory feedback to enable an immersive experience. We achieved this using a control environment designed to act on two levels, High-level augment multi-modal control and Low-level closed loop feedback control for the physical interface.

For the low-level side of control algorithms, we systematically modeled the PZT, soft liquid metal, and capacitive foam based sensors and developed corresponding signal conditioning algorithmsto have seamless integration and information transfer to high-level controller. FEA based tools were developed to optimize and preselect SPA-design with possibility feed forward control.

Finally, the multi-modal nature of the feeling of touch itself needs to be explored for the generation of a realistic and rich sensation through understanding the possible ways to recreate the haptic sensations like texture, size, and shape of an object. We integrated physical model for texture and size of object like orange using texture recording based on onboard sensing of SPA-skin and validated the texture generation with SPA actuation alongwith the size exploration property overlapped

The key findings during the development of a comprehensive control environment led to several research publications and contributed to the field by integrating the closed-loop control of high-fidelity soft systems and multi-modal tactile feedback generation using a soft wearable platform:

[1] **Sonar, H. A.** , & Paik, J., "SPA-skin with piezoelectric sensors for vibrotactile feedback". *Frontiers in Robotics and AI* , 2(38), 2016.

[2] **Sonar, H. A.** , Gerratt, A. P., Lacour, S. P., & Paik, J., "Closed-loop haptic feedback control using a self-sensing soft pneumatic actuator skin". *Soft robotics* , 7(1), 22-29, 2020.

[3] **Sonar, H. A.** , Huang, J.L. & Paik, J., "Soft Touch using SPA–Skin as a Wearable Haptic Feedback Device". *Advanced Intelligent Systems* , p. 2000168, 2021.

[4] Huang, J.-L., Zhakypov, Z., **Sonar, H. A.** , & Paik, J., "A Reconfigurable Interactive Interface for Controlling Robotic Origami in Virtual Environments", *The International Journal of Robotics Research (IJRR)* , 37(6), 2018.

How can we close the tactile virtual reality loop with human feedback?

For an effective wearable haptic feedback device, we require an accurate understanding of the physical interactions between the device and the wearer's perception. We proposed a two-component system to achieve a multi-experience tactile feedback and for the first time, human-in-loop 'physical' validation of user actions, closing the haptic feedback loop. We use SPA-skin for its low profile form factor, high-bandwidth capabilities and integrated sensing as an active bidirectional interface. Special design measured in PZT sensor signal conditioning like high sensitivity instrumentation amplifiers with noise filtering using coaxial cables and line noise notch-filters allow for on body placement and accurate measurements. We then designed and validated a haptic system in which the delivery of tactile feedback and spatial accuracy was quantitatively studied for bi-directional human-in-the-loop system. The tactile feedback loop was closed with human actions and was quantitatively validated for the level of immersion and quality of tactile feedback.

Similarly, we not only need to qualitatively measure the effectiveness of tactile feedback given to the body with user feedback, but the methods like fMRI imaging allow us to record a respective tactile stimulation in the sensory-motor cortex area of the brain and then use this information to tune the feedback modes. We develop a plug-n-play platform to integrate with existing fMRI device and obtain for the first time the hand and face representations for brain activities using SPA-skin. . We could *confirm* an overall classical somatotopic layout of the body in S1 region using SPA technology: The body regions where SPAs are placed and stimulated matches the expected somatotopic layout.

Our <u>exploratory</u> analysis suggested that for 3 out of 4 subjects were able to distinguish between the high and low amplitude stimulation applied via SPA technology, which effectively showed high activation level in the S1 region. To further zoom in on this effect we <u>explored activity</u> in the S1 hand area during thumb stimulation (the most sensitive body part tested, and also according to our participant subjective responses). We found significantly stronger activity during high amplitude thumb stimulation compared to low amplitude thumb stimulation. Our <u>exploratory</u> classification analysis further suggests differential patterns of activity during 5, 15, and 30 Hz stimulation applied using our SPA technology.(This doesn't allow to say something about the underlying physiology, it just tells us there is a difference in activity that could be based on spatial difference, activity levels etc.

The modular, adaptive and highly configurable nature of the soft actuator skin interface helped to extend the capabilities through it's augmented feedback while closing the tactile feedback loop with humans. The research led for following scientific contributions to the field:

[1] **Sonar, H. A.** , Huang, J.L. & Paik, J., "Soft Touch using SPA–Skin as a Wearable Haptic Feedback Device". *Advanced Intelligent Systems* , p. 2000168, 2021.

[2] Georgarakis, A. M., **Sonar, H. A.** , Rinderknecht, et al.,"Age-dependent asymmetry of wrist position sense Is not influenced by stochastic tactile stimulation", *Frontiers in human neuroscience* , 14, 65, 2020. *(Best PhD Paper Award, NCCR Robotics)*

[3] Kikkert, S., **Sonar, H. A.** , Freund, P., Paik, J., & Wenderoth, N., "Hand face somatotopy shown by MRI-safe vibrotactile stimulation with new soft pneumatic actuators", *In annual meetings, The Organization for Human Brain Mapping (OHBM)* , 2020

6.2 Future development

The future of robotics is soft, interactive and virtual. As the technology progressed and computing become ubiquitous so will the machines that we interact with in day to day life. The recent impact of COVID-19 pandemic have shown our reliance on virtual ways of living which, gives insights about need for such interactive interfaces spanning from assistive technologies, entertainment to at home rehabilitation scenario. I believe the foundational platforms I developed in terms of wearable hardware, software tools and control algorithm will fuel the upcoming progress in the field of wearable haptics in these directions

Specific future developments to the next generation of SPA-skin can be integration of sensing based on machine learning algorithms together with SPA actuation. The soft capacitive sensor skin we developed, has capacitance change in positive direction upon interaction and it will have a negative change upon inflation due to SPA-layers integrated in the foam structure. This will potentially enable a low cost and easy to manufacture solution for controlled vibratory actuation over a large surface area. Furthermore the sensing region is not only limited or coupled with the actuators anymore and can be used in double shift when actuators are inactive. Such interfaces would be ideally suited for the applications covering large surfaces like vehicle dash boards for an interactive tactile display being emerging based on the mode/application being used. Another addition, will be having multiple SPA-designs like bubble and ring actuator encircling each other to have a wider and more reliable feedback, it is also possible to have a two tone vibration similar to the one used in SPA-texture generation. The low frequency actuation can be delivered better by the bubble shaped SPA whereas high frequencies are better reproduced by the

In an effort to move towards, more portable solution, we have tried to incorporate a monolithic valve design using 3D printed AM based manufacturing techniques. Currently, we are still limited

by the off the shelf coil used to drive the PM. However, the 3 generation of rapid development within last 12 months showed a promising progress to have a fully integrated compliant valve mechanism that will be able to drive from wearable SPAs to other pneumatic flow control devices like insulin pumps, sleep apnea devices or portable massagers etc. One of the biggest advantages of such valves is the resin based monolithic nature that is completely airtight and is free from sealing components or moving mechanical assembly parts needed to be machined making them costly and bulky, not ideally suitable for wearable scenario.

Similarly, we used soft interactive interfaces to measure human somatosensory thresholds as well as measure of maximum information transfer rates or distances on locations like human fingers and forearm. Also, demonstrated multimodal texture and shape generation using SPA technology. There is plenty of room for further studies of multimodal perception with wearable soft haptic devices due to the customizability of both material properties and control frequencies. These preliminary studies open up discussion for the next generation of haptic feedback devices, which are not only mechanically transparent for human wearability but also provide ranges of tactile sensations inherent to the object and perceived by the human sense of touch.

References

[1]   R. Sigrist, G. Rauter, R. Riener, and P. Wolf, "Augmented visual, auditory, haptic, and multimodal feedback in motor learning: A review," *Psychon. Bull. Rev.*, vol. 20, no. 1, pp. 21–53, Feb. 2013, doi: 10.3758/s13423-012-0333-8.

[2]   E. P. Westebring-van der Putten, R. H. M. Goossens, J. J. Jakimowicz, and J. Dankelman, "Haptics in minimally invasive surgery--a review," *Minim. Invasive Ther. Allied Technol. MITAT Off. J. Soc. Minim. Invasive Ther.*, vol. 17, no. 1, pp. 3–16, 2008, doi: 10.1080/13645700701820242.

[3]   A. U. Alahakone and S. M. N. A. Senanayake, "Vibrotactile feedback systems: Current trends in rehabilitation, sports and information display," in *2009 IEEE/ASME International Conference on Advanced Intelligent Mechatronics*, Jul. 2009, pp. 1148–1153. doi: 10.1109/AIM.2009.5229741.

[4]   A. Bicchi *et al.*, "Physical human-robot interaction: Dependability, safety, and performance," in *2008 10th IEEE International Workshop on Advanced Motion Control*, Mar. 2008, pp. 9–14. doi: 10.1109/AMC.2008.4516033.

[5]   M. Laghi, M. G. Catalano, G. Grioli, and A. Bicchi, "A wearable wrist haptic display for motion tracking and force feedback in the operational space," *Wearable Technol.*, vol. 2, ed 2021, doi: 10.1017/wtc.2021.4.

[6]   P. Polygerinos *et al.*, "Towards a soft pneumatic glove for hand rehabilitation," in *2013 IEEE/RSJ International Conference on Intelligent Robots and Systems*, Nov. 2013, pp. 1512–1517. doi: 10.1109/IROS.2013.6696549.

[7]   Y. Mao and S. K. Agrawal, "Design of a Cable-Driven Arm Exoskeleton (CAREX) for Neural Rehabilitation," *IEEE Trans. Robot.*, vol. 28, no. 4, pp. 922–931, Aug. 2012, doi: 10.1109/TRO.2012.2189496.

[8]   H. Abidi and M. Cianchetti, "On Intrinsic Safety of Soft Robots," *Front. Robot. AI*, vol. 4, 2017, doi: 10.3389/frobt.2017.00005.

[9]   L. A. Jones, "Chapter 8 - Tactile communication systems: optimizing the display of information," in *Progress in Brain Research*, vol. 192, Elsevier, 2011, pp. 113–128. doi: 10.1016/B978-0-444-53355-5.00008-7.

[10]   R. W. Cholewiak and A. A. Collins, "Vibrotactile localization on the arm: Effects of place, space, and age," *Percept. Psychophys.*, vol. 65, no. 7, pp. 1058–1077, Oct. 2003, doi: 10.3758/BF03194834.

[11]   S. Yun, B. B. Kang, and K. Cho, "Exo-Glove PM: An Easily Customizable Modularized Pneumatic Assistive Glove," *IEEE Robot. Autom. Lett.*, vol. 2, no. 3, pp. 1725–1732, Jul. 2017, doi: 10.1109/LRA.2017.2678545.

[12]   J. C. Case, E. L. White, and R. K. Kramer, "Soft Material Characterization for Robotic Applications," *Soft Robot.*, vol. 2, no. 2, pp. 80–87, Jun. 2015, doi: 10.1089/soro.2015.0002.

[13]   P. Moseley, J. M. Florez, H. A. Sonar, G. Agarwal, W. Curtin, and J. Paik, "Modeling, Design, and Development of Soft Pneumatic Actuators with Finite Element Method," *Adv. Eng. Mater.*, vol. 18, no. 6, pp. 978–988, Jun. 2016, doi: 10.1002/adem.201500503.

[14]   "Soft Material Characterization for Robotic Applications | Soft Robotics." https://www.liebertpub.com/doi/abs/10.1089/soro.2015.0002 (accessed Oct. 09, 2018).

[15]   G. Cohen-Lazry, N. Katzman, A. Borowsky, and T. Oron-Gilad, "Directional tactile alerts for take-over requests in highly-automated driving," *Transp. Res. Part F Traffic Psychol. Behav.*, vol. 65, pp. 217–226, 2019, doi: 10.1016/j.trf.2019.07.025.

[16]   V. J. Barone, M. C. Yuen, R. Kramer-Boniglio, and K. H. Sienko, "Sensory garments with vibrotactile feedback for monitoring and informing seated posture," in *2019 2nd IEEE International Conference on Soft Robotics (RoboSoft)*, Apr. 2019, pp. 391–397. doi: 10.1109/ROBOSOFT.2019.8722795.

[17]   C. Cipriani, M. D'Alonzo, and M. C. Carrozza, "A Miniature Vibrotactile Sensory Substitution Device for Multifingered Hand Prosthetics," *IEEE Trans. Biomed. Eng.*, vol. 59, no. 2, pp. 400–408, Feb. 2012, doi: 10.1109/TBME.2011.2173342.

[18]   J. S. Schofield, K. R. Evans, J. P. Carey, and J. S. Hebert, "Applications of sensory feedback in motorized upper extremity prosthesis: a review," *Expert Rev. Med. Devices*, vol. 11, no. 5, pp. 499–511, Sep. 2014, doi: 10.1586/17434440.2014.929496.

[19]   V. Levesque, J. Pasquero, and V. Hayward, "Braille Display by Lateral Skin Deformation with the STReSS2 Tactile Transducer," in *Second Joint EuroHaptics Conference and Symposium on Haptic Interfaces for Virtual Environment and Teleoperator Systems (WHC'07)*, Mar. 2007, pp. 115–120. doi: 10.1109/WHC.2007.25.

[20]   J. Minogue and M. G. Jones, "Haptics in Education: Exploring an Untapped Sensory Modality," *Rev. Educ. Res.*, vol. 76, no. 3, pp. 317–348, Jan. 2006, doi: 10.3102/00346543076003317.

[21]   Vincent Hayward, Oliver R. Astley, Manuel Cruz-Hernandez, Danny Grant, and Gabriel Robles-De-La-Torre, "Haptic interfaces and devices," *Sens. Rev.*, vol. 24, no. 1, pp. 16–29, Mar. 2004, doi: 10.1108/02602280410515770.

[22]   "Vibration Motors | Precision Microdrives." https://www.precisionmicrodrives.com/vibration-motors (accessed May 11, 2017).

[23]   I. D. Johnston, D. K. McCluskey, C. K. L. Tan, and M. C. Tracey, "Mechanical characterization of bulk Sylgard 184 for microfluidics and microengineering," *J. Micromechanics Microengineering*, vol. 24, no. 3, p. 035017, 2014, doi: 10.1088/0960-1317/24/3/035017.

[24]   "Ecoflex® 00-30 Product Information," *Smooth-On, Inc.* https://www.smooth-on.com/products/ecoflex-00-30/ (accessed May 11, 2017).

[25]   S. Diridollou *et al.*, "In vivo model of the mechanical properties of the human skin under suction," *Skin Res. Technol.*, vol. 6, no. 4, pp. 214–221, doi: 10.1034/j.1600-0846.2000.006004214.x.

[26]   G. Alici, "Softer is Harder: What Differentiates Soft Robotics from Hard Robotics?," *MRS Adv.*, vol. 3, no. 28, pp. 1557–1568, ed 2018, doi: 10.1557/adv.2018.159.

[27]   S. Choi and K. J. Kuchenbecker, "Vibrotactile Display: Perception, Technology, and Applications," *Proc. IEEE*, vol. 101, no. 9, pp. 2093–2104, Sep. 2013, doi: 10.1109/JPROC.2012.2221071.

[28]   S. Bauer, S. Bauer-Gogonea, I. Graz, M. Kaltenbrunner, C. Keplinger, and R. Schwödiauer, "25th Anniversary Article: A Soft Future: From Robots and Sensor Skin to Energy Harvesters," *Adv. Mater.*, vol. 26, no. 1, pp. 149–162, Jan. 2014, doi: 10.1002/adma.201303349.

[29]   E. W. Hawkes, L. H. Blumenschein, J. D. Greer, and A. M. Okamura, "A soft robot that navigates its environment through growth," *Sci. Robot.*, vol. 2, no. 8, p. eaan3028, Jul. 2017, doi: 10.1126/scirobotics.aan3028.

[30]   P. Polygerinos *et al.*, "Soft Robotics: Review of Fluid-Driven Intrinsically Soft Devices; Manufacturing, Sensing, Control, and Applications in Human-Robot Interaction," *Adv. Eng. Mater.*, vol. 19, no. 12, p. 1700016, Dec. 2017, doi: 10.1002/adem.201700016.

[31]   M. Cianchetti, C. Laschi, A. Menciassi, and P. Dario, "Biomedical applications of soft robotics," *Nat. Rev. Mater.*, vol. 3, no. 6, p. 143, Jun. 2018, doi: 10.1038/s41578-018-0022-y.

[32]   N. Agharese *et al.*, "HapWRAP: Soft Growing Wearable Haptic Device," in *2018 IEEE International Conference on Robotics and Automation (ICRA)*, May 2018, pp. 1–5. doi: 10.1109/ICRA.2018.8460891.

[33]   H. Phung *et al.*, "Tactile display with rigid coupling based on soft actuator," *Meccanica*, vol. 50, no. 11, pp. 2825–2837, Nov. 2015, doi: 10.1007/s11012-015-0270-5.

[34]   A. Marette, A. Poulin, N. Besse, S. Rosset, D. Briand, and H. Shea, "Flexible Zinc–Tin Oxide Thin Film Transistors Operating at 1 kV for Integrated Switching of Dielectric Elastomer Actuators Arrays," *Adv. Mater.*, vol. 29, no. 30, p. 1700880, Aug. 2017, doi: 10.1002/adma.201700880.

[35]   R. Hinchet, V. Vechev, H. Shea, and O. Hilliges, "DextrES: Wearable Haptic Feedback for Grasping in VR via a Thin Form-Factor Electrostatic Brake," in *The 31st Annual ACM Symposium on User Interface Software and Technology - UIST '18*, Berlin, Germany, 2018, pp. 901–912. doi: 10.1145/3242587.3242657.

[36]   "Multimode Hydraulically Amplified Electrostatic Actuators for Wearable Haptics - Leroy - 2020 - Advanced Materials - Wiley Online Library." https://onlinelibrary.wiley.com/doi/10.1002/adma.202002564 (accessed May 17, 2021).

[37]   G. Agarwal, N. Besuchet, B. Audergon, and J. Paik, "Stretchable Materials for Robust Soft Actuators towards Assistive Wearable Devices," *Sci. Rep.*, vol. 6, Sep. 2016, doi: 10.1038/srep34224.

[38]   R. V. Martinez, A. C. Glavan, C. Keplinger, A. I. Oyetibo, and G. M. Whitesides, "Soft Actuators and Robots that Are Resistant to Mechanical Damage," *Adv. Funct. Mater.*, vol. 24, no. 20, pp. 3003–3010, May 2014, doi: 10.1002/adfm.201303676.

[39]   B. Mosadegh *et al.*, "Pneumatic Networks for Soft Robotics that Actuate Rapidly," *Adv. Funct. Mater.*, vol. 24, no. 15, pp. 2163–2170, Apr. 2014, doi: 10.1002/adfm.201303288.

[40]   M. A. Robertson and J. Paik, "New soft robots really suck: Vacuum-powered systems empower diverse capabilities," *Sci. Robot.*, vol. 2, no. 9, p. eaan6357, Aug. 2017, doi: 10.1126/scirobotics.aan6357.

[41] C. Larson *et al.*, "Highly stretchable electroluminescent skin for optical signaling and tactile sensing," *Science*, vol. 351, no. 6277, pp. 1071–1074, Mar. 2016, doi: 10.1126/science.aac5082.

[42] J. Shintake, H. Sonar, E. Piskarev, J. Paik, and D. Floreano, "Soft pneumatic gelatin actuator for edible robotics," in *2017 IEEE/RSJ International Conference on Intelligent Robots and Systems (IROS)*, Sep. 2017, pp. 6221–6226. doi: 10.1109/IROS.2017.8206525.

[43] D. Rus and M. T. Tolley, "Design, fabrication and control of soft robots," *Nature*, vol. 521, no. 7553, pp. 467–475, May 2015, doi: 10.1038/nature14543.

[44] M. Morioka, D. J. Whitehouse, and M. J. Griffin, "Vibrotactile thresholds at the fingertip, volar forearm, large toe, and heel," *Somatosens. Mot. Res.*, vol. 25, no. 2, pp. 101–112, Jan. 2008, doi: 10.1080/08990220802045574.

[45] I. Choi, H. Culbertson, M. R. Miller, A. Olwal, and S. Follmer, "Grabity: A Wearable Haptic Interface for Simulating Weight and Grasping in Virtual Reality," New York, NY, USA, 2017, pp. 119–130. doi: 10.1145/3126594.3126599.

[46] T. Q. Trung and N. Lee, "Flexible and Stretchable Physical Sensor Integrated Platforms for Wearable Human-Activity Monitoringand Personal Healthcare," *Adv. Mater.*, 2016.

[47] A. Hirsch, H. O. Michaud, A. P. Gerratt, S. de Mulatier, and S. P. Lacour, "Intrinsically Stretchable Biphasic (Solid–Liquid) Thin Metal Films," *Adv. Mater.*, vol. 28, no. 22, pp. 4507–4512, Jun. 2016, doi: 10.1002/adma.201506234.

[48] S. Nam *et al.*, "A Robust Soft Lens for Tunable Camera Application Using Dielectric Elastomer Actuators," *Soft Robot.*, Aug. 2018, doi: 10.1089/soro.2017.0146.

[49] H. Mößinger, H. Haus, M. Kauer, and H. F. Schlaak, "Tactile feedback to the palm using arbitrarily shaped DEA," Mar. 2014, vol. 9056, p. 90563C. doi: 10.1117/12.2045302.

[50] R. L. Truby *et al.*, "Soft Somatosensitive Actuators via Embedded 3D Printing," *Adv. Mater.*, 2018, doi: 10.1002/adma.201706383.

[51] C. E. Sherrick and R. Rogers, "Apparent haptic movement," *Percept. Psychophys.*, vol. 1, no. 3, pp. 175–180, May 1966, doi: 10.3758/BF03210054.

[52] Roger W Cholewiak, "The Perception of Tactile Distance: Influences of Body Site, Space, and Time," *Perception*, vol. 28, no. 7, pp. 851–875, Jul. 1999, doi: 10.1068/p2873.

[53] J. Nasir, B. Bruno, M. Chetouani, and P. Dillenbourg, "What if Social Robots Look for Productive Engagement?," *Int. J. Soc. Robot.*, Mar. 2021, doi: 10.1007/s12369-021-00766-w.

[54] H. A. Sonar and J. Paik, "Soft Pneumatic Actuator Skin with Piezoelectric Sensors for Vibrotactile Feedback," *Front. Robot. AI*, vol. 2, 2016, doi: 10.3389/frobt.2015.00038.

[55] H. A. Sonar, A. P. Gerratt, S. P. Lacour, and J. Paik, "Closed-loop haptic feedback control using a self-sensing soft pneumatic actuator skin," *Soft Robot.*, vol. 7, no. 1, pp. 22–29, 2020.

[56] H. A. Sonar, M. C. Yuen, R. Kramer-Bottiglio, and J. Paik, "An any-resolution pressure localization scheme using a soft capacitive sensor skin," in *2018 IEEE International Conference on Soft Robotics (RoboSoft)*, Apr. 2018, pp. 170–175. doi: 10.1109/ROBOSOFT.2018.8404915.

[57] P. Moseley, J. M. Florez, H. A. Sonar, G. Agarwal, W. Curtin, and J. Paik, "Modeling, Design, and Development of Soft Pneumatic Actuators with Finite Element Method," *Adv. Eng. Mater.*, vol. 18, no. 6, pp. 978–988, Jun. 2016, doi: 10.1002/adem.201500503.

[58] G. Agarwal, M. A. Robertson, H. Sonar, and J. Paik, "Design and Computational Modeling of a Modular, Compliant Robotic Assembly for Human Lumbar Unit and Spinal Cord Assistance," *Sci. Rep.*, vol. 7, no. 1, Art. no. 1, Oct. 2017, doi: 10.1038/s41598-017-14220-3.

[59] M. Hirose *et al.*, "HapticGEAR: the development of a wearable force display system for immersive projection displays," in *Virtual Reality, 2001. Proceedings. IEEE*, Yokohama, Japan, 2001, pp. 123–129.

[60] E. J. Shahoian, K. M. Martin, B. M. Schena, and D. F. Moore, *Vibrotactile haptic feedback devices*. Google Patents, 2004. [Online]. Available: http://www.google.com/patents/US6693622

[61] A. Viau, A. G. Feldman, B. J. McFadyen, and M. F. Levin, "Journal of NeuroEngineering and Rehabilitation," *J. Neuroengineering Rehabil.*, vol. 1, p. 11, 2004.

[62] T. Yoshioka and J. Zhou, "Factors Involved in Tactile Texture Perception Through Probes," *Adv. Robot.*, vol. 23, no. 6, pp. 747–766, Jan. 2009, doi: 10.1163/156855309X431703.

[63] R. W. Lindeman, R. Page, Y. Yanagida, and J. L. Sibert, "Towards Full-body Haptic Feedback: The Design and Deployment of a Spatialized Vibrotactile Feedback System," New York, NY, USA, 2004, pp. 146–149. doi: 10.1145/1077534.1077562.

[64] B. J. Mortimer, G. A. Zets, and R. W. Cholewiak, "Vibrotactile transduction and transducers," *J. Acoust. Soc. Am.*, vol. 121, no. 5, pp. 2970–2977, 2007.

[65] E. Leroy and H. R. Shea, "EAP-in-Action: HAXELS: Hydraulically amplified mm-scale actuators for wearable haptics," in *Electroactive Polymer Actuators and Devices (EAPAD) XXIII*, Mar. 2021, vol. 11587, p. 115870C. doi: 10.1117/12.2587094.

[66] J.-H. Youn, H. Mun, and K.-U. Kyung, "A Wearable Soft Tactile Actuator With High Output Force for Fingertip Interaction," *IEEE Access*, vol. 9, pp. 30206–30215, 2021, doi: 10.1109/AC-CESS.2021.3058979.

[67] "Flexible Active Skin: Large Reconfigurable Arrays of Individually Addressed Shape Memory Polymer Actuators - Besse - 2017 - Advanced Materials Technologies - Wiley Online Library." http://onlinelibrary.wiley.com/doi/10.1002/admt.201700102/abstract (accessed Jan. 15, 2018).

[68] T. Hulin, P. Kremer, R. Scheibe, S. Schaetzle, and C. Preusche, "Evaluating Two Novel Tactile Feedback Devices," presented at the 4th International Conference on Enactive Interfaces, Grenoble, France, Nov. 2007. Accessed: Jul. 13, 2021. [Online]. Available: https://elib.dlr.de/52949/

[69] M. Wehner *et al.*, "A lightweight soft exosuit for gait assistance," in *Robotics and Automation (ICRA), 2013 IEEE International Conference on*, 2013, pp. 3362–3369.

[70] G. Frediani, H. Boys, S. Poslad, and F. Carpi, "Enabling Wearable Soft Tactile Displays with Electroactive Smart Elastomers," in *Haptics: Perception, Devices, Control, and Applications*, Jul. 2016, pp. 326–334. doi: 10.1007/978-3-319-42324-1_32.

[71] N. Asamura, T. Shinohara, Y. Tojo, N. Koshida, and H. Shinoda, "Necessary spatial resolution for realistic tactile feeling display," in *IEEE International Conference on Robotics and Automation, 2001. Proceedings 2001 ICRA.*, Seoul, South Korea, May 2001, vol. 2, pp. 1851–1856. doi: 10.1109/RO-BOT.2001.932878.

[72] K. Kaczmarek, J. G. Webster, P. Bach-y-Rita, W. J. Tompkins, and others, "Electrotactile and vibrotactile displays for sensory substitution systems," *Biomed. Eng. IEEE Trans. On*, vol. 38, no. 1, pp. 1–16, 1991.

[73] C. Suh, J. C. Margarit, Y. S. Song, and J. Paik, "Soft Pneumatic Actuator skin with embedded sensors," in *2014 IEEE/RSJ International Conference on Intelligent Robots and Systems*, Sep. 2014, pp. 2783–2788. doi: 10.1109/IROS.2014.6942943.

[74] M. Acer, M. Salerno, K. Agbeviade, and J. Paik, "Development and characterization of silicone embedded distributed piezoelectric sensors for contact detection," *Smart Mater. Struct.*, vol. 24, no. 7, p. 075030, 2015, doi: 10.1088/0964-1726/24/7/075030.

[75] S. Rosset, B. M. O'Brien, T. Gisby, D. Xu, H. R. Shea, and I. A. Anderson, "Self-sensing dielectric elastomer actuators in closed-loop operation," *Smart Mater. Struct.*, vol. 22, no. 10, p. 104018, 2013.

[76] P. Maiolino, F. Galantini, F. Mastrogiovanni, G. Gallone, G. Cannata, and F. Carpi, "Soft dielectrics for capacitive sensing in robot skins: Performance of different elastomer types," *Sens. Actuators Phys.*, vol. 226, pp. 37–47, 2015, doi: http://dx.doi.org/10.1016/j.sna.2015.02.010.

[77] A. P. Gerratt, H. O. Michaud, and S. P. Lacour, "Elastomeric Electronic Skin for Prosthetic Tactile Sensation," *Adv Funct Mater*, vol. 25, no. 15, pp. 2287–2295, Apr. 2015, doi: 10.1002/adfm.201404365.

[78] S. Xu *et al.*, "Soft microfluidic assemblies of sensors, circuits, and radios for the skin," *Science*, vol. 344, no. 6179, pp. 70–74, 2014.

[79] D. Damjanovic, "Stress and frequency dependence of the direct piezoelectric effect in ferroelectric ceramics," *J. Appl. Phys.*, vol. 82, no. 4, pp. 1788–1797, 1997.

[80] D. Hall, "Review nonlinearity in piezoelectric ceramics," *J. Mater. Sci.*, vol. 36, no. 19, pp. 4575–4601, 2001.

[81] J. Zhao and Q. M. Zhang, "Effect of mechanical stress on the electromechanical performance of PZT and PMN-PT ceramics," in *Applications of Ferroelectrics, 1996. ISAF '96., Proceedings of the Tenth IEEE International Symposium on*, East Brunswick, NJ, Aug. 1996, vol. 2, pp. 971–974 vol.2. doi: 10.1109/ISAF.1996.598190.

[82] O. Lambercy, L. Dovat, R. Gassert, E. Burdet, C. L. Teo, and T. Milner, "A haptic knob for rehabilitation of hand function," *Neural Syst. Rehabil. Eng. IEEE Trans. On*, vol. 15, no. 3, pp. 356–366, 2007.

[83] B. J. P. Mortimer, G. A. Zets, and R. W. Cholewiak, "Vibrotactile transduction and transducers," *J. Acoust. Soc. Am.*, vol. 121, no. 5, pp. 2970–2977, May 2007, doi: 10.1121/1.2715669.

[84] K. A. Kaczmarek, J. G. Webster, P. Bach-y-Rita, and W. J. Tompkins, "Electrotactile and vibrotactile displays for sensory substitution systems," *IEEE Trans. Biomed. Eng.*, vol. 38, no. 1, pp. 1–16, Jan. 1991, doi: 10.1109/10.68204.

[85] F. Schneider, U. Wallrabe, T. Fellner, and J. Wilde, "Mechanical properties of silicones for MEMS," *J. Micromechanics Microengineering Struct. Devices Syst.*, vol. 18, no. 6, 2008, doi: 10.1088/0960-1317/18/6/065008.

[86] "Soft Robotics: Biological Inspiration, State of the Art, and Future Research." https://www.hindawi.com/journals/abb/2008/520417/ (accessed May 22, 2021).

[87] "Exotic materials for bio-organic electronics - Journal of Materials Chemistry (RSC Publishing)." https://pubs.rsc.org/en/content/articlelanding/2011/JM/c0jm02444a#!divAbstract (accessed May 22, 2021).

[88] M. Irimia-Vladu *et al.*, "Biocompatible and Biodegradable Materials for Organic Field-Effect Transistors," *Adv. Funct. Mater.*, vol. 20, no. 23, pp. 4069–4076, 2010, doi: https://doi.org/10.1002/adfm.201001031.

[89] H. Tao *et al.*, "Silk-based conformal, adhesive, edible food sensors," *Adv. Mater.*, vol. 24, no. 8, pp. 1067–1072, Feb. 2012, doi: 10.1002/adma.201103814.

[90] Y. J. Kim, S.-E. Chun, J. Whitacre, and C. J. Bettinger, "Self-deployable current sources fabricated from edible materials," *J. Mater. Chem. B*, vol. 1, no. 31, pp. 3781–3788, Jul. 2013, doi: 10.1039/C3TB20183J.

[91] "3D Printed Edible Hydrogel Electrodes | SpringerLink." https://link.springer.com/article/10.1557/adv.2015.10 (accessed May 22, 2021).

[92] X. Wang *et al.*, "Food-Materials-Based Edible Supercapacitors," *Adv. Mater. Technol.*, vol. 1, no. 3, p. 1600059, Jun. 2016, doi: 10.1002/admt.201600059.

[93] I. Ieropoulos, L. D. Chambers, J. Winfield, I. Ieropoulos, and J. Rossiter, "Biodegradable and edible gelatine actuators for use as artificial muscles," *Proc. SPIE*, vol. 9056, Jan. 2014, doi: 10.1117/12.2045104.

[94] "Here today, gone tomorrow: biodegradable soft robots." https://proceedings.spiedigitallibrary.org/conference-proceedings-of-spie/9798/97981S/Here-today-gone-tomorrow-biodegradable-soft-robots/10.1117/12.2220611.short?SSO=1 (accessed May 22, 2021).

[95] S. Miyashita, S. Guitron, K. Yoshida, Shuguang Li, D. D. Damian, and D. Rus, "Ingestible, controllable, and degradable origami robot for patching stomach wounds," in *2016 IEEE International Conference on Robotics and Automation (ICRA)*, Stockholm, Sweden, May 2016, pp. 909–916. doi: 10.1109/ICRA.2016.7487222.

[96] P. Bergo and P. J. A. Sobral, "Effects of plasticizer on physical properties of pigskin gelatin films," *Food Hydrocoll.*, vol. 21, no. 8, pp. 1285–1289, Dec. 2007, doi: 10.1016/j.foodhyd.2006.09.014.

[97] "ASTM D412 - 16e1 Standard Test Methods for Vulcanized Rubber and Thermoplastic Elastomers—Tension." https://www.astm.org/Standards/D412 (accessed May 22, 2021).

[98] Y.-L. Park, C. Majidi, R. Kramer, P. Bérard, and R. J. Wood, "Hyperelastic pressure sensing with a liquid-embedded elastomer," *J. Micromechanics Microengineering*, vol. 20, no. 12, p. 125029, 2010, doi: 10.1088/0960-1317/20/12/125029.

[99] I. D. Johnston, D. K. McCluskey, C. K. L. Tan, and M. C. Tracey, "Mechanical characterization of bulk Sylgard 184 for microfluidics and microengineering," *J. Micromechanics Microengineering*, vol. 24, no. 3, p. 035017, 2014.

[100] "Ecoflex™ 00-30 Product Information," *Smooth-On, Inc.* https://www.smooth-on.com/products/ecoflex-00-30/ (accessed May 22, 2021).

[101] K. Ogura, S. Wakimoto, K. Suzumori, and Y. Nishioka, "Micro pneumatic curling actuator - Nematode actuator -," in *2008 IEEE International Conference on Robotics and Biomimetics*, Feb. 2009, pp. 462–467. doi: 10.1109/ROBIO.2009.4913047.

[102] B. Marelli, M. A. Brenckle, D. L. Kaplan, and F. G. Omenetto, "Silk Fibroin as Edible Coating for Perishable Food Preservation," *Sci. Rep.*, vol. 6, no. 1, Art. no. 1, May 2016, doi: 10.1038/srep25263.

[103] I. S. Arvanitoyannis, A. Nakayama, and S. Aiba, "Chitosan and gelatin based edible films: state diagrams, mechanical and permeation properties," *Carbohydr. Polym.*, vol. 37, no. 4, pp. 371–382, Dec. 1998, doi: 10.1016/S0144-8617(98)00083-6.

[104] V. Cacucciolo, F. Renda, E. Poccia, C. Laschi, and M. Cianchetti, "Modelling the Nonlinear Response of Fibre-reinforced Bending Fluidic Actuators," *Smart Mater. Struct.*, vol. 25, May 2016, doi: 10.1088/0964-1726/25/10/105020.

[105] J. Krause, A. F. T. Winfield, and J.-L. Deneubourg, "Interactive robots in experimental biology," *Trends Ecol. Evol.*, vol. 26, no. 7, pp. 369–375, Jul. 2011, doi: 10.1016/j.tree.2011.03.015.

[106] "Towards High Power High Energy Aqueous Sodium-Ion Batteries: The NaTi2(PO4)3/Na0.44MnO2 System - Li - 2013 - Advanced Energy Materials - Wiley Online Library." https://onlinelibrary.wiley.com/doi/abs/10.1002/aenm.201200598 (accessed May 22, 2021).

[107] Y. J. Kim, W. Wu, S.-E. Chun, J. F. Whitacre, and C. J. Bettinger, "Biologically derived melanin electrodes in aqueous sodium-ion energy storage devices," *Proc. Natl. Acad. Sci. U. S. A.*, vol. 110, no. 52, pp. 20912–20917, Dec. 2013, doi: 10.1073/pnas.1314345110.

[108] W. Wu, A. Mohamed, and J. Whitacre, "Microwave Synthesized NaTi2(PO4)3 as an Aqueous Sodium-Ion Negative Electrode," *J. Electrochem. Soc.*, vol. 160, pp. A497–A504, Jan. 2013, doi: 10.1149/2.054303jes.

[109] "Autophagy in Octopus: South African Journal of Marine Science: Vol 20, No 1." https://www.tandfonline.com/doi/abs/10.2989/025776198784126502 (accessed May 22, 2021).

[110] M.-Y. Cheng, C.-M. Tsao, Y.-Z. Lai, and Y.-J. Yang, "The development of a highly twistable tactile sensing array with stretchable helical electrodes," *Sens. Actuators Phys.*, vol. 166, no. 2, pp. 226–233, Apr. 2011, doi: 10.1016/j.sna.2009.12.009.

[111] J. Engel, J. Chen, and C. Liu, "Development of polyimide flexible tactile sensor skin," *J Micromech Microeng*, vol. 13, no. 3, p. 359, 2003, doi: 10.1088/0960-1317/13/3/302.

[112] M. Knite, V. Teteris, A. Kiploka, and J. Kaupuzs, "Polyisoprene-carbon black nanocomposites as tensile strain and pressure sensor materials," *Sens. Actuators Phys.*, vol. 110, no. 1, pp. 142–149, Feb. 2004, doi: 10.1016/j.sna.2003.08.006.

[113] R. K. Kramer, C. Majidi, and R. J. Wood, "Wearable tactile keypad with stretchable artificial skin," in *Robotics and Automation (ICRA), 2011 IEEE International Conference on*, 2011, pp. 1103–1107.

[114] F. L. Hammond, Y. Meng��, and R. J. Wood, "Toward a modular soft sensor-embedded glove for human hand motion and tactile pressure measurement," in *2014 IEEE/RSJ International Conference on Intelligent Robots and Systems*, Sep. 2014, pp. 4000–4007. doi: 10.1109/IROS.2014.6943125.

[115] K. Noda, E. Iwase, K. Matsumoto, and I. Shimoyama, "Stretchable liquid tactile sensor for robot-joints," in *2010 IEEE International Conference on Robotics and Automation*, May 2010, pp. 4212–4217. doi: 10.1109/ROBOT.2010.5509301.

[116] B.-Y. Lee, J. Kim, H. Kim, C. Kim, and S.-D. Lee, "Low-cost flexible pressure sensor based on dielectric elastomer film with micro-pores," *Sens. Actuators Phys.*, vol. 240, pp. 103–109, Apr. 2016, doi: 10.1016/j.sna.2016.01.037.

[117] H. Vandeparre, D. Watson, and S. P. Lacour, "Extremely robust and conformable capacitive pressure sensors based on flexible polyurethane foams and stretchable metallization," *Appl Phys Lett*, vol. 103, no. 20, p. 204103, Nov. 2013, doi: 10.1063/1.4832416.

[118] S. C. B. Mannsfeld *et al.*, "Highly sensitive flexible pressure sensors with microstructured rubber dielectric layers," *Nat Mater*, vol. 9, no. 10, pp. 859–864, Oct. 2010, doi: 10.1038/nmat2834.

[119] R. D. Ponce Wong, J. D. Posner, and V. J. Santos, "Flexible microfluidic normal force sensor skin for tactile feedback," *Sens. Actuators Phys.*, vol. 179, pp. 62–69, Jun. 2012, doi: 10.1016/j.sna.2012.03.023.

[120] P. Roberts, D. D. Damian, W. Shan, T. Lu, and C. Majidi, "Soft-matter capacitive sensor for measuring shear and pressure deformation," in *2013 IEEE International Conference on Robotics and Automation (ICRA)*, May 2013, pp. 3529–3534. doi: 10.1109/ICRA.2013.6631071.

[121] C. Larson, J. Spjut, R. Knepper, and R. Shepherd, "OrbTouch: Recognizing Human Touch in Deformable Interfaces with Deep Neural Networks," *ArXiv170602542 Cs Stat*, Jun. 2017.

[122] D. Kwon *et al.*, "Highly Sensitive, Flexible and Wearable Pressure Sensor Based on a Giant Piezocapacitive Effect of Three-Dimensional Microporous Elastomeric Dielectric Layer," *ACS Appl. Mater. Interfaces*, Jun. 2016, doi: 10.1021/acsami.6b04225.

[123] J. Luo, F. R. Fan, T. Zhou, W. Tang, F. Xue, and Z. L. Wang, "Ultrasensitive self-powered pressure sensing system," *Extreme Mech. Lett.*, doi: 10.1016/j.eml.2015.01.008.

[124] S. Yao and Y. Zhu, "Wearable multifunctional sensors using printed stretchable conductors made of silver nanowires," *Nanoscale*, vol. 6, no. 4, pp. 2345–2352, Jan. 2014, doi: 10.1039/C3NR05496A.

[125] O. Atalay, A. Atalay, J. Gafford, and C. Walsh, "A Highly Sensitive Capacitive-Based Soft Pressure Sensor Based on a Conductive Fabric and a Microporous Dielectric Layer," *Adv. Mater. Technol.*, p. 1700237, Nov. 2017, doi: 10.1002/admt.201700237.

[126] N. Farrow, L. McIntire, and N. Correll, "Functionalized textiles for interactive soft robotics," in *2017 IEEE International Conference on Robotics and Automation (ICRA)*, May 2017, pp. 5525–5531. doi: 10.1109/ICRA.2017.7989651.

[127] J. Lee *et al.*, "Conductive Fiber-Based Ultrasensitive Textile Pressure Sensor for Wearable Electronics," *Adv Mater*, vol. 27, no. 15, pp. 2433–2439, Apr. 2015, doi: 10.1002/adma.201500009.

[128] C. Larson *et al.*, "Highly stretchable electroluminescent skin for optical signaling and tactile sensing," *Science*, vol. 351, no. 6277, pp. 1071–1074, Mar. 2016, doi: 10.1126/science.aac5082.

[129] D. J. Lipomi *et al.*, "Skin-like pressure and strain sensors based on transparent elastic films of carbon nanotubes," *Nat. Nanotechnol.*, vol. 6, no. 12, p. 788, Dec. 2011, doi: 10.1038/nnano.2011.184.

[130] D. Xu, A. Tairych, and I. A. Anderson, "Stretch not flex: programmable rubber keyboard," *Smart Mater Struct*, vol. 25, no. 1, p. 015012, 2016, doi: 10.1088/0964-1726/25/1/015012.

[131] D. Xu, A. Tairych, and I. A. Anderson, "Where the rubber meets the hand: Unlocking the sensing potential of dielectric elastomers," *J Polym Sci Part B Polym Phys*, no. 4, pp. 465–472, Feb. 2016.

[132] E. L. White, M. C. Yuen, and R. K. Kramer, "Distributed Sensing in Capacitive Conductive Composites," 2017.

[133] E. L. White, M. C. Yuen, J. C. Case, and R. K. Kramer, "Low-Cost, Facile, and Scalable Manufacturing of Capacitive Sensors for Soft Systems," *Adv Mater Technol*, vol. 2, no. 9, p. n/a-n/a, Sep. 2017, doi: 10.1002/admt.201700072.

[134] H. Meng *et al.*, "A transmission line model for high-frequency power line communication channel," in *Proceedings. International Conference on Power System Technology*, 2002, vol. 2, pp. 1290–1295 vol.2. doi: 10.1109/ICPST.2002.1047610.

[135] M. A. Hearst, S. T. Dumais, E. Osuna, J. Platt, and B. Scholkopf, "Support vector machines," *IEEE Intell. Syst. Their Appl.*, vol. 13, no. 4, pp. 18–28, Jul. 1998, doi: 10.1109/5254.708428.

[136] J. Weston and C. Watkins, "Multi-class support vector machines," Technical Report CSD-TR-98-04, Department of Computer Science, Royal Holloway, University of London, May, 1998.

[137] E. Kelasidi, G. Andrikopoulos, G. Nikolakopoulos, and S. Manesis, "A survey on pneumatic muscle actuators modeling," in *2011 IEEE International Symposium on Industrial Electronics*, Jun. 2011, pp. 1263–1269. doi: 10.1109/ISIE.2011.5984340.

[138] B. Verrelst, F. Daerden, D. Lefeber, R. V. Ham, and T. Fabri, "Pleated pneumatic artificial muscles: actuators for automation and robotics," in *in IEEE/ASME International Conference on Advanced Intelligent Mechatronics*, 2001, pp. 738–743.

[139] F. Ilievski, A. D. Mazzeo, R. F. Shepherd, X. Chen, and G. M. Whitesides, "Soft Robotics for Chemists," *Angew. Chem.*, vol. 123, no. 8, pp. 1930–1935, 2011, doi: https://doi.org/10.1002/ange.201006464.

[140] Y. Sun, Y. S. Song, and J. Paik, "Characterization of silicone rubber based soft pneumatic actuators," in *2013 IEEE/RSJ International Conference on Intelligent Robots and Systems*, Nov. 2013, pp. 4446–4453. doi: 10.1109/IROS.2013.6696995.

[141] R. Deimel and O. Brock, "Soft Hands for Reliable Grasping Strategies," in *Soft Robotics*, Berlin, Heidelberg, 2015, pp. 211–221. doi: 10.1007/978-3-662-44506-8_18.

[142] P. Polygerinos *et al.*, "Modeling of Soft Fiber-Reinforced Bending Actuators," *IEEE Trans. Robot.*, vol. 31, no. 3, pp. 778–789, Jun. 2015, doi: 10.1109/TRO.2015.2428504.

[143] H. Lipson, "Challenges and Opportunities for Design, Simulation, and Fabrication of Soft Robots," *Soft Robot.*, vol. 1, no. 1, pp. 21–27, Jul. 2013, doi: 10.1089/soro.2013.0007.

[144] K. Suzumori, S. Endo, T. Kanda, N. Kato, and H. Suzuki, "A Bending Pneumatic Rubber Actuator Realizing Soft-bodied Manta Swimming Robot," in *Proceedings 2007 IEEE International Conference on Robotics and Automation*, Apr. 2007, pp. 4975–4980. doi: 10.1109/ROBOT.2007.364246.

[145] G. Udupa, S. S. Rao, and K. V. Gangadharan, "Functionally Graded Composite Materials: An Overview," *Procedia Mater. Sci.*, vol. 5, pp. 1291–1299, Jan. 2014, doi: 10.1016/j.mspro.2014.07.442.

[146] E. T. Roche *et al.*, "A Bioinspired Soft Actuated Material," *Adv. Mater.*, vol. 26, no. 8, pp. 1200–1206, 2014, doi: https://doi.org/10.1002/adma.201304018.

[147] B. Mosadegh *et al.*, "Pneumatic networks for soft robotics that actuate rapidly," *Adv. Funct. Mater.*, vol. 24, no. 15, pp. 2163–2170, Apr. 2014, doi: 10.1002/adfm.201303288.

[148] F. Connolly, P. Polygerinos, C. J. Walsh, and K. Bertoldi, "Mechanical Programming of Soft Actuators by Varying Fiber Angle," *Soft Robot.*, vol. 2, no. 1, pp. 26–32, 2015.

[149] J. M. Florez, B. Shih, Y. Bai, and J. K. Paik, "Soft pneumatic actuators for legged locomotion," in *2014 IEEE International Conference on Robotics and Biomimetics (ROBIO 2014)*, Dec. 2014, pp. 27–34. doi: 10.1109/ROBIO.2014.7090302.

[150] O. Yeoh, "Some forms of the strain energy function for rubber," *Rubber Chem. Technol.*, vol. 66, no. 5, pp. 754–771, 1993.

[151] R. Ogden, "Large deformation isotropic elasticity-on the correlation of theory and experiment for incompressible rubberlike solids," 1972, vol. 326, pp. 565–584.

[152] R. S. Rivlin, D. W. Saunders, and E. N. D. C. Andrade, "Large elastic deformations of isotropic materials VII. Experiments on the deformation of rubber," *Philos. Trans. R. Soc. Lond. Ser. Math. Phys. Sci.*, vol. 243, no. 865, pp. 251–288, Apr. 1951, doi: 10.1098/rsta.1951.0004.

[153] "A Comparative Study of Several Material Models for Prediction of Hyperelastic Properties: Application to Silicone-Rubber and Soft Tissues - Martins - 2006 - Strain - Wiley Online Library." https://onlinelibrary.wiley.com/doi/full/10.1111/j.1475-1305.2006.00257.x?casa_token=_UTN61DkhtoAAAAA%3Apyk7Tcob3WIM1n2cggGhBRcCUNw6xJnx0t-vLfHOcAnouzMsiYbDA-CfVX0knLFEMKWMwERmpzu7YJ38 (accessed May 21, 2021).

[154] E. M. Arruda and M. C. Boyce, "A three-dimensional constitutive model for the large stretch behavior of rubber elastic materials," *J. Mech. Phys. Solids*, vol. 41, no. 2, pp. 389–412, Feb. 1993, doi: 10.1016/0022-5096(93)90013-6.

[155] H.-G. Kilian, H. F. Enderle, and K. Unseld, "The use of the van der Waals model to elucidate universal aspects of structure-property relationships in simply extended dry and swollen rubbers," *Colloid Polym. Sci.*, vol. 264, no. 10, pp. 866–876, Oct. 1986, doi: 10.1007/BF01410637.

[156] Y. Elsayed *et al.*, "Finite Element Analysis and Design Optimization of a Pneumatically Actuating Silicone Module for Robotic Surgery Applications," *Soft Robot.*, vol. 1, no. 4, pp. 255–262, Oct. 2014, doi: 10.1089/soro.2014.0016.

[157] R. W. Ogden, G. Saccomandi, and I. Sgura, "Fitting hyperelastic models to experimental data," *Comput. Mech.*, vol. 34, no. 6, pp. 484–502, Nov. 2004, doi: 10.1007/s00466-004-0593-y.

[158] Smooth$_$On$_$Inc., *Dragon Skin 30*. [Online].http://www.smooth-on.com/tb/files/DRAGON$_$SKIN$_$SERIES$_$TB.pdf, 2015.

[159] A. Georgarakis *et al.*, "A novel pneumatic stimulator for the investigation of noise-enhanced proprioception," in *2017 International Conference on Rehabilitation Robotics (ICORR)*, Jul. 2017, pp. 25–30. doi: 10.1109/ICORR.2017.8009216.

[160] A.-M. Georgarakis *et al.*, "Age-Dependent Asymmetry of Wrist Position Sense Is Not Influenced by Stochastic Tactile Stimulation," *Front. Hum. Neurosci.*, vol. 14, p. 65, Mar. 2020, doi: 10.3929/ethz-b-000409272.

[161] R. L. Klatzky, S. J. Lederman, and C. Reed, "There's more to touch than meets the eye: The salience of object attributes for haptics with and without vision.," *J. Exp. Psychol. Gen.*, vol. 116, no. 4, pp. 356–369, 1987, doi: 10.1037/0096-3445.116.4.356.

[162] S. Okamoto, H. Nagano, and Y. Yamada, "Psychophysical Dimensions of Tactile Perception of Textures," *IEEE Trans. Haptics*, vol. 6, no. 1, pp. 81–93, First 2013, doi: 10.1109/TOH.2012.32.

[163] D. Wang, K. Ohnishi, and W. Xu, "Multimodal Haptic Display for Virtual Reality: A Survey," *IEEE Trans. Ind. Electron.*, vol. 67, no. 1, pp. 610–623, Jan. 2020, doi: 10.1109/TIE.2019.2920602.

[164] S. B. Schorr and A. M. Okamura, "Fingertip Tactile Devices for Virtual Object Manipulation and Exploration," in *Proceedings of the 2017 CHI Conference on Human Factors in Computing Systems*, Denver, Colorado, USA, May 2017, pp. 3115–3119. doi: 10.1145/3025453.3025744.

[165] M. Gabardi, M. Solazzi, D. Leonardis, and A. Frisoli, "A new wearable fingertip haptic interface for the rendering of virtual shapes and surface features," in *2016 IEEE Haptics Symposium (HAPTICS)*, Apr. 2016, pp. 140–146. doi: 10.1109/HAPTICS.2016.7463168.

[166] F. Chinello, M. Malvezzi, C. Pacchierotti, and D. Prattichizzo, "A three DoFs wearable tactile display for exploration and manipulation of virtual objects," in *2012 IEEE Haptics Symposium (HAPTICS)*, Mar. 2012, pp. 71–76. doi: 10.1109/HAPTIC.2012.6183772.

[167] X. de Tinguy, C. Pacchierotti, M. Marchal, and A. Lecuyer, "Enhancing the Stiffness Perception of Tangible Objects in Mixed Reality Using Wearable Haptics," in *2018 IEEE Conference on Virtual Reality and 3D User Interfaces (VR)*, Reutlingen, Mar. 2018, pp. 81–90. doi: 10.1109/VR.2018.8446280.

[168] H. Zhao *et al.*, "A Wearable Soft Haptic Communicator Based on Dielectric Elastomer Actuators," *Soft Robot.*, Jan. 2020, doi: 10.1089/soro.2019.0113.

[169] F. Vidal-Verdu and M. Hafez, "Graphical Tactile Displays for Visually-Impaired People," *IEEE Trans. Neural Syst. Rehabil. Eng.*, vol. 15, no. 1, pp. 119–130, Mar. 2007, doi: 10.1109/TNSRE.2007.891375.

[170] S. Follmer, D. Leithinger, A. Olwal, A. Hogge, and H. Ishii, "inFORM: dynamic physical affordances and constraints through shape and object actuation," in *Proceedings of the 26th annual ACM symposium on User interface software and technology - UIST '13*, St. Andrews, Scotland, United Kingdom, 2013, pp. 417–426. doi: 10.1145/2501988.2502032.

[171] D. Leithinger, D. Lakatos, A. DeVincenzi, M. Blackshaw, and H. Ishii, "Direct and gestural interaction with relief: a 2.5D shape display," p. 8, 2011.

[172] K. Nakagaki *et al.*, "Materiable: Rendering Dynamic Material Properties in Response to Direct Physical Touch with Shape Changing Interfaces," in *Proceedings of the 2016 CHI Conference on Human Factors in Computing Systems*, San Jose California USA, May 2016, pp. 2764–2772. doi: 10.1145/2858036.2858104.

[173] K. Nakagaki, D. Fitzgerald, Z. (John) Ma, L. Vink, D. Levine, and H. Ishii, "inFORCE: Bi-directional `Force' Shape Display for Haptic Interaction," in *Proceedings of the Thirteenth International Conference on Tangible, Embedded, and Embodied Interaction*, Tempe Arizona USA, Mar. 2019, pp. 615–623. doi: 10.1145/3294109.3295621.

[174] L. Yao, R. Niiyama, J. Ou, S. Follmer, C. Della Silva, and H. Ishii, "PneUI: pneumatically actuated soft composite materials for shape changing interfaces," in *Proceedings of the 26th annual ACM symposium on User interface software and technology - UIST '13*, St. Andrews, Scotland, United Kingdom, 2013, pp. 13–22. doi: 10.1145/2501988.2502037.

[175] J. Ou *et al.*, "aeroMorph - Heat-sealing Inflatable Shape-change Materials for Interaction Design," in *Proceedings of the 29th Annual Symposium on User Interface Software and Technology*, Tokyo Japan, Oct. 2016, pp. 121–132. doi: 10.1145/2984511.2984520.

[176] N. Takizawa, H. Yano, H. Iwata, Y. Oshiro, and N. Ohkohchi, "Encountered-Type Haptic Interface for Representation of Shape and Rigidity of 3D Virtual Objects," *IEEE Trans. Haptics*, vol. 10, no. 4, pp. 500–510, Oct. 2017, doi: 10.1109/TOH.2017.2740934.

[177] S. Follmer, D. Leithinger, A. Olwal, N. Cheng, and H. Ishii, "Jamming user interfaces: programmable particle stiffness and sensing for malleable and shape-changing devices," in *Proceedings of the 25th annual ACM symposium on User interface software and technology*, 2012, pp. 519–528.

[178] A. Roudaut, A. Karnik, M. Löchtefeld, and S. Subramanian, "Morphees: toward high" shape resolution" in self-actuated flexible mobile devices," in *Proceedings of the SIGCHI Conference on Human Factors in Computing Systems*, 2013, pp. 593–602.

[179] J.-L. Huang, Z. Zhakypov, H. Sonar, and J. Paik, "A reconfigurable interactive interface for controlling robotic origami in virtual environments," *Int. J. Robot. Res.*, vol. 37, no. 6, pp. 629–647, May 2018, doi: 10.1177/0278364918769157.

[180] L.-K. Ma, Y. Zhang, Y. Liu, K. Zhou, and X. Tong, "Computational design and fabrication of soft pneumatic objects with desired deformations," *ACM Trans. Graph.*, vol. 36, no. 6, pp. 1–12, Nov. 2017, doi: 10.1145/3130800.3130850.

[181] M. Koehler, N. S. Usevitch, and A. M. Okamura, "Model-Based Design of a Soft 3-D Haptic Shape Display," *IEEE Trans. Robot.*, vol. 36, no. 3, pp. 613–628, Jun. 2020, doi: 10.1109/TRO.2020.2980114.

[182] F. Chinello, M. Malvezzi, D. Prattichizzo, and C. Pacchierotti, "A Modular Wearable Finger Interface for Cutaneous and Kinesthetic Interaction: Control and Evaluation," *IEEE Trans. Ind. Electron.*, vol. 67, no. 1, pp. 706–716, Jan. 2020, doi: 10.1109/TIE.2019.2899551.

[183] H. Benko, C. Holz, M. Sinclair, and E. Ofek, "NormalTouch and TextureTouch: High-fidelity 3D Haptic Shape Rendering on Handheld Virtual Reality Controllers," in *Proceedings of the 29th Annual Symposium on User Interface Software and Technology*, Tokyo Japan, Oct. 2016, pp. 717–728. doi: 10.1145/2984511.2984526.

[184] H. A. Sonar, J.-L. Huang, and J. Paik, "Soft Touch using Soft Pneumatic Actuator–Skin as a Wearable Haptic Feedback Device," *Adv. Intell. Syst.*, vol. 3, no. 3, p. 2000168, 2021, doi: https://doi.org/10.1002/aisy.202000168.

[185] Y. Jansen *et al.*, "Opportunities and Challenges for Data Physicalization," in *Proceedings of the 33rd Annual ACM Conference on Human Factors in Computing Systems*, Seoul, Republic of Korea, Apr. 2015, pp. 3227–3236. doi: 10.1145/2702123.2702180.

[186] A. B. Carlson, *Communication Systems: An Introduction to Signals and Noise in Electrical Communication*. New York, USA: McGraw-Hill Education; Internat.2r.e. edition (1986), 1986.

[187] J. L. Sparks *et al.*, "Use of silicone materials to simulate tissue biomechanics as related to deep tissue injury," *Adv. Skin Wound Care*, vol. 28, no. 2, pp. 59–68, Feb. 2015, doi: 10.1097/01.ASW.0000460127.47415.6e.

[188] F. Chinello, M. Malvezzi, C. Pacchierotti, and D. Prattichizzo, "A three DoFs wearable tactile display for exploration and manipulation of virtual objects," in *2012 IEEE Haptics Symposium (HAPTICS)*, Mar. 2012, pp. 71–76. doi: 10.1109/HAPTIC.2012.6183772.

[189] C. Weichel, J. Hardy, J. Alexander, and H. Gellersen, "ReForm: Integrating Physical and Digital Design through Bidirectional Fabrication," in *Proceedings of the 28th Annual ACM Symposium on User Interface Software & Technology - UIST '15*, Daegu, Kyungpook, Republic of Korea, 2015, pp. 93–102. doi: 10.1145/2807442.2807451.

[190] S. Mueller *et al.*, "FormFab: Continuous Interactive Fabrication," in *Proceedings of the Thirteenth International Conference on Tangible, Embedded, and Embodied Interaction*, Tempe Arizona USA, Mar. 2019, pp. 315–323. doi: 10.1145/3294109.3295620.

[191] D. Leithinger, S. Follmer, A. Olwal, and H. Ishii, "Physical telepresence: shape capture and display for embodied, computer-mediated remote collaboration," in *Proceedings of the 27th annual ACM symposium on User interface software and technology - UIST '14*, Honolulu, Hawaii, USA, 2014, pp. 461–470. doi: 10.1145/2642918.2647377.

[192] A. F. Siu, J. Miele, and S. Follmer, "An Accessible CAD Workflow Using Programming of 3D Models and Preview Rendering in A 2.5D Shape Display," in *Proceedings of the 20th International ACM SIGACCESS Conference on Computers and Accessibility*, Galway Ireland, Oct. 2018, pp. 343–345. doi: 10.1145/3234695.3240996.

[193] H. P. Saal and S. J. Bensmaia, "Touch is a team effort: interplay of submodalities in cutaneous sensibility," *Trends Neurosci.*, vol. 37, no. 12, pp. 689–697, Dec. 2014, doi: 10.1016/j.tins.2014.08.012.

[194] Z. Gao, H. Wang, G. Feng, F. Guo, H. Lv, and B. Li, "RealPot: an immersive virtual pottery system with handheld haptic devices," *Multimed. Tools Appl.*, vol. 78, no. 18, pp. 26569–26596, Sep. 2019, doi: 10.1007/s11042-019-07843-3.

[195] H. A. Sonar and J. Paik, "Soft Pneumatic Actuator Skin with Piezoelectric Sensors for Vibrotactile Feedback," *Front. Robot. AI*, vol. 2, p. 38, 2016, doi: 10.3389/frobt.2015.00038.

[196] J.-L. Rodríguez, R. Velázquez, C. Del-Valle-Soto, S. Gutiérrez, J. Varona, and J. Enríquez-Zarate, "Active and Passive Haptic Perception of Shape: Passive Haptics Can Support Navigation," *Electronics*, vol. 8, no. 3, Art. no. 3, Mar. 2019, doi: 10.3390/electronics8030355.

[197] A. I. Weber *et al.*, "Spatial and temporal codes mediate the tactile perception of natural textures," *Proc. Natl. Acad. Sci.*, vol. 110, no. 42, pp. 17107–17112, Oct. 2013, doi: 10.1073/pnas.1305509110.

[198] T. Yoshioka, J. C. Craig, G. C. Beck, and S. S. Hsiao, "Perceptual Constancy of Texture Roughness in the Tactile System," *J. Neurosci.*, vol. 31, no. 48, pp. 17603–17611, Nov. 2011, doi: 10.1523/JNEUROSCI.3907-11.2011.

[199] M. Hollins and S. R. Risner, "Evidence for the duplex theory of tactile texture perception," *Percept. Psychophys.*, vol. 62, no. 4, pp. 695–705, May 2000, doi: 10.3758/bf03206916.

[200] A. M. Smith, G. Gosselin, and B. Houde, "Deployment of fingertip forces in tactile exploration," *Exp. Brain Res.*, vol. 147, no. 2, pp. 209–218, Nov. 2002, doi: 10.1007/s00221-002-1240-4.

[201] S. Joshi, H. A. Sonar, and J. Paik, "Flow path optimization for soft pneumatic actuators: To-wards optimal performance and portability," *IEEE Robot. Autom. Lett.*, Feb. 2021.

[202] J. L. Sparks *et al.*, "Use of silicone materials to simulate tissue biomechanics as related to deep tissue injury," *Adv. Skin Wound Care*, vol. 28, no. 2, pp. 59–68, 2015.

[203] M. A. Robertson and J. Paik, "Trunk postural tracking of assistive soft pneumatic actuator belt," in *Dynamic Walking Conference*, 2016, no. EPFL-TALK-231820.

[204] M. Wehner *et al.*, "Pneumatic energy sources for autonomous and wearable soft robotics," *Soft Robot.*, vol. 1, no. 4, pp. 263–274, 2014.

[205] P. Rothemund *et al.*, "A soft, bistable valve for autonomous control of soft actuators," *Sci. Robot.*, vol. 3, no. 16, Mar. 2018, doi: 10.1126/scirobotics.aar7986.

[206] Y.-L. Park *et al.*, "Design and control of a bio-inspired soft wearable robotic device for ankle–foot rehabilitation," *Bioinspir. Biomim.*, vol. 9, no. 1, p. 016007, 2014.

[207] Y.-L. Park, J. Santos, K. G. Galloway, E. C. Goldfield, and R. J. Wood, "A soft wearable robotic device for active knee motions using flat pneumatic artificial muscles," in *Robotics and Automation (ICRA), 2014 IEEE International Conference on*, 2014, pp. 4805–4810.

[208] H. K. Yap, N. Kamaldin, J. H. Lim, F. Nasrallah, J. C. Goh, and C.-H. Yeow, "A magnetic resonance compatible soft wearable robotic glove for hand rehabilitation and brain imaging," *IEEE Trans. Neural Syst. Rehabil. Eng.*, 2016.

[209] M. T. Tolley *et al.*, "A Resilient, Untethered Soft Robot," *Soft Robot.*, vol. 1, no. 3, pp. 213–223, Aug. 2014, doi: 10.1089/soro.2014.0008.

[210] R. F. Shepherd *et al.*, "Multigait soft robot," *Proc. Natl. Acad. Sci.*, vol. 108, no. 51, pp. 20400–20403, Dec. 2011, doi: 10.1073/pnas.1116564108.

[211] C. D. Onal and D. Rus, "Autonomous undulatory serpentine locomotion utilizing body dynamics of a fluidic soft robot," *Bioinspir. Biomim.*, vol. 8, no. 2, p. 026003, 2013.

[212] A. D. Marchese, C. D. Onal, and D. Rus, "Autonomous soft robotic fish capable of escape maneuvers using fluidic elastomer actuators," *Soft Robot.*, vol. 1, no. 1, pp. 75–87, 2014.

[213] M. Luo, M. Agheli, and C. D. Onal, "Theoretical modeling and experimental analysis of a pressure-operated soft robotic snake," *Soft Robot.*, vol. 1, no. 2, pp. 136–146, 2014.

[214] A. A. Stokes, R. F. Shepherd, S. A. Morin, F. Ilievski, and G. M. Whitesides, "A hybrid combining hard and soft robots," *Soft Robot.*, vol. 1, no. 1, pp. 70–74, 2014.

[215] M. Manti, T. Hassan, G. Passetti, N. D'Elia, C. Laschi, and M. Cianchetti, "A bioinspired soft robotic gripper for adaptable and effective grasping," *Soft Robot.*, vol. 2, no. 3, pp. 107–116, 2015.

[216] J. Walker *et al.*, "Soft Robotics: A Review of Recent Developments of Pneumatic Soft Actuators," *Actuators*, vol. 9, no. 1, 2020, doi: 10.3390/act9010003.

[217] S. Joshi and J. Paik, "Pneumatic supply system parameter optimization for soft actuators," *Soft Robot.*, 2020.

[218] S. Joshi and J. Paik, "Multi-DoF Force Characterization of Soft Actuators," *IEEE Robot. Autom. Lett.*, vol. 4, no. 4, pp. 3679–3686, 2019.

[219] M. A. Robertson, H. Sadeghi, J. M. Florez, and J. Paik, "Soft Pneumatic Actuator Fascicles for High Force and Reliability," *Soft Robot.*, vol. 4, no. 1, pp. 23–32, Mar. 2017, doi: 10.1089/soro.2016.0029.

[220] R. A. Bilodeau, E. L. White, and R. K. Kramer, "Monolithic fabrication of sensors and actuators in a soft robotic gripper," in *2015 IEEE/RSJ International Conference on Intelligent Robots and Systems (IROS)*, 2015, pp. 2324–2329.

[221] G. Frediani and F. Carpi, "Tactile display of softness on fingertip," *Sci. Rep.*, vol. 10, no. 1, Art. no. 1, Nov. 2020, doi: 10.1038/s41598-020-77591-0.

[222] B. Mosadegh *et al.*, "Pneumatic Networks for Soft Robotics that Actuate Rapidly," *Adv. Funct. Mater.*, vol. 24, no. 15, pp. 2163–2170, 2014, doi: https://doi.org/10.1002/adfm.201303288.

[223] S. Terryn, J. Brancart, D. Lefeber, G. Van Assche, and B. Vanderborght, "Self-healing soft pneumatic robots," *Sci. Robot.*, vol. 2, no. 9, 2017.

[224] B.-S. Kang, C. S. Kothera, B. K. Woods, and N. M. Wereley, "Dynamic modeling of Mckibben pneumatic artificial muscles for antagonistic actuation," in *Robotics and Automation, 2009. ICRA'09. IEEE International Conference on*, 2009, pp. 182–187.

[225] T. Itto and K. Kogiso, "Hybrid modeling of McKibben pneumatic artificial muscle systems," in *Industrial Technology (ICIT), 2011 IEEE International Conference on*, 2011, pp. 65–70.

[226] X. Shen, "Nonlinear model-based control of pneumatic artificial muscle servo systems," *Control Eng. Pract.*, vol. 18, no. 3, pp. 311–317, 2010.

[227] T. Nguyen, J. Leavitt, F. Jabbari, and J. Bobrow, "Accurate sliding-mode control of pneumatic systems using low-cost solenoid valves," *IEEEASME Trans. Mechatron.*, vol. 12, no. 2, pp. 216–219, 2007.

[228] P. Beater, *Pneumatic drives: System Design, Modelling and Control*. Springer, 2007.

[229] P. G. Harris, G. E. O'Donnell, and T. Whelan, "Modelling and identification of industrial pneumatic drive system," *Int. J. Adv. Manuf. Technol.*, vol. 58, no. 9–12, pp. 1075–1086, 2012.

[230] J. Eckersten, "Simplified flow calculations for pneumatic components," *Atlas Copco Air Compend. Atlas Copco AB Tukholma*, pp. 183–192, 1975.

[231] *ISO 6358-1:2013*. 2013. [Online]. Available: https://www.iso.org/standard/56612.html

[232] R. W. Cholewiak and A. A. Collins, "The generation of vibrotactile patterns on a linear array: Influences of body site, time, and presentation mode," *Percept. Psychophys.*, vol. 62, no. 6, pp. 1220–1235, Sep. 2000, doi: 10.3758/BF03212124.

[233] J. J. Zwislocki and E. M. Relkin, "On a psychophysical transformed-rule up and down method converging on a 75% level of correct responses," *Proc. Natl. Acad. Sci.*, vol. 98, no. 8, pp. 4811–4814, Apr. 2001, doi: 10.1073/pnas.081082598.

[234] D. Chapuis, R. B. de Grave, O. Lambercy, and R. Gassert, "ReFlex, a haptic wrist interface for motor learning and rehabilitation," in *2010 IEEE Haptics Symposium*, Mar. 2010, pp. 417–424. doi: 10.1109/HAPTIC.2010.5444622.

[235] J. H. Kirman, "Tactile apparent movement: The effects of shape and type of motion," *Percept. Psychophys.*, vol. 34, no. 1, pp. 96–102, Jan. 1983, doi: 10.3758/BF03205902.

[236] S. J. Bolanowski, G. A. Gescheider, R. T. Verrillo, and C. M. Checkosky, "Four channels mediate the mechanical aspects of touch," *J. Acoust. Soc. Am.*, vol. 84, no. 5, pp. 1680–1694, Nov. 1988, doi: 10.1121/1.397184.

[237] J. P. Roll, J. P. Vedel, and E. Ribot, "Alteration of proprioceptive messages induced by tendon vibration in man: a microneurographic study," *Exp. Brain Res.*, vol. 76, no. 1, pp. 213–222, 1989, doi: 10.1007/BF00253639.

[238] E. Sejdić and L. A. Lipsitz, "Necessity of noise in physiology and medicine," *Comput. Methods Programs Biomed.*, vol. 111, no. 2, pp. 459–470, Aug. 2013, doi: 10.1016/j.cmpb.2013.03.014.

[239] F. Duan, F. Chapeau-Blondeau, and D. Abbott, "Stochastic Resonance with Colored Noise for Neural Signal Detection," *PLOS ONE*, vol. 9, no. 3, p. e91345, Mar. 2014, doi: 10.1371/journal.pone.0091345.

[240] W. H. Ehrenstein and A. Ehrenstein, "Psychophysical Methods," in *Modern Techniques in Neuroscience Research*, U. Windhorst and H. Johansson, Eds. Berlin, Heidelberg: Springer, 1999, pp. 1211–1241. doi: 10.1007/978-3-642-58552-4_43.

[241] J. C. Gilhodes, J. P. Roll, and M. F. Tardy-Gervet, "Perceptual and motor effects of agonist-antagonist muscle vibration in man," *Exp. Brain Res.*, vol. 61, no. 2, pp. 395–402, Jan. 1986, doi: 10.1007/BF00239528.

[242] S. Kikkert, H. A. Sonar, P. Freund, J. Paik, and N. Wenderoth, "Hand face somatotopy shown by MRI-safe vibrotactile stimulation with new soft pneumatic actuators," presented at the The Organization for Human Brain Mapping (OHBM), 2020.

[243] H. A. Sonar and J. Paik, "Soft pneumatic actuator skin with piezoelectric sensors for vibrotactile feedback," *Front. Robot. AI*, vol. 2, p. 38, 2016, doi: 10.3389/frobt.2015.00038.

[244] M. Jenkinson, P. Bannister, M. Brady, and S. M. Smith, "Improved optimization for the robust and accurate linear registration and motion correction of brain images," *NeuroImage*, vol. 17, no. 2, pp. 825–841, 2002, doi: 10.1016/S1053-8119(02)91132-8.

[245] S. M. Smith, "Fast robust automated brain extraction," *Hum. Brain Mapp.*, vol. 17, no. 3, pp. 143–155, 2002, doi: 10.1002/hbm.10062.

[246] M. Jenkinson and S. M. Smith, "A global optimization method for robust affine registration of brain images," *Med. Imaging Anal.*, vol. 5, pp. 143–156, 2001.

[247] D. N. Greve and B. Fischl, "Accurate and robust brain image alignment using boundary-based registration," *NeuroImage*, vol. 48, no. 1, pp. 63–72, 2009, doi: 10.1016/j.neuroimage.2009.06.060.

[248] S. Kikkert, D. Pfyffer, M. Verling, P. Freund, and N. Wenderoth, "Finger somatotopy is preserved after tetraplegia but deteriorates over time," *bioRxiv*, 2021.

Curriculum Vitae

Harshal A. Sonar

Doctoral Assistant, Reconfigurable Robotics Lab,
École Polytechnique Fédérale de Lausanne
Contact : Harshal.sonar@epfl.ch

EDUCATION

Ph.D. candidate, Robotics and Intelligent Systems
Thesis title: "Comprehensive Interactive Soft Interfaces For Wearable Tactile Feedback"
Supervisor: Prof. Jamie Paik
Reconfigurable Robotics Lab, EPFL, CH   Mar 15 - present

Master of Technology (M.Tech.)
Electrical Engineering (control and computing)   9.67/10
Indian Institute of Technology Bombay, Mumbai, IN   Jul 11 - Aug 14

Bachelor of Engineering (B.E.)
Electronics and Telecommunication   3.73/4
Pune Institute of Computer Technology, Pune, IN   Aug 07 - Jun 11

PUBLICATIONS

Journal Articles:

[4] **Sonar, H. A.** , & Paik, J., "SPA-skin with piezoelectric sensors for vibrotactile feedback". *Frontiers in Robotics and AI* , 2(38), 2016.

[5] Moseley, P., Florez, J. M., **Sonar, H. A.** , Agarwal, G., Curtin, W., & Paik, J., "Modeling, design, and development of soft pneumatic actuators with finite element method". Advanced engineering materials, 18(6), 978-988, 2016.

[6] **Sonar, H. A.** , Gerratt, A. P., Lacour, S. P., & Paik, J., "Closed-loop haptic feedback control using a self-sensing soft pneumatic actuator skin". *Soft robotics* , 7(1), 22-29, 2020.

[7] **Sonar, H. A.** , Huang, J.L. & Paik, J., "Soft Touch using SPA–Skin as a Wearable Haptic Feedback Device". *Advanced Intelligent Systems* , p. 2000168, 2021.

[8] Agarwal, G., Robertson, M. A., **Sonar, H. A.** , & Paik, J., "Design and computational modeling of a modular, compliant robotic assembly for human lumbar unit and spinal cord assistance". *Nature Scientific reports* , 7(1), 1-11, 2017.

[9] Huang, J.-L., Zhakypov, Z., **Sonar, H. A.** , & Paik, J., "A Reconfigurable Interactive Interface for Controlling Robotic Origami in Virtual Environments", *The International Journal of Robotics Research (IJRR)* , 37(6), 2018.

[10] Georgarakis, A. M., **Sonar, H. A.** , Rinderknecht, et al.,"Age-dependent asymmetry of wrist position sense Is not influenced by stochastic tactile stimulation", *Frontiers in human neuroscience* , 14, 65, 2020. *(Best PhD Paper Award, NCCR Robotics)*

[11] Joshi, S., **Sonar, H. A.** , & Paik, J., "Flow path optimization for soft pneumatic actuators: Towards optimal performance and portability", *IEEE Robotics and Automation Letters* , 2021. *(in Review)*

Conference Papers/Posters:

[12] Shintake, J., **Sonar, H. A.** , Piskarev, E., Paik, J., & Floreano, D.," Soft pneumatic gelatin actuator for edible robotics", *IEEE/RSJ International Conference on Robots and Systems (IROS17)* pp. 6221-6226, 2017

[13] Georgarakis, A.-M., **Sonar, H. A.** , Rinderknecht, M. D., Lambercy, O., Martin, B. J., Klamroth-Marganska, V.,Paik, J., Riener, R., & Duarte J. E., *IEEE International Conference on Rehabilitation Robotics (ICORR)* , pp. 25-30, 2017.

[14] **Sonar, H. A.** , Joshi, S. D., Robertson, M. A., & Paik, J., "Interactive soft pneumatic actuator skin. *In IEEE/RSJ*

International Conference on Intelligent Robots and Systems (IROS) , 2017. *(Best poster award)*

[15] **Sonar, H. A.** , Yuen, M. C. S., Kramer-Bottiglio, R., & Paik, J, "An any-resolution distributed pressure localization scheme using a capacitive soft sensor skin", *IEEE Int. Conference on Soft Robotics (RoboSoft)* ,pp. 170-175, 2018.

[16] Kikkert, S., **Sonar, H. A.** , Freund, P., Paik, J., & Wenderoth, N., "Hand face somatotopy shown by MRI-safe vibrotactile stimulation with new soft pneumatic actuators", *In annual meetings, The Organization for Human Brain Mapping (OHBM)* , 2020.

[17] Boudoire, F., **Sonar, H. A.** , Unterhofer, S., Dayat, D., Lani S. & Paik, J. , "Printing miniature valves by micro-SLA for soft robotics"., *21st EUSPEN international conference* , 2021. *(Submitted)*

PATENTS

[1] **Sonar, H.A.** , Robertson, M., Joshi, S., Bhatnagar, T., & Jamie, P., "A Soft Portable Wearable Pneumatic Interactive Suit", *U.S. Appl. No. 62/514,234* . (filed Jun. 2, 2017).

EXPERIENCE

Doctoral Assistant, CH

Reconfigurable Robotics Lab, EPFL, Lausanne   [Jan 15 – Present]

Design and implementation of novel soft-material based sensors, soft pneumatic actuators (SPA) and integrated robotic systems for human-machine interactive applications

Technologies : soft sensors, soft actuator fabrication, system identification, embedded mechatronic design, signal conditioning, material characterization, FEA, fMRI compliant systems, machine learning based sensor state estimation

Tools developed : Interactive SPA-skin hardware and embedded testbeds with highspeed data acquisition, closed loop soft-robotics controllers, spa-design-toolkit FEA software, edible robots.

Field of application : soft robotics, VR/AR haptics, wearable tactile feedback with artificial skin, fMRI compliant haptic actuators, rehabilitation robotics.

R & D Manager, IN

Engineering Research Centre, Tata Motors, Pune, India   [Sept. 14 - Nov. 14]

Gear Shift Advisor (GSA) design for Tata Prima truck: An embedded controller to communicate between ECU and Transmission Control Unit (TCU) over CAN protocol [ISO 14229] and extract the useful information to advise the driver about ideal gear suited for current driving condition.

Embedded coding for CAN:ISO 14229, firmware design, state estimation and control from noisy sensors

Research Assistant, IN

Electronics Measurement Lab, IIT Bombay, India   [Jul 11 - Aug 14]

Design and smooth running of experiments in electronics design and measurement including managing 600 students and 50 TAs with training for modern day sensing and measurement using basic components

Microcontroller programming, signal-conditioning, design of experiments, managing large teams

RESEARCH PROJECTS

- **SPA-Skin with Piezoelectric Sensors for Vibrotactile Feedback** [May 15 - Present]
  Advisor: Prof. Jamie Paik, EPFL.
  - **Description:** The project involves design and fabrication of the ultra thin soft pneumatic actuator (SPA) based interface that is integrated with piezoelectric sensors.[Published in *Frontiers in Robotics and AI, Bionics and Biomimetics*]
  - **Results:** The mechanical performance compared to the SPA model and the sensitivity of the sensors are examined in detail for its application in vibrotactile feedback.
  - The main contributions are the novel hardware design of the ultra-thin SPA actuators and unique integration process of the discrete PZT sensors to achieve accurate and distributed measure of soft contact sensing as well as closing the actuator control loop.

- **Bidirectional interactive wearable tactile interface using SPA-skin array** [Jun 17 - Present]
  Advisor: Prof. Jamie Paik, EPFL.
  - **Description:** The project involves adaptation and optimization of the PZT sensor integrated soft pneumatic actuator (SPA)-skin interface[Sonar et. al,*Frontiers in Robotics and AI,2016*], to develop a 4x4 sensor-actuator skin. The actuation of the SPA-skin is targeted to stimulate the 10-100 Hz range specifically, to explore and quantify the effects of vibration stimulus on the human skin in this range. This SPA-skin array provides a unique wearable platform for quantifying the somatosensory thresholds of actuation amplitude, traveling wave delay, and frequency difference perceived by the real human skin.
  - **Results:** The presented framework of the SPA-skin platform, experimental validation, and user studies enable the design of a dynamic tactile feedback device where geometrical parameters, dynamic actuation, and control sequences can be adapted to match the required in an application.

- **fMRI compatible tactile actuation using a portable plug-n-play soft controller**[Jun 18 - Present]
  Advisor: Prof. Jamie Paik, EPFL, Prof. Tamar Makin, UCL and Prof. Nicole Wenderoth, ETHZ
  - **Description:** The project involves a state of art design, parameter optimization for high bandwidth actuation of SPA-skin interface for 5-6 m tube length to stimulate specific locations on human body and record the respective brain activity in the sensory motor-cortex area using fMRI based brain imaging. The project requires a fMRI compliant actuator with high-fidelity of vibratory actuation (0-30 Hz) with portable system that can be seamlessly integrated and controlled with available brain imaging research tools (Matlab).
  - **Results:** The plug-n-play prototype system with ring-shape actuators and custom portable controller setup is able to provide 0-30Hz bandwidth with 1 N output force and 8 CH. vibrotactile control. It is being used in neuro imaging and motor control labs at UCL and ETHZ to replicate the known sensory-motor maps using SPA-skin technology and is further expanded to develop protocols and study abilities of healthy humans to differentiate different locations, amplitude and actuation frequencies distinctively, successfully.

- **Modeling and Characterization of Soft Pneumatic Actuators (SPA)** [Jan.15 - Jun.15]
  Advisor: Prof. Jamie Paik, EPFL.
  - **Description:** An open source FEM based software tool is developed which produces optimal design parameters for SPA of desired linear/angular displacement and desired blocked force. [Accepted in journal of Advanced Engineering Materials (AEM)]
  - Multiple hyperelastic material models are evaluated for soft material (Ecoflex 30) based SPAs for linear and bending motion using finite element methods and experimental validation.

- **My contributions:** Conducted design of experiments and testbed development to acquire material stress-strain data, planer/angular displacement data and blocked force data for variety of planer/bending SPAs. Hyperelastic model is then validated using experimental parameters obtained from these tests.

• **Embedded Testbed Design for Co-operative Control of Multiple Quadcopters**
  Thesis Advisor: Prof. Debraj Chakraborty, E.E. Dept., IIT Bombay.   [Jan.13-Jul.14]
    - **Description:** Design a testbed to test finite time consensus of two or more UAVs (quadcopters) which will co-operate with each other in a decentralized manner.
    - **Work done:** Quadcopter prototype has been built and tested in closed-loop stabilized flight mode.
    - Modification and customization of an open source autopilot program (Aeroquad) to embed/port capabilities like altitude hold, GPS navigation, obstacle detection, and real-time log telemetry to base station, is carried out. A single quadcopter with these autonomous navigation capabilities acts as an agent in the testbed.
    - **Results:** Simple co-operative control strategies like leader-follower with multiple quadcopters has been successfully tested. Work has recently been reported in the literature in the *10th international workshop on Robot Motion and Control (RoMoCo'15)* .

• **Gear Shift Advisor (GSA) for Tata Prima Truck** [Sept.14-Nov.14]
  Supervisor: Ashoka Kumar, DGM, Engines Dept., Engg.Research Centre, Tata Motors Ltd.
    - **Description:** To develope an embedded controller which communicates between ECU and Transmission Control Unit (TCU) over CAN protocol [ISO 14229] and extract the useful information about system states like throttle position, engine speed, current gear, clutch position, wheel speed etc.
  Then analyze the data to advise the driver about ideal gear suited for current driving condition.
    - **Results:** Initial road tests showed 15-20% increase in fuel efficiency with GSA. The final product will be integrated to the dashboard of a mass produced vehicle.

• **Automatic Frequency Response Plotter**   [Jan.13-Jun.13]
  Guide: Prof. P. C. Pandey, E.E. Dept., IIT Bombay.
    - Implemented a cost effective embedded system using 32-bit TI-MCU, built in fast capture 12-bit ADC and external 12-bit DAC with 10 Hz to 25 kHz frequency range.
    - Recorded frequency response of various filters and an audio amplifier automatically.

• **State Estimation and Control of Three Phase Induction Motor**   [Jul.12-Dec.12]
  Guide: Prof. Sachin C. Patwardhan, Chemical Dept., IIT Bombay.
    - Simulated nonlinear model of induction motor in a noisy environment.
    - Luenberger observer and Kalman filter for linearized model failed to follow actual states due to non-linearity. Therefore, **Unscented-KF** was used to estimate states of system and control motor using state feedback.

• **Hardware and Software Partitioning Methods and Algorithms**   [Aug.11-Dec.11]
  Guide: Prof. H. Narayanan,E.E. Dept.,IIT Bombay.
    - Presented an analysis of network graph partition algorithms Kernighan- Lin and Fiduccia-Mattheyses.
    - Effect of initial seed partition on graph convergence time is studied using *Application of Fast DC Analysis to Partitioning Hypergraphs* paper by Prof. H. Narayanan and Dr. G. Trivedi.
    - Also demonstrated, Algorithmic State Machine analysis as a procedure for hardware and software partitioning.

AREAS OF INTEREST

• **Soft robotics** : soft sensors, soft actuators, and closed loop control

• **Haptic interfaces** : Wearable tactile feedback, fMRI compliant haptics

• **Multi-agent autonomous systems** : state estimation, communication, system design, and control

TECHNICAL SKILLS

Programming Languages :	C, Embedded C/C++, MATLAB, SciLab, LabView, C#(Unity3D).
Hardware Platforms :	AVR, RaspberryPi, TI 32-bit Piccolo family, 8051, Beaglebone, Leapmotion, Teensy 4.1/3.6, Makerbot, HP 3D printer, Laser micro-machining.
Software Platforms :	Arduino, TI Code Composer Studio, X-CTU (Zigbee Config.), Eagle CAD, Proteus, Solid Works, AutoCAD, OpenCV, LₐTEX, Beamer, Github.

AWARDS & ACHIEVEMENTS

- Awarded "**Best PhD paper**" by NCCR Robitcs in 2021 for a co-authored publication [
- Awarded **Best poster** for "Interactive SPA-skin" in IEEE-IROS Conference, Vancouver. (in 2017)
- Awarded 1st **prize** in Bio-inspired robot design competition for multi terrain crawler at Robosoft, Soft robotics week, Italy. (in 2015)
- Awarded 1st **prize** in national level project competition Impetus and Concepts conducted by PICT, Pune under instrumentation and control category. (in 2011)
- Received **Gold medal** in Football at PG-Sports 2011, IIT Bombay.(in 2011)
- Won 1st **prize** in national level Electronic Design competition organised by IEEE and Thadomal Sahani Engineering College, Mumbai. (in 2011)

EXTRACURRICULAR ACTIVITIES

- **IT Manager** , Reconfigurable Robotics Lab, EPFL   [Mar.16-Present]
- **Core Member** , YUVA: Indian cutural accociation at EPFL   [Mar.16-Mar.17]
- **Computer Secretary** , Hostel 1, IIT Bombay   [Jul.13-Jul.14]
    - Responsible for smooth running of entire internet facility for student residence of 400 students.
- **Head Research Assistant of Experimental and Measurement Lab** [Jul.13-Jul.14] • **Core Member** , PICT Team, ROBOCON 2010 [Feb.09-Feb.10]
    - Represented PICT in national level robotics competition for first time.
    - Developed two autonomous and one manual robots under limited funding.
    - Core member of robot design and game strategy planning team and operator for manual robot.

HOBBIES

Sports (football, badminton, skiing) , hiking, automotive-model building, and painting.